Damage tolerance of composite stiffened structures

Kontis, Nikolaos

Award date:
2008

Awarding institution:
University of Bath

Damage Tolerance of Composite Stiffened Structures

Submitted by

Nikolaos Kontis

for the degree of Doctor of Philosophy

of the

University of Bath

Department of Mechanical Engineering

May 2008

To my mother and father

and

my beloved grandparents

Contents

Acknowledgements

The author would like to express his sincere appreciation to his supervisors, Dr. Richard Butler and Prof. Giles W. Hunt, for their expertise, guidance, encouragement and constant support throughout the duration of this work.

Others who the author would like to thank are Dr. Martin Gaitonde, Dr. Nihong and Mr. Phillip Brown from Airbus UK Ltd and Mr. Robert Lewis from Hexcel Composites Ltd for the valuable assistance with this research. Thanks are due to the University of Bath for their financial support and members of staff (both past and present) that were involved in various areas of this work. Mr. Tony Elley, Mr. Hilary Jones and Mr. Les Duddridge for their technical assistance, Dr. Beilei Hu for his advice on computational aspects of this work and all my fellow colleagues.

Last but not least, I would like to thank my family for their constant interest in my education and for their continual support.

This research was sponsored by Airbus UK Ltd., Hexcel Composites Ltd. and the University of Bath.

Abstract

Composite stiffened panels have been extensively used in primary aerospace applications, due to their efficient stiffness/weight ratio and the ability to tailor properties. Despite their apparent superiority to metals, the susceptibility of composites to damage has proved to be a critical factor. A common example in practice is the barely visible impact damage caused by a low velocity impact event. Such events can generate inter-laminar defects (delaminations), which under compressive loading can reduce the strength and stability of the structure. There is a need to establish the influence of such damage on composite stiffened structures. Current practice allows for delamination induced strength reduction by applying strain limits to the material that ensure delamination does not produce failure before ultimate levels of loading. However, these limits are established via coupon tests, which focus on the scale of the delamination only and do not account for the interaction at the structural scale.

The objective of the current work is to investigate the behaviour of the delaminated region in the presence of structural effects and coupling phenomena, and subsequently, identify the effect of the delamination itself in the pre- and post-buckling response of the structure. Therefore, efficiency and safety requirements in composite stiffened structures may be enhanced. In accordance to simplified plate and strut models, delaminations may have little or significant debilitating effect according to their position through the depth of the laminate. Thus, the current work investigates experimentally and theoretically the effect of delamination damage, in a variety of locations and through the thickness positions, on the strength and stability of a laminated thin-walled channel-section strut.

Both damaged and undamaged channel-section struts are designed according to novel design methods. The effectiveness of the methods is established by comparisons to

numerical and experimental results. Efficient manufacturing processes and modeling problems using finite element methods are presented and solved. The material behaviour of carbon-fibre reinforced plastics (CFRP) is also examined.

The most important conclusions and findings drawn with the aid of experimental results and their correlation to the finite element models developed are as follows. Contrary to delaminated coupons, at the structural level it is established that deeper-sited delaminations are the most dangerous for structural strength. Furthermore, delamination is not a symmetric phenomenon. Structural parameters may affect all aspects (i.e critical load, buckling mode and post-critical configuration) of the delamination buckling behaviour depending on its position within the structure, the depth and its position relative to the mid-surface of the laminate. The particular cases of thin-film buckling with in plane distortion and shearing mode are discovered at the structural level.

Generally, deeper-sited delaminations in the skin are potentially the most detrimental for structural stability, while deeper-sited delaminations in the stiffener are the most hazardous for the load-carrying capacity of the structure. The presence of the delamination more often than not significantly affects the structural buckling mode (that is, in comparison to the undamaged strut). It may also induce decoupling of interacting modes in the post-buckling region depending on the position and level of delamination. In the latter event mode-jumping will occur into a global mode of deformation defined by the aforementioned dependencies.

For well designed composite structures in the sense that sufficient post-buckling strength allowables are provided, the design ultimate loading conditions (DUL) will not be compromised even for particularly thin-walled structures (such as the one considered) with significant delaminations at various structural positions and depths. Thus, reductions in weight of composite stiffened structures may be achieved by designing for higher buckling strain allowables without comprising safety requirements. Finally, due to material non-linearity of CFRP it is more efficient to design highly strained composite stiffened structures to fail in a localized mode of buckling.

List of Figures

List of Tables

Notation

A_{ij} elements of the extensional stiffness matrix of the laminate

$\bar{A}_{sk}$ extensional stiffness of the skin laminate

$\bar{A}_{st}$ extensional stiffness of the stiffener laminate

b width of the skin of the channel cross-section strut

b_y width of a plate

c initial clearance in the exponential contact relationship

d diameter of circular/semi-circular delamination

E_{11} axial modulus

E_{22} transverse modulus

E_x effective modulus in the longitudinal direction

G_{12} in-plane shear modulus

G_{13} interlaminar axial shear modulus

G_{23} interlaminar transverse shear modulus

h height of the stiffener of the channel cross-section strut

k_{sk} stiffness of the skin

k_{sk}' reduced stiffness of the skin

k_{st} stiffness of the stiffeners

k layer number

L length of the channel section strut

l_x length of a plate

M_x bending moment along the longitudinal axis

M_{xy} bending moment acting in-plane

M_y bending moment along the transverse axis

N number of layers

N_x axial load per unit width

N_{xy} shear load per unit width

N_y transverse load per unit width

n delamination level

P total load applied

P_c buckling load of the undamaged channel-section strut

P_C^D delamination buckling load of the damaged channel-section strut

P_C^S structural buckling load of the damaged channel-section strut

P_G loading at the onset of delamination growth

P_I loading at which secondary instability occurs

P_U^S ultimate load of the damaged and undamaged channel-section struts

p_0 maximum pressure load in the exponential contact relationship

p_{sk} load in the skin

$p_{sk,cr}$ critical load in the skin

p_{st} load in the stiffeners

$p_{st,cr}$ critical load in the stiffeners

Q_{ij} elements of the transformed stiffness matrix of the laminate

T thickness of the laminate

t_c thickness of material-test coupons

t_{ply} thickness of a single ply

t_t thickness of the tabs

U_x longitudinal degree of freedom

U_y transverse degree of freedom

U_z normal degree of freedom

R_x rotational degree of freedom about the longitudinal axis

R_y rotational degree of freedom about the transverse axis

R_z rotational degree of freedom about the normal axis

u axial displacement

u^0 axial displacement of the mid-surface of the laminate

y' distance from the neutral axis

v transverse displacement

v^0 transverse displacement of the mid-surface of the laminate

v_{12} Poisson's ratio

z' distance of each layer from the mid-surface

$\bar{z}$ distance of the neutral axis from the bottom surface

w normal deflection

w^0 normal deflection of the mid-surface of the laminate

α factor of post-buckled strength

γ_{xy} shear strain

γ_x^0 shear strain in the mid-surface of the laminate

ε_C^D axial delamination buckling strain

ε_x axial strain

ε_x^0 axial strain in the mid-surface of the laminate

ε_y transverse strain

ε_y^0 transverse strain in the mid-surface of the laminate

η stiffness reduction parameter

θ angle of fibre orientation in respect to the global longitudinal axis

κ_x axial curvature

κ_{xy} in-plane curvature

κ_y transverse curvature

Chapter 1

Introduction

Over the past few decades the aeronautics and space industry has solidified its impact in the global economy and society, by the exploitation and development of leading technological advances. Currently however it is called upon to address the new challenges facing the future of the industry, which involve a more efficient, safer and environmental friendly aircraft. These objectives have been characterized as top level and identified in the "Vision 2020" report (European Commission, 2001). Amongst other factors, it is stated that significant reductions in fuel emissions and a five-fold reduction in accidents must be achieved. The significance, therefore, of the continuing quest for the design of the lowest weight aircraft structure, that can tolerate damage without jeopardizing safety requirements, becomes ever more critical.

The introduction of laminated carbon fiber-reinforced composites in primary loading bearers, such as the stiffened structural components, has been a substantial step in this direction. Their general lightweight allied with high strength and stiffness, fatigue strength and corrosion resistance, has associated them with high performance and significant weight-saving. Furthermore the design allowables, determined by the material's expected performance in service, has established them as a tremendous asset in a field where structural requirements are particularly challenging and often conflicting. More than ever before, the designer has the ability to manipulate the material accordingly, in order to satisfy the anticipated work load and environment of the individual structural component.

The incentive, however, to minimize the structural weight of the aircraft has stretched the factor of safety, which is defined as the ratio of the design limit load (DLL*)* and the design ultimate load (DUL), to a near zero positive margin above the designated ratio (Harris et al., 2002). Consequently, in the event of unanticipated damage, the structural integrity and safety requirements would be compromised. The realization of the hazardous nature of such an event has eventually evolved to a design philosophy that necessitates structural components to be able to tolerate damage until the point of detection and elimination, without their strength and stiffness falling to unacceptable levels. It thus becomes clear that a thorough understanding of the damage mechanisms involved is essential in order to determine the damage tolerance capability of safe-critical structural components.

Although significant knowledge has been gained over past decades by the incorporation of metals in primary loading bearers, nevertheless it cannot be directly applied to the design of composite structures. This is primarily attributed to the fact that composite technology differs practically in all aspects to metals. Their disparity is not only focused in the material itself, but is extended to the manufacturing processes, design methodology and, more significantly, to the means and nature of damage inflicted upon them (Hoskin and Baker, 1986). A common example in practice is the barely visible impact damage (BVID) caused by a low-energy impact event. In laminated composites such events can generate inter-laminar defects (delaminations), which under compressive loading can lead to the degradation of strength and loss of stability (buckling) of the structure.

Current practice allows for delamination induced strength reduction by applying strain limits to the material that ensure the delamination does not produce failure before ultimate levels of loading. However these limits are established via coupon tests, which focus on the scale of the delamination only and do not account for any interactions with the structure itself. Typically, for aircraft applications, these strain allowables are restricted between 0.3% and 0.4% (Davies et al., 1994; Cantwell et al. 1986) at ultimate level; arguably a low value considering that common undamaged carbon-reinforced

composites fail in excess of 1.2% strain (Reid and Zhou, 2000; Cantwell et al., 1986). Thus, the full potential of the composite system may not be attained and may lead to over-designed (heavier than necessary) components. In order such restriction be eliminated, or at least be less conservative, an accurate assessment of the behaviour of the delaminated structure must be conducted. In view of the fact that composite stiffened structures can carry significant load beyond initial instability and weight considerations are driving the design ultimate load to be defined within the initial post-buckled state, it is therefore imperative to identify the influence of structural coupling effects, in the delaminated structure, both for pre and post-buckling.

This thesis aims to make a contribution towards this area, by investigating both experimentally and theoretically the effect of embedded delaminations in a thin-walled composite channel-section strut. To achieve this, a variety of locations and through-thickness positions of delamination are being considered. The ultimate objective is to develop and refine the current design philosophy and promote confident use of composite materials in further primary positions. In this chapter important definitions, as well as the contribution of the current work, are discussed in more detail and an outline of the thesis is presented.

1.1 Stiffened Structures in Aircraft Applications

Stiffened or semi-monocoque structures have been extensively used in numerous engineering fields, where the utilization of a strong but light structural component is a primary design concern. The ability of such structures to combine these requirements is achieved by supporting thin shells, often referred as monocoque or skin, with stiffening members (stiffeners or stringers) with various cross-sectional shapes, Figure 1.1. According to the type and the number of the reinforcing members the designer is able to take advantage of the mechanical properties of a material in order to develop the required stiffness, strength and minimum structural weight. Their versatile nature has

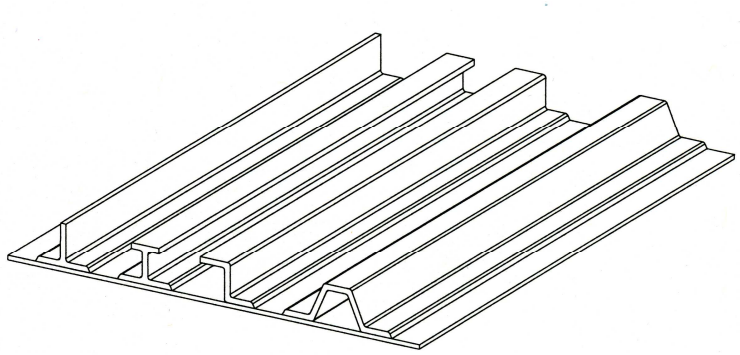

Figure 1.1. Isometric view of a stiffened panel showing, from left to right, blade, I, Z and hat stiffeners.

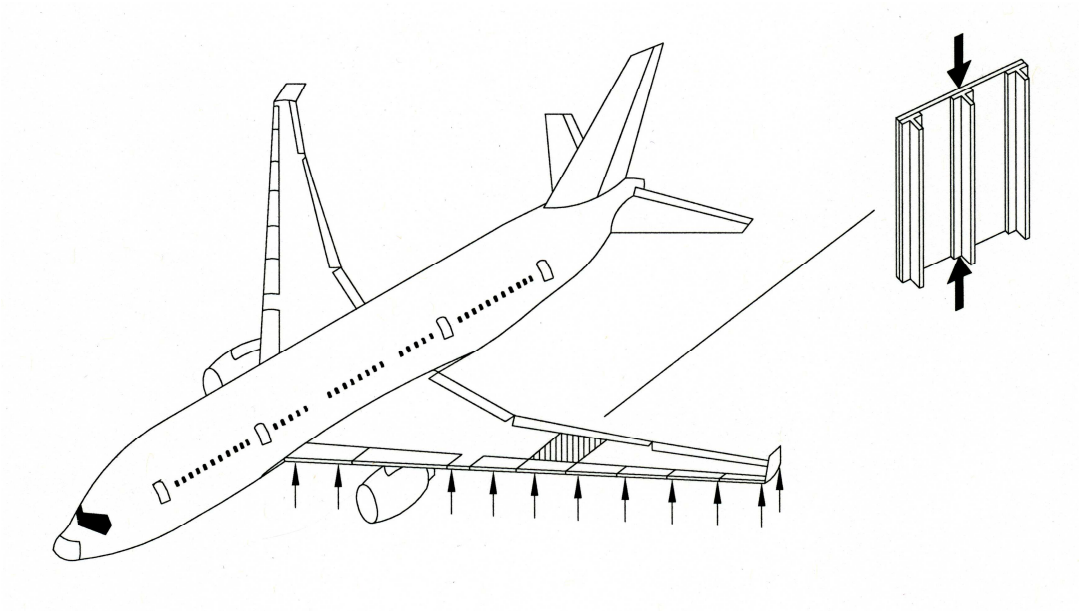

Figure 1.2. Stiffeners acting as stabilizers in the compressed top surface of the wing of the aircraft, due to aerodynamic loading.

seen them employed in many structural applications that extend from super-structures, such as the deck of long-span suspensional bridges, to the hulls and decks of ships.

The stressed-skin concept in the aeronautical and aerospace industry is paramount for maintaining the aerodynamic shape of the aircraft while minimizing the take-off weight and fuel consumption. This is evident in the skin of the wing, responsible for the generation of the lifting capability, where the attached stiffeners possess a stabilizing role in the wing-structure (Megson, 1999). During flight, the top and bottom surfaces of the wing are under a compressive and tensile state respectively. In contrast to tensile and shear loads, the thin shell is not capable of carrying sufficient compressive loads and buckling occurs. The incorporation of the reinforcing members partitions the skin into smaller panels, thereby increasing the buckling resistance and post-buckling strength (that is, the ability to sustain load far beyond initial buckling), which would otherwise require an increased skin thickness and thus heavier wing, Figure 1.2. In a similar manner they enhance the structural performance of the tailplane under aerodynamic loading, or the fuselage under static and pressure loading. The incorporation of the stressed-skin concept has also contributed towards reduced part count and excessive sub-assembly, typically encountered in traditional structures, economizing production costs (Noor, 1999).

However the development of a stronger and more cost-efficient structure would be inconsequential if the weight was increased proportionally. Therefore enhanced structural, and thus aircraft, performance is strongly affiliated with material selection, with perhaps the most influential factors being low specific gravity correlated to high strength and stiffness. In the early stages of aircraft construction, wood was implemented as the primary material. The successful experience gained by the design of wooden skin-stressed hulls in ships was translated in the design of the fuselage of the early aircraft carriers (Cutler, 1999). However the exhibited anisotropy along with humidity problems and the arising complexity of aircraft design concluded that wood was inadequate for future use (Megson, 1999). A decade before the gradual withdrawal of wood as a primary construction material (1920), the idea of a general application of

metals in aircraft structures was being contemplated (Megson, 1999). In 1930 the production of the “Boeing Monomail” marked a significant stride that revolutionized the aircraft design (Anderson 1999). It was the first airplane not only to incorporate the stressed skin concept in the wings, but also to be manufactured from metal. By 1935 (Horne, 1986) aluminium alloys dominated the industry. Despite the fact that tensile steel was also being developed at the time, it was not able to compete.

In comparison to steel, aluminium alloys, generally do not experience atmospheric corrosion and exhibit similar high strength-to-weight and stiffness-to-weight ratio. Moreover the continuous development of advanced alloys and manufacturing ease has promptly established them as the dominant construction material. Aluminum alloy technology is still under development and is considered as an important element in the aircraft industry to the present day. However the feasibility and cost-efficiency of further improvement of the mechanical properties of such alloys has been questioned (Gill, 1972).

During the 1960’s though, the development of high strength carbon (or graphite) fibres, and hence of the so called ‘advanced composites’, caught the attention of the industry. The military industry was first to attempt the transition from metallic to laminated carbon-fibre reinforced primary loading bearers, since their high specific stiffness (essential to structural stability and hence buckling resistance) is a critical factor in the performance and maneuverability of the fighter aircraft (Gibson, 1994). The initial skepticism displayed by the commercial aircraft manufacturers was soon dismissed by the prospective weight savings, and more importantly, by the composite’s inherent design flexibility to tailor their properties. After an initial trial period, where only lightly loaded secondary components were made from composites, primary components, such as the horizontal and vertical stabilizers, came into service (Harris et al., 2002). However, premature failures were observed that were attributed to the incomplete knowledge of the differences in the failure mechanisms of metallic and composite stiffened structures.

Since then substantial steps have been made in this direction, evident in the current increased application of composites in primary components of the aircraft by the two major manufactures (Airbus and Boeing); examples include the rear fuselage, horizontal tailplane, rear pressure bulkhead, centre wing box, spoilers, airbreaks and an all composite wing under development. In the military and aerospace industry the utilization of these high-performance composites has been even more extensive. Generally it could be argued that composite stiffened structures are the ideal amalgamation of material and structural efficiency. However, in order to achieve their full potential, a thorough understanding of the failure characteristics and rigorous computational optimization techniques (Butler, 1990) would be required.

1.2 Fibre-Reinforced Composites

But what is a composite material? Perhaps the most appropriate definition would be as follows: Composite material is one, which is composed of two or more constituents in a macroscopic structural element, in order to produce desired properties that would not have been attainable if the constituent parties were acting alone (Gibson, 1994). In simple terms, this means the combination of two or more distinct materials (that belong to any of the other three basic categories of materials: metals, ceramics and plastics) in order to create a new material with improved properties. The virtually limitless combinations of materials have provided many unique applications of composites that extend from everyday consumer products to superstructures.

Fibre-reinforced composites have been of particular importance owing to their exceptional specific properties and rising prospects for innovation and new design methods. The morphology of their structure is simple, yet effective; fibres bind within a matrix material. The fibres act as the primary loading bearers, while the matrix is responsible for the structural integrity of the unit, protection from environmental hazards and load distribution between the fibres (Edwards, 1998). They could be encountered as natural products, such as wood, bamboo and bones, or artificially produced. The most

common reinforcements in man-made composites are glass fibres, aramid fibres (commercially known as Kevlar), carbon fibres and boron fibres, which are usually impregnated in a polymeric based matrix. Their formation within this matrix, though, may vary according to the specific function of the composite; we have for example the continuous unidirectional, the woven, the chopped and the hybrid fibre composite (Gibson, 1994).

The earliest example of man-made fibre-reinforced composites is as old as the first steps of humanity into civilization. Ancient Egyptians and Israelites manufactured bricks by mixing straw with clay. Nevertheless the advantages of fiber reinforcement were illustrated for the first time by Griffith in 1920 (Griffith, 1920). He demonstrated that under tensile loading many materials are stronger and stiffer in the form of fibres than as a bulk material, due to smaller probability of failure from material and manufacturing imperfections. Moreover further contribution in stiffness and strength could be attained according to the material structure. For example, carbon fibres are chains of graphite crystals in an aligned formation processed in a manner such that the covalent bonds between the carbon atoms lie along the fibres, Figure 1.3, (Gill, 1972). Due to the strength of the covalent bond between the carbon atoms and the anisotropy of the crystal itself, carbon fibres exhibit high tensile strength along the fibres.

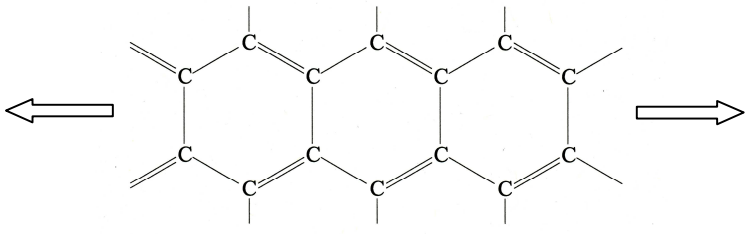

Figure 1.3. Ring structure of a carbon fibre that extends horizontally.

Their compressive and shear strength, however, is relatively weak due to the fibre columnar structure. The process developed to exploit such properties is the impregnation

of carbon fibres with resinous binders that form the matrix of the composite. Typically this irreversible process involves a thermoset polymer, which undergoes a curing process in a temperature and pressure controlled environment, for a designated period of time, or a chemical reaction with a catalyst (usually referred to as hardener), in order to create a strong interface bond with the fiber reinforcement. The quality of this bond is of particular importance to the strength and stiffness of the composite system and therefore has been subject to extensive research. Some of the factors identified, with predominant qualitative influence, include the strength of the resin, the size of the fibres, the treatment of the surface of the fibres and the quantity of the catalyst during the chemical process (Hughes, 1991). However, the strongest possible bond does not necessarily imply the best performance of the composite structure, since high strength and stiffness and high fracture resistance (particularly important when the composite structure is subjected to out-of-plane loading) are not usually compatible (Soutis, 2005). As an example, the brittle epoxy resin used in the advent applications of composites in aircraft construction had poor resistance to damage. Replacement of the epoxy resin though, has proved to be a rigorous task; other matrix systems, such as thermoplastics, that possess far more appealing toughness qualities, demonstrate poorer in-plane mechanical properties, especially under hot/wet environments (Bibo and Hogg, 1996). Furthermore epoxy resins display higher strength and interface bond quality in comparison to any other resin (thermoset) systems, such as polyesters and vinyl-esters. Improved toughness epoxy systems have significantly improved their damage resistance (Soutis, 2005). Carbon fibre-reinforced/epoxy composites belong to the so called *advanced composites* due to their exceptional high specific properties and are the most commonly used in aircraft construction (Vu-Khanh, 1987). Such composites are usually referred to as Carbon Fiber Reinforced Plastics or CFRP. In comparison to aluminum, CFRP can possess up to three times the specific stiffness and ten times the specific strength (Edwards, 1998).

Even though the configurations of reinforcing fibres within the matrix may vary, as mentioned earlier, the long continuous unidirectional fibre lamina (or ply) possesses the maximum loading capacity. This is attributed to the fact that the fibers are solely respon-

Advantages	Disadvantages
Weight reduction.	Cost of raw materials and fabrication.
High strength or stiffness to weight ratio	
Tailorable properties.	Transverse properties may be weak.
Tailorable strength and stiffness to be in	
the load direction.	Matrix is weak, low toughness
Redundant load paths (fibre to fibre).	
Longer life (no corrosion).	Difficult to attach.
Lower manufacturing costs because of	
less part count.	Analysis is difficult.
Inherent damping.	
Increased (or decreased) thermal or	Matrix subject to environmental
electrical conductivity.	degradation.

Table 1.1. Advantages/disadvantages of advanced composites. After Peters (1998)

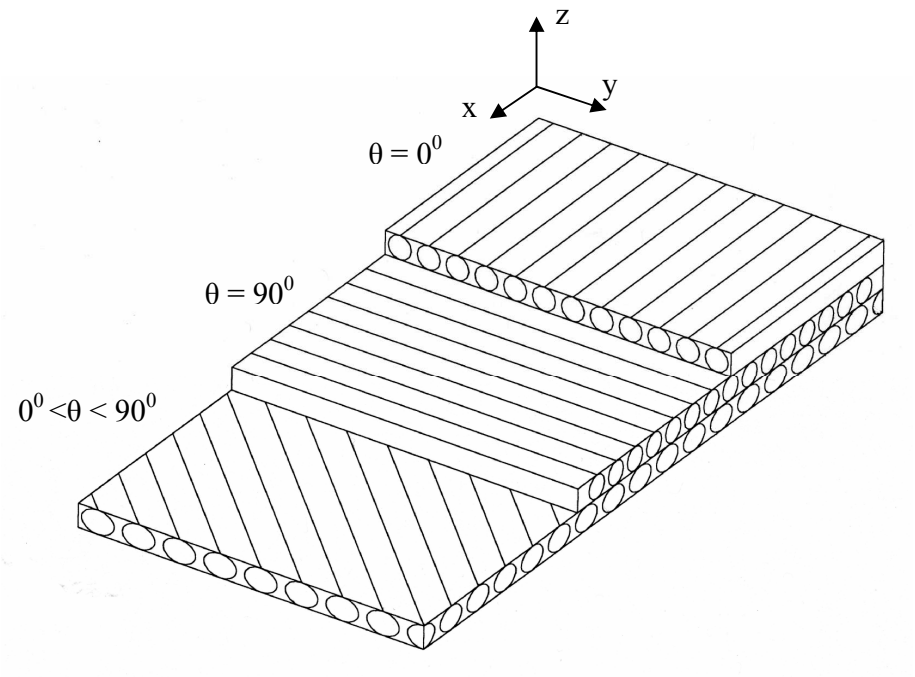

Figure 1.4. Combination of unidirectional fiber reinforced plies with varying orientation, forming a laminate structure.

-sible for the load carrying capability of the composite; positioning them in the direction in which primary stresses act, results in the elimination of the limitations that would otherwise be imposed by the matrix (Soutis, 2005). Such a configuration though is generally orthotropic, that is, mechanical and physical properties are different in the two in-plane orthogonal principal directions. Furthermore, the out-of-plane principal axis is correlated to the in-plane axis with the weakest properties. Therefore, a single lamina (or ply) is inappropriate for the structural level due to deficiency of transverse stiffness (Gibson, 1994). A viable composite structure is typically in the form of a laminate, which is produced by the bonding of multiple laminas with different orientations in desired directions, Figure 1.4. For example when the laminas are combined in such a way that fibre reinforcement approximates isotropy in all principal directions, it is known as quasi-isotropic; a direct comparison with isotropic aluminum shows that the first obtains almost twice the specific properties of the second. Such considerations, in addition to energy and cost savings, are a driving factor for the continuely increasing use of advanced composites. Further advantages, along with disadvantages, have been summarized in Table 1.1.

1.3 The Laminated Structure

> *"And the son of Peleus held the shield from him with his stout hand, being seized with dread; for he deemed that the far-shadowing spear of great-hearted Aeneas would lightly pierce it through- fool that he was, nor knew in his mind and heart that not easy are the glorious gifts of the gods for mortal men to master or that they give place withal. Nor did the mighty spear of wise-hearted Aeneas then break through the shield, for the gold stayed it, the gift of the god. Howbeit through two folds he drave it, yet were still three, for five layers had the crook-foot god welded, two of bronze, and two within of tin, and one of gold, in which the ash of spear was stayed."*
>
> *(Homer K., 1951. The Iliad of Homer, University of Chicago Press)*

The passage translated from Homer's epic Iliad describes the encounter between Achilles and Aeneas. The detailed account of the combat reveals that despite Achilles'divine origin, it was eventually his shield that provided an advantage over his opponent and led him to victory. Such a superior structure, however, was considered beyond mortal capacity, thus its manufacture could only be attributed to Hephaestus himself. According to the passage, the god of fire constructed the shield from five layers of three materials; two of bronze, two of tin and one of gold, stacked in a sequence of bronze/tin/gold/tin/bronze. The advanced performance of the shield was confirmed during battle, when Aeneas stroked his spear against Achilles but was not able to penetrate it beyond the second layer.

The latter passage is considered to be possibly the earliest testimonial of the advanced properties of laminated structures (Wadsworth and Lesuer, 2000). Since then laminated construction has been employed in order to enhance or produce various mechanical properties, such as strength, stiffness, fatigue behavior, corrosion resistance and toughness, create bulk material and compensate for limited material resources. Generally the level of efficiency of such structures is primarily dependent upon the selected material, the lamina attributes (i.e. layer thickness, isotropic or anisotropic characteristics), the selected stacking sequence and the production method adopted (Wadsworth and Lesuer, 2000).

On the other hand such dependencies affect the bond at the interface of the connected layers, which under certain conditions may prove to be the "Achilles heel" of the laminated structure. For instance under thermal expansion or flexural response, shear stresses are developed at the interfaces of the layers, which may result in the deterioration of the bond between them (Hoskin and Baker, 1986). This may act as a catalyst to the decomposition and eventually failure of the structure. Thus, in such events the laminated structure typically exhibits poor interlaminar strength (Bibo and Hogg, 1996), and therefore, through-thickness considerations must be included during the design process of the laminated structure, these in addition to the probable structural anisotropy comprise the main disparity between traditional homogeneous and composite

components (Soutis, 2005). Nevertheless laminates exhibit exceptional advantages in comparison and for that reason the motivation for the utilization of the laminate structure has always been driven by the insufficiency of the individual materials that compose the laminate.

In fibre-reinforced composite materials, as mentioned previously, laminated construction has been employed in order to compensate for poor transverse stiffness. For woven or short fibre composites this procedure mainly results in the formation of a bulk material (that is, a thick structural unit). In unidirectional fibre composites however, the practically unlimited combinations of ply stacking sequences and ply orientations obtained by the laminated architecture have contributed towards more adaptable designs that satisfy specific requirements.

The selection though, of the appropriate ply orientations, percentages within the laminate, and stacking sequence may prove to be a complicated task that lengthens the design process, but nevertheless is compensated by weight reductions and increased performance. Such complexities arise primarily from the following dependencies: the loads that the structure is expected to undertake, the design and limit loads specified and damage tolerance provisions (Weaver, 2006). Thus, optimization studies are required in order to develop the most efficient laminated structure according to what is anticipated to be the most critical parameter. In particular, optimization of the laminate architecture may account for the pre and post-buckling behaviour (Weaver, 2002), the structural shape (Liu, 2006), the characteristic failure signature (CFS or under the assumption of accumulated lamina failure, the anticipated failure pattern with a predictable effect in the stiffness of the laminate) (Harik, 2003) and damage initiation and growth (Bibo and Hogg, 1996). The impact of the laminate architecture in the pre and post-buckling behaviour and damage initiation and growth will be further elaborated on in due course. Unfortunately the design of an optimum composite laminated structure, that incorporates all the parameters mentioned, still remains elusive and is mainly attributed to the insufficiency of knowledge involving failure mechanisms in composites (Soutis, 2005). For instance, a laminated structure which incorporates an optimum combination of

strength and toughness is yet to be developed. Nevertheless, some general industrial rules have been adopted and are presented in Chapter 3.

1.4 Damage Tolerance of Fibre Reinforced Plastic (FRP) Composites

Damage tolerance design can by no means be considered a novelty of the twentieth century. A primitive design that nonetheless encapsulates the concept of damage tolerance is encountered in Leonardo Da Vinci's "flying machine" (Sierakowski and Newaz, 1995). In his study on the structure of the wing, Figure 1.5, he stated in his notebook that if one of the cords of the wing-structure broke under strain, then another one should be devised in a position that would enable it to serve the same function as the failed cord. The concept of the design is based on a multiple load path structure which includes redundant structural members in order to ensure that in the event of an individual member failure the applied loads would be safely redistributed to other members (De Florio, 2006). Such damage tolerant or fail-safe structures are currently an airworthiness requirement for commercial aircrafts. Obviously in modern aircraft design failure of an individual structural member, as portrayed in the Da Vinci wing-structure, would be catastrophic for its aerodynamic and safe operation and therefore it should be clarified that the incorporated redundancy applies to the ability of the structural member, in the event of localized damage (i.e cracks in the material), to redistribute the applied loads internally without this action actually resulting in failure of the member.

Hence, according to Joint Airworthiness Requirements (JAR), at the design limit load (DLL) of a primary structural component no permanent deformation can occur that would interfere with its safe operation up to that point. Furthermore the design ultimate load (DUL) must provide a factor of safety of 1.5 of the design limit load and be able to carry that load for at least 3s before failure (JAR-Section 1, 1991). Therefore, such structures must be able to tolerate an anticipated amount of damage, which might be encountered during in-service and manufacturing, without endangering the DLL and DUL (and thus, the aircraft safety) requirements (Chen et al., 2001). These requirements

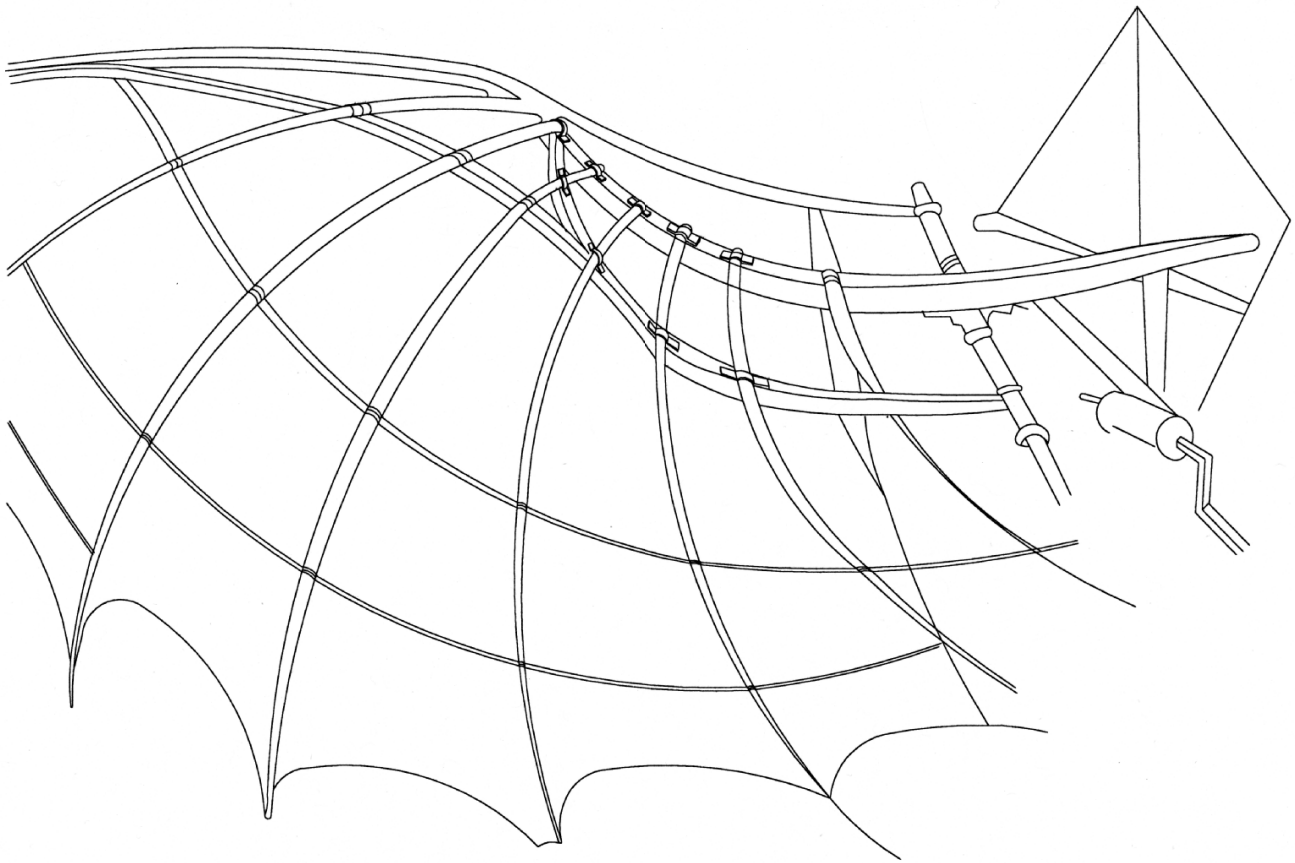

Figure 1.5. Leonardo da Vinci's study of the structure of a wing (1490).

have evolved into a damage tolerant design philosophy, according to which the following issues must be addressed (Reid and Zhou, 2000):

i. The recognition that damage would occur during manufacturing or the in-service life of the component.
ii. That the damage size should be large enough to be detected at predicted intervals of time, but growth of such damage is contained.
iii. That an existing non-destructive inspection system would be sufficient to detect such damage.
iv. That the anticipated damage would not result in the degradation of strength of the component, beyond unacceptable levels, under the maximum loading environment.

Such issues were originally introduced in metallic structures during the 1960's, but incorporated only damage events related to structural loading (Reid and Zhou, 2000). The recognition of damage due to manufacturing defects and in-service life (in essence the current damage tolerance requirements), was introduced a decade later and involved both metallic and composite structures. Even though, both have been subject to similar damage constraints, the design of damage tolerant advanced composites has proved to be more intricate, as a result of the heterogeneous nature of the material and the failure mechanisms involved (Hoskin and Baker, 1986).

1.4.1 Nature and Sources of Damage

In metals (homogeneous materials) any event that may lead to failure is likely to be accompanied by ductile deformation (plasticity or permanent deformation), in contrast to composite materials where the deformation is always nearly elastic up to failure (Bibo and Hogg, 1996). For instance, in the event of micro-cracking, the energy associated with fracture in metals, would be expended both at the crack tip and through plasticity, where in composites it would be fully expended on the crack tip (Elder et al., 2004).

Thus metals, due to their inherent ability to yield, are more able to cope with damage related events such as overload, impact, and general misuse (Bibo and Hogg, 1996).

In addition, the multiphase nature of the composite structure has been a major design concern for the structural integrity of the component, since damage may exist in any of the three structural phases; that is, the micro-structure, the meso-structure and the macro-structure. Micro-structural damage features, such as fibre/matrix debonding, cracks in the interface of the fibre/matrix bond, or microvoids in the matrix and fibre kinks, usually arise during the manufacturing processes (Silberschmidt, 2006), or exposure of the structure to severe working (Elder et al., 2004) and environmental conditions (Kalfon et al., 2005). Their existence not only contributes to the deterioration of the material properties of the composite, but also gives rise to the formation of stress concentrators, which in turn may initiate meso-structural damage features (Silberschmidt, 2006).

The internal damage which can be encountered in laminated composites (which in the literature can also be referred to as macro-structural, most likely when comparisons are drawn with microscopic features), is usually categorized to: interlaminar damage, which refers to the decomposition of the interface bond between laminae (delaminations), and intralaminar damage, which accounts for the damage features within a single lamina, i.e. fibre splitting, fibre fracture and matrix cracking (Kortschot and Zhang, 1993). In similarity with micro-structural sources of damage, such features can exist in any of the stages involved in the life of the composite structure i.e. manufacturing processing, in-service use, maintenance and sub-assembly. The latter stage actually refers to macro-structural damage issues, which can also be a primary factor in the development of both interlaminar and intralaminar damage.

For example, cut-outs and holes are defects which are intentionally incorporated in the design of the composite for joining and attachment purposes (Jen et al., 1993). It has been shown (Daniel, 1980) that around such free boundaries within the structure, regions of high stress concentration can be developed due to the deformation incompatibility of

the individual layers at the interface, which result in the initiation of cracks in the matrix, followed by delamination onset and growth, and ultimately, breaking of the fibres and total laminate failure. Regardless of the source, under specific loading or environmental conditions, such defects can serve as local failure mechanisms, which can have a significant effect on the mechanical properties of the laminate, and consequently their strength and stiffness (Greenhalgh et al., 1999), and therefore are a primary concern in damage tolerant design.

1.4.2 Damage Tolerant Design: Barely Visible Impact Damage (BVID)

Assessment of the damage tolerance capability of the composite structure (as in any structure) involves the recognition of the most critical source under the most critical loading environment (Reid and Zhou, 2000). Localized low-velocity impact events that might occur during the in-service life or maintenance of the composite structure have been identified as the most hazardous, since under a compressive environment reduction of up to 65% (Jones et al., 1988) in the compressive strength of an undamaged plate structure can be observed. In particular, a dropped tool or runway debris, are common examples in practice of low-velocity impact accidents - typically considered impacting masses less than 5 kg with velocity less than 5m/s (Rajbhandari et al., 2002). At the point of impact, an energy transfer takes place between the impacting mass and the composite structure, which entails the associated kinetic energy of the first being dissipated by the latter initially through elastic deformation heat and sound (Bibo and Hogg, 1996).

However this process is dynamic and therefore a threshold may be reached, above which, the elastic deformation capability of the component is exceeded and other processes, such as fracture, come into effect in order to accommodate the residual energy (Cantwell and Morton, 1991). This process typically entails preliminary failure (fracture) of the matrix, since it involves far less dissipation of energy than fibre fracture (Cantwell and Morton, 1991). In addition, as mentioned earlier, micro-cracks that are incorporated during the manufacturing process or produced by overstress of the matrix

material during impact, can act as initiators of fracture damage by concentrating stress and redistributing load in weak areas of the laminated structure (Elder et al., 2004), such as the lamina interface (see section 1.3) and the residue matrix dominated areas. When the toughness strength of the matrix material, and thus the elastic deformation threshold, is exceeded, micro-crack (void) growth is initiated in order to reduce the stress concentrated in the neighboring region around the crack-tip (Bonora el al., 1993). Typically, fracture growth will precipitate through the material traveling from fibre to fibre, when the latter are closely spaced due to the high stress concentration in the interface of the fibre/matrix bond, or across the matrix (Bonora et al., 1993), for example in resin rich areas such as the lamina interface where the fibres are well spaced and a higher probability of micro-crack presence exists. However, the initiation and fracture pattern of meso-structural damage is dependent upon the ability of the structure to deform elastically and the characteristics of low-velocity impact (Bibo and Hogg, 1996; Hull and Shi, 1993).

It has been demonstrated (Cantwell and Morton, 1989) that in a laminated composite plate structure two failure modes are involved in the initiation of damage; the local contact failure and flexural failure. The first mechanism implicates the transverse shear stress (that is, the shear stress acting in the plane normal and perpendicular to the plane of the laminate) that dominates the periphery of the point of impact, initiating intralaminar fracture in the matrix near the impacted surface (Hull and Shi, 1993), Figure 1.6(a). The second mechanism involves high tensile bending stress (Rajbhandari et al., 2002) developed by the flexural response of the laminate, initiating in turn intralaminar fracture of the matrix beneath the point of contact, but at the back face of the laminate (Cantwell and Morton, 1989), Figure 1.6(b). The prevailing mode is dependent upon the span-to-depth ratio of the laminate structure (Cantwell and Morton, 1991); typically in stiff (short and thick) laminates damage is initiated by the contact stresses, Figure 1.6(a), while in more flexible (longer and thinner) by the tensile bending stresses, Figure 1.6(b).

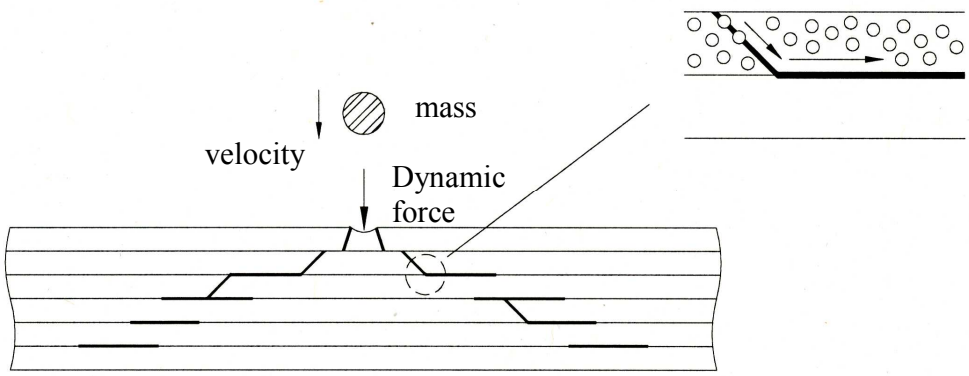

(a)

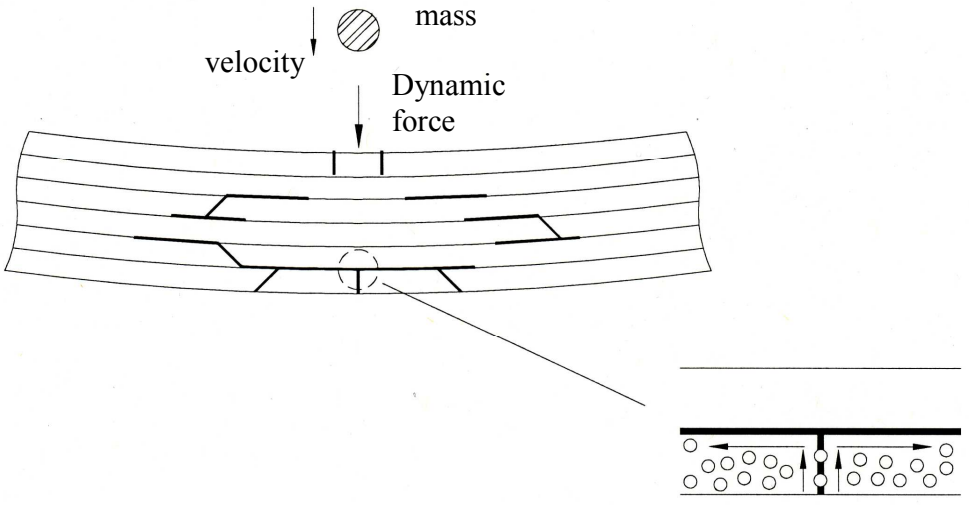

(b)

Figure 1.6. Cross-sectional view of barely visible damage, imposed by a low-velocity impact event in a (a) stiff and (b) flexible composite laminated structure.

In either case the evolution of damage in any structure occurs at higher levels of energy dissipation, which is expressed by the formation of major cracks and delaminations through the thickness. Major cracks emerging through the laminate thickness are distinguished to surface cracks (usually referred to in the literature as transverse cracks, but in order to avoid confusion this terminology will not be adopted), which emerge from the tensile surface (Bibo and Hogg, 1996), and internal cracks which are typically inclined due to the interlaminar shear stress field acting through the thickness and therefore frequently referred to as shear cracks (Hull and Shi, 1993). Experimental and numerical studies (Lammerant and Verpoest, 1994; Hull and Shi, 1993) have revealed that the formation of delaminations and major cracks are interrelated.

In particular, surface cracks or internal major cracks will propagate through the thickness until an interface composed by layers with dissimilar fibre orientations is encountered Figure 1.6 (a) and (b). Numerical analysis (Bibo and Hogg, 1996) has demonstrated that at this junction the high normal stresses generated at the tip of the crack act as triggering mechanism for interlaminar fracture. However, delamination growth is driven by the interlaminar stresses acting through the thickness and propagates in a direction parallel to the fibre axis of the lower sublaminate that composes the interface (Greenhalgh et al., 1999). The resulting shape of the delamination, typically resembles that of an elongated peanut with the major axis of its geometry lying in the direction of growth (Hull and Shi, 1993) and is primarily attributed to the existence of major cracks in the laminate (Liu, 1993). In turn, the crack-tip of the delamination area will instigate further transverse cracking and the process will be repeated throughout the thickness of the laminate.

It has been shown (Bibo and Hogg, 1996; Reid and Zhou, 2000) that the pattern of damage evolves into a ‘pine tree’ or ‘cone’ formation, where the highest concentration of matrix fracture is observed near the point of impact and perishes or increases as damage propagates towards (stiff laminates) or from (flexibly laminates) the back surface respectively. The total in-plane damaged region, generated by the conical

distribution, is in fact the summation of the individual shapes of the delaminated layers at various through-thickness positions (Davies et al., 1994) and could be roughly approximated by a circular (Hull and Shi, 1993) or an elliptic shape (Greenhalg et al., 1999). However, it has also been established (Bibo and Hogg, 1996) that flexible plate structures exhibit a lesser extent of damage in comparison to stiffer structures due to their ability to absorb energy more elastically. Nevertheless, eventually the increasing incident energy will result in extensive surface cracking - i.e. in flexible laminates, surface cracks at the compressed impact face may be observed due to the compressive bending stresses (Rajbhandari et al., 2002) - and fracture of the fibres (Cantwell et al., 1986), mainly at the surfaces and impact point of the laminate.

However, such high level of energy dissipation can be considered almost similar to the effects of ballistic impact and therefore it is unlikely to be encountered in low-velocity impact events, where typically the external reference is barely visible – that is, a small indentation mark at the point of impact, usually observed in thermoplastic matrices (Bibo et al., 1994). Therefore the corresponding preferred term for this type of damage is usually 'Barely Visible Impact Damage' or 'BVID'. In laminated composite structures the compressive residual strength after impact constitutes a measure of their ability to tolerate damage, which has developed to 'compression after impact' (or CAI) criteria (Prevorsek et al., 1993). In addition, BVID in comparison to visible damage and holes is considered potentially the most hazardous, since it is particularly hard to detect and similar or greater reduction in compression strength can be observed (Baker et al., 1986).

1.4.3 Reinforcement Architecture for Impact Damage Resistance (IDR) and Damage Tolerance

The realization of the detrimental effects of impact incidents on the structural integrity and specifically on the compressive residual strength of composite structures has instigated noteworthy efforts to improve the damage tolerance capability and resistance to impact damage. Both matrix systems and fibre reinforcement have been

under the scrutiny of the designer. For the first, toughened epoxy resins, for the reasons discussed in section 1.2, currently appear to provide the most appealing option for advanced aircraft applications. However, the incorporation of fabric (or textile) reinforcement and various through thickness reinforcement techniques have displayed significant improvements in toughness (transverse strength), and thus, resistance to impact damage. Therefore primary architectural reinforcements that exhibit significant potential to be incorporated in primary application need further discussion.

Perhaps the most distinct difference between fabric reinforcement and the unidirectional fibre reinforcement currently utilized for laminate construction, is the grouping of the fibres into tows (untwisted bundle of fibres) or yarns (twisted bundle of fibres) in the first (Hoskin and Baker, 1986) in contrast to distinct strands of fibers in the latter. There are two basic categories of fabric material; woven fabrics and nonwoven or noncrimp fabrics (Mazumdar, 2002). Typically woven patterns are produced by interlacing sets of yarns or tows, where the sequence and the number of wefts (yarns or tows with secondary structural position) going over and under successive warps (yarns or tows with primary structural position) can be altered accordingly (Bibo and Hogg, 1996). Conversely, advanced (multiaxial) noncrimp fabrics are produced by placing yarns parallel to each other in the horizontal plane and at a desired angle in the vertical plane and then stitched (through thickness reinforcement) together by a polyester thread (Edwards, 1998; Mazumdar, 2002). Similar to unidirectional reinforcement, fabric reinforcements are bound by a resin based matrix material and a viable structural unit is provided in the form of a laminate. However, the in-plane properties of such laminates have somewhat less attractive in-plane properties than the laminates composed of unidirectional prepreg tape (Bibo and Hogg, 1998; Hoskin and Baker, 1986).

In addition, an experimental investigation was conducted by Bibo and Hogg (1998) in order to assess and compare the impact resistance and residual compressive strength of laminated structures composed of unidirectional tape, woven fabric (eight-harness satin weave) and multiaxial noncrimp fabric, with quantitatively similar fibre reinforcement in all directions. The investigation concluded that woven fabrics displayed

the best resistance to impact damage, with minimal delamination damage in comparison, but possessed the poorest residual compressive strength after impact. The latter observation, infers that in practice impact damage resistance (IDR) and damage tolerance are not related, as perhaps anticipated (Reid and Zhou, 2000); on the contrary they frequently appear to be conflicting (Soutis, 2005). Even though the noncrimp fabric laminate possessed superior toughness compared to the unidirectional laminate laminate, it also exhibited similar delamination damage, and therefore comparable residual compressive strength.

An alternative to the polyester thread through thickness reinforcement technique that excites particular interest is the Z-fibre reinforcement or Z-pinned joints. This technique involves metallic or cured carbon-fibre pin inserts in the through thickness direction (which is typically prescribed as the Z-axis in the coordinate axis system) of the laminate (Zhang et al., 2006). Studies (Allegri and Zhang, 2007; Zhang et al., 2006) have shown that utilization of this technique can result in an increase in out-of-plane stiffness of 25% and a potential reduction in the impact damaged area, and consequently, in compressive residual strength of up to 50%. However 10% to 15% loss in mechanical properties was also reported and in addition further studies (Herszberg and Weller, 2006) have demonstrated that delamination resistance accounts only for the normal fracture mode (further elaboration on delamination fracture modes is undertaken in the following section). Thus, it appears that composite structural design is a trade off between mechanical properties, damage tolerance and impact damage resistance. Therefore, until optimal and certified solutions for fibre-reinforcement architecture and through-thickness reinforcement or alternative techniques are developed, the unidirectional laminated structure "*will dominate the high levels of structural efficiency required"* (Soutis, 2005). Accordingly, refinement of the current damage tolerance design methodology seems to be the primary course of action, and in particular aspects of the most critical form of impact damage, delamination.

1.5 Delamination in Laminated Composite Structures

Delamination damage has been endorsed as the predominant life limiting mode by a wealth of literature (i.e. Baker et al., 1985; Wilkings, 1982; Curtis et al., 1993), since its presence can result in significant reductions in compressive strength, yet be very difficult to detect. In particular, compressive strength degradation is the combined phenomenon of delamination buckling and growth, as stated by Chai et al. (1981). This coupling phenomenon instigated a series of studies that could be categorized into the basic areas of structural stability and delamination growth. A basic disparity between the two approaches arises from the fact that the first focuses on the post-buckling pattern itself, while the second emphasises the growth dependencies during the post-buckling state. Regardless of the approach, the plate structure has been the base line for the investigation of such issues and has provided an in-depth understanding of the mechanisms involved, which are addressed in the following sections, by their isolation from any structural interactions. Nevertheless, prior to the description of such mechanisms the characteristics of delamination damage must first be addressed. This primarily will involve the nature of its sources, position, size and area, and the involved stress field.

Delamination Sources

As described in the previous section, delaminations could develop in any of the stages involved in the life of the composite structure by a variety of sources, with impact damage constituting the most critical, but manufacturing flaws, such as the inclusion of foreign objects (i.e. release film) and fibre bridging (especially over sharp curvatures), and subassembly defects having a major contribution as well. Other significant sources of delamination include environmental degradation in the form of moisture absorption combined with non-uniform heating (Kalfon et al., 2005), typically referred to as hot/wet environment, and structural loading (Harris, 2003). For example, under compressive or bending regimes, the flexural response of the laminate may lead to the decomposition of the interface laminas; under tensile loading, delaminations may also initiate at the free

edges of the laminate (free-edge delamination; Lorriot, 2003). In addition, a special form of delamination initiation may be observed in the event of a sudden secondary structural instability or mode switch (Falzon and Hitchings; 2003), where even a small change in the shape of the buckling mode of the structure can be accompanied by large amplitude oscillating stresses that can act as initiators of interlaminar decomposition (Cerini, 2006).

The exposure to or formation of such sources of delamination damage in or under the most critical loading environment provides a realistic estimation of the effect of delaminations on the residual strength of the component that would be expected to be encountered in service. However, the multilevel complexity that is encountered in realistic damage events, in addition to unanticipated delamination positions and interactions, leads to less comprehensive conclusions on the effect of the delamination characteristics and mechanisms in structural strength and stability (Short et al., 2001). Therefore, artificial delaminations with known positions, sizes and shapes have been employed regularly in experimental studies in order to investigate such mechanisms and interactions in a controlled environment.

Delamination Position, Size and Area

Delaminations usually occur between layers with dissimilar material properties or fibre orientations (Yin, 1988). The existence, however, of such damage cannot be easily identified, posing an even greater threat to the integrity of the laminated component. Therefore, specified non-destructive techniques (NDT; Reid and Zhou, 2000), such as X-radiography (low-energy x-rays), ultrasonic scanning (ultrasonic pulse), and more recently, thermography (thermal imaging), have been incorporated in order to establish the geometric characteristics of delaminations; including the relative position within the structure, size and area.

Typically, the position of a delamination within a structure is defined according to its relative depth, since the axial and transverse positions are frequently well defined within the boundaries of the damaged area produced, for example, from low-velocity impact

events or non-uniform heating of moisturized laminates. Thus, in the literature the term “delamination depth” is utilized in order to refer to the through thickness position of the delamination relative to the upper surface (or the one defined by the selected positive normal direction) of the laminate. Given that, delaminations occur at the interfaces of the laminas, which are known distances from the reference surface, the actual depth of the delamination is usually defined by the interface “level”. For example, a second level delamination defines the delamination between the second and third layer, where the first layer forms the upper surface of the laminate.

Moreover, the delamination in-plane profile can be described by two basic geometric attributes (Hull and Shi, 1993); the “delamination diameter” (size) and the “delamination area”. Even though, the first definition implies a circular delamination shape, this is not usually the case in practice and may lead to misconceptions. In particular, in the event of impact damage, as described in the previous section, the area could be approximated by a peanut shape with its major axis lying in the direction of the fibres of the lower laminate comprising the interface. Therefore, the term “delamination diameter” corresponds to the maximum delamination distance encountered through the thickness of the laminate, while the summation of the individual delamination sites prescribes the “delamination area”. Such complexities though, obstruct confident evaluation of the compressive strength and growth criticality and therefore simplifications to the assumed geometry have been conducted.

This process typically has involved the incorporation of either one or more planar delaminations with geometric attributes analogous (or equal in the case of a single delamination) to the delamination diameter, area and depth, or one or more planar delaminations running across the width of the plate with constant length(s) analogous (or equal in the case of a single delamination) to the delamination diameter and depth only. The first are known as “embedded delaminations”, Figure 1.7(b), which in correlation with the impact damage area could be circular or elliptical in shape (without however, disregarding the possibility of a random shape resulting from a manufacturing defect) and represent a two-dimensional approximation of an impact event; while the second are

known as “through-the-width delaminations”, Figure 1.7(a), the width of which (and hence the area) is of no particular interest, since it can be approximated by a one-dimensional geometry. In either case, such approximation are comparatively easier to model and reproduce experimentally with the aid of artificial delaminations, and therefore, allow the effect of the geometry to be investigated in more detail (Short et al, 2001; Greenhalgh et al., 1999). It should be noted, however, that the one-dimensional approximation is not applicable to the structural level beyond that of coupons, and therefore its incorporation is more likely to have a qualitative rather than quantitative contribution to the understanding of real-life situations (Nilsson et al., 2001a). Thus, embedded delaminations are the key tool for the investigation of the influence of the geometrical parameters on the global compressive behaviour of a laminated structure (Riccio et al., 2001).

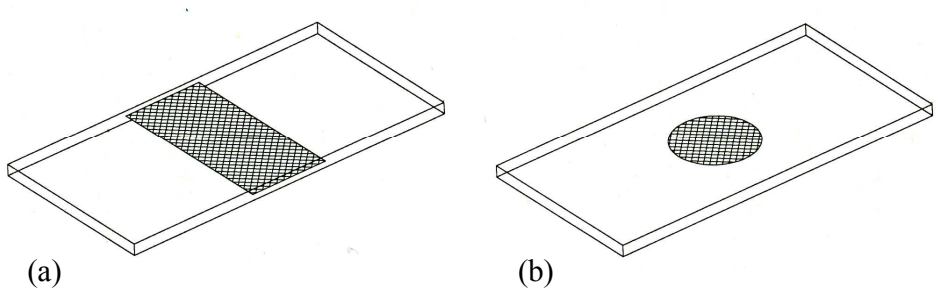

Figure 1.7. (a) The through-the-width delamination and (b) the embedded delamination.

Stress Field

On many occasions the resulting stress field acting through a laminated composite structure due to structural loading, as mentioned earlier, may prove to be a source of delamination itself, but its presence is particularly detrimental for laminates in which delamination damage has already been inflicted upon them (Baker et al., 1985). That is, the delaminated area behaves as a low modulus region (Baker et al., 1985), and therefore the interfaces of the layers near the tip of the delamination will be dominated by a high interlaminar stress field (Kachanov, 1988), which is composed singularly or in a combination of the direct (peel or normal) stresses and the interlaminar shear stresses

(Loriot et al., 2003; Baker et al., 1985). Even though, the stress field is not a feature of the delamination itself, nevertheless it is dependent on the features of the delamination and constitutes a characteristic factor in further development of the delamination front. In particular, in the event of delamination buckling, the latter stress field becomes exceptionally high (Kachanov, 1988), which may lead to delamination growth in order to dissolve the high stress concentration acting at the tip, by stress redistribution in the plies of the laminate (O'Brien, 1982).

Consequently, structural instability and reduction in the load bearing capability of the laminate may occur. Therefore, the understanding of the mechanisms involved is essential in order to determine the damage tolerance capability of laminated composite structures. Delamination buckling and growth is a coupled complex phenomenon, and therefore, in literature is frequently treated as one (Chai et al., 1981; Sheinman et al., 1998; Bottega, and Maewal, 1983). However, in the following sections the latter mechanisms are examined separately, in an attempt to identify the primary characteristics that influence their behaviour.

1.5.1 Delamination buckling and post-buckling response

Problems of local instability in the vicinity of the delaminated area have been the subject of intensive investigation over the past few decades (Chai et al., 1981; Nilsson et al., 2001). The presence of delaminations, in any laminated structure, effectively results in the development of bounding regions, which are dictated by the area, the through-thickness position of the delamination and the free surface (Hu et al., 1999). However, under in-plane compressive loading, local instability (delamination buckling) may arise in this region. Even though, the latter does not necessarily entail the ultimate loading capacity of the structure, which more often than not will be capable of sustaining higher loading conditions in a post-buckling mode (Sheinman and Soffer, 1991), nevertheless, it is responsible for promoting delamination growth (Bottega, and Maewal, 1983), and therefore, leads to further reductions in the load bearing capability of the structure (Sheinman et al., 1998; discussed in more detail in the following section). Thus,

identifying the buckling load and the subsequent post-buckling modes of the delaminated region is a critical factor regarding the ability of laminated structures to tolerate damage (Hu, et al., 1999). Therefore, it was considered prudent that the basis of the examination should be the parameters affecting the local instability and initial post-buckling configuration of the delamination.

In accordance with the previous section, the one-dimensional approximation of the delaminated plate geometry by an invariant cross-section through the width, inherits the least amount of complexity in the hierarchy, since it offers the opportunity to be treated in an analytical manner (Chai et al., 1981) and is easy to validate experimentally. Therefore, it has been readily employed since the early investigations into delaminated structures. It should be noted though, that early investigation did not take into consideration the laminated structure, since the delamination was assumed to occur within an orthotropic or isotropic plate structure (Chai et al., 1981, Simitses et al., 1985) and therefore their results cannot be directly related to the composite laminated structure (Simitses et al., 1985). Nevertheless, a basic understanding of the effect of the geometric features of the delamination in the buckling load and post-buckling region was achieved (Hunt et al., 2004) and therefore they are included in this discussion.

Critical Buckling Load

In particular, it was demonstrated (Simitses et al., 1985) that if the "delamination length" (referring to the delamination diameter/size due to the absence of area) was relatively small in respect to the length of the surrounding cross-section and was positioned near the surface, then its presence would not exhibit any significant effect in the critical buckling load. However, the effect would become more pronounced as the position of the delamination was shifted towards the mid-plane of the cross-section. Nevertheless, the biggest influence on the critical load was observed for delaminations, whose length was relatively large in relation to the length of the cross-section, and in particular for those positioned near the surface. Moreover, for the latter case, the relative axial position also appeared to contribute towards buckling load variation, with the quarter-way position identified as the most critical, in contrast to the end-position of the

first. In any case though, the effect of the boundaries was evident, since clamped supports were observed to result in higher critical values for the buckling load than the simple supports.

Qualitatively similar results on the effect of the delamination characteristics (length and depth) on the critical buckling load were observed (Chai and Babcock, 1985) for a plate structure with a circular embedded delamination, and therefore, in some sense validated the applicability of the one-dimensional approximation. However, it has also been demonstrated (Hu et al., 1999) that the latter statement would be valid only for a circular area, since for an elliptical delamination, the effect on the critical load would be more prominent if the minor axis lay in the load direction. More importantly though, the findings of the studies conducted for the isotropic/orthotropic delaminated geometries appeared to be in partial agreement with investigations conducted on composite delaminated structures (Gu and Chattopadhyay, 1999; Wang et al., 1985; Naik and Ramasimha, 2001; Hu et al., 1999). The general pattern suggested that as the delamination length and depth were increased in turn, the critical load decreased and increased respectively; but in some composite laminated structures inconsistency was observed as to whether the critical load, did in fact, increase or decrease as the delamination moved towards the mid-surface.

In particular, composite laminates with short/chopped fibres (Wang et al., 1985) and woven fabric (Naik and Raimashima, 2001) displayed the same behaviour as the isotropic/orthotropic counterparts, since they are governed by similar material characteristics. As the delamination depth increased, so did the critical buckling load, which is perhaps an anticipated result since the increased depth results in thicker delaminated layers that require higher buckling stresses (Naik et al., 2001). However, laminated structures with unidirectional layers in arbitrary stacking sequences did not necessarily follow that pattern (Hu et al., 1999). That is, even if a laminate structure was constructed in a manner that would resemble a quasi-isotropic (symmetric) behaviour, the existence of the delamination would effectively break that condition (Yin, 1988; Sheinman and Soffer, 1991; Kim, 1997). Consequently, sublaminates with anisotropic

characteristics would be generated that would be governed by bending-stretching coupling effects (please refer to Chapter 2). Such effects though, could impair the effective bending stiffness (that is, in comparison to the theoretical bending stiffness of the sublaminates in the absence of the coupling parameters), and thus, the critical buckling load (Chen et al., 1993). In addition, in the event of lateral displacement of the sublaminates further degradation of the critical load would occur, due to the formation of transverse shear stresses (Kardomateas and Schmusser, 1988; Wang et al., 1985; Gu and Chattopadhyay, 1999).

Therefore, the effect of the stacking sequence may prove to be significant, and hence, simplifications relating to the material (isotropic/orthotropic) will not always be able to predict the correct pattern. Nevertheless, the critical buckling load does not necessarily imply the ultimate loading capacity of any beam/plate under investigation and therefore post-buckling analysis is required in order to establish the residual strength and the possibility of delamination growth (Sheinman and Soffer, 1991).

Buckling Modes and Post-Buckling Response

Despite the lack of uniformity regarding the terminology used to describe the buckling modes, for convenience we have adopted, as some authors have (i.e., Kardomateas and Schmusser, 1988; Chai et al., 1981, Yin et al. 1986, Hu et al., 1999), the following: the local mode (Figure 1.8.1), the local/global mode (Figure 1.8.2) and the global mode (Figure 1.8.3). The local mode refers to the buckling configurations, as introduced by Chai et al. (1981), which regard delaminated plates/beams composed by a slender (thin and long) delaminated layer and either an infinitely thick (thin-film buckling), Figure 1.8.1(a), or a finite, but very thick in comparison (thick column), Figure 1.8.1(b). Due to the lack of a distinct supporting medium in the symmetric configuration, Figure 1.8.1(c), where the position of the delamination in the mid-surface of the laminate produces symmetry both in terms of thickness and laminate architecture, is also regarded as a local mode.

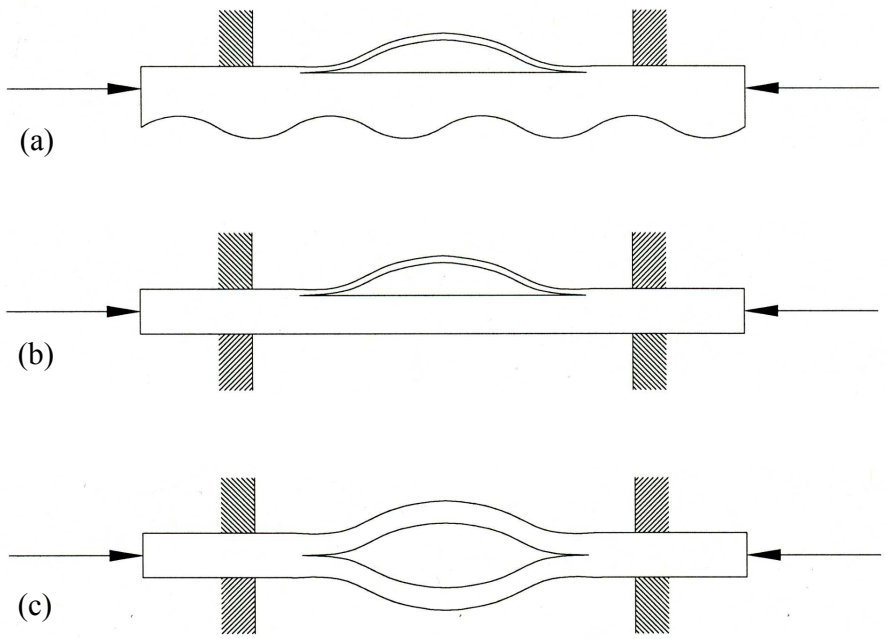

Figure 1.8.1. Local modes of buckling for (a) thin-film approximation with an infinitely thick sublaminate, (b) thick column assumption and (c) symmetric configuration.

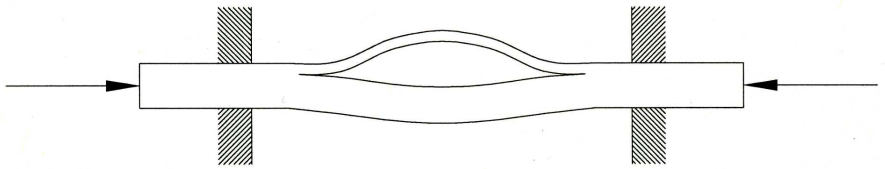

Figure 1.8.2. Local/global (or open) buckling mode

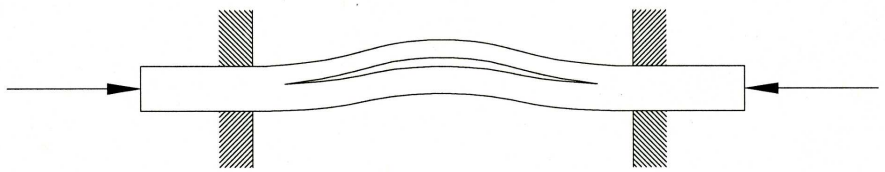

Figure 1.8.3. Global (or closed) buckling mode

In the global mode though, the supporting medium and the delaminated layer exhibit almost similar cylindrical bending in the same direction, due to the presence of a low slenderness delamination (Yin et al., 1986; Hu et al., 2004). However, between the two extremes (referring to the local and global mode) a global/local mode exists. Typically, the latter configuration reflects local buckling of the delaminated layer and cylindrical deformation of the supporting medium in the opposite direction, and corresponds to relatively slender configurations. In contrast to the local and global mode though, which under the assumption of an inconsequential supporting medium in the delaminated region and an overall response of the laminate to the loading environment, the mode corresponds to the immediate state upon critical buckling of the delaminated layer, the local/global mode is in fact developed during the post-buckling process. In particular, it has been demonstrated (Hunt et al., 2004; Short et al., 2001) that two mechanisms govern the post-buckling state; the closing process and the opening process. The first implicates the post-buckling mechanism, where the mid-points of the sublaminates move in the same direction, but are separated from each other, contrary to the second where they move in opposite directions (Hunt et al., 2004).

That is, when the delaminated layer has buckled locally, the initial out-of-plane deflection will result in the formation of a natural bending moment at the undelaminated structure (Wright, 2006), which will drive the supporting medium to deflect in the same sense as the delaminated layer. Therefore, the closing process is the immediate post-buckling mechanism (Hunt et al., 2004; Yin et al., 1986). However, the deflection of the delaminated layer, generates an effective shift of the neutral axis of the delaminated structure towards the lower surface, which effectively produces a moment in the opposite direction to the one formed by the deflection of the buckled delaminated layer (Wright, 2006). Consequently, the configuration of the buckling mode and the evolution of the post-buckling process will depend on the opposing moments.

Thus, if the natural moment produced by the shift of the neutral axis prevails in the post-buckling process, the global/local (which for simplicity and distinction from the following concepts, from further on it will be referred to as the “open mode”), will

occur. In the opposite scenario the global mode (accordingly, it will be referred to as the "closed mode") will develop even further. However, the open mode depending on the position of the delamination through the thickness may develop almost immediately after initial buckling or far into the post-buckling region (Hu et al., 2004). For example, the behaviour of a delamination positioned very close to the surface (and relatively long) at the critical buckling load could be approximated by the thin-film assumption, since the flexural response of the supporting medium would be very small due to the very weak natural bending moment (Hu et al., 2004). The increased deflection though, (and thus, the neutral axis) of the "thin film" layer would eventually result in the formation of the open mode, but at a significant load above the critical one. For relatively deeper delaminations (but still thin in comparison), bending of the supporting medium is more significant, due to a more substantial natural bending moment. Thus, the larger flexural response of the laminate will effectively produce a bigger shift of the neutral axis, and therefore, the open mode will develop soon after initial buckling. However, as the position of the delamination progresses towards the middle-surface, the natural moment becomes more pronounced and the shift of the neutral axis less important, and thus, the two modes become more competing.

Hunt et al. (2004) demonstrated that (under the assumption of a constant delamination length) the prevailing mode is dependent on the depth of the delamination. A "critical depth" exists where the response switches from opened to closed, as the position of the delamination progresses towards the middle surface. Since the open mode may actually develop in any stage of the post-buckling process, it is regarded as a general mode of the buckling process and not as a critical buckling mode, such as the local and closed mode. Nevertheless, as described to an extent, the local mode corresponds to delaminations very close to the surface; the open mode to delaminations located above the critical depth and the closed mode to delaminations below the critical depth.

Numerical and experimental studies (Hu et al., 1999; Short et al, 2001; Hu et al., 2004) have established that the latter pattern encompasses the composite laminated

structure, but in accordance with the aforesaid dependencies of the critical buckling load, the stacking sequence may exhibit a significant effect not only on the location of the critical depth, but in the correlation of the critical buckling load with the delamination depth (Hu et al., 1999). However, the lowest critical load is always related to the local mode (Wang et al., 1985) and generally it could be argued that for sequences in accordance to common industrial specifications (Hu et al., 2004) the open mode post-buckling configuration will be related to lower critical loads than the closed mode. Even though, the latter are both stable post-buckling responses (Hunt et al., 2004), nevertheless a significant difference between them in the evolution of the buckling mode is observed. That is, contrary to the closed mode which relieves the axial applied load in the buckled sublaminate and aggravates the applied load in the supporting sublaminate, in the open mode the applied compressive load is even more provoked by the decreasing wavelength of buckling crest (Yin et al., 1986). Consequently, in the first case the sublaminates will come into full contact as the compressive load in the delaminated plate reaches the overall buckling load, while in the second case the gap will remain partially open. Prior to those states being attained though, more likely than not delamination growth will have occurred. However, the onset and the extent of such growth, and thus, the ultimate loading capacity of the delaminated structure, depend on the governing mode (Hu et al., 2004).

1.5.2 Delamination growth

In literature, delamination is frequently referred to as “crack” even though this expression does not imply laminate characteristics (Yin et al., 1986). That is, delamination will always propagate in the plane of the laminae interface since crack deviation is restricted by the fibres (Wilkings et al., 1982) and the stress field (described earlier) is much more complicated in comparison to a homogeneous material with a planar crack (Yin, 1988). However parallelisms between them could be drawn, since delamination growth is subject to the same principles of fracture mechanics (Kachanov, 1988). Clearly, for the delamination to grow the applied stress must become equal to or greater than the fracture toughness of the material (that is, the critical stress required to

initiate fracture in a given material; Gibson, 1994). In accordance with the stress field acting at the tip of the crack, three possible crack modes can be observed (Lorriot et al., 2003); the peeling mode or Mode I, Figure 1.9(a), the forward shearing mode or Mode II, Figure 1.9(b), and the parallel shearing mode or Mode III (Wilkings et al., 1982). The latter modes correspond to the normal and interlaminar shear stress factors, whose intensity defines the relative fracture toughness of the damaged path (Gibson, 1994). In laminated composites the asymmetry of the material properties at the interface, in addition to non-symmetric loading and possible geometric variation may lead to a mixed mode fracture process (Hutchinson and Suo, 1992; Sheinman et al., 1998).

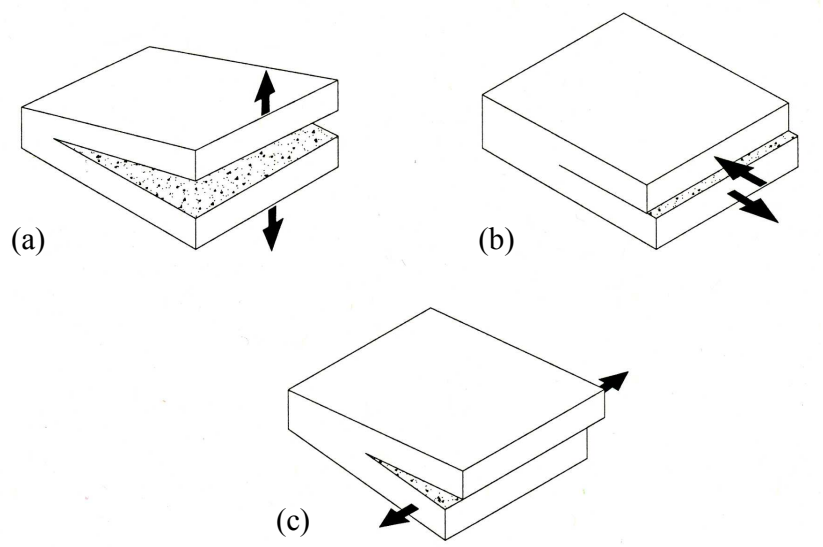

Figure 1.9. Modes of fracture illustrating (a) the peeling (or Mode I), (b) the forward shear (Mode II) and (c) the parallel shear (or Mode III) fracture processes.

However, contrary to isotropic materials, stress analysis of the crack tip region in composite laminated structures may prove to be a very complicated mathematical task, and therefore, an energy-based approach that offers a readily physical interpretation is preferred in order to investigate delamination onset and growth (Gibson, 1994). In particular, according to Griffith's theory, crack propagation is the outcome of an energy release, which flows in the crack tip and reduces the potential energy of the system (that

is, the difference in the elastic strain energy and the work conducted by the loading environment; Kachanov, 1988). Therefore, an energy-based criterion for fracture initiation emerges, which suggests that for fracture to initiate the fracture energy Γ_0 must equal the strain energy release G at the crack tip (Kachanov, 1988). The latter will be expended on different modes of fracture and in accordance with the ones described the components of the strain energy release will be G_I, G_{II} and G_{III} (Gibson, 1994).

Delamination growth though, is an irreversible process that changes the geometry of the problem, and thus, affects the parameters that sustain it (Yin et al., 1986). In particular, it has been demonstrated (Chai and Babcock, 1985) that an increase in the initial delamination length would result in lower levels of loading for onset of growth. However, a qualitatively similar influence of the delamination length may also be observed during growth, where in a displacement controlled environment any subsequent increase in the delamination length may result in a drop in the applied load (Yin et al., 1986; Bottega and Maewai, 1983). Thereafter, the delamination size is expected to increase along a stable monotonic path (Bottega and Maewai, 1983). On the contrary, in a force controlled environment delamination typically grows catastrophically to failure (Yin et al., 1986; Bottega and Maewai, 1983). However, stability of growth is reliant predominantly on the initial delamination length (Sheinman et al., 1998), and therefore, variations in the behaviour of growth may be observed under any loading conditions (Bottega and Maewai, 1983).

Typically, growth takes place when the post-buckling loading path intersects with the delamination growth loading path (Bottega and Maewai, 1983). However, this is not always the case. It has been demonstrated (Sheinman et al., 1998) that for a given delamination size and depth, the energy release rate is dependent on the slenderness of the plate/beam. In particular, for high slenderness ratios no growth was observed, but as the ratio decreased, growth initiation occurred and started to move closer to critical buckling. For very low ratios delamination growth even preceded local instability. The latter trend is primarily attributed to the fact that the less slender the adjacent undelaminated layer is the more energy release will occur (Butler et al., 2007).

However, the loading level at which delamination growth does occur is also dependent on the delamination depth, stacking sequence, transverse shear effects and the fracture energy (Chai et al., 1981; Kardomateas and Schmueser, 1988). Generally, it could be argued that the critical load for delamination growth increases as the depth of the delamination increases. However, in depths where local buckling is the dominant mechanism a reversal may be observed, where the load level at which growth occurs initially decreases and then increases (Butler et al., 2007; Chai and Babcock, 1985). This phenomenon has been observed for larger initial delamination sizes (Chai and Babcock, 1985) and has been reported in many studies on laminated composite plates (Butler et al, 2007) to occur between 10-20% of the laminate thickness.

The latter pattern may be attributed to the fact that for larger delaminations very near to the surface the critical energy release is mainly provided by the bending energy stored during the post-buckling deformation of the delaminated sublaminates. Even though local buckling for such delaminations may initiate at low levels of loading, the threshold energy release required to initiate growth will be attained very far into the post-buckling region. As the thickness of the delaminated layer increases, the extensional (membrane) energy released becomes more pronounced, but the energy released due to bending becomes available at higher loading levels. Nevertheless, their total contribution results in an increase in the energy released, which would eventually initiate growth in lower loading levels in relation to the near-surface delaminations. However, further increase in depth would eventually produce a limiting point, where the energy released due to bending would be attained at very high levels of loading, and the extensional energy release (despite being increased) would not be sufficient to balance the total energy release at similar load levels prior to the limiting point. The rate of the energy release rate though, is also dependent on the stacking sequence of the delaminated layer (Butler et al., 2007; Sheinman et al., 1998), and therefore, this may not always be the case.

More importantly however, the energy release rates, and consequently the modes of fracture that are expended on, are dependent on the post-buckling deformation both before and after delamination growth (Kardomateas and Schmueser, 1988). Despite the

fact that delamination growth is a mixed mode process, evidently the peeling fracture mode (or Mode I) will always dominate the propagation of the delamination in the local buckling mode (Riccio et al., 2001; Chai and Babcock, 1985; Butler et al., 2007), and hence, in the open mode post-buckling configuration, since the separation of the sublaminates in opposite directions amplifies its progression. However, according to the buckling modes, described earlier, delaminations positioned deeper through-the-thickness exhibit a closed mode buckling configuration. Furthermore, such delaminations have been observed to be governed by a forward shearing mode (Riccio et al., 2001; Sheinman et al., 1998; Nilsson et al., 2001b). Experimental results though, have demonstrated that the critical energy release required to initiate fracture in the shearing modes is far greater than the peeling mode (Chai and Babcock, 1985). Therefore, deeper delaminations will not promote a peeling fracture mode and the high strain energy release rate required to promote fracture in the shearing mode would probably restrict growth (at least until very high levels of loading).

Thus, an overall examination of the findings in the simple plate/beam laminated structure regarding the delamination buckling load, post-buckling response and growth dependencies suggest that delaminations positioned above the critical depth are potentially the most dangerous since they produce local instability at relatively low levels of loading and they are more likely to promote delamination growth that leads to failure at levels significantly lower than the ultimate loading capacity of the undelaminated configuration. By contrast, deeper sited are considered safer (Butler et al., 2007).

1.6 Damage Tolerance of Composite Stiffened Structures

It has been more than a decade since the realization that there are potential flaws in the assumption that composite plate structures would be sufficient calibrators of the damage tolerance capacity of real practice stiffened structures (Greenhalgh et al., 1999; Rajbhandari et al., 2002) and a more systematic investigation of this discrepancy was

begun. That is, structural characteristics, such as size, stiffness, mass, supporting sub-structure (i.e. sandwich structures; Jegley, 1992), location and configuration, would influence not only the structural response during a damage incident (for example BVID), but also the following structural behaviour upon critical loading (Davies and Zhang, 1995; 2000). However, the inherent complexities of the design and the increased costs and labour have posed a large barrier in a thorough account of the interaction of the structural configuration and the local damaged region and vice-versa, and therefore, considerably less studies have been conducted in comparison to plate structures. In addition, the majority of the previous studies have been mostly concerned with the compression after impact (CAI) strength of the structure rather than the structural behaviour upon critical loading. Nonetheless, essential understanding in certain aspects related to this work could be gained, and therefore, some of the main points derived will be further discussed, in addition to the limited number of investigations conducted on stiffened structures with embedded delaminations.

Generally, it is acknowledged that stiffened structures can accommodate an impact event more elastically (or otherwise be more impact damage resistant) than their plate counterparts and that the extent of such damage is dependent upon the structural position of the impact site (Wiggenraad et al., 1996; Greenhalgh et al., 1999). In particular, an impacted skin area between the stiffeners (web), as opposed to the skin area directly underneath or in the close vicinity of the stiffener, would typically result in more extensive delamination damage due to the development of higher deflections and insufficiency of elastic structural response (Greenhalgh et al., 1999). More importantly, primary (high buckling strain) stiffened structures impacted on the web would produce the highest reduction in compressive strength. Even though the latter observation would perhaps be anticipated to be directly related to the development of more extensive delaminations in the web, nevertheless, as described earlier, high impact damage resistance (IDR) and damage tolerance do not necessarily coalesce and investigations on stiffened structures with artificial or impact induced delaminations have demonstrated that structural buckling, and to an extent, the presence of the stiffened members are the most critical factors (Wiggenraad et al., 1996; Greenhalgh et al., 1999).

That is, delaminations positioned in the web of the structure would effectively result in a local softening (reduced stiffness) and high stress concentration at the delamination front, which would promote large deformations at the damaged region (Chen et al., 2001). However, such deformations are initially restricted by the presence of the stiffeners in the expense of higher stress endurance, which is transferred from the skin in the form of shear at the skin/stiffener junction (Chen et al., 2001). Thus, the buckling performance of the stiffened panel is reduced, and consequently the failure strength (Wiggenraad et al., 1996). It should be noted though, that investigations (Falzon et al., 2000) on undamaged stiffened structures have demonstrated that the skin/stiffener junction is a weak area in the structure, where both the in-plane load and the subsequent twist of the stiffener during buckling would contribute equally to development of interlaminar shear stresses, and consequently, detachment of the stiffener and failure of the panel. Therefore, the design buckling load and the quality of the bond in such structures will be important factors, since they may act as catalysts in the presence of a delamination (that is, promote delamination growth). The latter observation may partially explain the reason why impacts beneath the stiffener in low stiffness panels would result in lower residual strength. Another important factor may be attributed to the initial detachment length caused by the impact event that may significantly impair the buckling strain (Gadke et al., 1996).

Nevertheless, delaminations in the web of primary structures, which are of more interest to the current work, have a more substantial influence on the buckling load and residual strength due to their ability to propagate at lower levels of loading (Wiggenraad et al., 1996). Specifically, the delaminated sublaminates in the web may be allowed to buckle in an open mode, and thus, promote a Mode I fracture process. That is in contrast to the region beneath the stiffener, where such configurations are suppressed (Wiggenraad et al., 1996; Greenhalgh et al., 1999). It has been demonstrated (Greenhalgh et al., 1999; Wiggenraad et al., 1996; Nilsson et al., 2001b) that growth will occur in a direction orthogonal to loading, and therefore, towards the stiffeners. However, as the extent of the delamination approaches the stiffeners, growth is accelerated until the delamination front reaches the vicinity of the stiffener, where the

process is reversed and growth is detained (Wiggenraad et al., 1996; Ishikawa et al., 1991). Therefore, stiffened structures with more distantly spaced stiffeners would usually be more damage tolerant (Greenhalgh et al., 1999). Nonetheless, the ability of stiffened structures to tolerate damage would be mainly dependent on the interaction of damage growth and structural buckling (Wiggenraad et al., 1996). That is, delamination growth would not only promote further degradation of the local stiffness, but also reduce the ability to transfer the load to the stiffeners that would appreciably obstract growth (Graesser and Tuttle, 1996). In addition, it has been demonstrated (Nilsson et al., 20001; Ishikawa et al., 1991) that the flexural response (buckling) of the delaminated member would promote delamination growth.

According to Greenhalgh et al. (1999) the buckling strain may experience reductions in the region of 20% for impact induced damage and 10% for artificial defects of the same size. However, it has also been acknowledged by the authors that generally fibre fracture occurred at the impact event and that the through-the-thickness position of the artificial delamination in the panel was not likely to be representative of the critical delamination induced by the impact event. The latter observation probably justifies similar differences in the residual strength, which generally may vary appreciably according to the parameters described, and to an extent, stresses the importance of the delamination depth. Nevertheless, it is generally recognized that the residual strength of stiffened structures is significantly higher than that of coupons (Greenhalgh et al., 1999; Rajbhandari et al., 2002).

The previous studies though, provided limited (if not any at all) information on the effect of the delamination characteristics on the pre- and post-buckling response of the structure, or the structural effect on the delaminated sublaminates structural behaviour. Unfortunately research on this area is scarce (Bai and Chen, 2004), and therefore, the understanding of the aforementioned interactions is at an embryonic stage. Nevertheless, the few investigations conducted (that is, to the author's knowledge) have demonstrated that the initial delamination size would significantly impair the critical buckling load and strength of the stiffened structure (Thomson and Scott, 2000; Bai and Chen, 2004), but

no specific trend could be established. More importantly, it has been suggested (Yap et al., 2004) that a critical delamination depth exists, which displays the most significant influence on the buckling load of the structure. However, the latter investigation is based only on numerical work that incorporates no experimental evidence and provides no insight into the mechanisms involved. In addition it has been suggested that the post-buckling response, and consequently the residual strength, of the delaminated structure would not be affected by the through-thickness position of the delamination.

However, variations of the delamination size have revealed that changes of the structural buckling mode shape in respect to the one predicted for the undamaged structure (Thomson and Scott, 2000) may be observed, which would significantly affect the post-buckling behaviour of the structure. Furthermore, with the aid of a stiffened structure with a circular cut-out it has been demonstrated that local stiffness loss would significantly affect the buckling behaviour, but not necessarily the buckling strength (Falzon, 2001). That is, the cut-out may redirect the load path to a stiffer region of the structure (i.e stiffeners), which could even result in an increase in the buckling load (that is, in relation to the undamaged panel). No evidence has been found though, on the relation of the structural buckling configuration and the sublaminates buckling mode. Nevertheless, it has been proven (Thomson and Scott, 2000) that the buckling configuration of the sublaminates is dependent on the compliance of the structural component. Finally, it is worth mentioning that the resulting post-buckling response of the delaminated structure may not be jeopardized if the buckling mode is portrayed by a long wave with mild displacements (Wiggenraad et al., 1996), contrary to the localized one which may result in a potentially very dangerous situation of mode jumping (Thomson and Scott, 2000). Thus, the pre- and post-buckling behaviour of delaminated stiffened structures is a complicated problem which must be examined globally and not in isolation (at least at the initial stage of the design) and is dependent both on the delamination and structural characteristics.

1.7 Thesis Objective and Originality

Research on delaminated coupons has demonstrated that the position of the delamination through-the-thickness of the laminate is critical when considering the ability of the structure to tolerate damage. Following the discussion of the previous section it is apparent that the matter has not been properly dealt with in more realistic structural configurations, such as the primary stiffened structural components. In addition, the limited number of investigations that have been conducted on delaminated stiffened structures in order to identify some of the aspects concerning damage tolerant design, have only considered delaminations in various positions in the skin of the panel. However, stiffeners are also subject to delamination damage as a result of manufacturing defects or high stress concentration in the connecting regions or even the post-buckling response of the structure in the form of free-edge delamination (Falzon et al., 2000; Flesher and Herakovich, 2006). Currently, the identification of the effect of delaminations positioned in the stiffeners constitutes a key industrial issue. Thus, in order to identify the ability of stiffened structures to tolerate damage answers must be provided to design concerns that are currently pending. Accordingly the following questions must be addressed:

i. Does a critical delamination depth exist in the structural configurations, which would be considered potentially the most hazardous, as identified in coupons?
ii. Would the influence of the delamination depth on the buckling and ultimate load of the structure change according to the structural position of the delamination (i.e skin and stiffeners)?
iii. What structural position would then be the most critical and how would the trends differ?
iv. What would be the effect of the structural compliance on the buckling load and configuration of the delaminated layers, and consequently, the structural buckling configuration?
v. How would the delamination influence the post-buckling response of the structure in the presence of structural coupling phenomena?

The objective of the current work is to provide an answer to the questions raised, and therefore, contribute to the development of a more refined and realistic damage tolerant design philosophy of composite stiffened structures. That is, identification of the critical factors that display the greatest influence on the structural performance would not only contribute to the development of appropriate design limits (contrary to those specified by coupon testing), but consequently also enable the designer to exploit to the utmost the potential of the material and structural system. Or in simpler terms, lighter structural components that can tolerate damage without jeopardizing aircraft safety requirements may be developed.

1.8 Thesis Synopsis

This thesis investigates both experimentally and analytically the underlying mechanics of a composite stiffened structure with artificially induced delaminations in a variety of through-thickness positions in the skin and stiffener sub-components. An integrally stiffened structure is employed in order to eliminate any limitations that would otherwise be imposed by the weak bonding region of the skin and stiffener in the investigation of the post-buckling behaviour of the delaminated structure. The selected geometry utilized is a channel-section strut, which allows not only a reduction in the expected cost and labour involved in such an undertaking, but also exhibits similar structural behaviour to a stiffened panel. More importantly, the structure is designed to the upper limits, if not somewhat higher, than the current design industrial specifications (design ultimate levels of loading) in order not to deviate from them significantly, but at the same time be consistent with the future trend that compels higher design loads (lighter structures) that are currently restrained by damage tolerance provisions.

Nevertheless, prior to design and testing of composite stiffened structure the engineering and mathematical analysis of the composite laminated structure must be presented in order to assist in the understanding of the physical interpretation of the structural phenomena encountered. The latter analysis is conducted in Chapter 2, along

with important definitions that are utilized through-out this work. Additionally, the theory presented is utilized in order to develop a mathematical model that establishes the position of the neutral plane of a laminated structure in the direction of loading.

Chapter 3 reviews some of the key findings regarding structural instability of channel-section struts and analytical modeling of the critical instability of composite plate structures. In addition, an approximate method to track the post-buckling behaviour of the stiffened structure is presented. The selected method is known as the Shanley model approach and is preferred due to its ability to simplify complex structural problems that require excessive mathematical analysis. The latter method along with the analytical models presented is employed for the first time in the design of a composite stiffened structure according to critical buckling and post-buckling strength requirements. The method developed is compared against the results produced by finite element analysis for the corresponding structure.

In Chapter 4 a semi-analytical and semi-numerical method is developed in order to define the critical buckling load of a delaminated sublaminate. The numerical approach is based on a finite-strip methodology that offers modeling and computational ease. The effectiveness of the method developed is verified with the aid of experimental results obtained in the literature, which tested coupons with embedded delaminations. An assessment of the capabilities and limitations of the method are discussed.

Chapter 5 portrays the finite element modeling of the undamaged and damaged (delaminated) channel section struts. The results of the linear analysis are discussed in more detail. In particular, the delamination and the structural buckling configurations and loads are examined with regard to the position and depth of delamination in the structure. Unique modes of delamination buckling are presented and discussed. Finally, comparisons are drawn. In Chapter 6 the manufacturing processes of the undamaged and damaged specimens and coupons for material testing are presented. In addition, manufacturing and processing techniques are proposed in certain areas that were found

to contribute to a qualitatively enhanced end-product. Finally, the set-up for the individual tests conducted is presented.

Chapter 7 is divided in three main parts, where the individual experimental results are reported. In the first, the material behaviour of carbon-fibre reinforced composites is examined. In the second, the buckling behaviour of the undamaged channel-section struts is investigated and comparisons are drawn with the FEA results. Likewise, the damaged channel-section struts are commented on and compared. The final conclusions are drawn in Chapter 8.

Chapter 2

Laminate Analysis

One of the main differences between laminated plates and homogeneous materials is the stress-strain relationships fashioned during loading (Gibson, 1994). That is, in the laminated structure possible assymetries in the stacking sequence (in relation to the mid-plane) and material anisotropy may induce complex coupling phenomena between (or as a combination of) the extensional, flexural, torsional and shear deformations (Diaconu and Weaver, 2004; Gibson, 1994). A number of studies have been devoted to the analysis of laminated structures, and consequently, the evolution of what is now considered as the Classical Lamination Theory, some of which could be dated back to the 1950's (Gibson, 1994). For example some of the early pioneering work was conducted by Stavsky and Reiner (1961, 1964), but a more detailed list of references could be found in the wealth of literature (i.e. Gibson, 1994; Hoskin and Baker, 1985) that has dealt with the analysis of the subject in a more detailed manner.

In this chapter the Classical Lamination Theory is synoptically analyzed and is based on the method of analysis developed by Kollar and Springer (2003) and Gibson (1994). Additionally, the terminology commonly employed to characterize typical laminate configurations is presented and the Classical Lamination Theory is utilized in order to determine the neutral axis of the laminate in the direction of loading, which for the reasons discussed in the corresponding section could prove to be a considerable aid in a more accurate prediction of the physical response of the laminate under a given loading

environment. Finally before conclusions are drawn, the effect of transverse shear effects, which is not accounted for in the Classical Lamination Theory, is briefly discussed.

2.1 Classical Lamination Theory

The principal axis system of the laminated plate, portrayed in Figure 2.1, is positioned at its mid-plane, where the x, y and z axis correspond to the u^0, v^0 and w^0 displacements of the mid-plane. Assuming that the thickness of the plate is constant and relatively small compared to the width and length of the plate, but more importantly that the transverse shear stresses can be neglected, and therefore, (in-plane) displacements u and v at any coordinate of the laminated can be linearly correlated to the w (out-of-plane) displacement, Kirchhoff's hypothesis can be applied. That is, during deformation of the laminate the normals to the mid-plane remain straight and normal. Hence, the expressions employed to represent the displacement of any point within the laminate are:

$$\begin{aligned} u &= u^0 - z\frac{\partial w^0}{\partial x} \\ v &= v^0 - z\frac{\partial w^0}{\partial x} \\ w &= w^0 \end{aligned} \tag{2.1}$$

However, the strain-displacement relation for small in-plane strains of a flat plate is

$$\begin{aligned} \varepsilon_x &= \frac{\partial u}{\partial x} \\ \varepsilon_y &= \frac{\partial v}{\partial y} \\ \gamma_{xy} &= \frac{\partial u}{\partial y} + \frac{\partial v}{\partial x} \end{aligned} \tag{2.2}$$

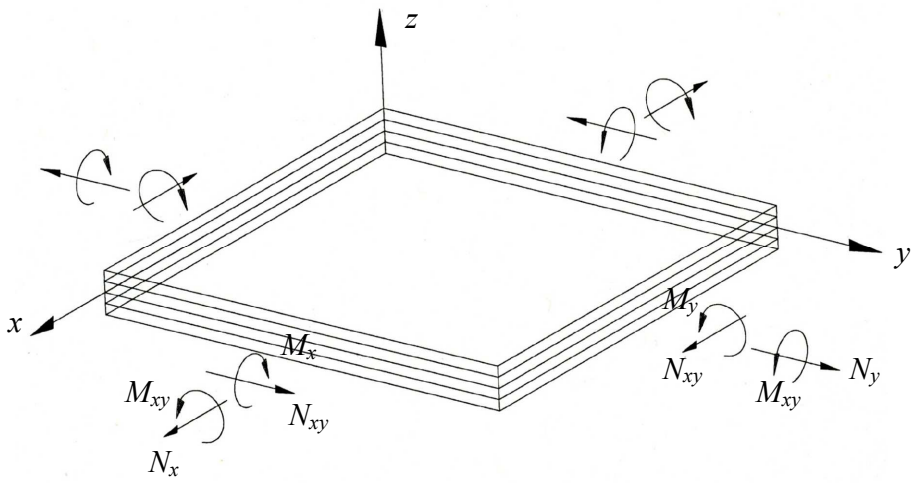

Figure 2.1. Stress resultants in the principal coordinate axis of a laminated plate in accordance with the Classical Lamination Theory.

Substituting Equation 2.1 in the strain-displacement relation gives,

$$\varepsilon_x = \frac{\partial u^0}{\partial x} - z\frac{\partial^2 w^0}{\partial x^2}$$
$$\varepsilon_y = \frac{\partial v^0}{\partial y} - z\frac{\partial^2 w^0}{\partial y^2} \qquad (2.3)$$
$$\gamma_{xy} = \frac{\partial u^0}{\partial y} + \frac{\partial v^0}{\partial x} - z\frac{2\partial^2 w^0}{\partial x \partial y}$$

Hence, the in plain strains of the laminate at any distance from the mid-plane of the laminate can be expressed as a function of the strains and the curvatures of the mid-plane of the laminate since

$$\varepsilon_x^0 = \frac{\partial u^0}{\partial x},\ \varepsilon_y^0 = \frac{\partial v^0}{\partial y} \text{ and } \gamma_{xy}^0 = \frac{\partial u^0}{\partial y} + \frac{\partial v^0}{\partial x} \qquad (2.4)$$

and the curvatures are

$$\kappa_x = -\frac{\partial^2 w}{\partial x^2},\ \kappa_y = -\frac{\partial^2 w}{\partial y^2} \text{ and } \kappa_{xy} = -2\frac{\partial^2 w}{\partial x \partial y} \tag{2.5}$$

According to Equations 2.4 and 2.5, Equation 2.3 can be rewritten in the form

$$\begin{Bmatrix} \varepsilon_x \\ \varepsilon_y \\ \gamma_{xy} \end{Bmatrix} = \begin{Bmatrix} \varepsilon_x^0 \\ \varepsilon_y^0 \\ \gamma_{xy}^0 \end{Bmatrix} + z \begin{Bmatrix} \kappa_x \\ \kappa_y \\ \kappa_{xy} \end{Bmatrix} \tag{2.6}$$

But, for the plain strain condition the stress-strain relationships for each ply of the laminate are

$$\begin{Bmatrix} \sigma_x \\ \sigma_y \\ \tau_{xy} \end{Bmatrix} = \begin{bmatrix} \overline{Q}_{11} & \overline{Q}_{12} & \overline{Q}_{16} \\ \overline{Q}_{12} & \overline{Q}_{22} & \overline{Q}_{26} \\ \overline{Q}_{16} & \overline{Q}_{26} & \overline{Q}_{66} \end{bmatrix} \begin{Bmatrix} \varepsilon_x \\ \varepsilon_y \\ \gamma_{xy} \end{Bmatrix} \tag{2.7}$$

$\overline{Q}_{ij}$ are the elements of the transformed stiffness matrix (that is, from the local to the principal coordinate system of the plate) of a single ply. The transformation is conducted according to the following set of equations:

$$\begin{aligned}
\overline{Q}_{11} &= Q_{11}\cos^4\theta + Q_{22}\sin^4\theta + 2(Q_{12} + 2Q_{66})\sin^2\theta\cos^2\theta \\
\overline{Q}_{12} &= (Q_{11} + Q_{22} - 4Q_{66})\sin^2\theta\cos^2\theta + Q_{12}(\cos^4\theta + \sin^4\theta) \\
\overline{Q}_{16} &= (Q_{11} - Q_{22} - 2Q_{66})\cos^3\theta\sin\theta - (Q_{22} - Q_{12} - 2Q_{66})\cos\theta\sin^3\theta \\
\overline{Q}_{22} &= Q_{11}\sin^4\theta + Q_{22}\cos^4\theta + 2(Q_{12} + 2Q_{66})\sin^2\theta\cos^2\theta \\
\overline{Q}_{26} &= (Q_{11} - Q_{22} - 2Q_{66})\sin^3\theta\cos\theta + (Q_{12} - Q_{22} + 2Q_{66})\sin\theta\cos^3\theta \\
\overline{Q}_{66} &= (Q_{11} + Q_{22} - 2Q_{12} - 2Q_{66})\cos^2\theta\sin^2\theta + Q_{66}(\sin^4\theta + \cos^4\theta)
\end{aligned} \tag{2.8}$$

In the previous equations θ represents the angle between the local axis in the fibre direction (axis-1) and the principal axial direction of the laminated plate, Figure 2.2, or

in simpler terms the ply orientation, and Q_{ij} are the elements of the local stiffness matrix, which are a function of the corresponding material properties, defined as follows:

$$Q_{11} = \frac{E_{11}}{1-\nu_{12}\nu_{21}}, Q_{12} = \frac{\nu_{12}E_{22}}{1-\nu_{12}\nu_{21}}, \; Q_{22} = \frac{E_{22}}{1-\nu_{12}\nu_{21}} \text{ and } Q_{66} = G_{12} \tag{2.9}$$

where E_{11}, E_{22} and G_{12} are the longitudinal, transverse and shear modulus respectively and v_{12} and v_{21} are the in-plane Poisson's ratios.

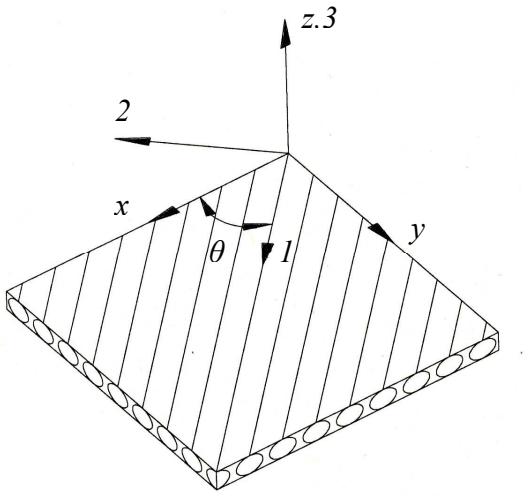

Figure 2.2. Illustration of the principal and local coordinate system portrayed by the subscripts *x, y, z* and *1, 2, 3* respectively and the resulting angle θ defining the relative orientation of the lamina.

However, Equation 2.7 is not a very useful tool in terms of comprehension of the response of the laminated structure to external loads or moments, and therefore, static equilibriums must be considered. Thus, the load and moment per unit width is given by,

$$N_x = \int_{-T/2}^{T/2} \sigma_x dz \text{ or } N_x = \sum_{k=1}^{k=N} \int_{z_{n-1}}^{z_n} (\sigma_x)_k dz$$
$$M_x = \int_{-T/2}^{T/2} \sigma_x z dz \text{ or } M_x = \sum_{k=1}^{k=N} \int_{z_{n-1}}^{z_n} (\sigma_x)_k z dz \quad (2.8)$$

where T is the laminate thickness, N is the total number of plies, $(\sigma_x)_k$ is the stress at the kth layer, z defines the distance from the mid-plane of the laminate.

Substitution of Equation 2.7 into 2.8 and solving similarly for the remaining stress resultants, the in-plane forces and moments acting on the laminate can be expressed in matrix form as

$$\begin{Bmatrix} N_x \\ N_y \\ N_{xy} \\ M_x \\ M_y \\ M_{xy} \end{Bmatrix} = \begin{bmatrix} A_{11} & A_{12} & A_{16} & B_{11} & B_{12} & B_{16} \\ A_{12} & A_{22} & A_{26} & B_{12} & B_{22} & B_{26} \\ A_{16} & A_{26} & A_{66} & B_{16} & B_{26} & B_{66} \\ B_{11} & B_{12} & B_{16} & D_{11} & D_{12} & D_{16} \\ B_{12} & B_{22} & B_{26} & D_{12} & D_{22} & D_{26} \\ B_{16} & B_{26} & B_{66} & D_{16} & D_{26} & D_{66} \end{bmatrix} \begin{Bmatrix} \varepsilon_x^0 \\ \varepsilon_y^0 \\ \gamma_{xy}^0 \\ \kappa_x \\ \kappa_y \\ \kappa_{xy} \end{Bmatrix} \quad (2.9)$$

where $[A_{ij}]$ are the elements of the extensional stiffness matrix and are given by

$$A_{ij} = \sum_{k=1}^{k=N} (\overline{Q}_{ij})_k (z_k - z_{k-1}) \quad (2.10)$$

$[B_{ij}]$ are the elements of the coupling stiffness matrix and are given by

$$B_{ij} = \frac{1}{2} \sum_{k=1}^{k=N} (\overline{Q}_{ij})_k (z_k^2 - z_{k-1}^2) \quad (2.11)$$

and $[D_{ij}]$ are the elements of the bending stiffness matrix and are given by

$$D_{ij} = \frac{1}{3} \sum_{k=1}^{k=N} (\overline{Q}_{ij})_k (z_k^3 - z_{k-1}^3) \quad (2.12)$$

2.2 Stiffness Characteristics of Common Laminate Configurations

A closer inspection of the elements of the stiffness matrix of the laminate, Equation 2.9, reveals that two types of deformation coupling could occur (Gibson, 1994). The first is derived by the probable material anisotropy (that is, material property variation with the local axis) and the formation of non-zero *16* and *26* terms in the stiffness matrix, which would not only result in the development of shear deformation under extensional displacements, but also promote coupling phenomena at the structural level (Gibson, 1994). That is, the second type of coupling that may arise in a laminated structure, where in-plane and out-of-plane, bending and twisting and extensional and twisting deformation couplings take place (Kollar and Springer, 2003). However, such coupling phenomena can occur even in laminated structures constructed with isotropic layers due to the formation of a non-zero $[B_{ij}]$ by geometric or stacking sequence (material) asymmetry in respect to the mid-plane of the laminate (Gibson, 1994).

Thus, for arbitrary asymmetric laminate stacking sequences and anisotropic material behaviour any of the coupling phenomena described earlier could take place. However, such laminated structures are impractical and rather disadvantageous in terms of design and performance. That is, coupling phenomena such as the bending-stretching deformation, act similarly to imperfections in homogeneous structure (Sheinman and Soffer, 1991) that could compromise, for example, the required buckling load and the anticipated post-buckling configuration. Therefore, in common practice aircraft structures are typically symmetrically laminated in order to produce the condition of a zero stiffness B-matrix. Additionally, in the event of a balance between the negative and positive fibre directions within the laminate the A_{16} and A_{26} terms become zero (Kollar and Springer, 2003), and thus, eliminate the likelihood of the development of extensional-shearing coupling; or otherwise referred to as membrane anisotropy (Diaconu and Weaver, 2004).

Elimination of coupling terms in the stiffness matrix of the laminate can also be achieved by considering only the relative fibre orientations of the adjacent laminas. In

particular, as described in the previous chapter, a laminate may be considered quasi-isotropic if fibre-reinforcement exists in all directions of the laminate. However, in practice as quasi-isotropic can be regarded as any laminate that is composed by three or more layers, whose directions produce similar angles between adjacent layers, equal ply thickness throughout and equal number of layers with identical fiber directions (Gibson, 1994; Kollar and Springer, 2003). Such a configuration exhibits similar extensional behaviour as isotropic material (that is, the A_{16} and A_{26} terms become obsolete), without however the latter necessarily affecting the flexural and coupling stiffness terms (Gibson, 1994). Finally, in the event of an alignment of the fibre directions of all the plies, or the symmetry axis of two adjacent layers that may be considered as one, with the orthotropy axis of the laminated structure, then all A_{16} and A_{26} terms become zero and the laminate is referred to as orthotropic.

2.3 Determination of the Laminate Neutral Axis in the Direction of Loading

Generally it is acknowledged (Kollar and Springer, 2003) that for an anisotropic (typically unsymmetrical) laminate, the *B*-matrix will not be zero regardless of the reference plane. Or in simpler terms, the existence of a neutral plane (or axis) is not a plausible scenario in anisotropic composite laminated structures. That is, the fibre directions considered, for example, in the loading direction would transform in the orthogonal (transverse) axis, and thus, result in two independent neutral planes. Therefore, positioning the reference plane, and consequently the applied load, in either of the latter planes would typically not produce elimination of all of the coupling terms. However, establishing the position of the neutral axis, especially in the direction of loading, appears to be of practical importance for design purposes.

Previous work (Hu et al, 2004) on delaminated plates has demonstrated that experimental results appeared to be in better agreement with finite element models, for which the load was transferred from the undelaminated plate segments to the neutral

plane (in the loading direction) of the delaminated ones. In contrast, the models in which the load was transferred through the mid-plane of the sublaminates underestimated the value of the buckling load. The latter observations suggested that the bending-stretching coupling effects were not as significant as initially considered. Physically this may be attributed to the fact that the applied load is transferred through the structure by displacement of the material rather than specific points/planes within the structure, or otherwise, embedded delaminated anisotropic laminates, prior to buckling, would strain both axially and transversely in a similar way to the surrounding material. Consequently, the loads would have to be transferred through the neutral planes. Therefore, the damaged structure would behave as its undamaged counterpart until the critical load of the sublaminate is attained. It should be noted however, that the buckling load of a given laminated plate is dependent on the flexural stiffness about the in-plane neutral axes of the plate (Weaver, 2006). Nevertheless it is more strongly related to the geometry of the edge of the plate, upon which the load is applied, and thus, establishing the neutral plane in the loading direction appears to be more critical. In order to define such a plane, a simple model was developed as follows.

In accordance with the laminated plate of Figure 2.3, where the coordinate system defined is assumed to originate at the bottom surface of the nth layer, the position of the neutral axis will be:

$$\bar{z} = \frac{\sum_{k=1}^{k=n} E_{x,k} A_k z_k'}{\sum_{k=1}^{k=n} E_{x,k} A_k} \tag{2.13}$$

where $E_{x,k}$ is the effective modulus of each ply in the axial direction, A_k is the cross-sectional area of each ply and $\bar{z}$ and z_k' are, respectively, the distances of the neutral axis and the mid-plane of each layer from the bottom surface of the laminate.

In practice for laminated plates, b_y and t_{ply} are equal for each lamina, and thus A_k is equal to a constant value C. Therefore Equation 2.3 can be rewritten in the form,

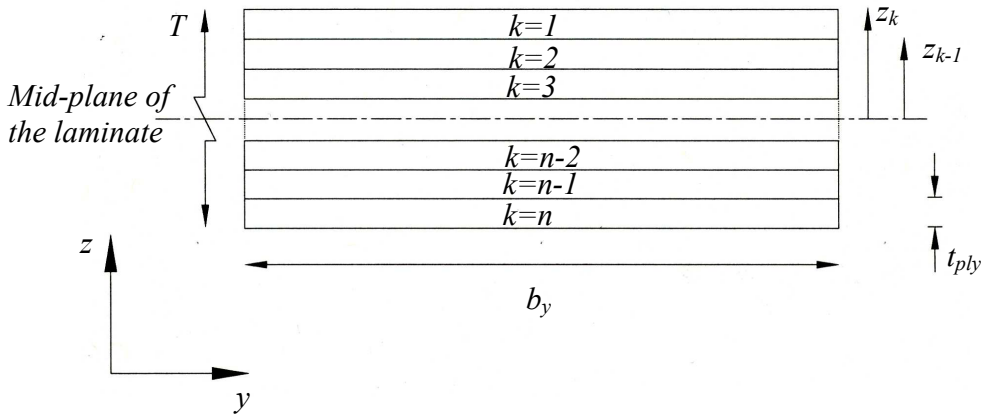

Figure 2.3. Laminated plate of width b and thickness T composed of n layers of thickness t.

$$\bar{z} = \frac{\sum_{k=1}^{k=n} E_{x,k} z_k'}{\sum_{k=1}^{k=n} E_{x,k}} \tag{2.14}$$

Furthermore, in accordance with Gibson (1994) the effective modulus may be correlated to the stress-strain relationship as follows:

$$E_{x,k} = \frac{\sigma_{x,k}}{\varepsilon_{x,k}} \tag{2.15}$$

However, relating the stress-strain to the lamina stiffness, Equation 2.7, we obtain

$$E_{x,k} = \frac{\overline{Q}_{11,k}\varepsilon_x + \overline{Q}_{12,k}\varepsilon_y + \overline{Q}_{16,k}\gamma_{xy}}{\varepsilon_{x,k}} \tag{2.16}$$

Substitution of the above equation into Equation 2.14 gives

$$\bar{z} = \frac{\sum_{k=1}^{k=n}\left(\frac{\overline{Q}_{11,k}\varepsilon_{x,k} + \overline{Q}_{12,k}\varepsilon_{y,k} + \overline{Q}_{16.k}\gamma_{xy,k}}{\varepsilon_{x,k}}\right)z_k'}{\sum_{i=1}^{i=N}\frac{\overline{Q}_{11,i}\varepsilon_{x,k} + \overline{Q}_{12,k}\varepsilon_{y,k} + \overline{Q}_{16,i}\gamma_{xy,k}}{\varepsilon_{x,k}}} \tag{2.17}$$

But $\varepsilon_{x,k}$ is a constant value, ε_x, for all the plies in the laminate since we assume uniform end-strain in the boundaries of the laminated plate and Equation 2.17 becomes:

$$\bar{z} = \frac{\sum_{k=1}^{k=n}\overline{Q}_{11,k}\varepsilon_x z_k' + \overline{Q}_{12,k}\varepsilon_y z_k' + \overline{Q}_{16,k}\gamma_{xy} z_k'}{\sum_{k=1}^{k=n}\overline{Q}_{11,k}\varepsilon_x + \overline{Q}_{12,k}\varepsilon_y + \overline{Q}_{16,k}\gamma_{xy}}$$

or

$$\bar{z} = \frac{\sum_{i=1}^{i=N}\overline{Q}_{11,k}\varepsilon_x z_i' + \overline{Q}_{12,k}\varepsilon_y z_i' + \overline{Q}_{16,k}\gamma_{xy} z_k'}{\overline{Q}_{11,T}\varepsilon_x + \overline{Q}_{12,T}\varepsilon_y + \overline{Q}_{16,T}\gamma_{xy}} \tag{2.18}$$

where $\overline{Q}_{ij,T}$ is the summation of all the $\overline{Q}_{ij}$ terms with identical subscripts.

Moreover, from Lamination Theory we know that:

$$N_y = A_{12}\varepsilon_x + A_{22}\varepsilon_y + A_{26}\gamma_{xy} + B_{12}\kappa_x + B_{22}\kappa_y + B_{26}\kappa_{xy} \tag{2.19}$$

Since the load is applied to the neutral axis of the laminate plain strain conditions are considered, and thus, the coupling terms are eliminated. Therefore, Equation 2.19 reduces to

$$\varepsilon_y = -\frac{A_{12}}{A_{22}}\varepsilon_x \tag{2.20}$$

From Equation 2.10 though we know that,

$$A_{IJ} = \sum_{k=1}^{k=n}\left(\overline{Q}_{ij}\right)_k\left(z_k - z_{k-1}\right) \quad \text{or} \quad A_{ij} = t\overline{Q}_{ij,T}$$

Substituting the above relationship into Equation 2.20 we obtain

$$\varepsilon_y = -\frac{\overline{Q}_{12,T}}{\overline{Q}_{22,T}}\varepsilon_x \tag{2.21}$$

Finally by substitution of Equation 2.21 in Equation 2.18 the position of the neutral axis can be defined as

$$\bar{z} = \frac{\sum_{k=1}^{k=n}\left[\overline{Q}_{11,k} - \overline{Q}_{12,k}\left(\frac{\overline{Q}_{12,T}}{\overline{Q}_{22,T}}\right)\right]z_k'}{\overline{Q}_{11,T} - \frac{\overline{Q}_{12,T}^2}{\overline{Q}_{22,T}}} \tag{2.22}$$

Chapter 3

Design Methodology for a Channel-Section Strut

Applications and further advances of Carbon-Fibre Reinforced Plastics in primary aircraft components necessitate a thorough understanding of their performance under critical flight conditions. In accordance with their metallic predecessors primary emphasis is attributed to instability related issues, which arise under compressive loading, and must be addressed at the design stage in order to ensure a viable operation of the composite structure. This also entails, as mentioned in Chapter1, appropriate levels of post-buckling reserve of strength.

It is well documented that analytical modeling of the non-linear post-buckling behaviour of composite stiffened structures may prove to be a complicated task, which nevertheless is essential, especially at the early stages of the design process. However this process can be simplified by delineating the underlying phenomena, with the aid of a spring-system equivalence of the stiffened structure, commonly known as the Shanley model approach. Single or more degree of freedom Shanley models have extensively been used in isotropic stiffened structures in order to achieve this (Thompson et al., 1976; Lillico et al., 2003).

The aim of this chapter is to develop a simple design model for a composite channel-strut according to post-buckling requirements, in view of the fact that such geometry bares comparisons with stiffened panels. This includes tracing of the pre and post-buckling stiffness and determination of the critical and ultimate load of the composite channel-section. The selected design geometry is based on post-buckling strength requirements that ensure that the design ultimate loading conditions would be attained, even in the presence of damage.

3.1 Introduction to Thin-Walled Structures

A thin-walled structure is a combination of thin plates with common edges, where the thicknesses of the plates are small in comparison to the overall cross-sectional geometry, which more often than not is also small in comparison to the overall length (Murray, 1984). The plate segments that compose such structures are usually distinguished in terms of the number of the common edges. In particular, the plates that possess two common edges along their length are defined as webs, contrary to the so called flanges which have one common and one free edge, Figure 3.1.

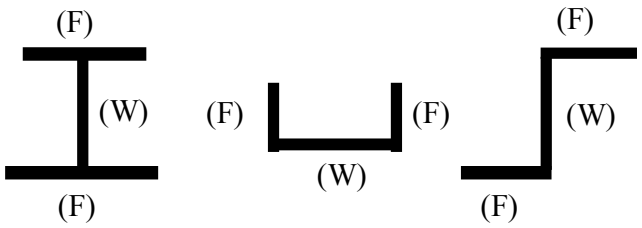

(W): Web, (F): Flange

Figure 3.1. Illustration of the web and flange plates in common structural configurations.

As materials get stronger thin-walled structures become thinner, as for example stiffened panels in the aircraft industry and structural beams in civil engineering applications. Therefore, applications of such structures will continue to expand and improve (that is, further reduction in structural weight) as long as stronger materials are developed, offering not only economic but also unique solutions to design problems (Novozhilov, 1959).

Unfortunately, such structures under a compressive or bending environment are susceptible to buckling instabilities (Singer et al., 1998). Stability therefore, is a key issue, which must be addressed at the early stages of the design process. Such process though, must account for both the individual plate elements and the resulting structure. That is, instabilities may occur both locally in the individual plate elements and globally for the whole structure. In particular, local instability is typically characterized by the repeating half-waves running across the length and width of the plates, contrary to the global instability, which occurs in the form of a single and long continuous mode. For example, the whole structure may undergo flexural bending in a single half-wave similar to one developed in an Euler column (for each given boundary), and hence, the latter global buckling configuration may also be referred to as Euler buckling in the literature (i.e. Powell et al., 1998).

Despite the morphological disparity of the buckling modes, under which instability occurs in the aforementioned structural levels, a more qualitative difference in terms of structural design can be observed. Contrary to global buckling, local buckling (instability) is generally associated with significant post-buckling reserve of structural strength, which typically implies the ultimate loading capacity of the structure (Powell et al., 1998; Lillico et al., 2003). However, global instability or otherwise the overall bending deformation, is dependent on local instability (Kolakowski and Kubiak, 2005). That is, local instability induces an overall stiffness loss in the structure which consequently promotes the development of global instability. Even though the opposite scenario (that is, the influence of global instability on the development of the local one) would be inconsequential, nevertheless the global pre-critical bending deformation of

the structure would effectively accelerate the development of local instability, due to the formation of additional lateral loads (Kolakowski and Kubiak, 2005).

Typically, global pre-critical bending deformation may arise due to the existence of an initial flexural configuration, produced during the manufacturing or assembly processes (Kolakowski and Kubiak, 2005). The latter configuration is generally regarded as an initial deviation from the ideal structural geometry, and is referred to as an imperfection. Imperfection sensitivity of flat stiffened structures (which is the main focus of the current work) is an issue that mostly concerns the structural configuration rather than the individual thin-walled plate elements, which are rather imperfection-insensitive (Bazant and Cedolin, 1991).

Structural coupling phenomena and nonlinear interaction between modes of instability may be observed in the post-critical range of thin-walled structures (Thompson et al., 1976), which may lead to failure of the structure by a combination of local and global buckling (Singer et al., 2002). However, it has been demonstrated (Neut, 1969; Koiter and Pignataro, 1976) that the effect of imperfection would be more adverse in the event of a simultaneous development of linearly independent modes of instability, since it would initiate premature failure. Therefore, optimization of thin-walled structures by equalizing the modes of instability that occur at similar levels of loading has been characterized as a naïve design approach (Koiter and Pignataro, 1976). Furthermore, it has been demonstrated (Rothwell, 1974) that maximum strength would be achieved if global instability preceded local. However, that would probably also entail thicker plate segments, and thus heavier components. Thus, the latter arguments suggest that the most appropriate design for thin-walled structures would be the one that would ensure that critical instabilities would not occur simultaneously and a significant post-buckling reserve of strength would be retained between local and overall buckling, even in the presence of significant imperfections.

Clearly, such designs require a thorough understanding and a detailed account of the pre- and post-buckling behaviour of thin-walled structures. Over the past decades, a

significant amount of literature has been presented that has dealt with such issues. The latter includes work based on early empirical data (a list of which is given by ESDU 78020) and experimental and theoretical (numerical and analytical) work for both isotropic (i.e. Koiter and Pignataro, 1976; Lillico et al., 2003) and composite thin-walled structures (i.e Lanzi and Giavotto, 2006; Banks and Rhodes, 1981; Kollar and Springer, 2003). Even though a number of methodologies have been adopted in order to model general instability issues in the linear elastic range of thin-walled structures - a detailed account of which is presented by Springer et al. (2002) - the most efficient (Springer et al., 2002) is regarded the decomposition of the structure into its plate elements. This is conducted assuming either that all the plate elements become unstable simultaneously (Banks and Rhodes, 1981), satisfying continuity conditions at the intersections, or that every plate segment is an individual plate and is rotationally restrained by stiffer adjoining plate members (Kollar and Springer, 2003).

In the post-buckling range, the deformation of the geometry that follows local instability introduces non-linear effects under which the stresses and strains developed are amplified (Bazant and Celodin, 1991), and thus, its analytical formulation is a rather complicated task, which generally requires significant numerical computation. Additionally, high efficiency numerical analysis (i.e finite element analysis), which are the primary tool of post-buckling analysis of thin-walled structures, may prove to be time and labour consuming, especially when post-buckling requirements (stiffness and ultimate load) are the subject of interest.

However, such a complicated task may be simplified with the aid of the Shanley model (Shanley, 1947), that utilizes a two-dimensional spring-system equivalent in order to represent the pre- and post-buckled state of the structure. Even though, the model was originally introduced to study the buckling instability of aluminium columns, it has nevertheless been extensively modified in order to investigate several aspects of buckling instability of isotropic thin-walled structures (Thompson et al., 1976; Lillico et al., 2003, Hunt and Burgan, 1985). However, to the author's knowledge, a Shanley model approach has never been utilized for thin-walled composite structures, which

currently suffer from the insufficiency of design methodologies that operate subject to post-buckling requirements (Lanzi and Giavotto, 2006).

3.2 Instability of Thin-walled Structures

As described earlier, thin-walled structures may fail in various modes, and consequently, at various levels of loading. Perhaps, the most detailed account of such variation would be observed in open-section struts, whose geometry exhibits symmetry in a single axis (mono-symmetric). That is, double-symmetric structures would buckle in pure bending or twisting, contrary to their mono-symmetric counterparts that may display a coupled mode. The different modes of instability could be fully portrayed by considering a lipped channel section strut, Figure 3.2(a), of varying length (Singer et al., 1998). In parallel, significant insight would be gained in the buckling modes of the plain channel section strut, Figure 3.2(b), which is the primary focus of the current work.

In particular, under the hypothesis of a sinusoidal variation of lateral deflection across the length of the component under uniaxial compression, the following modes of local and global instability may be observed (Singer et al., 1998; ESDU, 76023):

Global Modes

i. Relatively long columns (or struts) with a high slenderness parameter λ/b (where λ is the half sine wave and b the width of the web) buckle in the aforementioned Euler mode (or flexural mode), Figure 3.3(a).
ii. Shorter columns (or struts) with a lower slenderness parameter may rotate but not translate, resulting in the torsional mode, Figure 3.3(b).
iii. However, for intermediate lengths of columns (in correlation with the above), a coupling of the previous modes may be observed, and such instability is referred to as torsional-flexural, Figure 3.3(c).

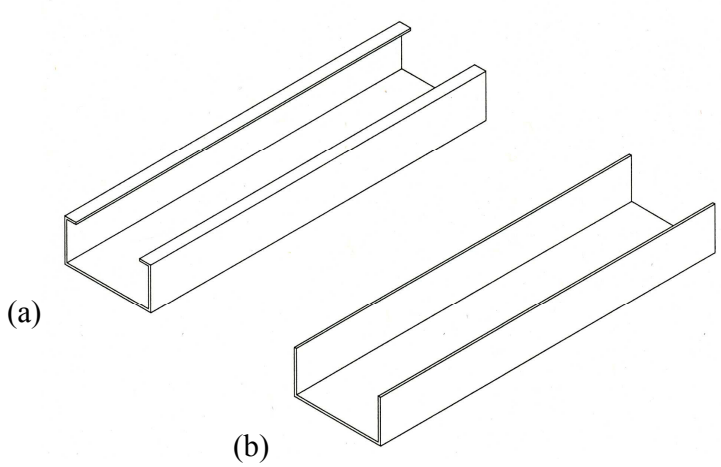

Figure 3.2. Isometric view of (a) a lipped channel-section strut and (b) of a (plain) channel-section strut.

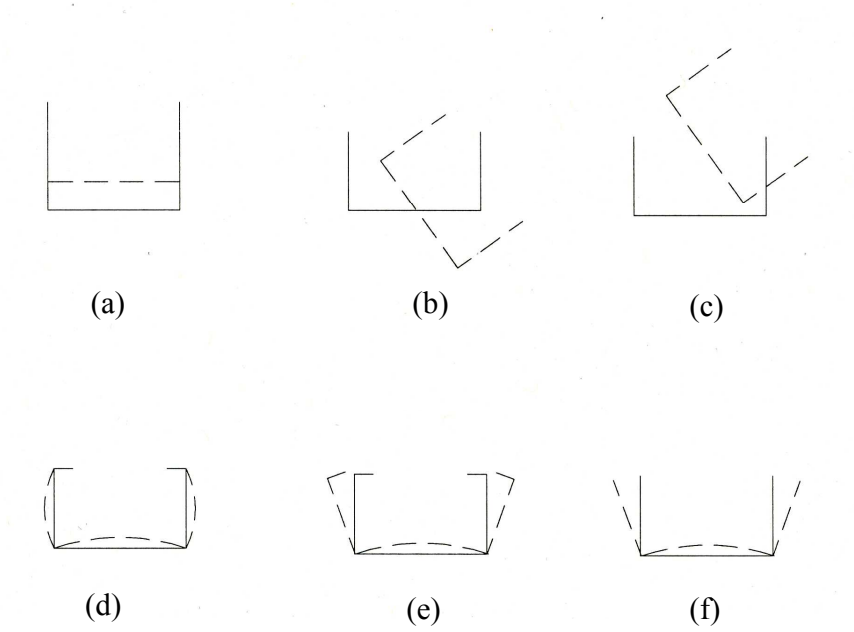

Figure 3.3. Cross-sectional view about the mid-length of a lipped and plain channel-section strut illustrating (a) the Euler (or flexural) mode, (b) the torsional mode, (c) the torsional-flexural mode, (d) local mode where the centres of all the plates displace out-of plane, (e) the distortional mode and (f) the generic local mode for (plain) channel-section struts.

Local Modes

iv. Localized instability, where the centres of all the plate elements (excluding the lip-plates) deform by out-of-plane displacement, Figure 3.2(d).

v. Localized instability, where the web deforms by out-of-plane displacement and the flanges by rotation about the flange-web junction (Hancock et al., 1994), Figure 3.2(e). The latter mode in the literature is typically referred to as distortional mode (Hancock et al., 1994; Singer et al., 1998), but the expressions local-torsional (Sridharan, 1982) and stiffener mode (Singer et al., 1998) have also been utilized.

Global instability in plain and lipped channel-section struts exhibits qualitatively the same behaviour, and therefore, only the modes of the first have been illustrated in Figures 3.3 (a), (b) and (c). However, in local buckling the principal dimensions and the geometry of the cross-section have a crucial effect on the local mode configuration (ESDU, 78021; 76023). In particular, if the web of the lipped channel-section strut was responsible for buckling (plate with the lowest critical buckling load) then the half wavelength would be comparable to the width of the web (ESDU, 78020). However, if the flanges were responsible, the wavelength would be considerably larger (ESDU, 78020). Nevertheless, both cases are subject to the condition that the flange edges are fully restrained against rotation and translation by the lip-plates, and therefore, all the plates deform by out-of-plane displacement while their junctions remain straight (Singer 1998; ESDU, 76023).

However, in the event of the lip-plates being unable to prevent rotation and translation of the flanges, then the distortional mode would occur, Figure 3.2(e), where only some of the junctions would remain straight and the wavelength of the buckling mode would be correlated to the one induced by the flanges (Singer et al., 1988; ESDU, 78021) despite the fact that the web would be responsible for the induced instability. Interestingly enough, for the (plain) channel-section strut the two local modes are indistinguishable (ESDU, 76023), Figure 3.2(f). Even though, in distortional buckling (or local for the generic plain channel-section strut) a significant reduction in the

stiffness of the structures would perhaps be anticipated due to the dependency of the latter to the flanges performance (Rothwell, 1974), nevertheless studies (Kwon and Hancock, 1992; Hancock et al., 1994; Rothwell, 1974) have demonstrated that a considerable post-buckling reserve of strength may be maintained in the distorted structure, even when local-distortional coupling (lipped channel-section struts) occurred.

Since local instability is characterized by relatively short half-wavelengths, the boundaries at the end of the strut would have a trivial influence (ESDU, 76023), and therefore, more often than not the investigation of the local critical buckling load draws on the assumption of an infinite length (i.e. Kollar and Springer, 2003). In contrast, the ultimate loading capacity is primarily related to the formation of global buckling, which evolves in wavelengths comparable to the length of the strut, and thus, is strongly affected by the boundary conditions and load eccentricity (ESDU, 76023; Kwon and Hancock, 1992). Furthermore, in accordance with the previous section, an initial imperfection may accelerate the formation of initial instability and degrade the anticipated strength. However, experimental and theoretical work on channel-section struts (Rothwell, 1974; Kwon and Hancock, 1992) has shown that imperfection sensitivity is dependent on the imperfection shape, and in contrast to a local imperfection, a global one would be almost insignificant for intermediate channel-section lengths.

3.3 Channel-Section Strut Geometry Design

The current analysis draws on two single degree of freedom spring-system models; a *full stiffness* model and a *reduced stiffness model*. These models assume that all plate segments of the structure under investigation maintain their individuality and each plate (or a combination of identical plates) is represented by a single spring. The stiffness of the reduced stiffness model is correlated to a given factor of post-buckling strength α and an assumed stiffness reduction η in the critical plate. Here the reduced (or post-buckled) stiffness represents the stiffness of web of the channel-section strut,

subsequently referred to as the skin since correlations are drawn with a stiffened panel composed by skin and stiffeners, following initial buckling.

In accordance to the previous sections, failure of the channel is assumed to occur when the flanges, referred to as the stiffeners, reach their buckling load. That is, in constant thickness channel-section struts local and stiffener buckling are indistinguishable. However after initial buckling, the deformation of the skin plate and the distortion of the stiffeners results in further reduction in stiffness. As a result an overall mode is initiated in the skin and stiffeners, causing the wavelength to increase. When the wavelength has increased enough, the stiffeners have insufficient post-buckling reserve of strength and behave as a plate with one free and three simply-supported edges with no warping restraint. As a consequence Euler buckling is observed. Therefore stiffener buckling can be taken as the ultimate load, after which the structure buckles in an Euler mode.

As described earlier, buckling analysis of thin walled structures involves two approaches; the first considers that the whole structure becomes unstable, satisfying continuity conditions at the intersections, while the second regards every plate segment as individual and rotationally restrained by stiffer adjoining plate members. In the current analysis though, each plate is considered individually and does not take into account any interaction or restraint between them. The latter assumption has been also drawn in early analytical models (Desmond et al., 1981) that allowed for post-buckling reserve of strength (Hancock et al., 1994). Furthermore, in the current model, initial imperfection, shear deformation and fillet radius effects at the intersection are ignored. Since in accordance with the previous section, for intermediate channel section strut lengths, imperfection of the overall type, which is considered to be typical in laminated structures, has a minor effect; ignoring the radius effect may lead to a minor underestimation of the buckling load (ESDU, 78021). Thus, a design formula that enables geometry selection according to post-buckling requirements is produced as follows.

For the channel-section strut both *full* and *reduced stiffness* models will be represented by two springs, in which one represents the skin stiffness k_{sk} the other the stiffeners k_{st}, as illustrated in Figure 3.4. The stiffness of the plate segments for a balanced symmetric laminate under pure in-plane axial stress are,

$$k_{sk} = b\overline{A}_{sk} \quad \text{and} \quad k_{st} = 2h\overline{A}_{st} \tag{3.1}$$

where $\overline{A}_{sk} = \left(A_{11} - \frac{A_{12}^{\,2}}{A_{22}} \right)_{sk}$, $\overline{A}_{st} = \left(A_{11} - \frac{A_{12}^{\,2}}{A_{22}} \right)_{st}$ and A_{ij} are the elements of the extensional stiffness matrix of the skin and stiffener laminates, respectively.

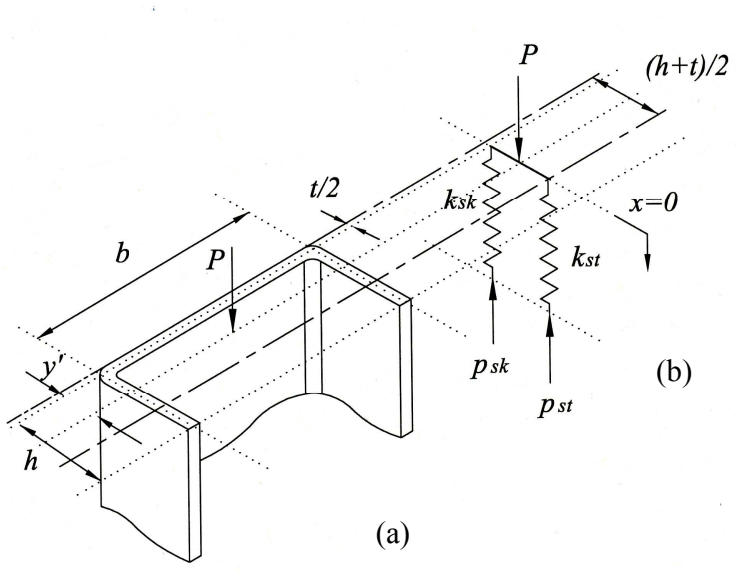

Figure 3.4. Modified Shanley Model concept for the channel-section strut. (a) Isometric view of the channel thickness *t* and (b) equivalent Shanley spring model.

The total load P is applied on the neutral axis, and any rotation either before or after initial buckling at the ends is prevented. This arrangement is, for example, representative of a long wing cover panel (Lillico et. al, 2003), which resists the applied bending moment via a compressive force applied to the neutral axis of the panel both before and after initial buckling. Before initial buckling the force and moment equilibrium in the spring system give,

$$P = p_{sk} + p_{st} \tag{3.2}$$

and

$$y' = \left(\frac{p_{sk}}{p_{st} + p_{sk}} \right) \frac{h}{2} \tag{3.3}$$

Applying Hooke's Law for linear elastic springs, Equations 3.1 and 3.2 become,

$$P = \left(k_{sk} + k_{st}\right)x \tag{3.4}$$

and

$$y' = \left(\frac{k_{sk}}{k_{st} + k_{sk}} \right) \frac{h}{2} \tag{3.5}$$

where x is axial strain. Equating Equations 3.3 and 3.5 and substituting in Equation 3.2 we obtain,

$$P = \left(\frac{k_{st} + k_{sk}}{k_{sk}} \right) p_{sk} \tag{3.6}$$

and

$$p_{sk} = \left(\frac{k_{sk}}{k_{st}} \right) p_{st} \ . \tag{3.7}$$

The above equations reveal the force distribution in the skin and stiffeners of the channel-section strut, while Equation 3.4 describes the linear function of the total load applied, represented by line *OA* in Figure 3.5, according to strain *x* of the spring system.

At a strain x_{sk}, skin buckling occurs and the structure reduces in stiffness. Therefore a *reduced stiffness* model is considered where the equivalent spring of the skin now has a reduced stiffness,

$$k_{sk}' = \eta b \bar{A}_{sk} \tag{3.8}$$

where η is the assumed stiffness reduction factor, corresponding to a buckled plate, simply-supported along the unloaded edges. The reduced stiffness model is equivalent to a Shanley hypothetical column, where the slope of the reduced stiffness system is equivalent to the summation of the full stiffener stiffness k_{st} and the reduced skin stiffness k_{sk}', see region *AB* of Figure 3.5. In order to describe this region it is necessary to understand the hypothetical region *DA*, which represents the load-strain relationship of the reduced stiffness system prior to skin buckling at P_{sk}.

At *D* there is no load in the skin spring, and the stiffener spring carries a tensile force P_{st}', as an effect of a negative *x*, as defined in the spring system, and taking into account the initial assumption of plate independence. Since the stiffness of the stiffeners spring does not change, it must be extended by $-x_0$, see region *OD,* which in conjunction with the reduced stiffness of the skin spring, produce the hypothetical region *DA*. Negative *x* corresponds to tensile strain.

The total applied in the reduced stiffness model is given by,

$$P = p_{sk}' + p_{st} + P_0 \tag{3.9}$$

or

$$P = \left(k_{sk}' + k_{st}\right)x + k_{sk}' x_0 \tag{3.10}$$

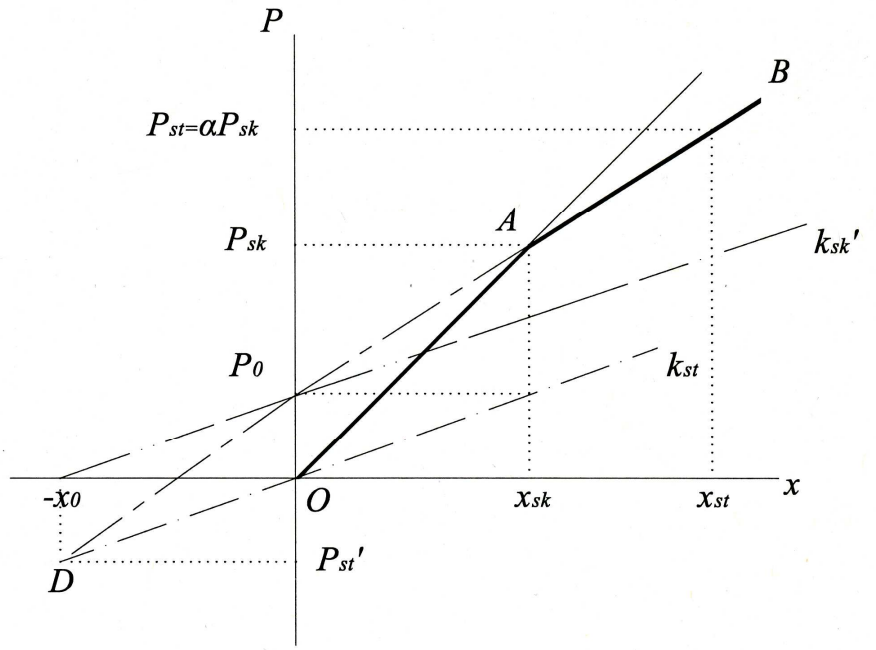

Fig. 3.5. Plot of end-shortening strain against total load and individual skin and stiffener load of full stiffness (*OA*) and reduced stiffness model (*AB*).

Where P_0 is the total applied force on the reduced stiffness model at $x=0$. At strain x_{sk} the skin buckles and we can equate Equations 3.4 and 3.10. Hence the following relationship is obtained,

$$x_0 = \frac{1-\eta}{\eta} x_{sk} \tag{3.11}$$

Assuming that the load is applied once more at the new neutral axis, restricting rotation, Equation 3.7 can be rewritten as

$$p_{sk} = \left(\frac{k_{sk}'}{k_{st}} \right) p_{st} \tag{3.12}$$

Substituting Equations 3.12 and 3.11 into Equation 3.9 we obtain the following relationship

$$P = \left(\frac{k_{st} + k_{sk}'}{k_{st}} \right) p_{st} + (1-\eta) k_{sk} x_{sk} \tag{3.13}$$

For the original model when the load applied is equal to the skin buckling load, $P=P_{sk}$, then the load applied on the skin is equal to the local skin buckling load, $p_{sk}=p_{sk,cr}$ and Equation 3.6 becomes

$$P_{sk} = \left(\frac{k_{st} + k_{sk}}{k_{sk}} \right) p_{sk,cr} \tag{3.14}$$

When the load applied P becomes equal to the stiffener buckling load, $P=P_{st}$, then the load applied on the stiffener p_{st} is equal to the local stiffener buckling load, $p_{st,cr}$ and Equation 3.13 becomes

$$P_{st} = \left(\frac{k_{st} + k_{sk}'}{k_{st}} \right) p_{st,cr} + (1-\eta) p_{sk,cr} \tag{3.15}$$

However from the initial assumption that stiffener buckling precipitates failure of the channel-section, and that this should occur at factor α above P_{sk}, we have $P_{st}=\alpha P_{sk}$. Substituting Equation (3.14) into Equation (3.15),

$$\alpha \left(\frac{k_{st} + k_{sk}}{k_{sk}} \right) p_{sk,cr} = \left(\frac{k_{st} + k_{sk}'}{k_{st}} \right) p_{st,cr} + (1-\eta) p_{sk,cr} \tag{3.16}$$

or

$$\frac{p_{st,cr}}{p_{sk,cr}} = \frac{\alpha k_{st}^2 + (\alpha + \eta - 1) k_{sk} k_{st}}{\eta k_{sk}^2 + k_{sk} k_{st}} \tag{3.17}$$

Assuming that the skin plate is a simply supported orthotropic plate with straight unloaded edges and the stiffener is pinned at the skin edges, the following standard equations for buckling apply (Kollar and Springer, 2003),

$$N_{x,cr} = \frac{12D_{66}}{b_y^{\,2}} + \frac{D_{11}}{l_x^{\,2}} \tag{3.18}$$

$$\text{and} \quad N_{x,cr} = \frac{\pi^2}{b_y^{\,2}}\left[2\sqrt{D_{11}D_{22}} + 2\left(D_{12} + 2D_{66}\right)\right] \tag{3.19}$$

Where b_y and l_x are the plate distances in the transverse and axial direction respectively, while Equation 3.18 and 3.19 refer to the critical load per unit width of a plate with three simply-supported edges and one edge free and all the edges simply supported. For relative large lengths the second term of the sum in Equation 3.18 can be disregarded as it becomes insignificant in comparison to the first. Rewriting the latter equations in terms of the critical loads of the stiffener and skin plates gives,

$$p_{st,cr} = \frac{24D_{66}}{h} \tag{3.20}$$

$$\text{and} \quad p_{sk,cr} = \frac{\pi^2}{b}\left[2\sqrt{D_{11}D_{22}} + 2\left(D_{12} + 2D_{66}\right)\right] \tag{3.21}$$

For a constant thickness laminated structure $\bar{A}_{st}=\bar{A}_{sk}$; substituting the latter and the above equations into Equation (3.17) we obtain the following design formula,

$$12\eta D_{66}\left(\frac{b}{h}\right)^3 + 24D_{66}\left(\frac{b}{h}\right)^2 - \pi^2\left(\alpha+\eta-1\right)\left[2\sqrt{D_{11}D_{22}} + 2\left(D_{12}+2D_{66}\right)\right]\left(\frac{b}{h}\right) -$$

$$2\pi^2\alpha\left[2\sqrt{D_{11}D_{22}} + 2\left(D_{12}+2D_{66}\right)\right] = 0 \tag{3.22}$$

Solving the cubic function for given values of η and α we obtain three real roots, two negative and one positive. The solution, which gives the required breadth to height ratio b/h for the channel, is the real positive root.

Since an existing lamination mould for the channel-section strut was available, the skin width b was fixed. Therefore, solution of Equation 3.20 would be dependent upon the required factor of post-buckling strength α, the assumed skin stiffness reduction factor η and the laminate architecture.

3.3.1 Laminate Architecture for the Channel-Section Strut

Selecting the most appropriate laminate architecture may prove to be a very complicated task. The source of such complexity lies in the vast number of orientations of the layers, as well as the number of ways that they can be combined together (Weaver, 2002). For example, Weaver (2002) suggested that even in the case of restricting the selection to four orientation angles (typically conducted in industry for reasons which will be discussed), still there would be 4^N possible combinations. However, in order to assist and ensure, to some extent, an efficient design the following industrial rules have been adopted.

i. Typically, the fibre orientations chosen are $\pm 45^0$, 0^0 and 90^0 mainly due to the ease of manufacture, with the associated costs maintained at low levels (Weaver, 2006). However, the selected orientations do not necessarily imply the most efficient laminate. For example, when anisotropic elastic tailoring is considered, 30^0 and 60^0 orientations would be able to produce a more optimum structure (Weaver, 2006).
ii. Balanced and symmetric laminates are usually preferred in order to eliminate the adverse effects of material coupling (Bader, 1996; Weaver, 2006) and a highly complicated structural design, which is already troubled by structural coupling phenomena.

iii. Any laminate must include at least 10% of the total number of layers in the 90^0 direction (Bader, 1996). The latter requirement is more commonly known as the 10% rule, and it has been established in order to provide a minimum level of strength in directions other than that of the primary loading axis (Weaver, 2006).

iv. Furthermore, if possible the 90^0 layers must be separated from each other in order to reduce interlaminar shear and normal stresses (Liu, 2005).

v. Typically, no more than three layers of the same orientation will be grouped together (Liu, 2005). The latter constraint arises from damage tolerance provisions, and in particular, impact damage resistance (IDR) requirements (Cantwell and Morton, 1991). That is, laminates with unidirectional orientations fail by fibre splitting at very low levels of energy (Cantwell and Morton, 1991), classifying them as unsuitable energy absorbers in the event of impact.

vi. Additionally, positioning the $\pm 45^0$ layers in the surface of the laminate would not only protect the primary loading barriers (0^0 fibres) from potential damage (Cantwell and Morton, 1991), but also increase the buckling resistance to in-plane loading (Weaver, 2002).

Taking into account the first three constraints presented above, it becomes obvious that the minimum number of layers of the laminate would be eight. Even though the number of possible configurations would be reduced to 4^4 by the required symmetry, nevertheless the number would still be excessive. However, constraint (*vi*) in the stacking sequence selection process would dramatically reduce the remaining possible configurations, since it requires that the $\pm 45^0$ layers must be positioned at the surface of the laminate. Therefore, only two positions for the 0^0 and 90^0 layers are possible. Even though, condition (*iv*) suggested that grouping of 90^0 plies should be avoided (if possible), it was decided that 0^0 layers should be positioned closer to the surface of the laminate in order to obtain a more detailed account of the effect of the delamination on the structural behaviour (that is, delaminated sublaminates that include primary loading bearing layers). It should be noted though, that constraint *v* would not have been violated

in any case. Thus the resulting stacking sequence for the thin-walled channel-section strut will be $[45/-45/0/90]_s$.

3.3.2 Post-Buckling Stiffness of Laminated Plates

The success of the design model developed for the channel-section strut is dependent upon the selection of an appropriate skin stiffness reduction factor η. Simple approximate solutions with differing boundary conditions have been developed for isotropic plates (Koiter and Pignataro, 1976), orthotropic laminates (Stein, 1983), laminates that exhibit extensional-bending coupling (Harris, 1975), and to an extent, the most generic case of anisotropic laminated plate (Diaconu and Weaver, 2006). Even though it has been demonstrated (Harris, 1975) that the post-buckling stiffness would be dependent on the coupling effects and the aspect ratio of the plate, nevertheless such considerations are currently beyond the scope of applicability of the model developed. The latter concentrates on balanced-symmetric laminates and infinite long plates. Furthermore, for a homogeneous lay-up (or otherwise for a balanced symmetric laminate) the post-buckling stiffness would be qualitatively and quantitatively similar to isotropic plates (Powell et al., 1998; Weaver, 2006). Contrary to the more general laminate configurations, the post-buckling stiffness of isotropic and balanced symmetric plate structures would be governed by the imposed boundaries. Therefore, a physical interpretation and a close approximation of the resulting boundary conditions in the skin-stiffener junctions are essential. By contrast, the boundary conditions on the loading edges may be neglected due to the assumption of an infinite long strut.

Even though the boundaries of the unloaded edges were assumed to be simply supported in the development of the design, nevertheless the selection of an appropriate skin stiffness reduction η is not straight-forward, since the unloaded edges may be considered undistorted or stress-free (Singer et al., 1998). However, it has been mentioned earlier that channel buckling is developed in a distortional mode, in which only some of the junctions between the web and flanges remain straight. Therefore, the assumption of stress free boundaries at the unloaded edges would be a safer and perhaps

more realistic approximation. The latter assumption though, would result in a lower bound post-buckling stiffness in comparison to the plate with straight edges (Singer et al, 1998; Powell et al., 1998).

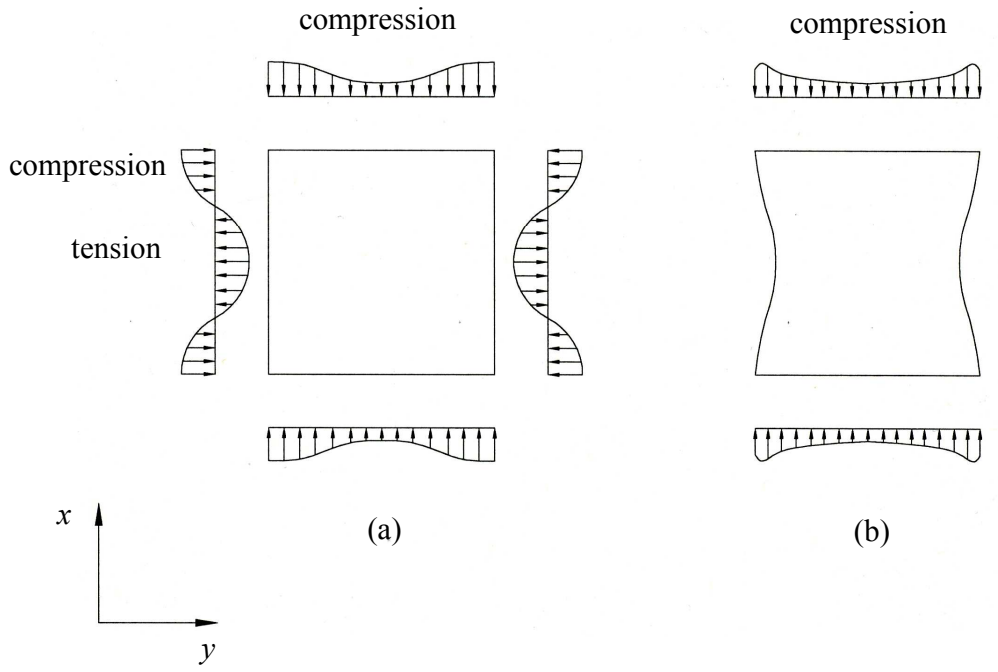

Figure 3.6. Post-buckling stress distribution at the edges of a square plate with (a) undistorted unloaded edges and (b) stress free (free to distort) unloaded edges.

That is, in the case where the unloaded edges were being held straight the tensile stresses would be developed in the central region of the plate, which would vary according to the lateral deflection of the developed buckling contour, Figure 3.6(a) (Singer et al., 1998). Such stresses though, would considerably restrain the plate from further lateral deflection, and thus, result in a stiffer post-buckling path (Singer et al., 1998), where η is equal to *0.5*. Since such stresses are absent when the unloaded edges are free to deform according to the contour shape, Figure 3.6(b), a less stiff post-buckling path would be observed with η equal to *0.33*. It should be noted though, that in

Figures (a) and (b), the variation of the axial stresses has also been included in order to represent the non-uniform distribution of loading after critical buckling (Singer et al., 1998) and portray a more accurate representation of the stresses developed when a single half-wavelength in the axial and transverse direction is being considered with the aid of a square plate.

3.3.3 Post-Buckling Strength

As described to an extent in Chapter 1, the current design criteria of primary composite stiffened structures restrain the ultimate load of the structure to the point of buckling, and thus, do not take advantage of the potential of such structures to carry sufficient loading after initial buckling. However, the realization of the potential weight-saving (that is, lighter/thinner structures) that could be attained by the design of ultimate loads within the post-buckling range has recently received much attention. A specific value of post-buckling reserve of strength, or otherwise a given factor of post-buckling strength α, has not been yet been established. Nevertheless, the aim of such a task would obviously be to ensure that under any given conditions the safety requirement would not be comprised. For example, even in the presence of destructive mechanisms such as the presence of damage, structural and material coupling phenomena and material degradation, the design ultimate load would be attained. The selected factor in the current work is assumed to be *1.4* of the initial buckling load of a channel-section strut.

3.4 Application of the Design Methodology

As stated in Chapter 1, one of the main considerations of the current work is to investigate the criticality of damage tolerance of thin-walled composite stiffened structures, which are designed to the upper limits of ultimate loading specifications in order to conform to future requirements of lighter aircraft components. Therefore, buckling of the channel-section strut would be required to occur at material strain of approximately 4000 micro-strain. Since the skin width was fixed and the stacking

sequence decided, a simple investigation of an appropriate thickness *T* for a laminate manufactured using the high strength composite material M21/35%/268/T800S (the properties of which are listed in Table 3.1 as provided by the manufacturer), suggested a *2 mm* thick laminate. Thus, for a skin stiffness reduction (*η)* equal to *0.33,* a height to breadth ratio *b/h* may be established for any given factor of post-buckling strength *α*, Figure 3.7.

Property	*Symbol*	*Units*	*Value*
Axial Compression Modulus	E_{11}	kN/mm^2	136
Transverse Compression Modulus	E_{22}	kN/mm^2	9.4
In-Plane Shear Modulus	G_{12}	kN/mm^2	4.9
Interlaminar Axial Shear Modulus	G_{13}	kN/mm^2	4.9
InterlaminarTransverse Shear Modulus	G_{23}	kN/mm^2	2.5
In-Plane Poisson's Ratio	v_{12}	-	0.33

Table 3.1. Material properties of the M21/35%/268/T800 prepreg.

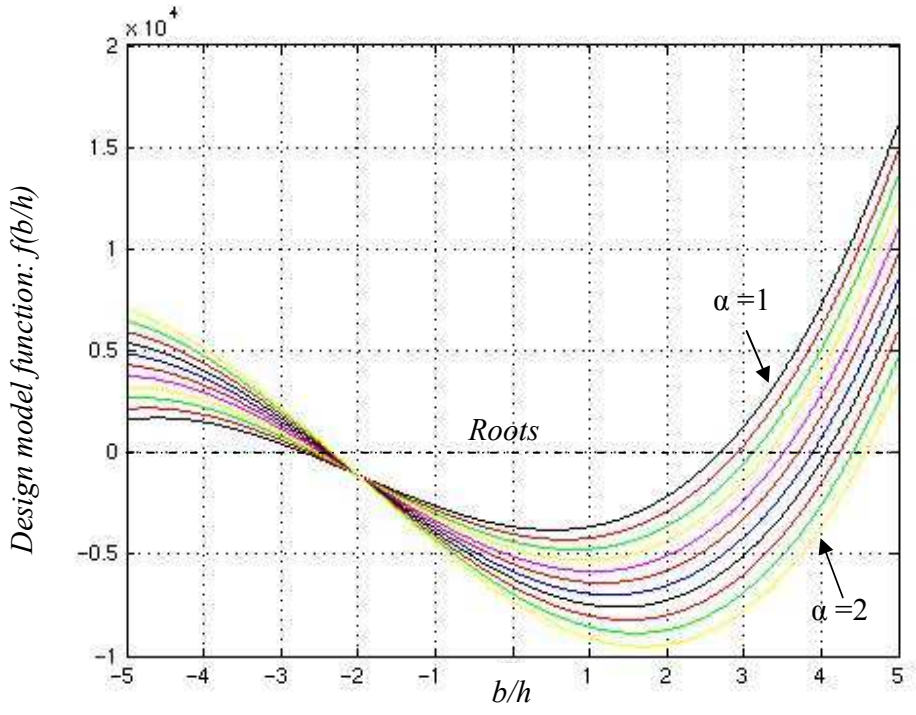

Figure 3.7. Roots of the design model, where positive values specify the breadth to width ratio of the channel-section strut for various factors of post-buckling strength α.

3.4.1 Infinite-Length Channel-Section Strut

The design model was compared first with a finite element model for the case of a channel-section strut with infinite length. However, since an infinite length finite element model is unrealistic, a length equal to the width of the skin is modeled instead (the methodology of which is presented in Chapter 5). That is, assuming simply-supported boundaries at the loaded edges of the channel-section strut, buckling would occur in a single half-sine-wavelength similar to the periodic half-sine wave that would evolve along an infinite long strut. The equivalent model is based on the assumption drawn by Banks and Rhodes (1981) for the post-buckling analysis of plates and sections. Even though the equivalent model would probably yield a sufficient portrayal of the efficiency of the design model in terms of critical load and post-buckling stiffness, nevertheless conclusions about the ultimate strength capability would not be possible to be attained. That is, in the finite element model the length of the strut is short enough to restrict global/Euler buckling to occur at comparable loads to the local/critical buckling load. Or in simpler terms, the effective stiffness loss in both skin and stiffener is not sufficient to promote global buckling.

The validity of the efficiency of the critical load and post-buckling stiffness is conducted for various breadth to width ratios, Figure 3.8, selected for specific post-buckling strength requirements or stiffener heights. In any case, a very good correlation is observed between the design model and the finite element analysis (FEA) in terms of the critical load and the pre- and post-buckling stiffness. The small deviations observed in the buckling load could be attributed to the rounding of dimension parameters in the FEA model (for example for $b/h=3.56$ the design model yields a stiffener height of *18.9 mm*, which has been approximated to *19 mm*) and the inclusion of a radius. Additionally, the deviations observed in the post-buckling stiffness at higher loading levels, are primarily attributed to structural coupling and will be discussed later in more detail with the aid of a finite-length model. The results, have been summarized in Table 3.1 along with the ultimate load predictions of the design model that confirm the required factor of

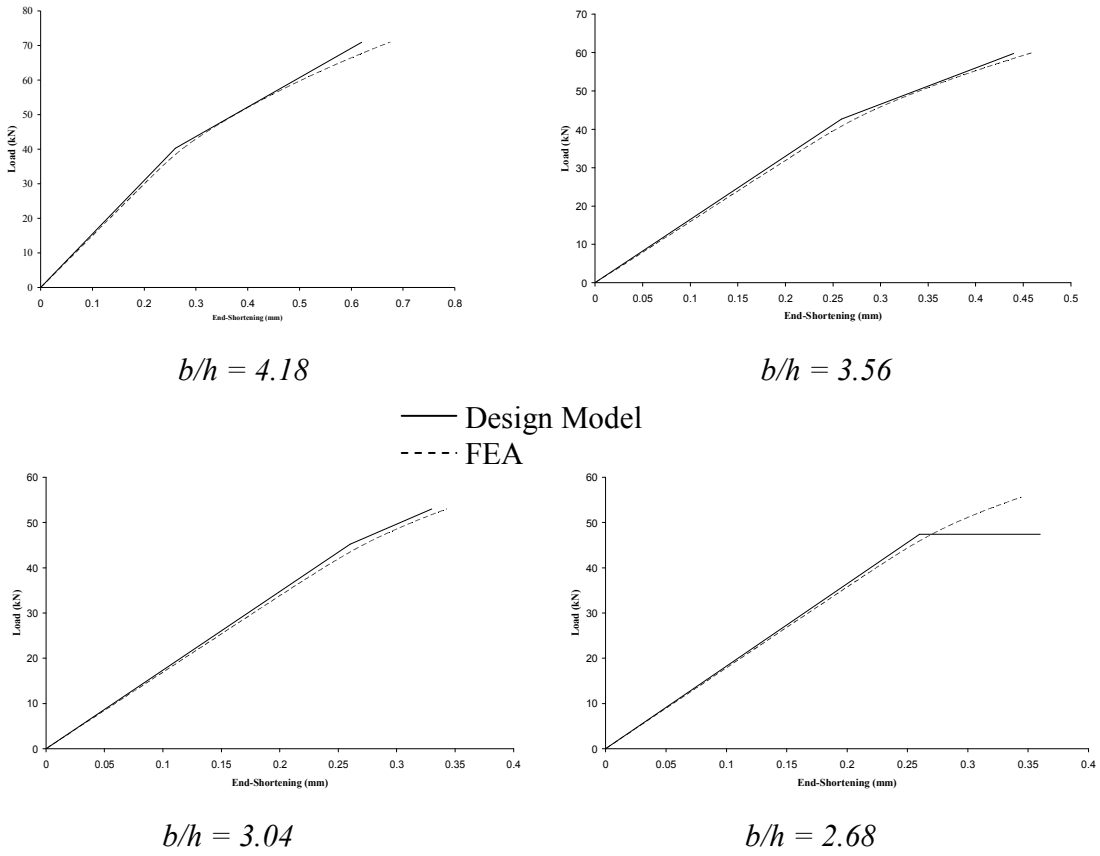

Figure 3.8. Plots of load versus end-shortening for various breadth to width ratios, as predicted by the design model and FEA.

Load/(b/h)	*Design model* *b/h*				*Finite Element* *b/h*			
	2.68	*3.04*	*3.56*	*4.18*	*2.68*	*3.04*	*3.56*	*4.18*
Buckling Load (kN)	47.4	45.2	42.7	40.3	46.2	44.7	42.4	39.2
Ultimate Load (kN)	47.4	52.9	59.7	70.9	-	-	-	-

Table 3.2. Comparison of buckling load prediction between the design model and finite element analysis for an infinitely long channel-section strut and presentation of the ultimate load predictions of the design model satisfying various post-buckling factors of strength.

post-buckling strength in relation to the given breadth to width ratio. It should be noted that for the special case of the breadth to width ratio (*b/h=2.68*) that yields a factor of post-buckling strength equal to *1.0* (stiffener and skin buckling occurring simultaneously) no post-buckling path can be predicted by the design model.

3.4.2 Finite-Length Channel-Section Strut

In order to establish whether or not the design model can predict the ultimate loading capacity of a channel-section strut, a finite length must be considered. However, the latter must comply with the infinite-length assumption. According to Kollar and Springer (2003), such an approximation would be valid when,

$$l_x > 3b_y \sqrt[4]{D_{11}/D_{22}} \tag{3.21}$$

Thus, a minimum length for the channel-section strut may be considered (and for the parameters defined earlier will be approximately *L>213 mm*). Therefore, for *α=1.4* (or otherwise *b/h=3.56*) the length effect may be examined for intermediate values, Figure 3.9. Even though a very good agreement is still observed in terms of critical instability and pre-buckling stiffness, the design model is not able to predict the correct post-buckling path or ultimate load.

From the finite element model it is apparent that structural coupling is initiated at buckling, where the local instability promotes and evolves along with Euler buckling, the extent of which is dependent on the length of the strut. As perhaps would be anticipated, the longer the strut the more adverse such coupling appears to be, affecting both ultimate level of loading and post-buckling stiffness. The latter effect can also be observed in the relatively short struts of the finite element models for the infinite length-assumption, but it occurs at levels of loading significantly above critical instability and could be considered inconsequential in respect to the ability to draw conclusions on the efficiency of the design model. Thus, it appears that the aforementioned coupling

phenomenon is a distinctive behaviour of the channel-section configuration, which contradicts the initial assumption of no mode interaction (upon which the design model is based on). Nevertheless, a comparison of the approximated infinite-length and finite-length model can provide valuable insight into the effect of structural coupling in the post-buckling region.

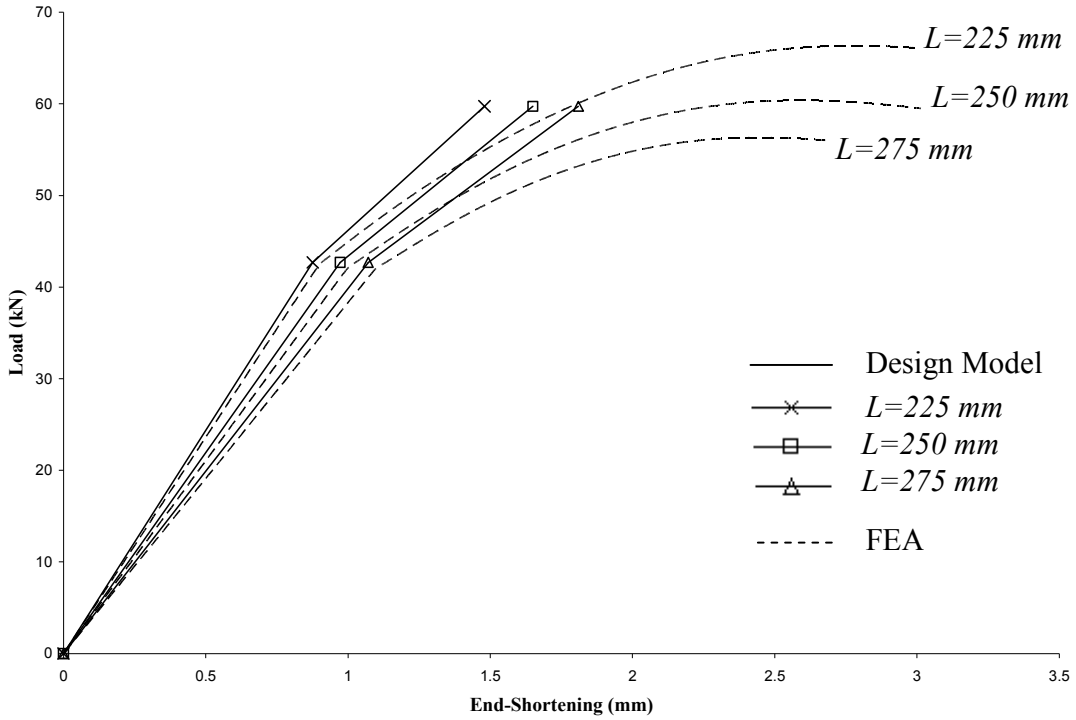

Figure 3.9. Plot of load versus end shortening for a channel-section strut with *b/h=3.56* and varying length as predicted by the design model and the finite element analysis.

3.5 Concluding Remarks

A simplified design model was developed with the aid of the Shanley model approach in order to account for post-buckling constraints. The latter appeared to be validated to an extent by the finite element analysis for the case of an approximated infinite-length model, contrary to the finite-length one, where significant structural coupling occurred upon critical instability. Even-though in either case a good agreement was observed in terms of pre-buckling stiffness and buckling load, in the first, the nature of the selected configuration and the unrealistic infinite length model did not allow conclusions to be drawn in regard to ultimate loading conditions, while in the second the length effected not only the ultimate level of loading, but also the extent of coupling, and thus the post-buckling stiffness.

The success of the design model though, would be better evaluated in terms of the infinite-length model, for which initial assumptions were drawn. Previous investigations (Banks and Rhodes, 1981) with higher complexity and numerical effort have followed the same route. Nevertheless, the model was designed with realistic behaviour of aircraft structural components, such as the blade stiffened panels, in mind. For typical geometries of the latter, it is strongly believed that the infinite-length assumption of the design model should not only be able to predict pre- and post-buckling stiffness and critical load (as it was established for the channel-section), but also be able to account for ultimate load levels.

Nevertheless, it should be emphasised that the main objective of the simplified design model was to minimize the parametric investigation of the appropriate geometry that would satisfy pre- and post-buckling constraints. With no direction, such a process would have been extremely time-consuming, since a large number of finite element models would probably need to have been constructed until the conditions were met. In that respect, the design model was successful, since it minimized the varying parameters to one (that is, the length). However, since the Shanley model was originally developed in order to account for structural interaction, it is more likely than not that the model can

and will be altered in order to account for the length effect. Nevertheless, the ultimate objective is to incorporate damage considerations into the Shanley model by means of spring de-stiffening, which currently suffer from lack of analytical solutions and extremely complicated numerical models.

Finally, the derived geometry and stacking sequence of the channel-section strut composed by the M21/35%/268/T800S material system has been summarized in Table 3.3 and illustrated in Figure 3.10. However, for clarification it should be noted that the initial geometry was determined for the undamaged channel-section strut composed of the M21/35%/268/AS7 material system, as for all the undamaged structures. For reasons explained in more detail in Chapter 6, the latter material system was not available for testing of the undamaged structure, and therefore, the M21/35%/268/T800S was incorporated instead. Nevertheless, due to the similarity of their material properties the derived specifications of its geometry were not compromised. The material properties of M21/35%/268/AS7 have been determined by experimental testing, and therefore, are presented in Chapter 7.

Skin width, b*	67 mm
Stiffener height, h*	19 mm
Channel length, L	250 mm
Stacking sequence	$[45/-45/0/90]_s$

*Distances from the mid-surface of the laminate

Table 3.3. Summary of the design specifications for the channel-section strut.

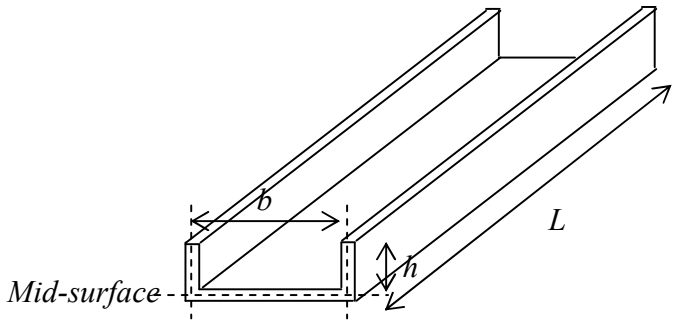

Figure 3.10. Channel-section strut geometry.

Chapter 4

Design Methodology for the Damaged Channel-Section Struts

Perhaps, one of the most critical issues in the design of damage tolerant structures is the identification of the critical load of the delamination. Or otherwise, that the strain level at which delamination buckling occurs is within the anticipated strain allowbles. This is particularly true for thin-walled laminates for which delamination growth, and thus ultimately failure, is always preceded by delamination buckling. However, establishing such loads/strain levels in the structural echelon usually involves complex computational work, such as that presented in the following chapter, and rigorous testing.

In this chapter a semi-analytical and semi-numerical method is developed in order to define the critical buckling load of the delaminated sublaminate. The numerical part is solved by VICONOPT (Williams et al., 1996), which is a finite-strip package that offers modeling and computational ease, and therefore, some of its main features are presented. The effectiveness of the method developed is based on the assumption that the critical sublaminate can be investigated in isolation from the surrounding structure, but nevertheless take into account the stress field imposed by the surrounding structure. Hence, the method developed was incorporated into the design of the damaged/delaminated channel-section struts in order to define an appropriate delamination size.

4.1 Design of the Delaminated Channel-Section Struts

For the design of the damaged (delaminated) structures, circular and semi-circular delaminations were considered in the skin and the stiffeners respectively, in the positions shown in Figures 4.1 (a) and (b). These were, the centre-point of the skin and the mid-length of the right stiffener, since preliminary analysis on the undamaged channel-section strut suggested that these were the most critical points/areas of the stress concentration under axial loading. As has been more thoroughly discussed in Chapter 1, the embedded delamination is considered as an approximation to BVID and the free-edge delamination as the result of manufacturing defects or high stress concentrations. Even though such events are not expected to produce similar delamination diameters, nevertheless for comparison reasons they are equated. The size of which was chosen according to the following criteria.

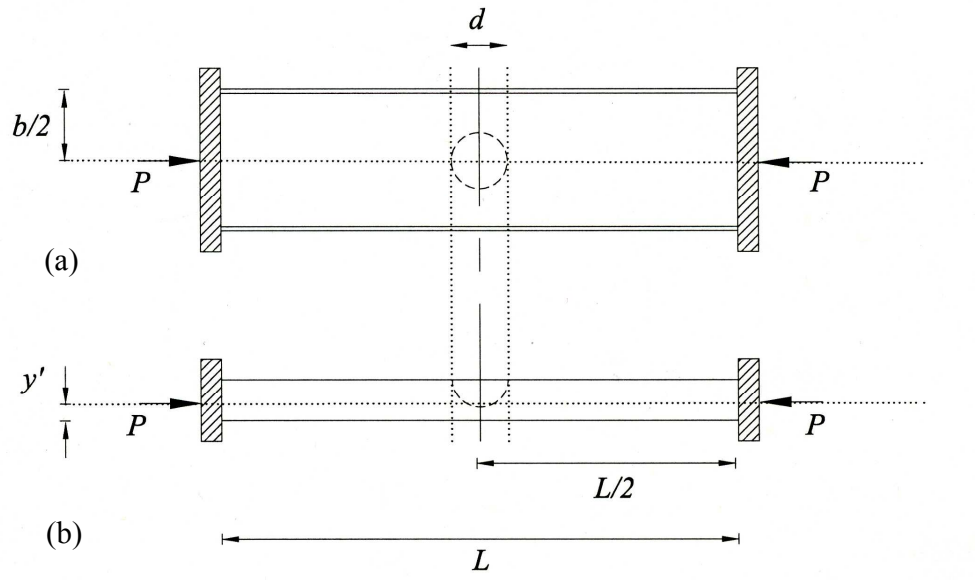

Figure 4.1. (a) Plan-view with (enclosed) circular delamination in the skin and, (b) side-view with semi-circular (free-edge) delamination in the right stiffener.

i. The delamination size *d* should be large enough to be realizable experimentally by the inclusion of the PTFE patches (artificial delaminations). Or otherwise, the PTFE patches should be large enough to sustain their position throughout the curing cycle without being dislocated by the resin flow.

ii. The delamination size should be approximately equal to the size resulting from low velocity impact. In particular, from experimental evidence (Curtis et al., 1993) it has been demonstrated that a low velocity impact event of 7 Joule in a *2mm* thick balanced-symmetric laminate, composed by a similar fiber/epoxy system to the one utilized in the current work, would produce a delamination diameter of up to *27mm*. Even though this size is an approximation of the impact event that could be modified for analysis purposes, nevertheless subsequent analysis suggested that for the given size all the required conditions would have been satisfied for the majority of the levels of delamination, see Figure 4.2.

iii. Delamination buckling at any level (through-thickness) should be below the initial local buckling load of the undamaged structure. The aforementioned condition is critical in the evaluation of the damage tolerance capability of the structure, since the influence of the delaminated region (damage) must be examined in correlation to the design ultimate load (structural buckling). The post-buckling behaviour, and consequently, the ultimate loading conditions are examined as a consequence of the latter allowable.

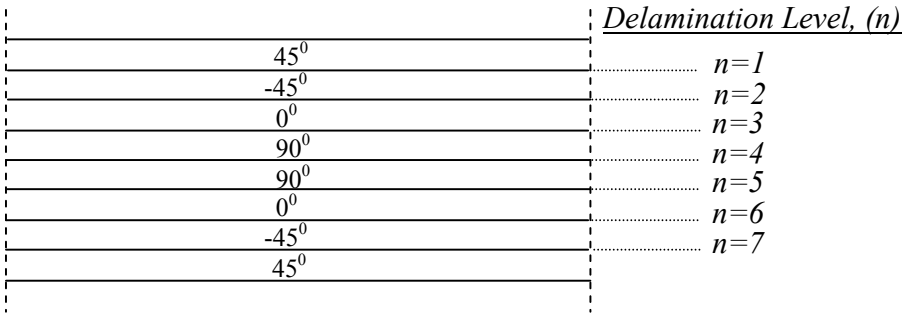

Figure 4.2. Illustration of possible levels of delamination in the balanced-symmetric laminate.

Finally, it should be noted that even though the onset of delamination growth is not considered in the analysis, nevertheless it is understood that it could occur at any stage after delamination buckling.

4.2 Finite Strip Analysis

The finite strip methodology may be utilized for the analysis of any structure with longitudinally invariant cross-section (prismatic) and distributed in-plane uniform loading (Williams et al., 1996). The theory is based on the discretization of the structure into strips by longitudinal lines, Figure 4.3, that are assumed to be connected to each other at their nodal lines, or otherwise at their longitudinal boundaries (Cheung, 1976). At the intersections of neighboring strips compatibility is satisfied by assigned displacement functions, which have been appropriately selected to represent the displacement, and consequently, the stress/strain field.

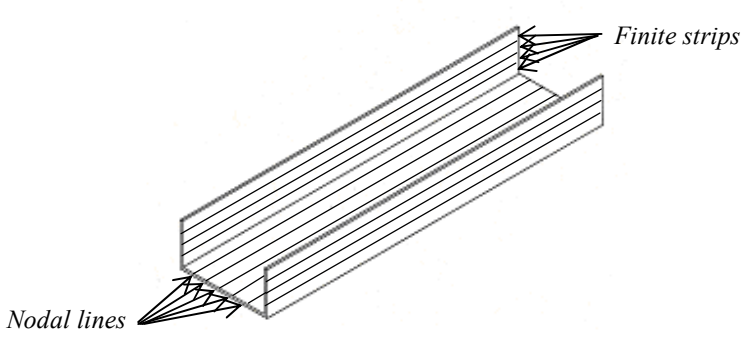

Figure 4.3. Prismatic structure discretized by finite strips.

Typically, the displacement function, or otherwise the imposed shape function, is the product of a polynomial or a trigonometric function and a series that relate the degrees-of-freedom of each nodal line to their displacements and rotations in respect to the transverse direction (Cheung, 1976). Thus, a displacement matrix for each strip may

be constructed, from which the stiffness matrix and load matrices may be obtained. By summation of all the individual matrices, a set of overall stiffness equations for the structures can be derived. Generally, the finite strip method is a special category of finite element analysis (which is discussed in detail in the following chapter). The slight loss in accuracy of results of the finite strip method in comparison to those compared by the finite element analysis is compensated by significantly less computational and modeling expense.

In the current work the finite strip analysis package VICONOPT was incorporated into the modeling methodology of the damaged channel-section struts. VICONOPT is a FORTRAN 77 computer program that exploits a particular finite strip theory that was developed by Wittrick and Williams in the late 1960's and early 1970's (Butler and Liu, 2008). The theory utilizes an exact method of analysis by assuming a trigonometric shape function in the form of sinusoidal variation of the buckling deformation in the axial direction and infinitely long structures with repeating supports and constraints at the longitudinal intervals defined by the length of the structure under investigation (Butler and Liu, 2008). Thus, with the aid of an eigenvalue analysis the critical loads can be obtained for any chosen half-wavelength that divides the length of the structure unerringly (Williams et al., 1996). In the event of absence of shear loading and simply-supported boundaries at the intersections the latter method of analysis gives reasonably accurate results for either laminated or anisotropic structures.

However, if the presence of shear loading is significant or clamped end conditions must be enforced then VICONOPT offers the option of incorporating the latter conditions in the analysis by coupling the response of a series of longitudinal half-wavelengths, and thus, the appropriate shape function can be derived. Moreover, in the presence of transverse shear the Classical Lamination Theory based on Kirchhoff's assumption is inappropriate, and therefore, an approximation for the first order shear deformation theory is incorporated (Butler and Liu, 2008).

4.3 Transverse Shear Effects

The employment of Classical Lamination Theory may not always be successful, since it is based on Kirchhoff's hypothesis that assumes that the transverse shear stresses can be neglected. However, as described in the previous chapter, transverse shear would not only result in the degradation of the critical load (Chen et al., 1993; Kardomateas and Schmueser, 1988), but also promote delamination growth in delaminated structures (Kardomateas and Schmueser, 1988). Therefore, the incorporation of such effect may prove to be critical in the design of an undamaged or damaged laminated structure.

The criticality of transverse shear effects in laminated structures has been shown (Arnold and Mayers, 1984) to be dependent primarily on the slenderness and stacking sequence of the laminated plate/beam. In particular, low slenderness plates/beams would be subject to greater transverse shear stresses, and thus, their critical buckling load would be noticeably less than the predictions of analytical models that assume negligible transverse shear stresses. On the contrary, for high slenderness plates/beams Kirchhoff's hypothesis can provide an adequate solution. Therefore, assuming a constant plate width, an increase in the plate thickness would result in an increase in the influence of transverse shear. Similar findings have been observed for delaminated plates, when the depth of the delamination was increased (Kardomateas and Schmuesser, 1988).

Thus, it appears that even in relatively thin-walled structures, where elimination of the transverse shear stresses would not affect significantly the buckling load, the presence of the delamination would essentially result in lower-slenderness plate segments within the structure, and hence, the critical buckling load of which would be greatly influenced by the presence of transverse shear. Therefore, in the design methodology of the damaged composite channel-section struts, transverse shear stresses must be accounted for by the allowance of non-perpendicular transverse normals to the mid-surface of the laminate. Consequently, transverse shear stresses are incorporated in the buckling analysis of the delamination.

4.4 Method of Analysis

As described in Chapter 2, a delaminated structure under uniform end-shortening will become aware of the presence of delamination after delamination buckling has occurred. That is, prior to buckling a uniform strain field is effectively applied in the delaminated structure, identical to that of the undelaminated laminate. In accordance with the Classical Lamination Theory (Equation 2.9) the in-plane strain field acting on the laminate, is correlated to the in-plane forces as follows;

$$\begin{aligned} N_x &= A_{11}\varepsilon_X + A_{12}\varepsilon_y + A_{16}\gamma_{xy} + B_{11}\kappa_x + B_{12}\kappa_y + B_{16}\kappa_{xy} \\ N_y &= A_{12}\varepsilon_X + A_{22}\varepsilon_y + A_{26}\gamma_{xy} + B_{12}\kappa_x + B_{22}\kappa_y + B_{26}\kappa_{xy} \\ N_{xy} &= A_{16}\varepsilon_X + A_{26}\varepsilon_y + A_{66}\gamma_{xy} + B_{16}\kappa_x + B_{26}\kappa_y + B_{66}\kappa_{xy} \end{aligned} \tag{4.1}$$

However, for a balanced-symmetric laminate the *B*-matrix and the extensional coupling terms are zero. Thus, for the laminate under discussion, subject solely to axial loading, the above equation reduces to,

$$\begin{aligned} N_x &= A_{11}\varepsilon_X + A_{12}\varepsilon_y \\ 0 &= A_{12}\varepsilon_X + A_{22}\varepsilon_y \\ 0 &= A_{66}\gamma_{xy} \end{aligned} \tag{4.2}$$

which yields the strain ratio,

$$\varepsilon_y = -\frac{A_{12}}{A_{22}}\varepsilon_x \quad \text{and} \quad \gamma_{xy} = 0 \tag{4.3}$$

Thus, the sublaminates within the structure must strain according to Equation 4.3. However, this condition effectively forms a stress field acting at the boundaries of the delaminated region due to the disparity of the Poisson's ratio of the delaminated laminate and the full laminate. For the critical sublaminate, the in-plane force resultants are given by substitution of Equation 4.3 into the stress-strain relationship defined by the Classical Lamination Theory. Hence,

$$
\begin{aligned}
N_{x,S} &= A_{11,S}\varepsilon_x - A_{12,S}\left(\frac{A_{12}}{A_{22}}\right)\varepsilon_x + B_{11,S}\kappa_x + B_{12,S}\kappa_y + B_{16,S}\kappa_{xy} \\
N_{y,S} &= A_{12,S}\varepsilon_x - A_{22,S}\left(\frac{A_{12}}{A_{22}}\right)\varepsilon_x + B_{12,S}\kappa_x + B_{22,S}\kappa_y + B_{26,S}\kappa_{xy} \\
N_{xy,S} &= A_{16,S}\varepsilon_x - A_{26,S}\left(\frac{A_{12}}{A_{22}}\right)\varepsilon_x + B_{16,S}\kappa_x + B_{26,S}\kappa_y + B_{66,S}\kappa_{xy}
\end{aligned}
\tag{4.4}
$$

Where S denotes the sublaminate. But, prior to buckling only in-plane displacements are allowed to occur, and therefore, Equation 4.4 reduces to,

$$
\begin{aligned}
N_{x,S} &= A_{11,S}\varepsilon_x - A_{12,S}\left(\frac{A_{12}}{A_{22}}\right)\varepsilon_x \\
N_{y,S} &= A_{12,S}\varepsilon_x - A_{22,S}\left(\frac{A_{12}}{A_{22}}\right)\varepsilon_x \\
N_{xy,S} &= A_{16,S}\varepsilon_x - A_{26,S}\left(\frac{A_{12}}{A_{22}}\right)\varepsilon_x
\end{aligned}
\tag{4.5}
$$

Hence, for any given value of axial strain, the force field acting per unit length of the edges of the critical sublaminate can be estimated. A closer examination of Equation 4.5 reveals that the transverse resultant could be either tensile or compressive in nature, conditional on whether the Poisson's ratio of the sublaminate is bigger or smaller than that of the full laminate.

In VICONOPT, the longitudinal invariant force field acting at the edges of the critical sublaminate can be treated as live load components of the eigenvalue problem, for which the critical load factor λ is estimated (Williams et al., 1996). Consequently, the critical axial strain, ε_C^D, applied in the structure is determined, since in accordance with Equation 4.5 it is linearly correlated to the in-plane force field acting at the edges of the critical sublaminate.

4.5 The Finite-Strip Delaminated Models

In the finite-strip analysis the critical sublaminate in either case was modeled as a single plate that was discretized into 6 equal width strips. For the embedded delamination, a square plate whose length and width was equal to the delamination diameter [Figure 4.4(a)] was created in VICONOPT, while for the free-edge delamination, one whose length and width was equal to and half of the delamination diameter was created [Figure 4.4(b)]. The circular and semi-circular boundaries of the delaminated plates were formulated by generating the nodes in appropriate longitudinal positions at the junctions of the constituent strips. Finally, all the degrees of freedom of the generated nodes were fixed in order to simulate the approximated clamped perimeter of the buckling sublaminate, which was assumed to be a thin film.

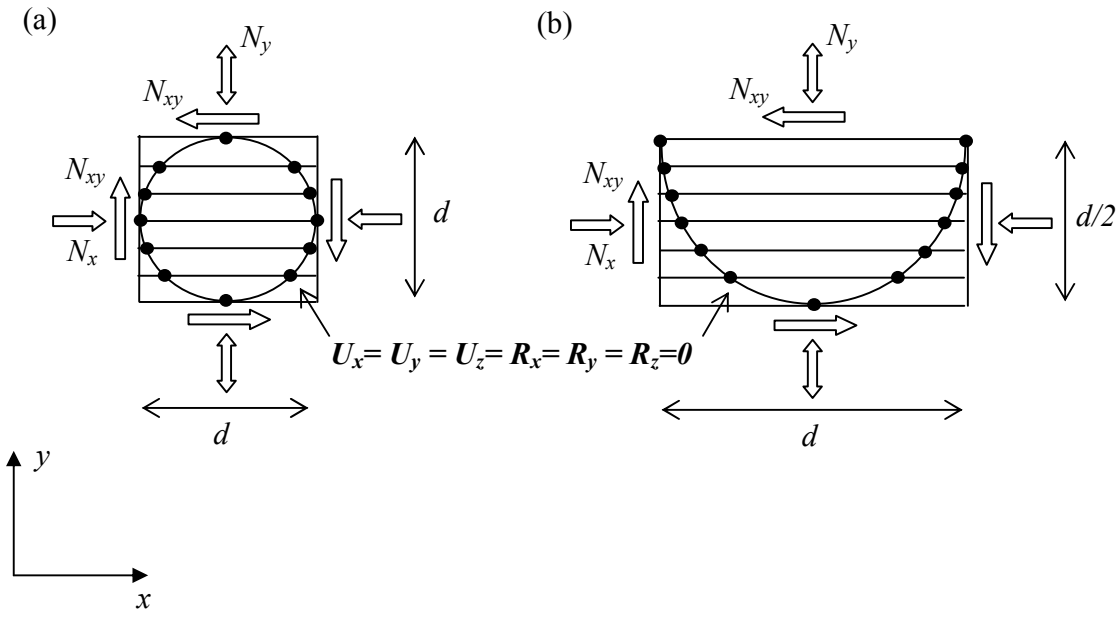

Figure 4.4. Finite strip models of the thin film (a) enclosed and (b) free-edge delamination.

4.6 Validity of the Design Methodology

The validity of the method of analysis developed was investigated via a range of experimental tests on thin-film delaminated coupons with embedded circular delaminations. Even though the availability of such data in the literature was surprisingly scarce, nevertheless the model was compared to an adequate variety of materials (see Table 4.1), stacking sequences, delamination levels and diameters and size of coupons, Table 4.2. For comparison reasons, the critical buckling load given in the experiments was converted into axial strain in accordance with Equation A.1 (Appendix A).

Generally, a very good correlation was observed between the experimental and the VICONOPT critical buckling strains, with the mean value deviation being somewhat less than 9%. Deviations as such, between theoretical models and experimental results, are within the anticipated region, but nevertheless deterministic factors that give rise to the latter disparity are very difficult to establish. That is, deviations could be attributed to any number or combination of parameters, such as approximations of the actual geometry and boundaries of the plate and delamination area, the material properties and the presence of imperfections. It is worth noting though, that the design methodology developed is subject to further validation when comparisons will be drawn with the results of the finite element eigenvalue analysis of the damaged channel-section struts with skin delamination.

Validation of the design method in respect to the free-edge (semi-circular) delamination would have been of no consequence, since the assumed stress field acting at the boundaries of the delamination was obviously unrealistic. That is, the free edge of the delamination is allowed to deform in-plane independently of the structure, while the perimeter of the delamination must displace in accordance with the surrounding structure in order continuity to be maintained. Thus, a complex stress field arises at the perimeter of the delamination, whose quantitative and qualitative expression are very difficult to be defined in the analytical approach and the finite-strip method respectively.

Material	E_{11} *(MPa)*	E_{22} *(MPa)*	E_{12} *(MPa)*	E_{23} *(MPa)*	E_{13} *(MPa)*	v_{12}	t_{ply} *(mm)*
HTA/913C†	135	18.5	5.98	5.98	2.99	0.29	0.13
*HTA/6376C**	131	11.7	5.2	5.2	3.9	0.3	0.13

†Hu et al., 2004; *Nilsson et al, 2001a

Note: For *HTA/913C a ply thickness of 0.13 instead of the 0.134 was utilized since to the author's knowledge and experience the second refers to the uncured thickness. Moreover, the value of the transverse modulus provided is excessively large, and therefore, bigger deviations in the results are anticipated in laminates where the* 90^0 *is most influential.*

Table 4.1. Properties of the materials utilized in the delaminated coupons.

Material	*Lay-up*	*Level, n*	*Diameter, d (mm)*	*Sublaminate Thickness /Laminate Thickness*	*Buckling Strain ,μ*	
					Experiment (load in kN)	*VICONOPT*
HTA/913C†	$[(45/0/-45/90)_2]_S$	3	30	18.75%	870 (10.1)†	885
HTA/913C†	$[(45/0/-45/90)_2]_S$	4	30	25%	1491 (17.3)†	1760
*HTA/6376C**	$[(90/0)_{17}/90]$	3	60	8.75%	209 (10)‡	215
*HTA/6376C**	$[(90/0)_{17}/90]$	5	60	14.28%	858 (41)‡	813
*HTA/6376C**	$[(90/0)_{17}/90]$	7	60	20%	1466 (70)‡	1610
*HTA/6376C**	$(90/-45/45/0_2/45/-45/90/0/45/-45/90_2/-45/45/0)_2$	27	60	15.62%	576 (21)*	646

†Hu et al., 2004; ‡ Asp et al., 2001; *Nilsson et al, 2001a

Table 4.2. Comparison of the experimental buckling strain with the design model for various delamination sizes, materials, stacking sequences and coupon sizes.

Therefore it was not possible to establish an exact value of critical strain for the free-edge delamination. Nevertheless, the exact solution could be bound by the two extremes of including and excluding the transverse stress component, providing a range of strain at which buckling must occur.

Perhaps, an exact value could also be established for the free edge delamination by adopting an alternative approach to the current philosophy. In particular, instead of the applied stress-field and boundary constraint strategy, stiffness constraints could be utilized at the perimeter of the delaminated region. Such constraints would be analogous to the stiffness characteristics of the undelaminated laminate and would effectively account for all displacements and rotations of the sublaminate. This method is yet to be developed.

4.7 Design Specifications of the Damaged Channel-Section Struts

Taking into account the aforementioned criteria for design of delaminated structures, the design methodology was incorporated in order to establish the allowable levels of delamination in the damaged channel-section struts, and consequently, their critical buckling strains for the selected delamination diameter *d=27mm* and material M21/35%/268/AS7. The results have been summarized in Table. 4.3, where for simplicity reasons, the delamination depth and position in the damaged structures are abbreviated as *n=i-Position*. For example, a damaged channel-section strut with a second level delamination in the skin is termed as *n=2-Skin*. From this point forward the latter terminology will be adopted throughout this work.

In accordance with the design criteria and methodology it was suggested that the effect of a 1^{st} and 7^{th} and 4^{th} level of delamination would be of secondary importance, and therefore, these positions were excluded in order to maintain an attainable amount of experimental work. In particular, the 1^{st} and 7^{th} level delamination were disregarded from the investigation based on experimental evidence from delaminated coupons (Hu et

al., 2004) that demonstrated that a critical depth (where the delamination buckling mode switches from opening to closing) was more likely to be present at 25% of the laminate thickness. The 1st and 7th accounted for 12.5% of the laminate thickness. Additionally, buckling of the 4th level delamination was found to be well in excess of the anticipated buckling load of the undamaged channel-section strut. Therefore, the particular level did not comply with the design specifications of the delaminated struts that were outlined in section 4.1.

Specimen	*Delamination Level /size d (mm)*	*Stacking Sequence*	*Buckling Strain,* ε_C^D (μ)
n=2-Skin	2/27	[45/-45/DEL/0/90/90/0/-45/45]	1606
n=3-Skin	3/27	[45/-45/0/DEL/90/90/0/-45/45]	2983
n=5-Skin	5/27	[45/-45/0/90/90/DEL/0/-45/45]	2983
n=6-Skin	6/27	[45/-45/0/90/90/0/DEL/-45/45]	1606
n=2-Stiffener	2/27	[45/-45/DEL/0/90/90/0/-45/45]	1464^1-3439^2
n=3-Stiffener	3/27	[45/-45/0/DEL/90/90/0/-45/45]	2823^1-4200^2
n=5-Stiffener	5/27	[45/-45/0/90/90/DEL/0/-45/45]	2823^1-4200^2
n=6-Stiffener	6/27	[45/-45/0/90/90/0/DEL/-45/45]	1464^1-3439^2

Note: Superscripts [1] and [2], respectively, refer to inclusion and exclusion of the transverse stress component

Table 4.3. Design specifications of the damaged channel-section struts

In contrast, for the remaining levels of delaminations the critical buckling loads were found to be significantly less than that of the undamaged channel. For the embedded (circular) delaminations in the skin, the most critical depths were the ones closer to the surfaces of the laminate (2nd and 6th). Unfortunately, for the free-edge delaminations in the stiffener a critical depth could not be defined, for the reasons explained earlier. Nevertheless, in all cases the buckling mode approximated the assumed thin-film configurations, Figures 4.5 (a) and (b). Finally, it should be noted that for the mirror delaminations (2nd and 6th, 3rd and 5th) the predicted bucking strains were identical, since in the simplified methodology adopted the effect of the structural configuration was not

taken into account. Verification of the results will be conducted with the aid of finite element analysis and experimental testing in Chapters 5 and 7, where the effect of the structural configuration on the criticality of the sublaminates will be investigated.

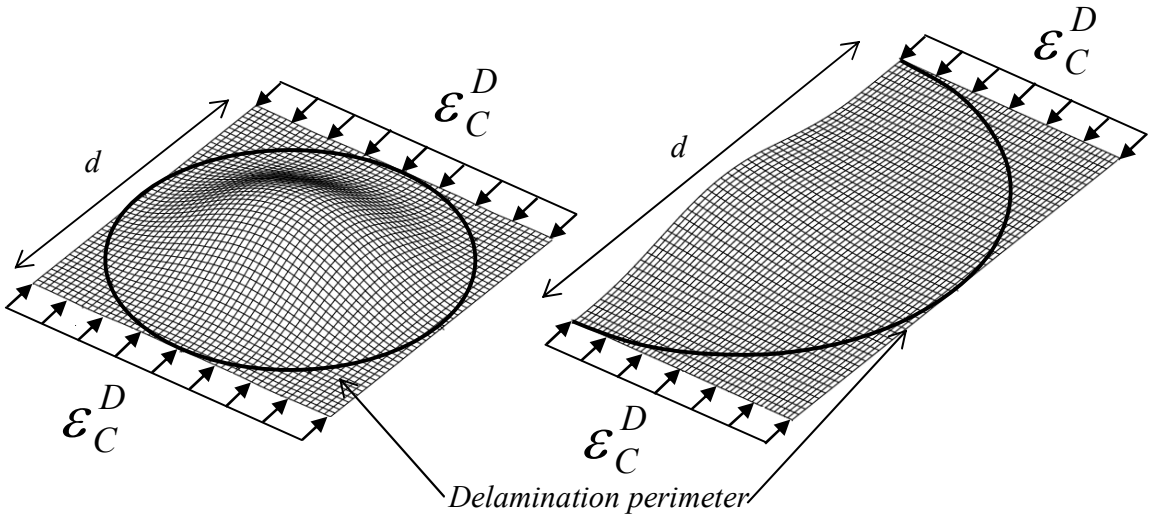

Figure 4.5. Buckling modes of (a) a circular delamination and (b) a free-edge delamination with clamped boundaries at their perimeters.

4.8 Concluding Remarks

A simplified methodology was developed for the design of the delaminated structures. The method was based on semi-analytical and semi-numerical approach that offered significantly less computational and labour cost in comparison to more complex finite element designs. Correlations with experimental results on delaminated coupons, found in the literature, validated to a satisfactory extent the efficiency of the method developed. Currently, the model has been incorporated into the investigation of the compressive strength of delaminated plates with enclosed delaminations (Butler et al,

2007) and has enjoyed particular success. The main weakness of the design lies within its initial assumptions, and therefore, it appears that its success is confined solely to embedded delaminations. Nevertheless, for the case of free-edge delaminations an alternative approach that lies within the same philosophy has been suggested and could potentially prove to be of similar success. Currently, the issue is being investigated as part of a research project in the department. Finally, it should be pointed out that even though the method does not take into account the structural configuration, comparisons with linear finite element results (to a first stage) will assist in evaluating the actual influence of the structural configuration on the criticality of the sublaminates.

Chapter 5

Numerical Modeling of the Undamaged and Damaged Channel-Section Struts

More often than not practical engineering problems are governed by complex shapes, constraints, boundary and loading conditions. In such complicated problems exact analytical solutions are unattainable due to the number and difficulty of the arising equations, and therefore, numerical approximations must be utilized (Moaveni, 1999). The most efficient numerical tool is the finite element analysis (FEA).

In this chapter the finite element method is introduced along with the FEA package employed (ABAQUS) in order to investigate both the linear buckling solution and the non-linear post-buckling behaviour. Furthermore, the techniques and methodologies adopted to model the undamaged and damaged channel-section struts are presented. Finally, the predicted critical loads derived from the linear buckling results of the damaged channel-section struts are compared with those from the semi-analytical methodology developed in Chapter 4 and the critical instability modes for the delaminated area and the structure as a whole are portrayed. It should be noted that to avoid repetition the non-linear results are presented in Chapter 7, where they are compared with the experimental results.

5.1 The Finite Element Method

The finite element method is based on the discretisation of a complex structural shape into nodes (points) and elements. The total number of elements and nodes encompassing the structure are frequently referred to as the mesh of the structure. More specifically, the elements are structural units formed by the aforementioned neighboring points, for which an approximate solution can be obtained (Moaveni, 1999). However, in order to monitor the physical behaviour of the system throughout its loading history all the elements must be assembled (and hence the individual solutions), and allowances must be made for the continuity and internal and surrounding boundary conditions (Moaveni, 1999). Thus, in order to obtain a realistic response of the structure under investigation, a detailed model that contains accurate approximations of the conditions that the structure is subject to must be developed and a powerful computer code (finite element package) must be utilized in order to obtain the solution.

In the current work the "ABAQUS" (ABAQUS, 2001a) general-purpose finite element package was employed in order to conduct both a linear and non-linear analysis of the damaged and undamaged channels. ABAQUS is a very versatile finite element package since it is not only equipped to deal with problems with various level of complexity (that may range from linearized eigenvalue analysis to non-linear dynamics), but also to deal with an extensive range of engineering applications, due to its enriched element library (i.e. shell, rigid, contact elements). In similarity to other commercial packages, ABAQUS follows the necessitated logical sequence in order to express a physical situation in mathematical terms. That is, the definition of the geometric aspects of the problem, the physical behaviour of the element, the interactions and constraints, the loading and boundary conditions and the method of analysis. A detailed description of the definitions developed for the undamaged and damaged channel-section struts is presented in the following sub-sections.

5.1.1 Finite Element Model Geometry of the Undamaged and Damaged Channel-Section Struts

Typically in finite element analysis thin-walled structures are modeled as shells, or otherwise, as idealized three-dimensional plates that are reduced to a two-dimensional problem by transferring their mechanical properties to the mid-surface. Therefore, more often than not the generated nodal and elemental mesh of such models refers to the discretisation of the mid-surface of all the plate segments composing the structure. In a similar manner, in the finite element model of the undamaged channel-section strut the nodes were generated across the mid-surface of the structure, Figure 5.1(a). Consequently, a continuous and homogeneous (no element size/shape variation within the constituent shells) mesh was produced that was composed of *1647* elements.

In contrast to the undamaged model, the presence of the delamination within the damaged counterpart resulted in the formation of three distinct regions; the surrounding structure (undelaminated part) and the upper and lower delaminated shells/plates. In ABAQUS the delaminated plates were modeled as two overlaying layers with identical mesh patterns that maintained mesh continuity with the surrounding structure by mapping their nodes accordingly, Figure 5.1 (b) and (c). In total *2558* and *1980* elements were generated respectively for the models with skin and stiffener delamination.

Moreover, their reference planes (the planes upon which the nodes are generated) were offset at their neutral axis in the direction of loading, Figure 5.2. In particular, to model such an offset two parameters had to be considered; the relative position of the reference plane (that is to the mid-surface of the undelaminated part) and the relative position of the reference plane within the delaminated part. Neglecting one or the other would have effectively resulted in incorrect load transfer through the nodal connection and overlapping of materials. The relative position of the reference surface of the sublaminates was calculated with the aid of Equation 2.13. However, since

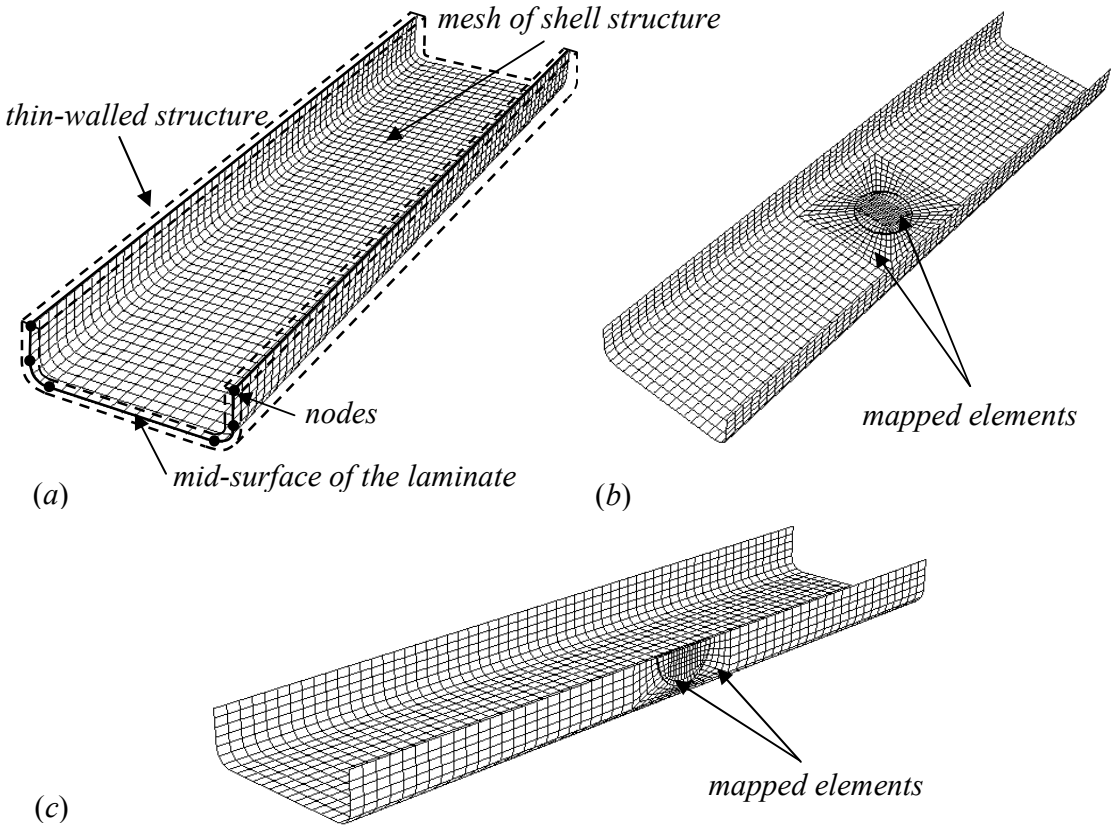

Figure 5.1. Finite element mesh of (a) the undamaged channel-section strut, (b) the channel-section strut with skin delamination and (c) the damaged channel-section strut with stiffener delamination.

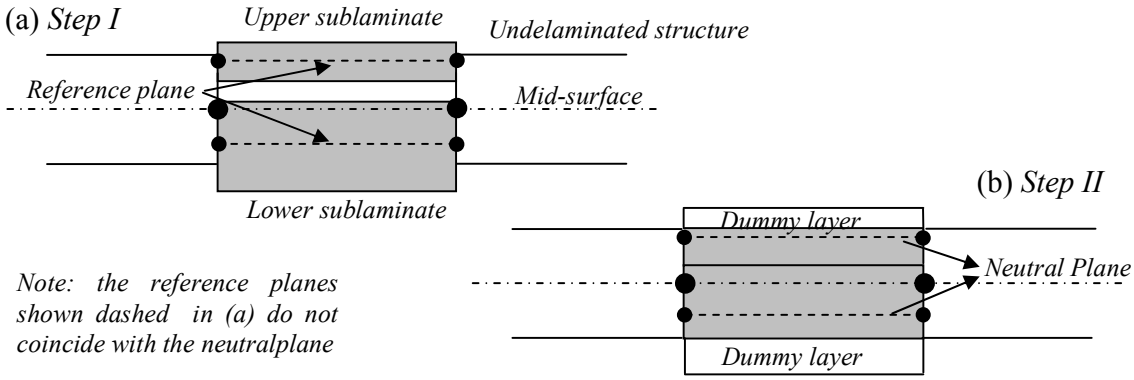

Figure 5.2. Illustration of the offset technique of the reference plane of the sublaminates to their neutral axis. (a) Positioning of the sublaminates reference surface in respect to the mid-surface of the undelaminated structure. (b) Positioning of the reference surface at the neutral plane.

ABAQUS by default considers the mid-surface as the reference plane in order to model the internal offset of the reference surface, in the delaminated parts a negligible stiffness layer was added appropriately at the surfaces. The utilization of the offset was imperative in order to generate a realistic response, as has been more thoroughly discussed in Chapter 2.

In compliance with the quest for accuracy and consistency in the finite element models with the realistic structures, the cross-sectional geometry of the channel-section struts was slightly altered in comparison to the one provided by the design model, Figure 3.9. In the finite element model the 6mm radius, as measured in the components produced (please see Chapter 6), at the skin/stiffener junctions was accounted for. More importantly though, in the finite element analysis the part of the structure that was potted in resin blocks, in order for appropriate boundary conditions be developed for experimental testing, was incorporated into the model along with the appropriate constraints. Justification of this is thoroughly discussed in Chapter 7 in conjunction with its significance. Finally it is worth mentioning that despite the fact that ABAQUS offers a comprehensive interface environment for model generation, element distortion and node positioning issues required all the models to be manually written in the form of an input file.

5.1.2 Finite Strain Shell Element

The channel-section struts were modeled using the ABAQUS "general-purpose" element S4R, which was offered in the ABAQUS library. The S4R element is a finite-strain element that is structured by four nodes with six-degrees of freedom. It is termed as "general-purpose" since under a given strain field, which can be large or small, the thickness of the element is accounted for (ABAQUS, 2001a). This is achieved by utilizing thin-shell theory (Kirchhoff's hypothesis) when the thickness is small (typically less than 1/15 of the element length) and thick-shell theory when it is relatively large. Or in more simple terms, the effect of transverse shear deformation becomes more pronounced as the thickness increases and vice-versa.

In the current work laminate characteristics were attributed to the element under discussion, the architecture and material systems of which were in accordance with the design models in Chapter 3 and 4. For the linear analysis method all channels are composed of the M21/35%/268/AS7 material system, while for the non-linear procedure the M21/35%/268/T800S is also considered in order to allow correlations with the experimental results to be deduced.

5.1.3 Kinematics and Contact Constraints

Kinematics

Since the delaminated shells were physically separated in space by the surrounding structure, displacement compatibility equations had to be imposed at the intersections of the sublaminates and the undelaminated structure, Figure 5.3. Hence, the displacements of the nodes of the sublaminates positioned at the intersection were constrained in accordance with the following equations.

$$\begin{aligned} u_i &= u_i - z_i\theta_{yi}, \\ v_j &= v_i + z_i\theta_{xi}, \\ w_j &= w_i, \\ \theta_{xj} &= \theta_{xi}, \\ \theta_{yj} &= \theta_{yi}, \\ \theta_{xj} &= \theta_{xi} \end{aligned} \tag{5.1}$$

Where u, v, and w are the translations about the x, y and z-axis respectively and θ_x, θ_y and θ_z the rotations about the x, y and z-axis respectively, as illustrated in Figure 5.3. In the latter figure the direction of the y-axis is towards the reader. Moreover, displacement compatibility constraints were imposed at the loading edge of the struts in order to simulate the experimental conditions. Specifically, all the nodes generated at the loading edge of the channel-section struts were constrained to displace axially in a uniform manner, see Section 5.1.4.

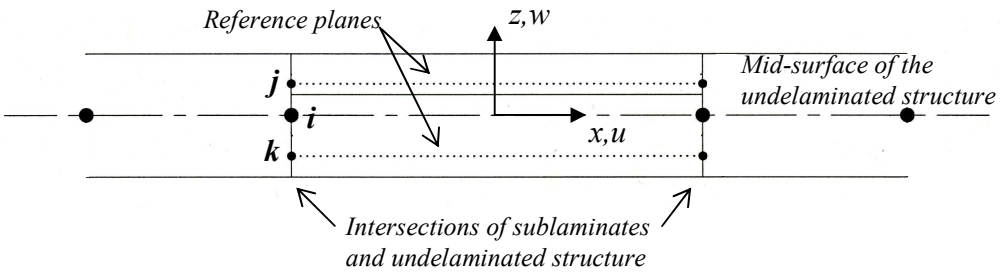

Figure 5.3. Displacement compatibility at the intersection of the sublaminates and the undelaminated structure.

Contact

Contact constraints were applied in the delaminated models in order to prevent nodal displacements of the overlaying shells within the space defined by their reference planes, and thus, imitate the physical restriction of inter-penetration of the sublaminate plates. In ABAQUS the latter condition was simulated by defining a normal behaviour for the opposing surfaces of the overlaying shells. In particular, in the event of a decrease in the initial clearance c of the surfaces (hypothetical overclosure), a normal pressure load was transmitted from the stiffer to the less stiff idealized sublaminate in accordance with an exponential relationship that was defined in terms of its spatial boundaries, see Figure 5.4. Those were the initial clearance c and zero clearance, at which the transmitted pressure load was set to zero and to a selected maximum value p_0 respectively. In the analysis an infinitely large value p_0 of 30×10^{30} N/mm^2 was utilized, which ensured that even an infinitesimal decrease in the initial clearance was accompanied by relatively large pressures. Therefore the transmitted load was able to counteract subsequent reductions, and thus, allowed the initial clearance to be essentially maintained. It should be noted however, that the contact constraints were not taken into account in the eigenvalue analysis.

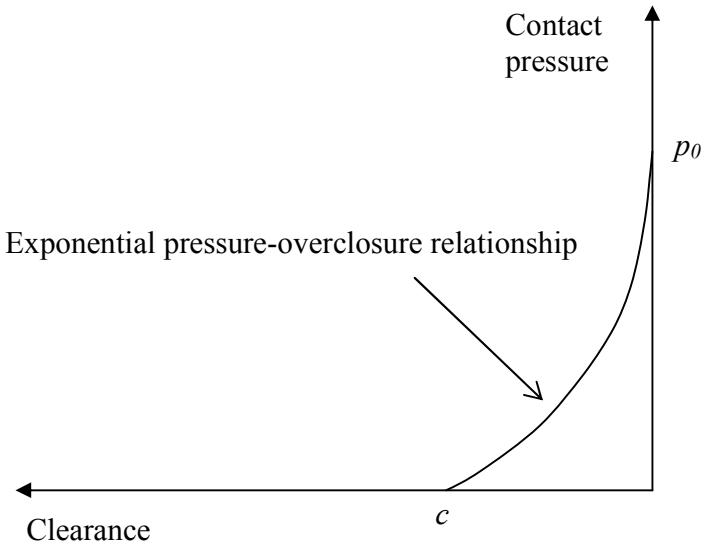

Figure 5.4. Pressure-overclosure relationship, as illustrated in ABAQUS manual (2001b).

5.1.4 Boundaries and Loading

With the exception of axial displacement at the loading edge, all the degrees of freedom of the nodes composing the ends of the structures were fixed. However, all the nodes at the loading edge were constrained to displace in a uniform manner. Thus, under a point load positioned at the mid-length of the edge of the skin, the experimental clamped conditions (as imposed by large stiffened plates) were simulated. Nevertheless, all the nodes within 20mm from the edges of the structure (excluding the ones positioned at the edges) were only allowed to displace axially. That was conducted in order to account for the resin blocks introduced at the ends of the structure so as to eliminate possible chattering within the loading plates. An illustration of the aforementioned boundaries and constraints are presented in Figure 5.5, not only for the detailed model described, but also for a simplified version of it for which the potting length, and consequently, the constraints have been excluded.

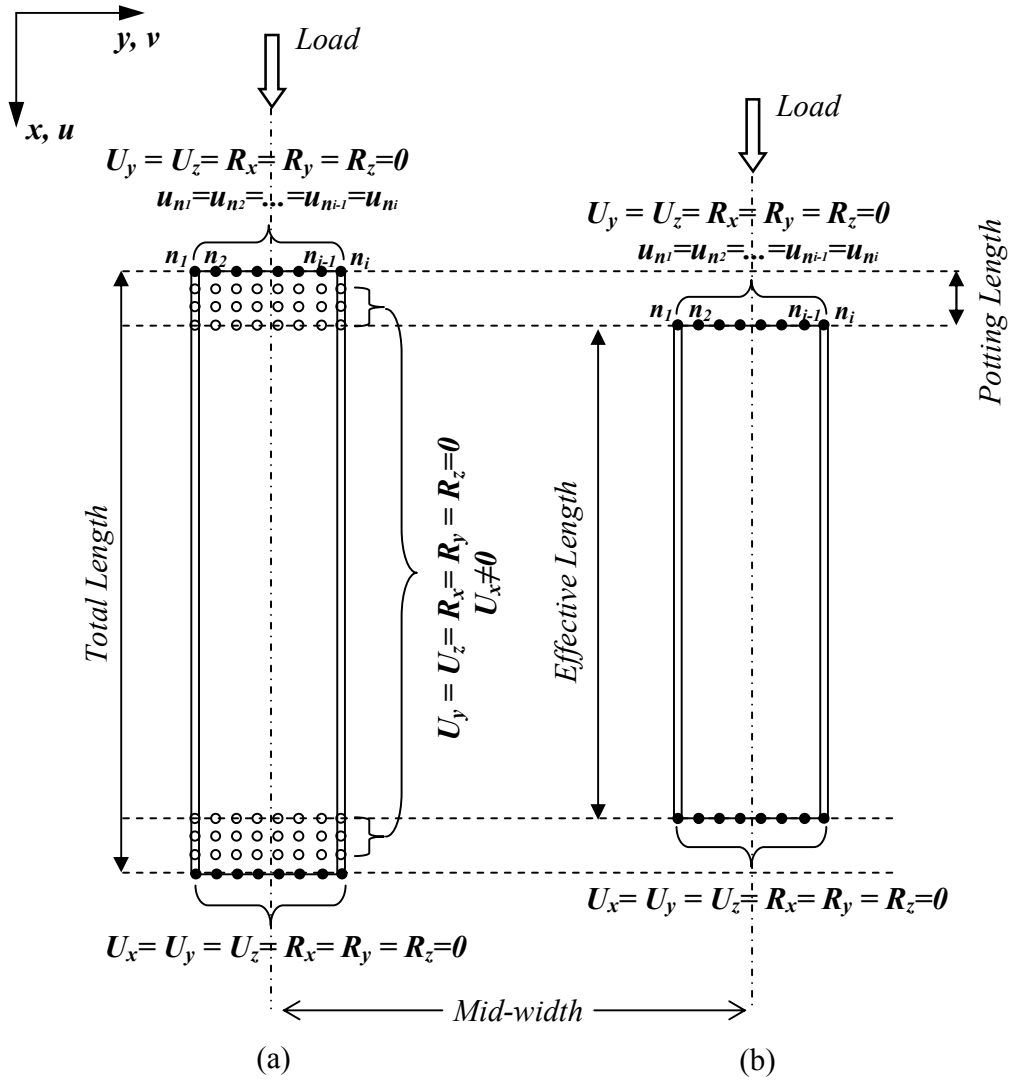

- *Nodes generated at the edges of the model*
- ∘ *Nodes generated within the potting length distance of the model*

Figure 5.5. Planar view of the boundary conditions, loading and constraints imposed in the finite element models (a) including and (b) excluding the potting length of the channel-section strut.

5.1.5 Method of Analysis

Linear (Eigenvalue) Analysis

Eigenvalue analysis was utilized in order to obtain an estimation of the critical buckling loads and the corresponding mode shapes of the undamaged and damaged channel-section struts. The merits of the analysis were not solely confined to the identification of the lowest critical state, but also allowed insight into possible post-buckling scenarios and collapse states. The latter became more evident in the analysis of the delaminated channel-section struts, where the lowest critical loads and configurations for both the delaminated region and the structure (as a whole) had to be identified. The eigenvalue analysis was also of particular importance in the investigation of the imperfection sensitivity of the undamaged channel-section strut.

Non-Linear Analysis

Geometrically non-linear analysis is generally required in problems where buckling instability occurs. Contrary to eigenvalue analysis, the non-linear analysis monitors the evolution of the buckling phenomenon and provides a better evaluation of the design (ABAQUS, 2001c) in all three principal areas of interest. These are the pre-buckling path, the post-buckling path and the ultimate load. In particular, with the aid of a load-displacement (stiffness) diagram the energy state of the system can be evaluated at any given load. For example, geometric parameters (imperfections) may induce non-linearity in the slope of the load-deflection diagram prior to buckling, consequently affecting the anticipated critical state (that is, critical load and mode shape). Moreover, the existence of instabilities (i.e. secondary bifurcations) in the post-buckling path, in which the structure releases energy in order to remain in equilibrium, is typically illustrated as negative stiffness in the diagram. In a similar manner an ultimate loading state is depicted, but for which the stiffness remains negative until the structure is fully unloaded.

In ABAQUS the Riks method was utilized in order to monitor the static equilibrium states in the aforementioned load-displacement space. The method utilizes the arc length along the equilibrium path in the force-displacement diagram as the governing parameter, thus allowing for the load and displacement to be unknown parameters of the solution (ABAQUS, 2001c). Therefore, a solution is attainable regardless the stability of the path (ABAQUS, 2001c).

However, more often than not the post-buckling solution cannot be directly attained due to the discontinuity of the equilibrium path at the point of bifurcation (ABAQUS, 2001c). Thus, an initial imperfection must be specified. In the non-linear analyses of the delaminated channel-section struts the lowest critical "structural modes" derived from the eigenvalue analyses were incorporated in order that convergence of the solution to be realized. In contrast, in the analyses of the undamaged channel section-struts the incorporation of an imperfection for convergence reasons would be of no substance, since the highly non-linear nature of the geometry resulted in a continuous response at the point of bifurcation.

Nevertheless, an initial imperfection in the form of the first eigenvalue was utilized in order to account for the measured geometric imperfection in the undamaged components produced. In addition, an imperfection in the form of the lowest critical mode shape of delamination buckling was built into the damaged models, in order to account for the geometric imperfection that arose due to the inclusion of the PTFE during the lamination process (please see Chapter 6). Unfortunately, the inclusion of a local imperfection in the sublaminates was feasible only for the specimens at which the delamination level was positioned close to the outer surface. This was primarily attributed to the fact that critical mode shapes could not be obtained by the eigenvalue analyses for the thicker sublaminates.

5.2 Linear Analysis Results

5.2.1 Buckling of the Undamaged Channel-Section Strut

In accordance with the design specifications, the eigenvalue analysis predicted that instability was instigated in the skin of the undamaged channel-section strut at a critical load $P_C = 41.2\,\text{kN}$. Buckling occurred in three half-sinwaves along its length with lengths comparable to that of the width of the skin, Figure 5.6. However, a closer examination of the buckling configuration revealed an asymmetry in respect to its longitudinal and transverse axis; or otherwise, an in-plane skew in the buckling mode. Such skewness in balanced symmetric laminates arises due to the presence of the non-zero D_{16} and D_{26} terms of in the bending stiffness matrix (Weaver, 2006). The latter terms indicate a coupled behaviour upon buckling, where the structure must twist in order to bend. Consequently, an in-plane skew evolves in the plate segments at buckling.

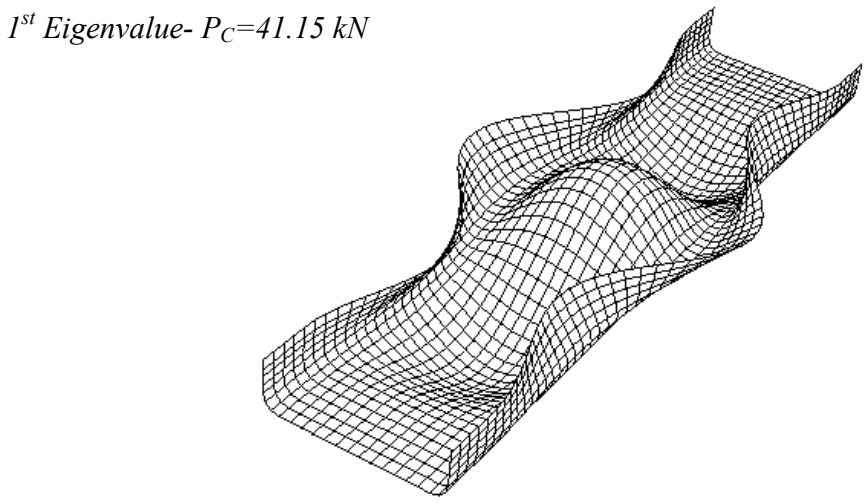

Figure 5.6. Illustration of the critical buckling mode configuration of the undamaged channel-section strut, as predicted by the linear finite element analysis.

More specifically, in balanced symmetric laminates such coupling terms evolve due to the effective difference in the bending stiffness of the plies that compose the laminate. For example, the bending stiffness of a particular layer (which for simplicity can be considered as *EI*) increases at more distant positions from the neutral axis due to the subsequent increase in the second moment of area. Therefore, for the laminate under consideration, $[45^0/-45^0/0^0/90^0]_s$, the 45^0 layers will be stiffer in bending than the -45^0 layers. Thus, bend-twist coupling occurs. Consequently, at buckling the anti-nodal lines of the buckling crest skew towards the stiffer laminate. The latter is attributed to the fact that longer wavelengths occur in stiffer layers, in contrast to less stiff where the wavelength is shorter. This is verified by the eigenvalue analysis of a channel-section strut composed of $[-45^0/45^0/0^0/90^0]_s$ laminate, which buckled in a mirror image of the $[45^0/-45^0/0^0/90^0]_s$ configuration, Figure 5.7. Nevertheless, quantitatively the terms, and consequently the critical load, are not affected by changing the 45^0 layers to -45^0 and vice-versa.

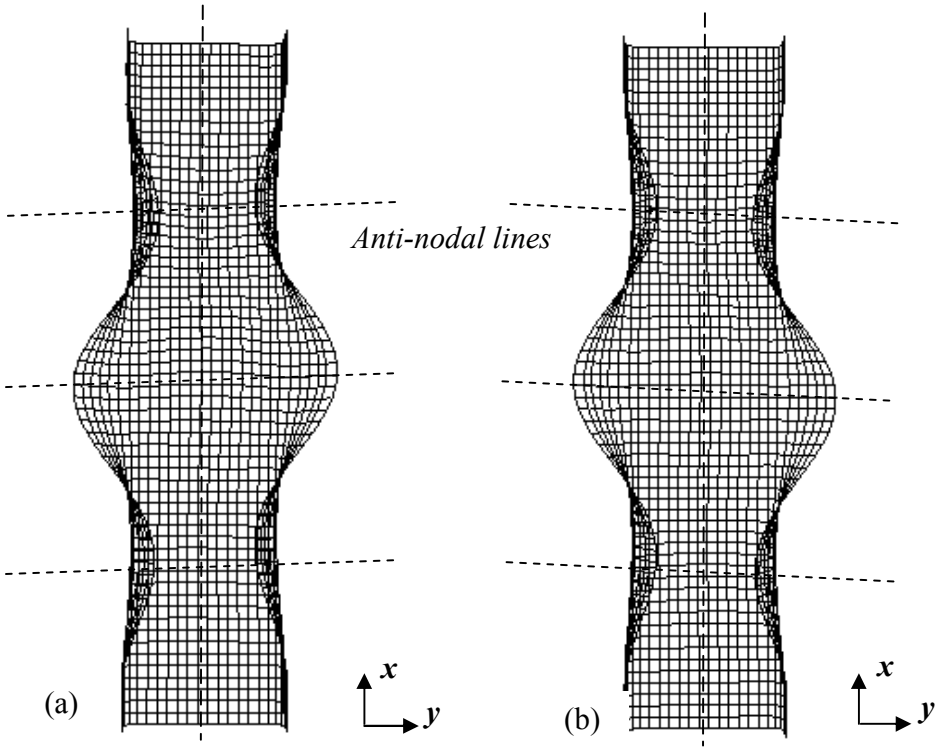

Figure 5.7. Buckling mode configuration of a the undamaged channel-section strut composed of (a) a $[45^0/-45^0/0^0/90^0]_s$ and (b) a $[-45^0/45^0/0^0/90^0]_s$ laminate.

Therefore, in thin-walled composite structures (such as the channel-section strut) that are frequently comprised by a relatively few number of layers, the importance of the position of the individual laminas within the laminate becomes more pronounced. That is, as seen in due course, similar coupling effects as such can severely affect the anticipated buckling strength. The phenomenon described brings to the surface the importance of scaling effects, where similar coupling effects are almost alleviated in thicker and "multi-lamina" structures. Such anisotropic effects in composites have been under invstigation by various authors (i.e. Diaconu and Weaver, 2006 and Nemeth 1986).

5.2.2 Characterization of the critical mode shapes

From the linear analysis results two critical modes were of interest in each case; the first critical delamination buckling mode and the first structural buckling mode. They correspond, respectively, to the first and a higher eigenvalue solution of the analysis. Both critical modes are illustrated for each of the damaged channel-section struts considered in Figure 5.8

Delamination buckling modes

Regardless of the position and depth of the delamination, the delamination buckling configurations were essentially similar to the local buckling mode assumed by the thin-film approximation, as seen by the relative magnitudes of displacements in the contour plots. Nevertheless, it was evident that their proximity depended not only on the delamination depth, but also on the position of the delamination. In particular, for the delaminations positioned closer to the surfaces (2^{nd} and 6^{th}) of the skin, Figures 5.8(a) and (g), and the stiffener, Figures 5.8(i) and (m), buckling occurred in a manner similar to that of the thin-film assumption with virtually no out-of-plane deformation of the thicker sublaminate. Or otherwise, the deflections of the supporting sublaminate and surrounding structure could be approximated to be of zero amplitude in relation to the buckled sublaminate.

n=2- Skin

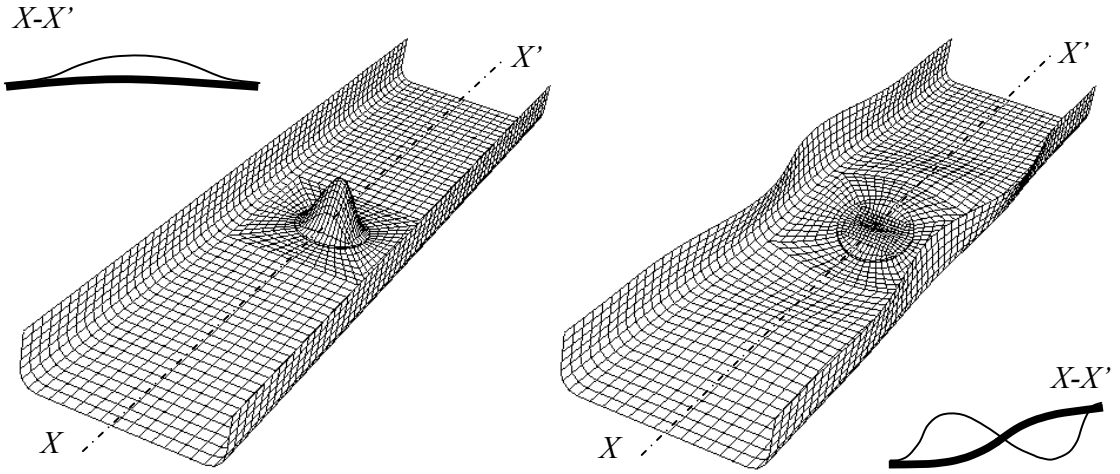

(a) *1st Eigenvalue-* P_C^D *=15.85 kN* (b) *4th Eigenvalue-* P_C^S *=40.16 kN*

n=3- Skin

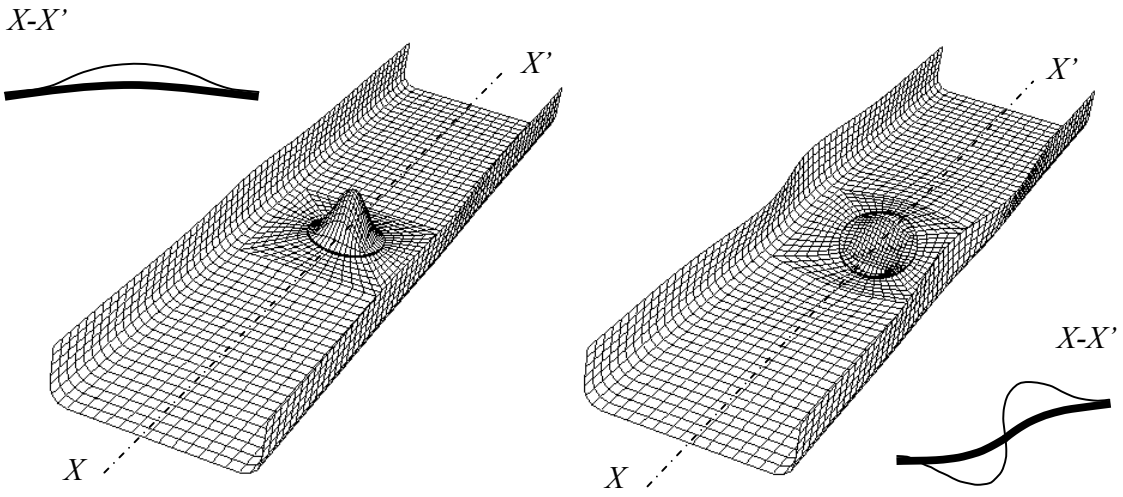

(c) *1st Eigenvalue-* P_C^D *=30.29 kN* (d) *5th Eigenvalue-* P_C^S *=35.05 kN*

n=5- Skin

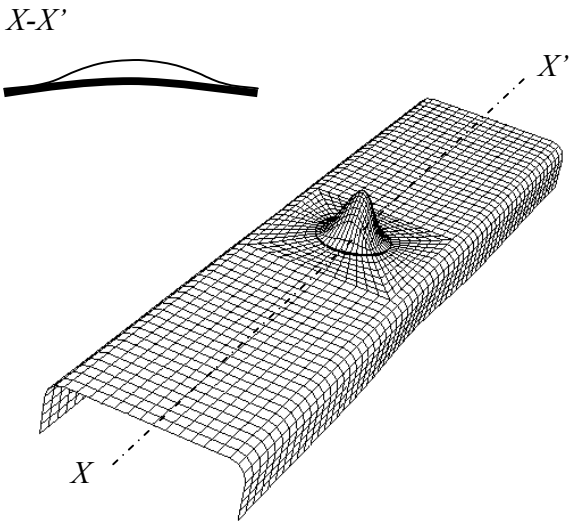

(e) *1st Eigenvalue- P_C^D =30.19 kN*

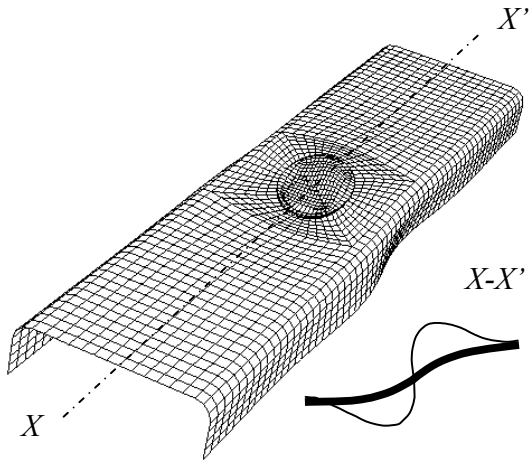

(f) *5th Eigenvalue- P_C^S =35.06 kN*

n=6- Skin

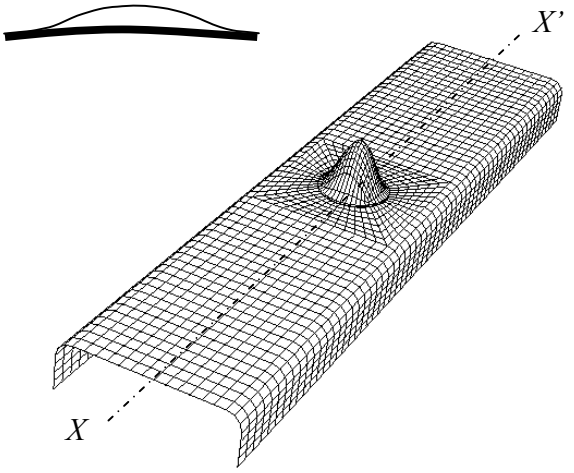

(g) *1st Eigenvalue- P_C^D =15.87 kN*

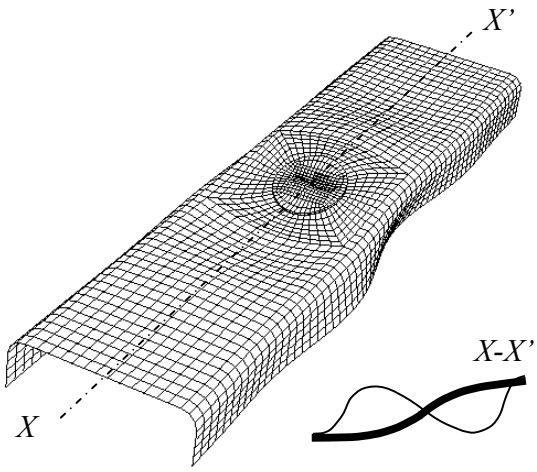

(h) *4th Eigenvalue- P_C^S =40.17 kN*

n=2- Stiffener

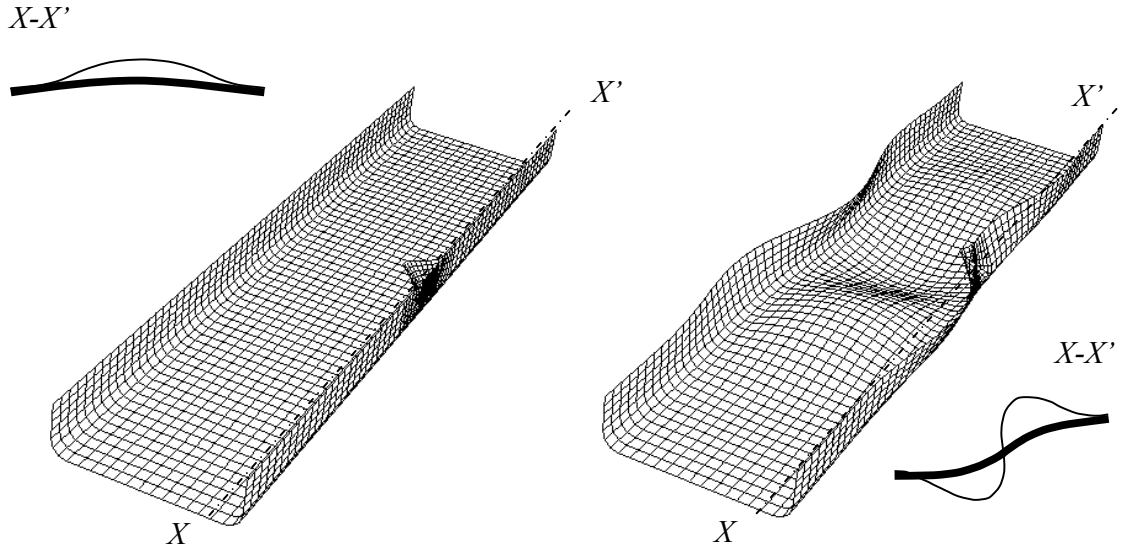

(i) *1st Eigenvalue- P_C^D =33.23 kN*

(j) *2nd Eigenvalue- P_C^S =40.50 kN*

n=3- Stiffener

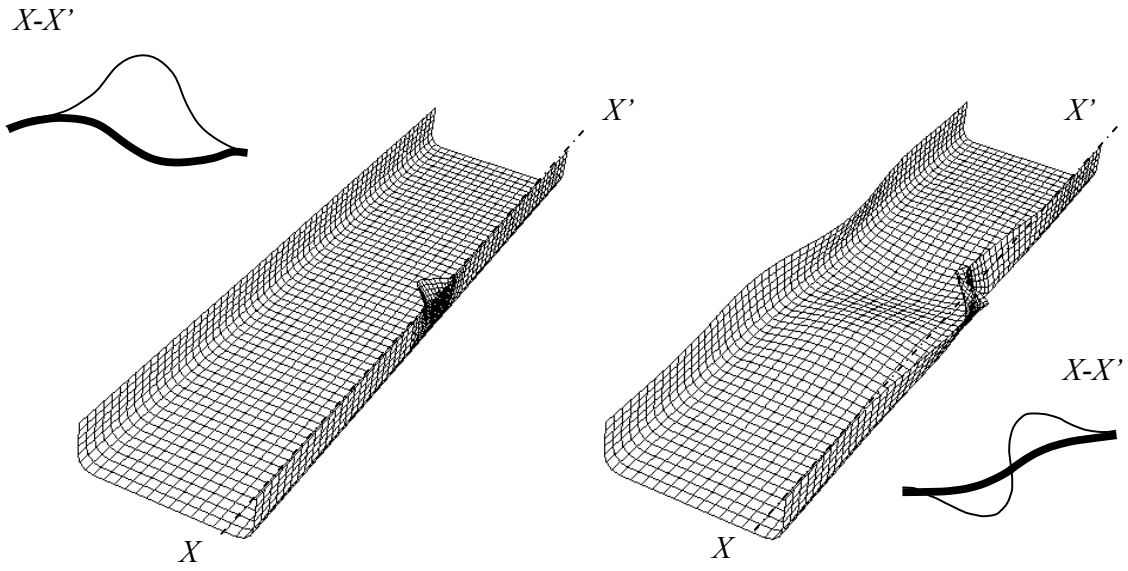

(k) *1st Eigenvalue- P_C^D =30.82 kN*

(l) *2nd Eigenvalue- P_C^S =38.56 kN*

n=5- Stiffener

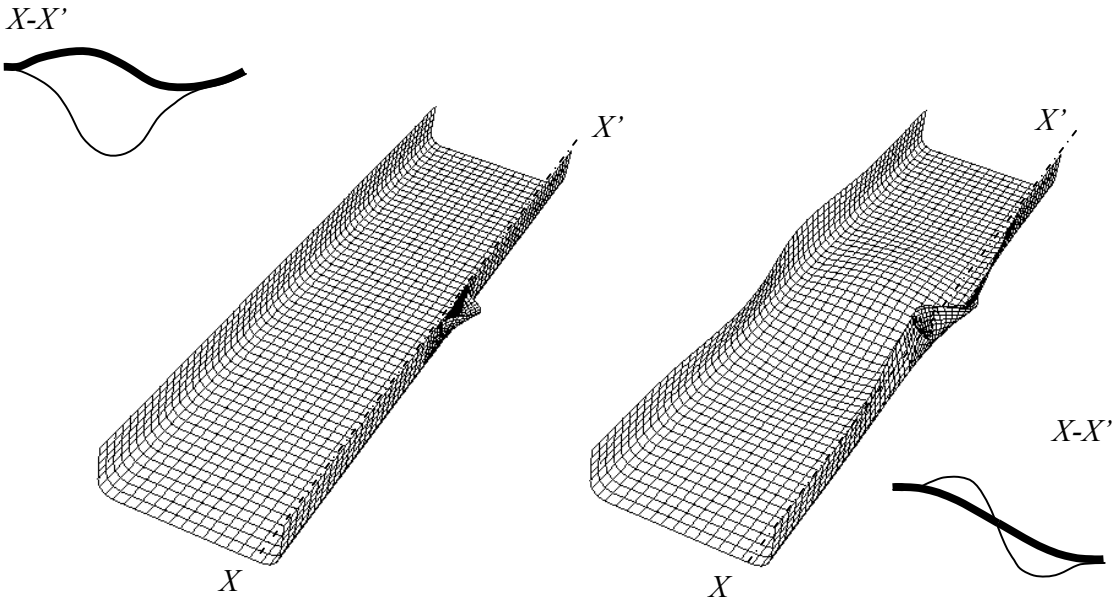

(m) *1st Eigenvalue- P_C^D =31.38 kN* (n) *2nd Eigenvalue- P_C^S =38.94 kN*

n=6- Stiffener

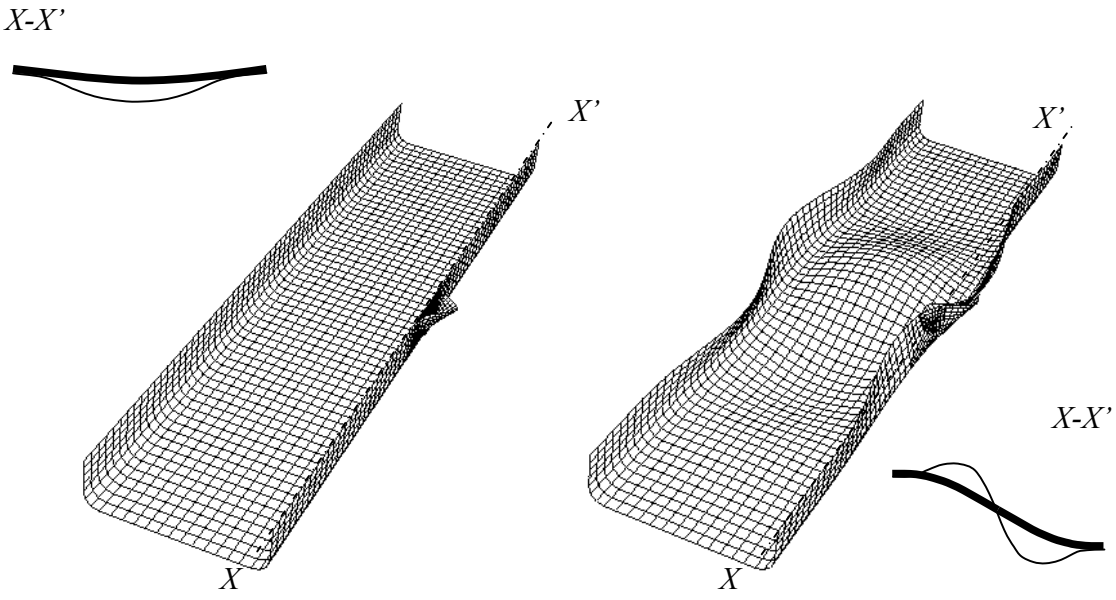

(o) *1st Eigenvalue- P_C^D =34.07 kN* (p) *2nd Eigenvalue- P_C^S =40.60 kN*

Figure 5.8. (a)-(p) Illustration of the critical delamination and structural buckling mode configurations, derived by the eigenvalue analysis.

However, in deeper sited delaminations in the skin (3^{rd} and 5^{th}), Figures 5.8(c) and (e), a very small cylindrical deformation was observed in the thicker counterpart that corresponded to particularly small, but nonetheless, finite deflections. The emerging cylindrical deformation is attributed to the larger rotations imposed by the thicker buckling sublaminate at the delamination perimeter. Interestingly enough, for the deeper sited delaminations in the stiffener, Figures 5.8(o) and (k), the deflections of the supporting sublaminates were of similar amplitude to the near-surface ones (that is, small enough to be neglected), but the deformations modes were of higher order. The latter phenomenon will be further discussed in due course.

At this point it should be clarified that such distortions of the supporting sublaminates in the stiffener are not clearly visible on the eigenvalue analysis contour plots, since as already stated, such deflections are approximated to be of zero magnitude in comparison to the deflections of the critical sublaminate. Therefore, extremely large scales must be utilized in the plots of the deformed shapes in order for the latter deflections to become visible. For later discussion and comprehension purposes, the author felt obliged to produce exact sketches of the cross-section of the delaminated region at buckling with the deformed shapes plotted in ABAQUS at very large scales. Similar scales were not utilized for the critical deformed shapes illustrated in Figure 5.8, in order to encapsulate as many features of the deformed shape as possible, but also maintain clarity of the mode shape.

Nonetheless, in all instances delamination buckling occurred under a single half-sinewave in the critical sublaminate, analogous to the one formulated for the Euler strut with fixed ends, and with very small or virtually no deformation in the supporting sublaminate. Even though, this validates the initial assumption made in the design methodology (i.e all levels of delamination buckling in a thin-film configuration), it contradicts the general perception that deeper-sited delaminations buckle in a global mode. However, this perception is based on tests conducted on delaminated coupons which do not account for the structural configuration. In accordance with Chen et al. (2001), large deformations of the delaminated region are initially restricted by the

presence of the stiffeners. This is attributed to the redistribution of stress within the structure that leads to a reduction in the stresses that would have developed in damaged region and an increase in the stresses of the stiffeners.

Structural Deformation at Delamination Buckling

As discussed earlier, regardless of the depth of the delamination, buckling of the critical sublaminate would effectively impose bending moments at the delamination interface. Therefore, realistically even extremely small deflections are bound to occur in the thicker sublaminates, and consequently, the surrounding structure. For example, for the selected deformation scale in Figures 5.8(c) and (e), buckling of the critical sublaminate in the deeper-sited delaminations in the skin was accompanied by a small distortion of the stiffeners. Even though such deflections do not possess any quantitative or qualitative attributes in the eigenvalue solution, nevertheless they raise the issue of whether judgements could be drawn on the influence of delamination buckling on the structural behaviour.

Thus, for extremely large scales of the deformed shape of the damaged structures, very small deformations were observed in the surrounding plates of the buckled sublaminates and the adjoining plate segments. Such deflections arise as a result of continuity conditions and stress redistribution within the structure. In particular, delamination buckling at the free-edge of the stiffener resulted in out-of-plane deformation of the skin, but mostly confined to the vicinity of the skin-stiffener junction underlying the delaminations. In contrast, the delaminations positioned in the skin induced more extensive deformation in the critical plate (i.e the plate responsible for the instability in the structure). Consequently, the higher stresses generated at the critical plate segment would induce a more debilitating effect in structural stability. Therefore, the greater reduction in the structural buckling load is anticipated to occur for the damaged channel-section struts with skin delamination. Moreover, the greatest reduction would occur for the deeper-sited delaminations, which induce the highest deformation in the eigenvalue contour plots, due to the reduced stiffness of the supporting sublaminate.

However, the inability of the delaminated structures with free edge delamination to redistribute the stress field more globally within the structure, as for example the delaminations in the skin that instigate distortions in both stiffeners, might lead to higher stress concentration at the delaminated edge. Therefore, this may be potentially the most hazardous scenario in terms of the structural post-buckling strength. Even though such judgements are based on the deformation plots of the critical mode shapes at extremely large scales, nevertheless they illustrate the response of the structure at delamination buckling and may indicate the tendacies of the damaged structure.

Deformation of the Sublaminates at Structural Buckling (Shearing Mode)

The presence of the delamination in all the damaged channels had a profound influence on the structural buckling mode that would have evolved in their absence, as shown in Figures 5.8(b), (d), (f), (h), (j), (l), (n) and (p). Despite the obvious dissimilarities of the structural buckling modes in accordance with the structural position and depth of the delamination, nevertheless it became apparent that all the structural buckling configurations had a distinct and common element. The delaminated plate segments were all dominated by local antisymmetric half-sine waves about their mid-length. In particular, according to Harrison and Butler (2001) the presence of the delamination in a structure reduces the shear rigidity in the delaminated region. However, the degradation of the shear stiffness implies that the delaminated region is potentially subject to the highest shear stresses. Consequently, upon structural buckling the delaminated region attracts regions of the buckling mode subject to the highest shear stresses, such as the point of contra-flexure between adjacent buckles (Figure 5.9). Thus, anti-symmetric buckles are generated about the skewed nodal line at the mid-length of the strut, and subsequently, the sublaminates.

The latter phenomenon highlights the reciprocal relationship between delamination and structural buckling. Furthermore, to the author's knowledge the particular buckling configuration of the sublaminates has not been reported in the literature, and therefore, a specific terminology has not been adopted. Thus, in the current work from this point forward it will be referred to as the "shearing mode". Nevertheless, the validity and the

actual configuration of such a mode are pending experimental testing and non-linear analysis, in which the unrealistic inter-penetration of the sublaminates observed in Figures 5.8(b), (d), (f), (h), (j), (l), (n) and (p) is eliminated.

The Contact effect

For the discussion of the structural buckling configuration it is suggested that the observed overlap of the sublaminates in the critical structural mode be disregarded. This argument is brought forward not in an attempt to moderate the importance of the physical violation and promote the eigenvalue solution, but as a consequence of the method of analysis and the efforts made to alleviate the latter phenomenon. In particular, due to the incompatibility of the eigenvalue analysis with contact constraints, alternative methods were utilized to prevent the inter-penetration of the sublaminates in the structural buckling mode. Namely, these were normal forces acting at the central nodes of the buckling sublaminates, in directions that would otherwise ensure that the sublaminates would remain in separation at the critical state, additional dummy layers and nodal offsets. Nevertheless, qualitatively the outcome of such efforts was fruitless. Thus, the predicted structural buckling configurations are presented as indicative solutions, where the delaminated regions are regarded as areas of local stiffness degradation. The effect of the observed overlap of the subalminates in the structural buckling load and mode will be examined in the non-linear analysis, and to some extent the validity of models often encountered in literature with similar simplifications (i.e. holes) can be assesed in regards to their validity.

Structural Buckling Modes

In accordance with the linear analysis results, structural buckling in all the damaged channel-section struts occurs in asymmetric modes. That is, the skewed configuration imposed by the bending-twisting coupling effects would always dominate the structural mode shape, effectively breaking any symmetry that might otherwise have evolved. For comparison reasons the characterization of the individual buckling modes of the channel-section struts is conducted on the basis of the mode that evolves solely in the skin of the channel-section strut. Moreover, the skewness of the mode is neglected by

considering the longitudinal cross-section at mid-width of the skin. For example, under such simplifications the buckling mode of the undamaged channel-section is depicted as symmetric, as shown in Figure 5.9(a).

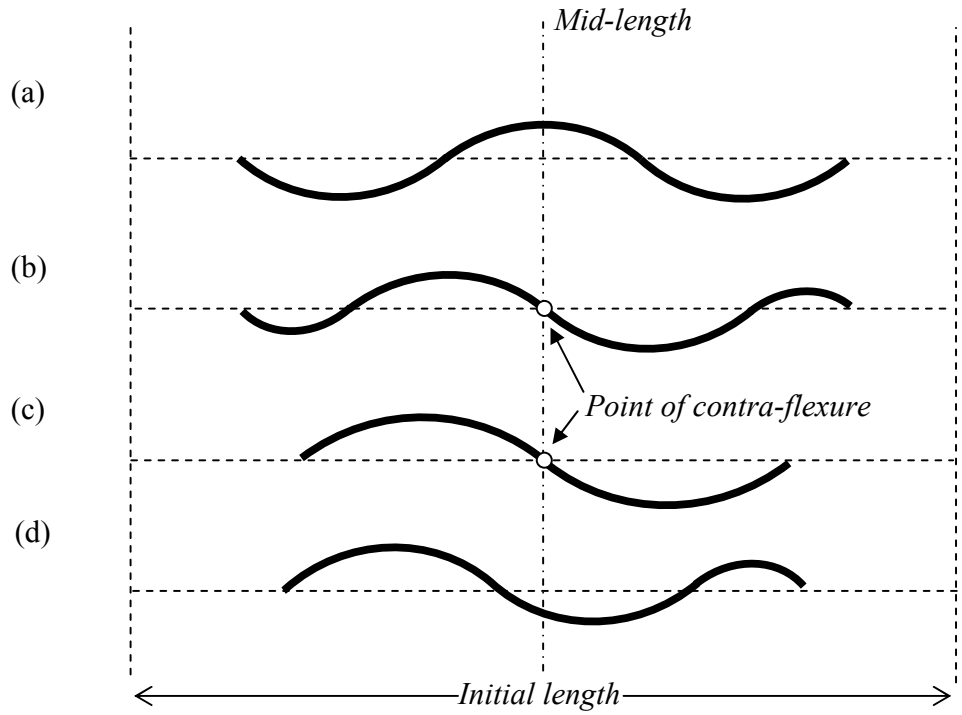

Figure 5.9. Schematic cross-section view along the mid-length of the skin of (a) the undamaged, (b) the damaged channel-section struts with near surface and (c) deeper-sited delaminations and (d) with free edge delaminations in the stiffener.

In particular, the channel-section struts with a centrally located delamination in the skin buckled in antisymmetric configurations. Nevertheless, in accordance with the delamination depth the critical mode shapes evolved in a differing number of half-sine waves. For the skin delaminations positioned closer to the surfaces of the laminate, the modes were composed of two long half-sine waves about the mid-length and two short ones, Figure 5.9(b). On the contrary, for the deeper cited delaminations the buckling mode shapes were composed of two half-sinewaves, Figure 5.9(c). Interestingly enough,

the channel-section struts with free edge delamination in the stiffener, buckled in an asymmetric mode that was comprised of two long antisymmetric half-sine waves and one short, as shown in Figure 5.9 (d). It should be noted that for the latter case the point of contra-flexure of the antisymmetric buckles does not coincide with the mid-length due to the skewness of the of the nodal line.

It is of interest to note that the observed variation in the hierarchy of the structural buckling mode according to the delamination depth in the skin is believed to be related to the actual reduction in shear rigidity. In particular, the *n=2* and *n=6* skin delaminations are less stiff in shear in comparison to the *n=3* and *n=5*, since under a shear environment the sublaminates would slide more relative to each other. However, the higher the reduction in shear stiffness causes higher shear stresses in the delaminated region, and consequently, higher slope gradients at the point of contra-flexure. In turn, the latter result in the formation of higher order buckling modes.

In contrast, the delamination depth of the free-edge delamination in the stiffener had no qualitative influence on the order of the critical buckling mode, Figure 5.8(j), (l), (n) and (p). The latter phenomenon is more likely than not related to the fact that the free-edge delaminations are positioned at a non-critical plate segment of the structure, and therefore, do not influence directly the shear stiffness of the critical structural plate segment. In this case the evolved mode is believed to be the modal coupling between the modes in the skin and the delaminated stiffener. This could also be justified by the observed asymmetry in all the damaged channel-section struts with stiffener delamination.

5.2.3 Delamination and structural buckling loads

Delamination buckling-Thin film buckling with out-of-plane distortion

In Table 5.1 the delamination buckling strains derived by the finite element eigenvalue analysis and the design methodology have been summarized and compared. For the damaged channel-sections in the skin, a very satisfactory agreement between the

design and predicted buckling strains is observed. In either method of analysis the delamination buckling strain increases as the delamination depth shifts towards the mid-surface of the laminate. Interestingly enough, a similar trend is not predicted by the linear finite element analysis of the channel-section struts with stiffener delamination.

As shown in Table 5.1, the critical buckling strains increase as the through-thickness position of the delamination approaches the surfaces of the laminate. Similar trends have readily been reported for delaminated coupons in the literature. However, through the width delaminations are considered, where bending-stretching coupling severely affect the effective bending stiffness. This is not the case for the delaminated stiffener, since due to initial conditions in the model the load is transferred through the neutral plane, and therefore, such coupling effects are eliminated.

Channel	*Delamination Buckling Strain* ε_C^D , μ	
	ABAQUS	*VICONOPT*
n=2-Skin	1575	1606
n=3-Skin	3010	2983
n=5-Skin	3001	2983
n=6-Skin	1577	1606
n=2-Stiffener	3303	1464-3439
n=3-Stiffener	3063	2823-4200
n=5-Stiffener	3119	2823-4200
n=6-Stiffener	3386	1464-3439

Table 5.1. Comparison of the delamination buckling strains derived by the finite element eigenvalue analysis and the design methodology.

It is more likely, however, that the reasoning lies in the particular configuration of thin-film buckling for the deeper-sited delaminations in the stiffener. That is, typically in

delamination buckling modes that approximate the thin-film assumption the supporting sublaminate deflects with very small amplitudes and in a cylindrical configuration. Interestingly enough, a higher order mode is predicted for the supporting sublaminate for the deeper-sited delaminations in the stiffener [see Figure 5.10(a)]. The uniqueness of this configuration of delamination buckling is not just limited to the fact that, to the author's knowledge, it has never been reported, but more importantly that it appears to be a particular configuration of thin-film buckling.

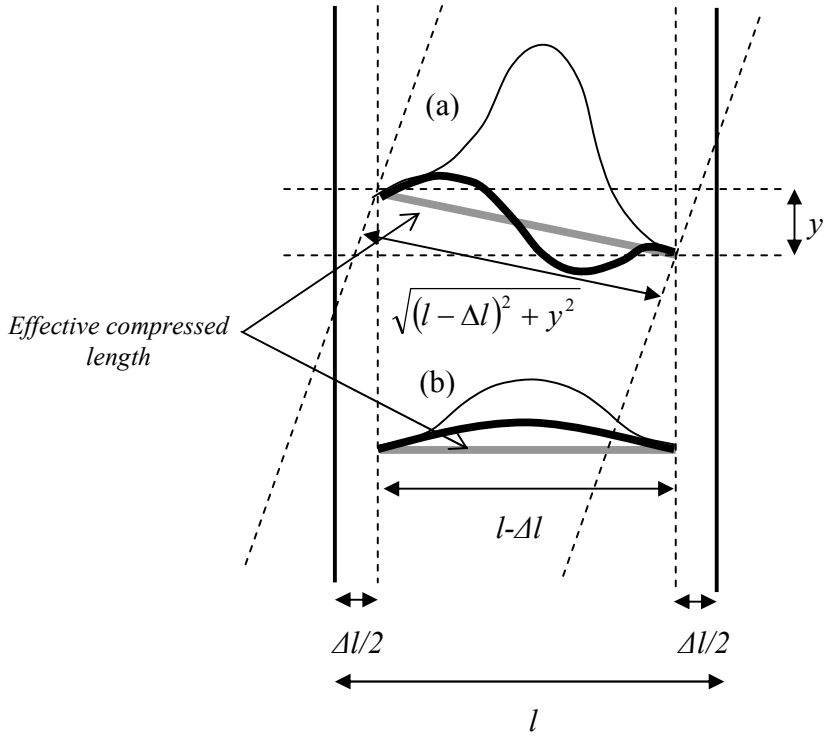

Figure 5.10. Compression of the supporting sublaminate with (a) a high order and (b) a half-sinewave buckling mode under unit end-shortening.

Perhaps, an example would be the best way to elucidate the conditions under which such a buckling configuration evolves. Thus, under the assumption of plain-strain conditions in the channel-section strut and a delamination level at which thin-film buckling occurs, the high order buckling mode shape of Figure 5.10 (a) and the typical case of Figure 5.10 (b) are both considered. In either mode, it is assumed that buckling

occurs at similar strain levels. By comparison of the two buckling configurations, it is easily observed that the out-of-plane distortion of the intersection of the sublaminates in the high order buckling configuration has resulted in a smaller compressed length in the sublaminates in comparison to the typical case. Therefore, less extensional energy must be offered to the structural system in order for buckling to occur. In contrast, the higher order of the buckling mode in the supporting sublaminate is associated with higher bending energies. Thus, a trade-off between extensional and bending energy in the system is observed.

This suggests that if the intersections of the sublaminates were allowed to distort out of the plane of the applied load, as in the case of the free-edge delamination, then the higher buckling mode in the supporting sublaminate could depict the critical configuration. Nevertheless, the occurance of such a configuration would also be dependent on the laminate architecture, and consequently, to the level of delamination. That is, the reduction in the bending stiffness of the supporting sublaminate, by the increase in the delamination depth, implies that that the expenditure of the available strain energy in higher order buckling deformations is less substantial. Therefore, the gain in stretching (compression) energy by distortion could sufficiently outweigh the losses in bending energy.

As is evident from the linear analysis results, for the deeper-sited delaminations in the stiffener the evolution of thin-film buckling with distortion resulted in a reduction in the buckling load in comparison to the one predicted for the near-surface ones. Thus, it could be said that for delaminations positioned at structural members that are prone to distortion, such as the stiffeners, the alternative thin-film configuration is more likely to occur at increasing depths. The latter, is also supported by the delamination buckling configurations in the skin, for all levels of delamination, where distortions as such are restricted by the imposed boundaries.

Re-examination of the design methodology reveals that for a free-edge delamination positioned near the surfaces of a laminate, which lies within the classical assumption of

thin-film buckling, the deviation of the upper solution (assumes that the sublaminates must strain transversely in accordance to the laminate) with the ABAQUS prediction is within 5%. On the contrary, for the deeper-cited delaminations the deviation reaches 27%. Therefore, the design methodology may be able to predict critical buckling strains of free-edge delaminations that comply with the assumption of a uniformly strained supporting sublaminate, within a satisfying level of accuracy. Nevertheless, this requires validation by further numerical and experimental work.

Structural buckling

The deeper-sited delaminations in the skin and stiffener resulted in higher reductions in the structural buckling load. In particular, reductions of nearly 15% and 6% can be accounted for the deeper-sited delaminations positioned in the skin and stiffener respectively (that is, in respect to the structural buckling load of the undamaged strut). By contrast, the near-surface delaminations induced reductions that were less than 3%, with slightly higher reductions, though, being predicted for the ones in the skin. Thus, it is evident the most critical delamination position is the skin (or otherwise, the critical plate) of the strut. As suggested by the deformed configurations of the damaged channel-section struts upon delamination buckling, this may be attributed to the higher degradation of the bending stiffness of the critical plate that instigates instability. That is, in comparison to the one imposed by stiffener delamination as a result of stress restribution within the structure. This becomes more evident as the delamination level reduces and the losses in the bending stiffness of the supporting sublaminates become more profound. All the critical delamination and structural loads have been summarized in Table 5.2. The small deviations observed in the critical delamination buckling and structural loads between the mirror delamination depths (that is, in respect to the mid-surface) are more likely than not structural effects, which will be examined in more detail with the aid of the non-linear analysis.

Channel	*Delamination Buckling (kN)*	*Channel Buckling (kN)*
Undamaged Channel (M21/AS7)	-	41.40
Damaged-Skin-2nd Level	15.85	40.16
Damaged-Skin-3rd Level	30.29	35.05
Damaged-Skin-5th Level	30.19	35.06
Damaged-Skin-6th Level	15.87	40.17
Damaged-Stiffener-2nd Level	33.23	40.50
Damaged-Stiffener-3rd Level	30.82	38.56
Damaged-Stiffener-5th Level	31.38	38.94
Damaged-Stiffener-6th Level	34.07	40.60

Table 5.2. Delamination and structural buckling loads for the undamaged and damaged channel-section struts, derived by the eigenvalue analyses.

5.3 Concluding Remarks

Preliminary conclusions could be drawn on the effect of the delamination depth and position on structural criticality and on the effect of structural configuration on delamination buckling. Nevertheless, it is should be remembered that contact constraint effects in the delaminated region and geometric non-linear effects that may alter the response of the structure, are not incorporated in the eigenvalue analysis, and therefore, some of the conclusions drawn must be viewed with some precaution. Nevertheless, from the eigenvalue analysis it was demonstrated that,

i. Scaling down the thickness of the laminate gives rise to bending-twisting coupling effects, and consequently, to asymmetric and skewed asymmetric buckling configuration. The direction of skew will depict the orientation of the outermost 45^0 layer that obtains the highest bending stiffness.

ii. Regardless of the position and delamination depth incorporated in the model, the sublaminates buckled in a thin-film buckling configuration.

iii. The critical buckling loads for the damaged channels with skin delamination were found to be in very good agreement with those derived by the design method adopted.

iv. The delamination position had a profound influence on the delamination buckling load. For the damaged channel-section struts with skin delamination the critical load increased with depth. In contrast for the ones with stiffener delamination it decreased.

v. A particular thin-film buckling configuration was identified in the deeper sited delaminations in the stiffeners. The configuration exhibited similar trends to the thin-film buckling configuration, but the delamination perimeter distorts out-of-plane.

vi. The design methodology may also be efficient for modeling free-edge delaminations that comply with the classical assumptions of thin-film buckling.

vii. Deeper-sited delaminations possessed the most debilitating effect on the structural buckling load.

viii. Delaminations positioned in plate segments that are responsible for the structural instability, such as the skin, would impose the greatest reduction in the structural buckling load. However, delaminations positioned in members where the stress is redistributed in a local manner, such as the stiffeners, and possess a stabilizing role in the structure, may significantly affect the post-buckling strength.

ix. The evolved buckling mode configuration is both dependent on the position and depth of the delamination.

x. A global buckling mode configuration may evolve at structural buckling due to the degradation of the shear rigidity. The latter mode identified has been termed the “shear mode”.

Chapter 6

Manufacturing and Experimental Testing

A successful investigation of structural mechanics problems must encompass both theoretical and experimental work. However, the focus on the development of more refined analytical and numerical tools has somewhat left experimental work trailing, even though in many cases the theoretical models were not able to correlate with the experimental results (Singer et al., 1998). Thus,

> *"One should remember that though judiciously chosen mathematical models may predict the expected physical behaviour, it is up to careful experiments to verify this predicted behaviour and validate the calculations. Furthermore, the experiments may bring out elements of behaviour of real structures, which have not been considered in our, by necessity, simplified models. This second role of experimentation is often overlooked".*
>
> *(Singer, J., Arbocz, J. and Weller, T., 1998. Buckling Experiments)*

Therefore, the manufacturing processes, material quality and testing consistency are not only critical for validation of the design methodology adopted but also for a thorough understanding of the mechanism involved. In this chapter, the latter factors are discussed in more detail. In particular, the manufacturing processes and the experimental set-up for material test-coupons, the damaged and undamaged channel-section struts are presented. It should be noted that even though material testing was motivated by the lack of the properties of the material M21/35%/268/AS7, kindly provided by Hexcel

Composites Ltd., it nevertheless provided a unique opportunity to study the nature of carbon-fibre reinforced plastic (CFRP) material. For fibre-reinforced laminas under a compressive environment this mainly entails the identification and behaviour of the axial and transverse compression modulus and in-plane shear modulus. Finally, developed techniques in certain aspects of the manufacturing process that were found to contribute to a qualitatively enhanced end-product are presented.

6.1 Manufacturing Processing

The manufacturing processes involved in the production of thermoset composites are quite unique and relatively new, and therefore, by no means could comparisons or similarities could be drawn with the long-established processes for metals. Nevertheless, the growth of composites and continuous employment in further primary structural positions has coincided with the development and refinement of the manufacturing processes involved. Currently the latter have attained a stage of maturity (Mazumdar, 2002), which produces an efficient end-product, without however implying that limitations and concerns have been eradicated or their further development is obsolete. Thus, the production of the specimens was an amalgamation of the developed techniques and experienced gained during the manufacturing processes. Generally, the manufacturing stages in the production of fibre-reinforced laminated composite aircraft components are the lay-up, the bagging, and the curing and machining and cutting processes. For the material-test coupons these processes are presented in Appendix B.

6.1.1 Prepreg Lay-up Process

The most common method of production of laminated composite structures adopted by the aircraft industry is the prepreg lay-up process, since complicated structures with very high fibre volume ratios can be produced (Mazumdar, 2002). The prepreg material is a unidirectional fibre-reinforced composite system, which has been preimpregnated with resinous binders and frozen in order to protect it from environmental degradation.

Therefore, the rolls of the high-strength carbon/epoxy prepreg acquired for the current work were stored in a freezer below -18^0 C and tightly sealed in order to ensure that moisture would not produce voids within the composite. Furthermore, additional protection of the prepreg was achieved by the employment of bags of silicon seeds, that would absorb potential moisture trapped within the sealing bag.

On the same basis, defrosting of the prepreg in every occasion took place within the sealing bag, which was brought slowly to room temperature (usually around 20^0 C) overnight. However, the duration of the exposure of the prepreg to environmental conditions is an important consideration, since the lifetime of the prepreg (that is, at room temperature) that was proposed by the manufacturer was 28 days. Therefore, it was essential the cutting period for the required laminas to be kept to a minimum in order to ensure that sufficient time in the life expectancy of the prepreg would be allowed for the production of the required components/specimens. The cutting procedure for laminas was conducted manually inside a room with very clean atmosphere and surfaces (usually referred to as the 'clean-room'), where the prepreg was laid on a cutting board and aligned against a fixed steel ruler. With the aid of a steel knife and a steel orthogonal plate, laminas with 0^0, 90^0 and 45^0 (since the -45^0 is the opposing face of the last) orientations were cut at dimensions and numbers required for the individual applications as follows. It should be noted however, that the cutting process in the industry has been fully automated (Mazumdar, 2002) in order to reduce the cost and considerable labour involved in the production of large volumes.

Lay-up Process for the Undamaged Channel-Section Struts

An important consideration prior to the construction of any laminated structure is the tool of lamination, and in particular, the related parameters such as the thermal expansion of material of the tool, the configuration, the tolerances specified and the surface finish (Niu, 1992). Even though, the male channel-section tool, as already mentioned, was already available, nevertheless its compliance with the required previous parameters was investigated. In brief, the tool was made from aluminium, which is

perhaps the most common material due to its excellent thermal conductivity (which is essential for a uniform temperature field during curing) and lightness (Liu, 2005). However, its high coefficient of thermal expansion (that is, compared to most composites), which is of particular importance for slender structures, makes aluminium an inappropriate material for temperatures above 200^0 C (Niu, 1992; Liu 2005). Nevertheless, for temperatures below this threshold it is considered more than adequate, and thus, readily used. Induced strains in the composite part though, may be fashioned due to the metal contraction during the cooling process (Niu, 1992). Due to the particular cross-section, curing occurs on a single piece tool, and therefore, issues often encountered in two-part moulds (i.e. Z-cross-sections) such as uniform distribution of pressure and temperature uniformity (Niu, 1992) were not of any relevance. The tool was inspected and was found to be of excellent surface quality and designed within (or under) a *0.01mm* tolerance.

Laminas were cut into the appropriate orientations, the dimensions of which were obtained considering the required dimensions (specified in Table 3.1), the trimming of the edges, the potting length (that is, the portion of the strut which is fixed within a pot in order to simulate the required boundary conditions) and the radius effect. In particular,

$$\textit{Lamina length} = \textit{Required specimen length} + 2\times(\textit{Trimming length}) + 2\times(\textit{Potting length})$$

and

$$\textit{Lamina width} = 2\times(\textit{Heigth of the tools vertical face}) + \textit{Width of the tools horizontal face} + \pi(\textit{Fillet radius} + \textit{Precured thickness})$$

Prior to the lamination process the release agent Freekote 770NC was applied to all surfaces that it was anticipated would come into contact with the prepreg or with excess resin flow during the curing cycle, in order to prevent solid bonding of the composite structure to the tool. Several coatings were applied, and between each coating sufficient time was allowed for the release agent to solidify. The tool was required to be pre-heated prior to lamination not only to obtain a tight fit between the faces of the tool and the first

layer, but also to assist with the very cumbersome process of laminating over tightly curved surfaces, such as the corner fillets. As it has been pointed out in the literature (Niu, 1992) and has sometimes been experienced in the duration of this current work, the fillet is an area of potential damage such as fibre bridging and distortion that requires the upmost concentration and skill. In the event of occurrence of such damage the partially laminated structure should be, and was, disposed at the expense though of valuable material, and more importantly time and effort.

During the lay-up process debulking (compacting of the layers) was required after the first layer and every four layers after that. That is, trapped air within the layers of the laminate may be responsible for the formation of voids within the layers and delaminated areas at the interfaces. Additionally, trapped air underneath the surface of the laminate (first layer) would also result in surface imperfecions. Debulking was conducted for fifteen to twenty minutes every time and under a vacuum of *25''of Hg* with the assistance of a specially built bagging system (that is, to the curing bagging system described in the next section and where individual materials are described in more detail). An illustration of the vacuum bagging system, which was utilized both for the coupons and channel-section struts, is displayed in Figure 6.1

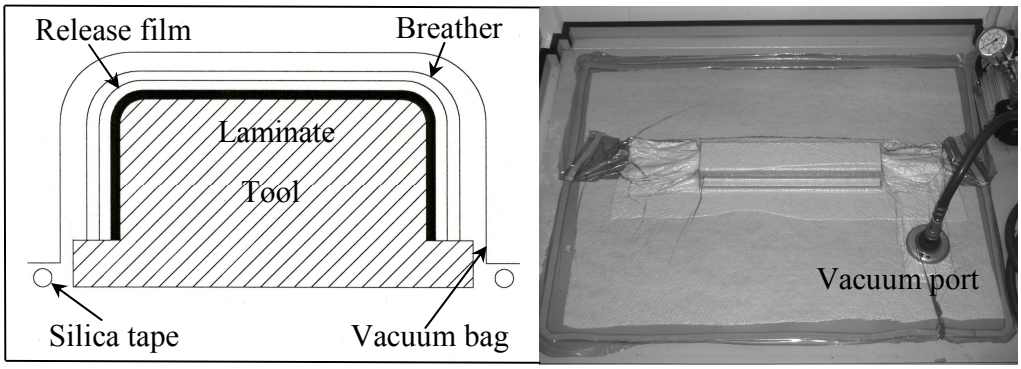

Figure 6.1. Illustration of the debulking system.

Lay-up Process for the Damaged Channel-Section Struts

The initial stages of the lay-up process for the damaged channel-section struts were perhaps as anticipated similar to the ones described for the undamaged channel-section strut. However, during the lay-up process an artificial delamination in the form of a circular, or nearly circular, PTFE patch was introduced at various levels and positions, as specified in Chapter 4. (It should be noted, that the nearly circular delamination patches refer to ones positioned in the stiffener, whose dimensions are such, so as to obtain a semi-circular delamination after axial edge trimming). The thicknesses of the PTFE film utilized were *0.1* and *0.25 mm*. The first was introduced in the complete set of the specified damaged channel-section struts, contrary to the second which was introduced only in the channels, where the delamination was positioned at the 2^{nd} and 6^{th} level of the skin and stiffener respectively. For any given thickness, the circular geometry was created with the aid of a puncher that was manufactured for the required "delamination" size (*d=27 mm)*. Furthermore, the cutting tool was hardened in order to produce a smooth peripheral edge, and to an extent, the desired sharp front of the impact-induced delamination.

In order to position the PTFE patch with accuracy and consistency on every occasion, two steel masks were manufactured, which fitted tightly on the channel tool and whose inner faces were covered with PTFE cloth in order to protect the underlying prepreg. The circular (or nearly circular) cut-outs drawn at the exact mid-length of the masks marked the delamination area, Figure 6.2. After positioning the artificial delamination, special care was taken during the lay-up process of the overlying layer to ensure that no gaps were formed around the boundaries of the previous, and therefore, in addition to those defined earlier, debulking was conducted immediately after, as a precautionary measure.

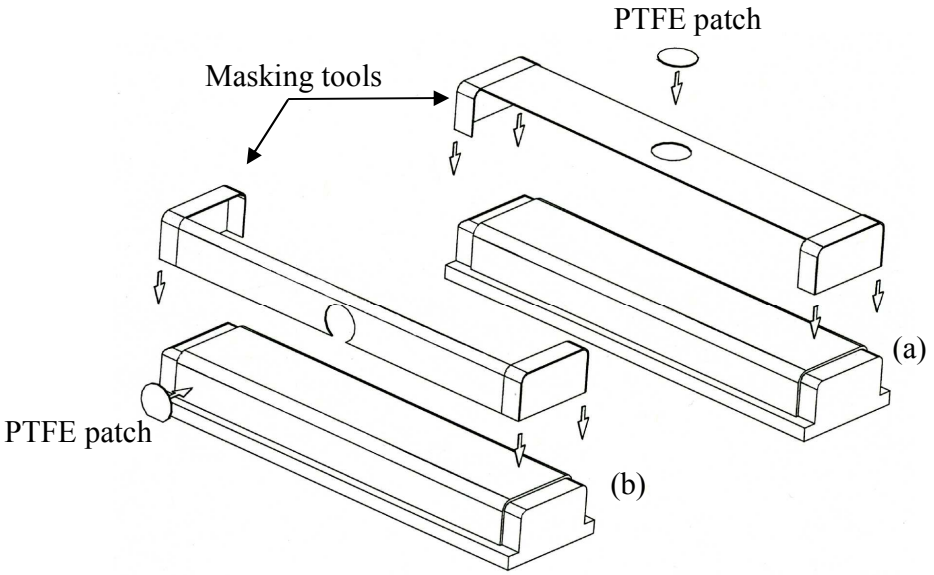

Figure 6.2. Illustration of the artificial delamination process in (a) the skin and (b) the stiffener.

6.1.2 The Bagging System

The selection of an appropriate bagging-system during curing and consolidation of the composite component is an essential factor in controlling the quality of the end-product. Generally, it is responsible for controlling the flow of the resin, the realization of the target thickness and the prevention of defects, such as porosity and voids that may arise during the curing cycle (Niu, 1992). The bagging system utilized was primarily devised on the suggestions made by the manufacturer (for the M21 matrix-based prepreg), current practise in industry and trial at the initial stages of the development of the relevant manufacturing processes. The main steps required for the bagging system of the material-test coupons, Figure B.2 (Appendix B), and damaged and undamaged channels, Figure 6.3 were:

i. Cork was utilized in order to seal the free edges of the laminates, and thus, restrict resin bleeding from the edges. The heights of the resulting dams were slightly thicker (*2.5 mm*) than the laminate in order to avoid rounding of the edge of the laminate due to the presence of the curing bag (Niu, 1992). The cork

was pre-heated in order to maximize its adhesion qualities. It should be noted that for the damaged and undamaged channels, the cork was fixed and maintained in position overnight to prevent the spring-back phenomenon that occurred in the area around the fillets.

ii. River cut-outs were created in the cork surrounding the two most distant edges in order to allow access of the thermocouples without distorting the laminate.

iii. A layer of peel-ply was applied on top (and bottom for the case of the material-test coupons) of the laminate. The peel-ply is a perforated Teflon coated fabric material, which is utilized in order to control the resin flow from the laminate and the surface roughness (Niu, 1992).

iv. The release film was applied on top of the peel-ply. The latter is a non-porous PTFE cloth that is utilized in order to restrict the resin flow to the vacuum system, which can significantly impair its operation (Niu, 1992).

v. Three layers of bleeder were applied on the release film. The bleeder is a woven glass fabric that normally serves as an absorber of excess resin and allows the escape of volatiles (Niu, 1992). The particular style of fabric though, can also serve as protection against possible damage induced during the curing cycle by the curing bag.

vi. Two layers of breather were applied on the bleeders. The purpose of the breather is to allow air and chemical volatiles to escape through venting and to produce an even pressure field around the component (Mazumdar, 2002).

vii. Finally, the curing bag was placed on top of the component and sealed around all edges with silica tape.

It is worth mentioning that typically in industry after the lay-up has been conducted on a male channel-section tool, the laminate is transferred and cured on a female one in order to minimize the complexity of the bagging system, but more importantly, the flow of the excess resin from the edges of the laminate. Something similar was observed in the early trials of the production of channel-section struts, in which the edges were resin-pour (or starved) resulting in a noticeable variation of thickness across the channel. However, the incorporation of dams in the longitudinal and vertical edges proved to be

quite successful in minimizing the previous phenomenon. Additionally, it was observed that restriction of the peel-ply in the close vicinity of the boundaries of the laminate (*3mm* longer fully stretched) had an additional contribution, to the development of a truly consistent and satisfactory end-product (with insignificant variation of thickness across the length). More recently, it has come to the author's attention that manufacturing techniques are being pursued and developed in industry for a single-tool lay-up and curing process.

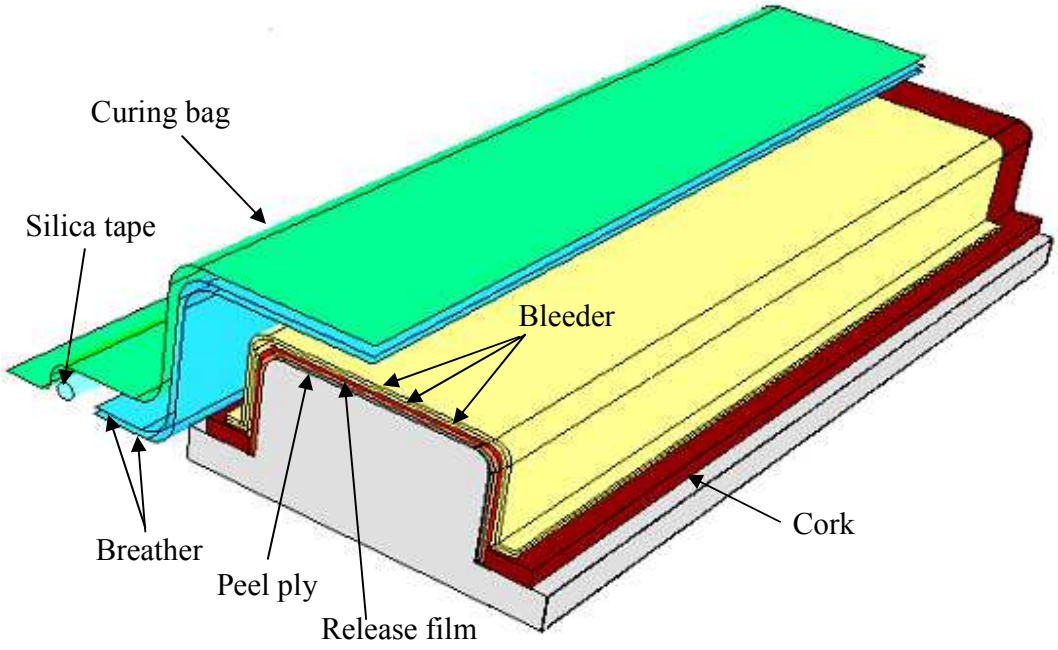

Figure 6.3. Bagging systems for for the undamaged and damaged channel-section struts.

6.1.3 Curing Cycle

The composite components were cured in an autoclave, which is perhaps the most standardized and reliable method of curing composite structures. The autoclave is a pressure vessel which applies heat and pressure to its contents while they are kept under a vacuum, Figure 6.4. In accordance with the manufacturer, the M21 epoxy resin was cured for 2 hours at 180^0 C, with a heat-up rate of 2^0 C/min, and held at constant pressure of 100 psi. The tolerance of the temperature was set at $\pm 3^0$ C. The two

thermocouples fitted at the edges of each component were utilized in order to measure the temperature variation across the laminates, and control the air temperature accordingly.

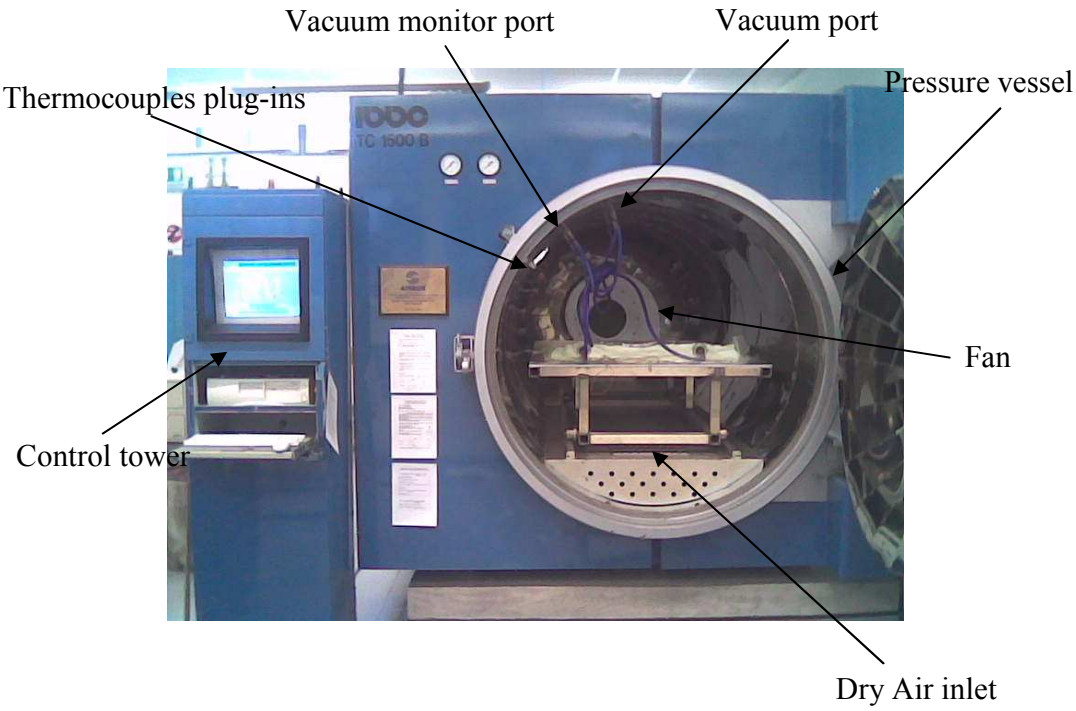

Figure 6.4. Illustration of the autoclave and the set-up of a composite component.

6.1.4 Quality Control with Non-Destructive Techniques (NDT)

Upon the completion of the curing cycle all specimens were checked for surface imperfections and thickness deviations. Generally, most of the specimens were found to be in very good agreement with the required standards. In the odd case of a substandard specimen the manufacturing process was repeated. However, in laminated composites assessment of the quality of the end-product and examination of possible defects requires specified non-destructive techniques. Thus, the C-scan method was employed for all the damaged and undamaged channel-section struts. That is, a transmitted ultrasonic pulse, the energy levels of which may be attenuated by the presence of defects or material inhomogeneities (Reid and Zhou, 2000). The scan images produced, Figure 6.5, suggested a successful manufacturing methodology.

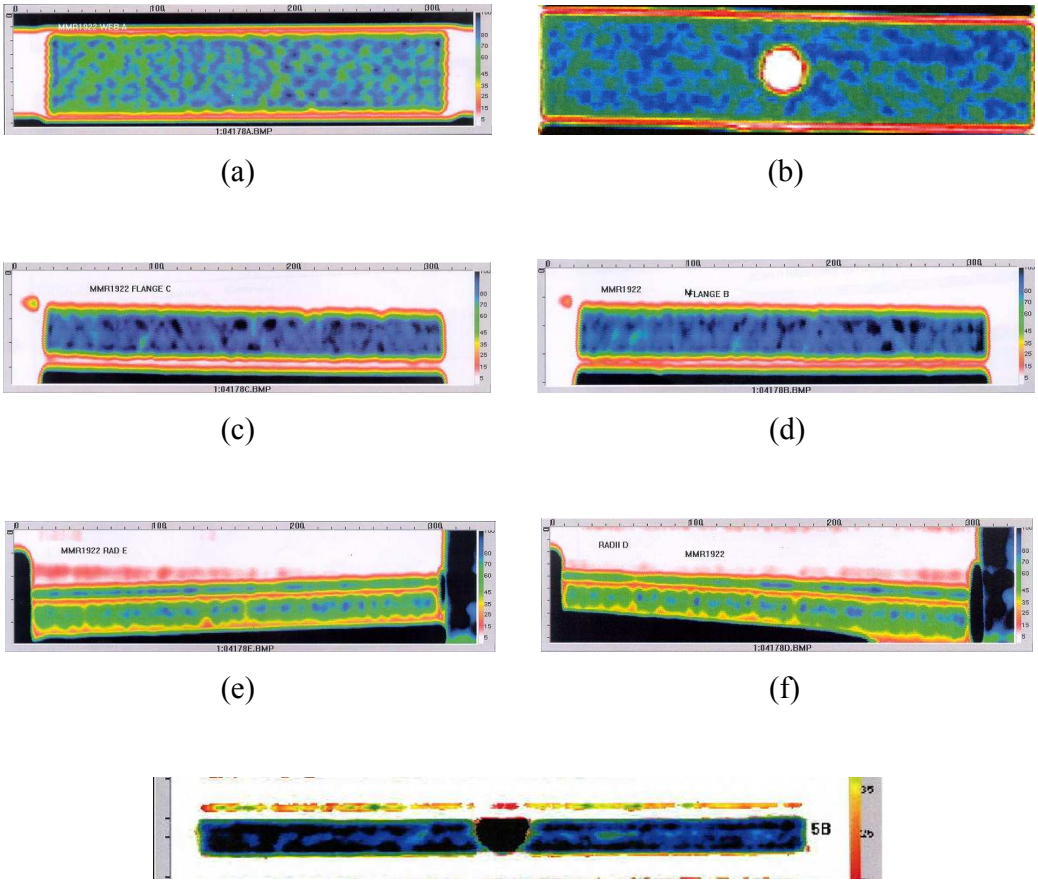

(a) (b) (c) (d) (e) (f) (g)

Figure 6.5. C-scan images of (a) the skin, (b) the skin with an embedded delamination, (c) the left and (d) right stiffener, (e) the left and (f) right fillet and (g) the stiffener with a free edge delamination.

In particular, minor variations in ultrasound attenuation were generally observed in all channel-section struts in the skin [i.e. Figures 6.5(a) and 6.5(b)], flanges [i.e. Figures 6.5(c), 6.5(d) and 6.5(g)], and fillets [i.e. Figures 6.5(e) and 6.5(f)], which could also be attributed to the uneven stiffener edges (due to cork residual) that did not allow the specimen to sit squarely. More importantly however, the images revealed well-formed circular and nearly-circular delaminated areas in the skin [i.e. Figure 6.5(b)] and stiffener respectively [i.e. Figure 6.5(g)]. It is worth mentioning that the contrasting images of total attenuation in the delaminated area in the skin and no attenuation in the delaminated area in the stiffener may be attributed to the penetration of the coupling

medium (de-ionized water) in the latter case, or simply, to the way the specimens were positioned.

6.1.5 Machining and Cutting of the Specimens

All the specimens were cut at the desired dimensions with a diamond-blade cutting machine and in the presence of cooling liquid in order to avoid the build-up of heat and to obtain a good finish on the edges. Unfortunately it was observed that even the high precision cutting machine utilized could only attain relative accuracy in terms of straightness and parallelism of the edges, possibly due to minor deviations in flatness of the cutting disc and the incompatibility of the coefficients of thermal expansion of the fibres and the resin (Mazumdar, 2002). Even though such deviations would probably have an inconsequential effect in thicker components, for the relatively thin laminated structure under investigation they proved to be more profound. In other terms, a uniform distribution of loading could not be realized due to the misalignment of the loading edges.

However, machining the composite laminated structure proved to be a great challenge, since a manual abrasive action could not produce the high accuracy required and the well-established methods for metals more likely than not would result in edge delaminations and the built-up of heat. Therefore, the system portrayed in Figure 6.6 was developed. In particular, a wet abrasive (400-grid) paper was adhered at the surface of a solid aluminum cylinder, manufactured to the highest possible surface finish and accuracy, and fitted into the rotating slot of a milling machining. The channel-section struts were mounted back on the lamination tool, but with the edge of the laminate leading the edge of the tool. The latter in turn was mounted onto the milling-machine. Having established that the tool was placed parallel to the bed of the milling machine, it was clamped into position. A micro-meter dial-gauge was placed on the cutting edge and the channel-section struts were clamped on the tool. The resulting displacement was counter-acted by an adjustable support, which was positioned underneath the exposed part of the channel-section struts. Finally, the rotating trimming tool was placed in

position and sufficient runs were made across the edge, trimming *0.005 mm* in each run with a rotational velocity of a *1000 rpm*.

The edges of the trimmed channels were inspected optically and with the aid of a micro-meter dial gauge. All the specimens were found to be within the required standards, and therefore, it was concluded that the method was quite successful. It is worth mentioning that the method employed for trimming the channel-section struts could also be employed for stiffened panels, by replacing the lamination tool with point-supports. Finally, a 0.1 mm hole was drilled at the center of the circular delaminations embedded in the skin in order to release any vacuum (possibly created in the delamination interface during the manufacturing process), which may have restricted the onset of delamination buckling.

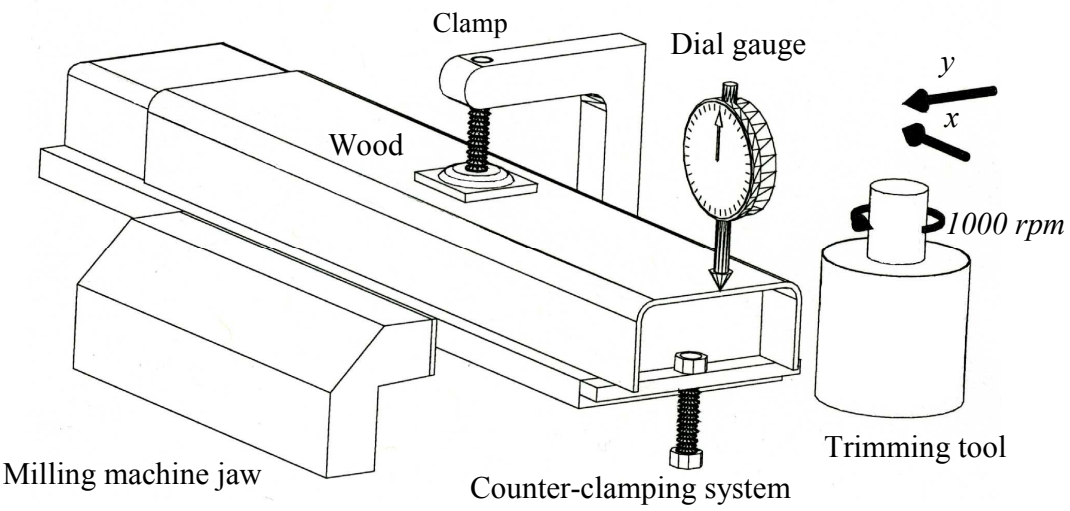

Figure 6.6. Illustration of the system developed for trimming composite laminated structures.

6.2 Experimental Set-up and Testing

6.2.1 Experimental Set-up of the Damaged and Undamaged Channel-Section Struts

All the test specimens manufactured were strain-gauged at various positions, as illustrated in Figures 6.7, in order to monitor the delamination and structural (i.e overall) buckling of the damaged and undamaged channel-section struts. In particular, 12 and 11 strain-gauges were attached to the undamaged and damaged channel-section struts respectively. All the strain-gauges were positioned to measure the strain in the axial direction. The channel-section ends were positioned in two specially-made pots, ensuring that their centroid was aligned with the center-point of the pots, and potted into a 20 mm thick block epoxy resin (Ciba AW106/HV/953/HV997; 100:45:45 by weight) in order to secure them in-place. Prior to potting of each edge, readings were taken across the surface of the loading plates of the pots, so as to certify that flatness and parallelism of the edges was maintained.

In order to observe the overall buckling mode configuration of each specimen, the stiffener edges were painted white. Furthermore, a linear variable displacement transducer (LVDT) was firmly attached at the top pot of all damaged and undamaged channels, which measured the end-shortening of the channel-sections against a rigid bar that was firmly attached at the bottom pot, Figure 6.7. Finally, to investigate the delamination buckling mode configurations of the damaged channels with a skin delamination, a second LVDT and a laser distance-calibrator were connected to two separate lever mechanisms that allowed the measuring devices to be accurately positioned at the delamination centre, Figures 6.7(b) and 6.7(c). In turn, the latter were attached at the loading plate of the top pot.

It should be noted that the laser always calibrated the out-of-plane displacement of the thinner sublaminate so as to ensure that the spring resistance of the LVDT would not restrict the onset of delamination buckling. On the same grounds no strain gauge was

(a)

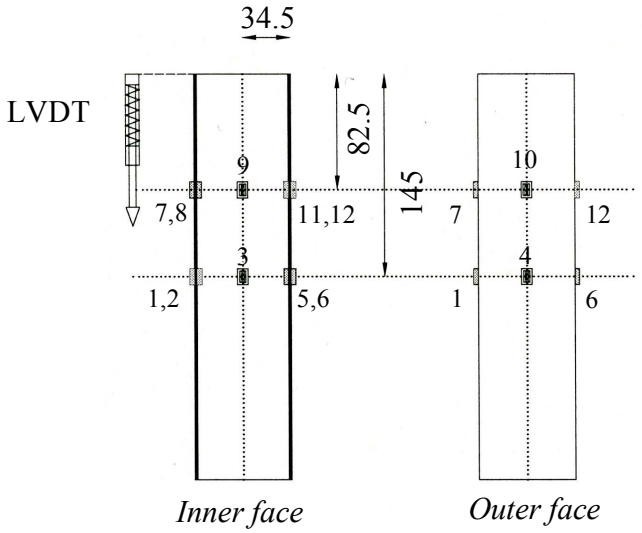
34.5
LVDT
82.5
145
9
10
7,8
11,12
7
12
3
4
1,2
5,6
1
6
Inner face
Outer face

(b)

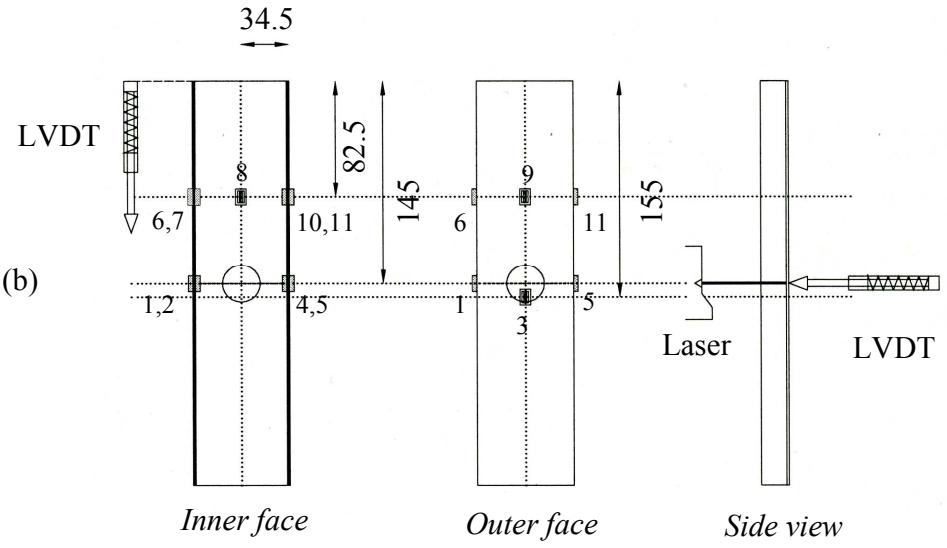
34.5
LVDT
82.5
145
155
8
9
6,7
10,11
6
11
1,2
4,5
1
5
3
Laser
LVDT
Inner face
Outer face
Side view

(c)

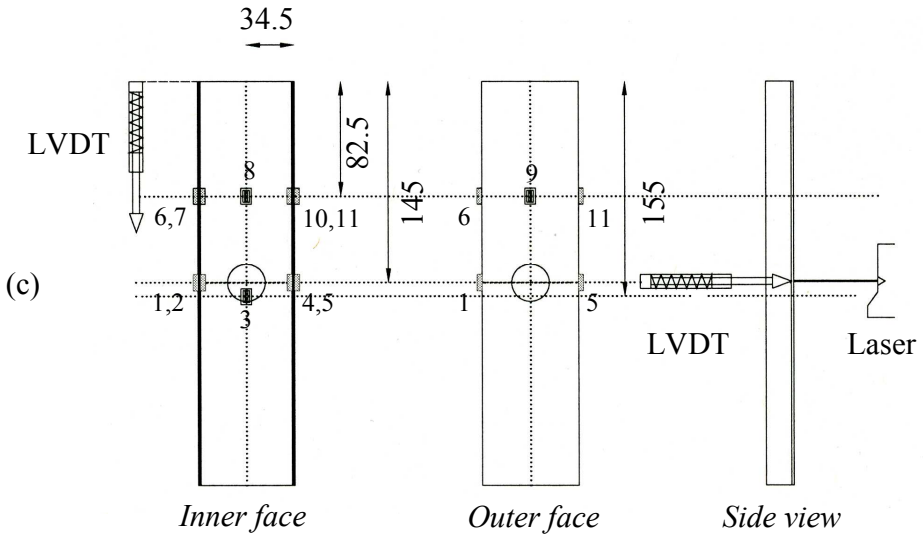
34.5
LVDT
82.5
145
155
8
9
6,7
10,11
6
11
1,2
3
4,5
1
5
LVDT
Laser
Inner face
Outer face
Side view

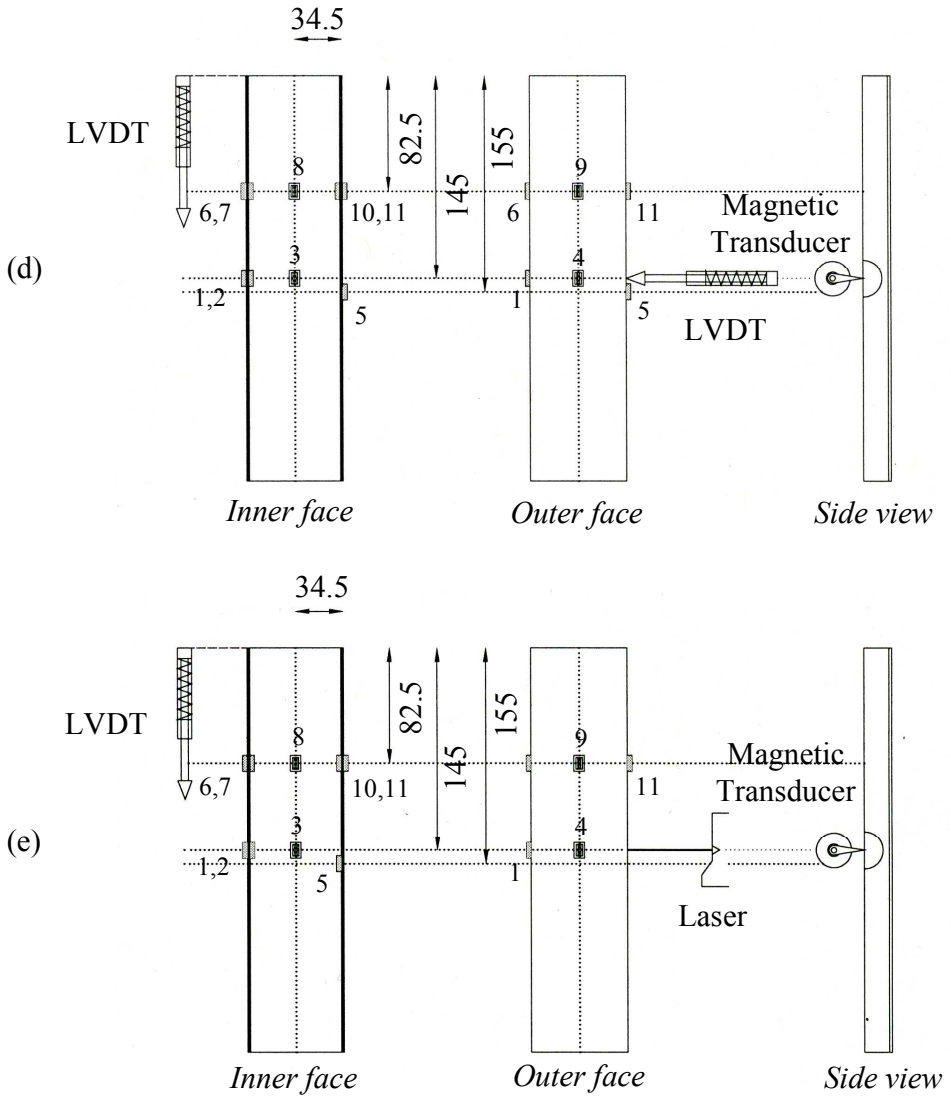

Figure 6.7. Strain gauge and instrumentation positioning for the (a) undamaged channels, the channels with skin delamination closer to (b) the inner surface and (c) the outer surface and the channels with stiffener delamination closer to (d) the inner surface and (e) the outer surface.

attached to the thinner sublaminate. For the stiffener edge delaminations a modified magnetic transducer was employed to measure the out-of-plane displacement of the inner surface of all channels, Figures 6.7(d) and 6.7(e), while for the case of a thinner sublaminate in the outer surface the laser distance-calibrator was utilized, Figure 6.7(e), and for the thicker the LVDT, Figure 6.7(d).

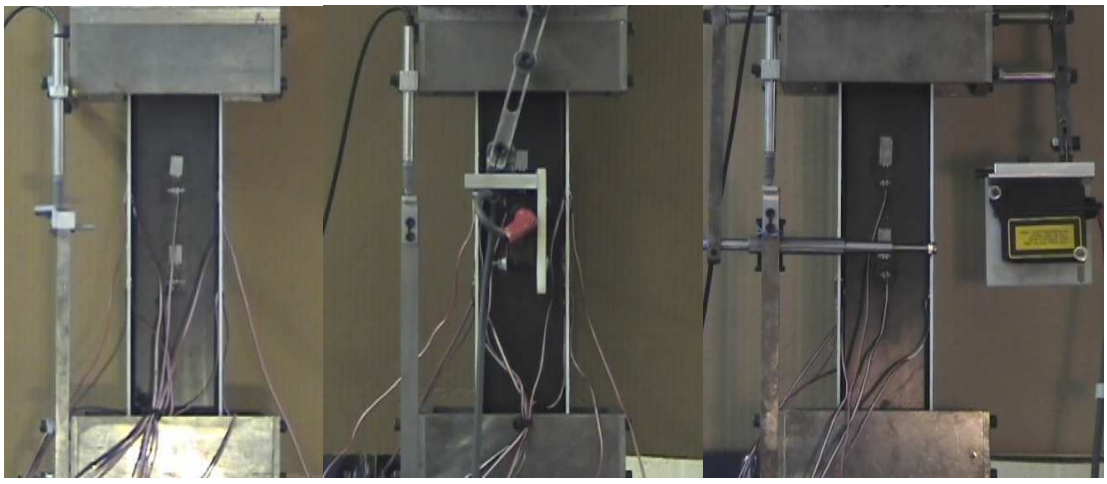

(a) (b) (c)

Figure 6.8. Experimental set-up for (a) the undamaged channels, (b) damaged channels with skin delamination and (c) damaged channels with stiffener delamination. In each case, the white paint on the edges of the stiffeners is clearly seen.

6.2.2 Testing of the Damaged and Undamaged Channel-Section Strus

Testing of the damaged and undamaged channel-section struts was performed in the tension/compression “Instron 1332” machine and all the strain-gauges and transducers were connected to the Spider-8 600Hz data acquisition system. In turn the latter was imported into the computer data-base that also monitored the load and end-shortening of the cross-head. The specimens were loaded in compression (i.e. Figure 6.8) with a controlled end-shortening speed of 5 mm/min. Initial test runs were conducted in each case to up to 20% of the critical load in order to determine the uniformity of strain in the

structure. Minor adjustments had to be conducted in each test with the aid of aluminium shims until all the strain gauges displayed similar readings. The initial deviations in strains arose from the minor double curvature of the loading plates, which were probably formulated during the welding action of the loading plate to the gripping plate. All the channel-section struts were tested to failure.

Unfortunately, during testing of the undamaged channel-section strut it was observed that a subsequent loss in the boundaries had occurred, due to failure of the loading plates. Therefore, the results were disregarded. However, the material initially used (M21/35%/268/AS7) was no longer available and therefore an alternative material (M21/35%/268/T800S) that had properties similar to the ones defined in the material-test experiments was utilized.

6.3 Concluding Remarks

A number of material-test coupons, undamaged and damaged channel-sections were manufactured and tested, Table 6.1. Significant lessons were learned about the manufacturing processes involved in composite structures. Particular attention should be drawn to the single-tool lay-up methodology adopted as an alternative to the two-part manufacturing process of channel-section struts. Moreover an effective and accurate trimming system for composite structures was developed in order to ensure flatness and parallelism of the loading edges. The latter was found to be of great importance for the thinner walled structures, where deviations from flatness and parallelism are scaled.

	Number of specimens	*Level of Delamination*	*Material*	*PTFE thickness*
Axial Compression Coupons	5	-	M21/AS7	-
Transverse Compression Coupons	5	-	M21/AS7	-
Shear Coupons	5	-	M21/AS7	-
Undamaged Channel	1	-	M21/AS7	-
Undamaged Channel	2	-	M21/T800	-
Damaged Channel with Skin Delamination	1	2	M21/AS7	0.1 mm
Damaged Channel with Skin Delamination	1	3	M21/AS7	0.1 mm
Damaged Channel with Skin Delamination	1	5	M21/AS7	0.1 mm
Damaged Channel with Skin Delamination	1	6	M21/AS7	0.1 mm
Damaged Channel with Skin Delamination	1	6	M21/AS7	0.25 mm
Damaged Channel with Stiffener Delamination	1	2	M21/AS7	0.1 mm
Damaged Channel with Stiffener Delamination	1	3	M21/AS7	0.1 mm
Damaged Channel with Stiffener Delamination	1	5	M21/AS7	0.1 mm
Damaged Channel with Stiffener Delamination	1	6	M21/AS7	0.1 mm
Damaged Channel with Stiffener Delamination	1	2	M21/AS7	0.25 mm

Table 6.1. List of material-test coupons, undamaged and damaged channel-section struts produced and tested.

Chapter 7

Experimental Results and Comparisons with Numerical Simulations

A number of channel-section struts with and without artificially induced delaminations were manufactured and tested under uniaxial compression. Embedded delaminations were introduced both in the skin and stiffener at various levels. The main objective of the aforementioned experiments was to investigate the influence of the delamination depth according to its relative position (that is, in the structure) in the pre- and post-buckling structural behaviour (or otherwise depth and position criticality). A secondary aim was to monitor the buckling response of the sublaminates at the structural level both in the pre and post-buckling region.

In this chapter the experimental results are compared according to the position of the delamination, the depth of the delamination and ultimately against the undamaged channel-section struts. Therefore, prior to the analysis of the results obtained for the delaminated structures, the results for the undamaged channel-section struts are examined. Even though the latter were manufactured using the two different prepregs (due to the first being not available from the manufacturer), M21/35%/268/AS7 and M21/35%/268/T800S, nevertheless the similarity of their properties allowed for confident examination of the structural behaviour and identification of critical loading levels. All the damaged and undamaged tests results are compared with those obtained by the corresponding numerical simulation at the end of each section. It should be

remembered though, that the numerical results do not account for delamination growth, creeping and material non-linearity. The differences in the testing results and the numerical results are commented on and justified, along with important observations that lead to better agreement. Partial explanation of the differences observed is drawn from the material testing, and therefore, will be presented first.

7.1 Material Test Results

From the stress-strain relationships of the material-test coupons the axial and transverse compressive and in-plane shear properties of the M21/35%/268/AS7 were determined. The latter relationships along with calculations and validation of the results are presented in Appendix B. All the material properties of interest have been summarized in Table 7.1, which include not only the ones derived by experimental testing but also the properties provided by the manufacturer or assumed. In particular, the Poisson's ratio effect along with the tensile properties of the material was provided by the manufacturer, therefore relevant testing was not required. Additionally, the interlaminar axial shear modulous G_{13} can be equated to the in-plane shear modulus G_{12}, since the material under discussion may be considered transversely isotropic (Gibson, 1994), while for typical CFRP the interlaminar transverse shear modulous G_{23} can be approximated to half of the in-plane one.

Property	*Symbol*	*Units*	*Value*
Axial Compression Modulous	E_{11}	kN/mm^2	131.9
Transverse Compression Modulous	E_{22}	kN/mm^2	9.6
In-Plane Shear Modulous	G_{12}	kN/mm^2	4.6
Interlaminar Axial Shear Modulous	G_{13}	kN/mm^2	4.6
InterlaminarTransverse Shear Modulous	G_{23}	kN/mm^2	2.3
In-Plane Poisson's Ratio	v_{12}	-	*0.3*

Table 7.1. Material properties of the M21/35%/268/AS7 prepreg.

Typically, all the aforementioned material properties of CFRP are considered to be linear elastic. Even though they may initially appear to be valid for a rather superficial examination of the stress-strain relationships, Appendix B, the material properties determined by the aforementioned tests may not necessarily be consistent throughout the straining/loading history of the composite material. That is, the stress-strain relationships are in fact nonlinear, and therefore, the material properties are derived by considering a tangential line on the stress-strain curve at a given strain range (Harper and Heumann, 1987). Consequently any change in modulus that may occur before failure would not be accounted for (Harper and Heumann, 1987). Thus, the variation in modulous over the measured strain range must be examined more carefully in order for deterministic conclusions of the material behaviour to be drawn. The axial and transverse compression and in-plane shear modulus variation are illustrated in Figures 7.1, 7.2 and 7.3 respectively. It should be clarified that even though the variation of modulus and not the tangent modulus is plotted, nevertheless their trends are qualitatively similar and their variation values quantitatively similar.

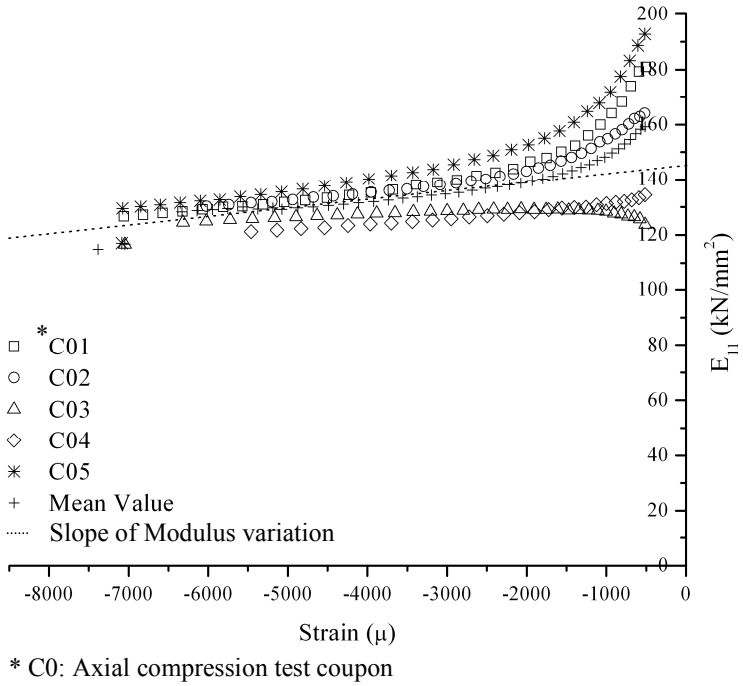

Figure 7.1. Axial Compression Modulus variation as a function of the axial strain.

In particular, Figure 7.1 illustrates that in all five specimens the axial compression modulus decreases with increasing strain, and thus, demonstrates a non-linear elastic behaviour. Neglecting the initial strain region, where unrealisticly high modulus values are observed (but are nevertheless sharply decreasing) due to some initial misalignment within the compression fixture (further discussed in Appendix B), the mean value variation of modulus may be approximated by a straight line. The latter approximation leads to the conclusion that the modulus decreases almost linearly with increasing loading conditions. Nevertheless, of particular interest to the current work is the strain region above 0.4% strain, where the channel-section struts are designed to buckle and the proximity of the tangent modulous evaluation begins to decay. For comparison reasons the approximated gradient of the mean modulous variation is slightly extended to 0.8% strain (since the selected strain measuring range of the data acquisition system terminated at 0.73% strain and prior to failure of the specimens).

Thus, the reduction in the axial compression modulus for the region between 0.4% and 0.8% strain was approximately 8.3%. The latter result compares well with the 8.9% prediction of Harper and Heumann (1987), which studied the variation in axial compression and tensile modulus. Harper and Heumann, by eliminating the possibility of the material non-linearity being attributed either to thermal stresses induced during the curing cycle or to fibre buckling under high loading conditions, demonstrated that the non-linear stress-strain behaviour of the carbon fibres is primarily responsible. A variation in modulus can also be observed in the transverse compression material-test coupons, Figure 7.2. However, a distinct pattern cannot be readily identified since even neglecting the adjustment strain region (in which the fixture is properly aligned with the axial load) the modulus clearly increases up to 0.35% strain, remains nearly constant up to 0.6% strain and finally decreases. Nevertheless, the almost constant region and the actual contribution of the transverse compression modulus suggest that the consideration of such variation would be of secondary importance (or if any at all), and thus, to the author’s knowledge no relative literature has been developed.

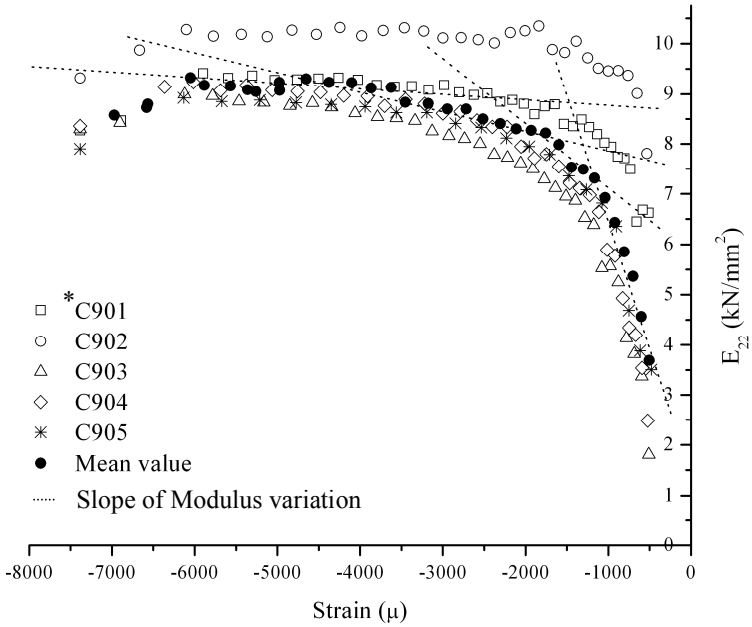

* C90: Transverse compression test coupon

Figure 7.2. Transverse Compression Modulus variation as a function of the axial strain.

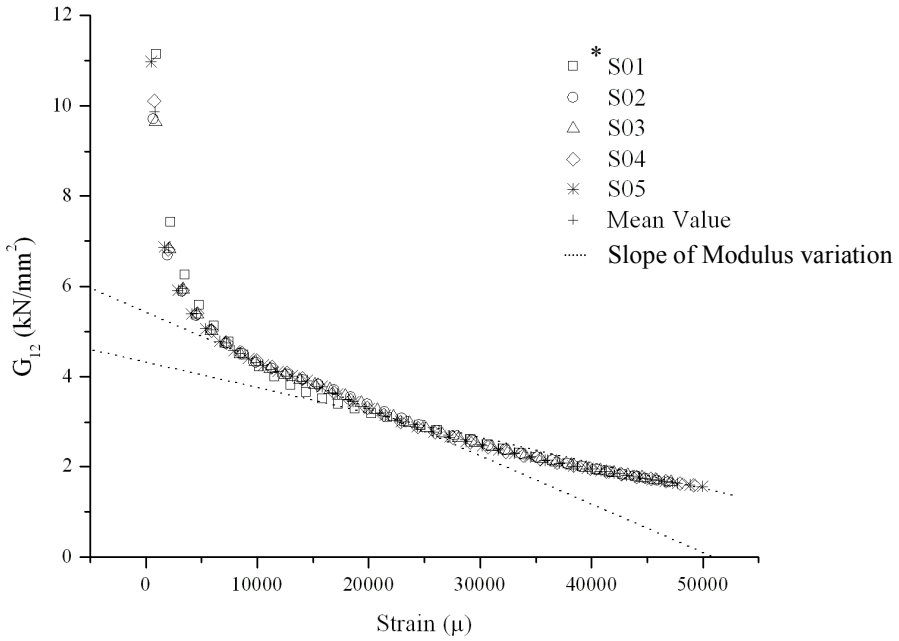

* S0: In-plane shear test coupon

Figure 7.3. In-Plane Shear Modulus variation as a function of the shear strain.

Finally, clearly a non-linear variation of in-plane shear modulus is evident in Figure 7.3. Such an observation perhaps may be anticipated since the shear stress-strain relationships (Appendix B) are obviously non-linear. Thus, a significant reduction in modulous of approximately 17% may account for the strain region between 0.4% and 0.8%. An 18% reduction has also been reported by Hady and Vautrin (1987) but for the strain region of 0.1% and 0.5% strain and with no further evidence of the shear modulus variation at higher strain levels. Nevertheless, they suggested that such non-linearity is the outcome of the visco-elastic nature of the matrix. Thus, the fibres are able to distort from their given orientations.

Even though the non-linear elastic nature of CFRP has been reported and verified since the 1970's (Harper and Heumann), still they are usually referred to as linearly (or almost linearly) elastic. For primary aircraft structures, to an extent, that would be valid since the current design allows no deformation to occur prior to ultimate loading conditions (DUL), which are maintained at relative low levels of axial strain. However, the importance of material non-linearity would be more profound when considering the post-buckling behaviour of such structures. Even though the design failure load may not be affected by the exclusion of the material non-linearity since rather conservative values, known as the B-basis, have been adopted by the industry, nevertheless it may also lead to underestimation of the critical loading conditions, as further discussed in due course.

7.2 Undamaged Channel-Section Struts Results

7.2.1 Pre-Buckling Stiffness

A phenomenon which has been readily reported and discussed in literature is the frequent poor correlation between the experimental evidence and the finite element prediction of the overall pre-buckling stiffness (that is, the stiffness estimated by the load versus end-shortening) of composite structures. In an attempt to produce a better

agreement between the aforementioned sets of results it has become standard practice to employ the B-basis material properties (i.e Liu, 2005) or to adjust the material properties accordingly.

For example, a 9% and 16% reduction in the nominal material properties has been reported by Nagendra et al. (1994), Falzon and Steven (1997) and Cerini (2006). To an extent, a reduction in the nominal properties of the composite material is valid. That is, the nominal properties represent the averaged value between the compression (lower bound) and tensile (higher bound) values, and therefore, in the pre-buckling region, where the structure is almost in uniform compression, the overall stiffness would be overestimated. However, it has also been observed that adjustment of the nominal properties to achieve the experimental overall pre-buckling stiffness is accompanied by a noticeable reduction in the buckling load (Cerini, 2006; Nagendra, 1994).

Even though similar evidence on the correlation of the overall pre-buckling stiffness between the experimental and FEA results that utilizes the B-basis properties were unverifiable, nevertheless Liu et al. (2006) reported that the employment of the B-basis values were rather conservative and led to the underestimation of the buckling load. Evidently, modifying or utilizing conservative material properties may lead to inaccurate critical load predictions. However, utilization even of the compressive properties (that comprise the lower bound) may initially appear to result in inaccurate results. Therefore, the solution must be sought within the design approximations conducted in the finite element model.

More specifically, in the initial finite element model the length of the channel-section strut under discussion was equated to the exposed length of the strut (or more simply the material within the resin blocks was neglected) and appropriate boundary conditions were applied. However, the nonlinear analysis overestimated the overall pre-buckling stiffness by 16% (near critical buckling) in comparison to the experimental, Figure 7.4. Nevertheless a closer examination revealed that locally (back-to-back strain

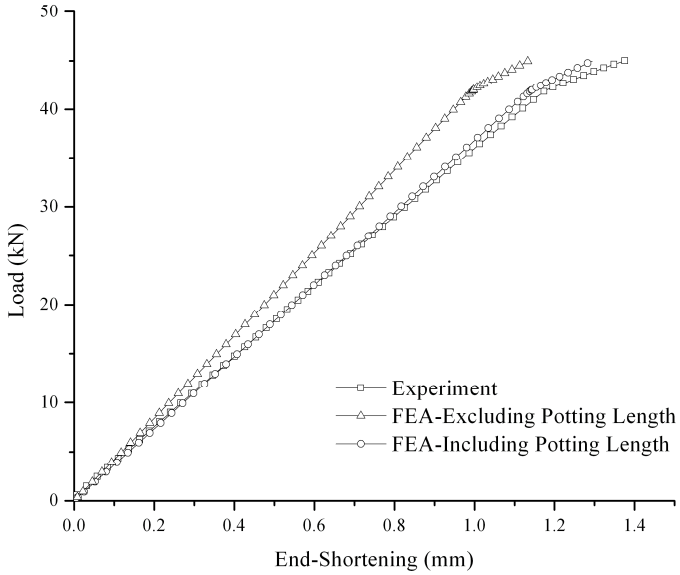

Figure 7.4. Comparison of the experimental and finite element models overall pre-buckling stiffness.

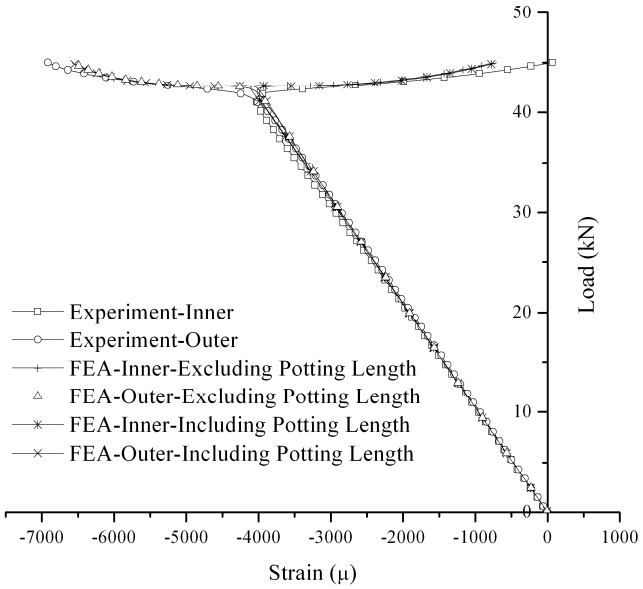

Figure 7.5. Comparison of the experimental and finite element models local pre-buckling stiffness as illustrated by the strain measurements at the mid-point of the skin.

gauges) the experimental and the finite element pre-buckling stiffness were in very good agreement, Figure 7.5, a finding that has also been reported by Nagendra et al (1994). Moreover, the critical buckling loads were similar (less than 1% deviation). Thus, it was concluded that the utilization of the axial and transverse compression material properties was correct and consequently adjustment or utilization of the B-basis properties would not be valid.

Therefore the only remaining parameter that could affect the overall pre-buckling stiffness, but excluded for simplification reasons, was the proportion of the material within the resin blocks. Incorporating the latter in the finite element model meant an excellent correlation was observed in terms of both overall and local pre-buckling stiffness with the experimental results. The latter observation suggests that the material within the pots is allowed to strain axially within the resin blocks, while all other displacements and rotations are restricted by the surrounding environment. Furthermore, boundary conditions severely affect the stiffness distribution in the structure by the formation of areas of localized stiffness, which even in the pre-buckling state (uniform strain) may vary significantly in relation to the overall stiffness of the structure. Hence, it is essential to include the full length of the channel-section strut in the analysis in order to obtain a realistic estimation of stiffness. Finally, the small deviations observed in Figures 7.4 and 7.5, may be attributed to initial imperfections and to a lesser extent to material non-linearity.

7.2.2 Buckling Mode Configuration (Imperfection Sensitivity)

Experimental evidence revealed two distinct (and reversed) buckling configurations of the undamaged channel-section struts. The first was characterized by the mid-point (or central crest) of the skin deflecting towards the inner surface of the laminate (positive direction), while the mid-point at the edge of the stiffeners spreading outwards [Figure 7.6(a) and (c)]. In contrast, the opposite phenomenon was observed in the second configuration, Figure 7.6(d) and (f). In correlation to the direction of the

deflections at the mid-length, from this point forwards, the first configuration will be referred to as the “positive mode” and the second as the “negative mode”.

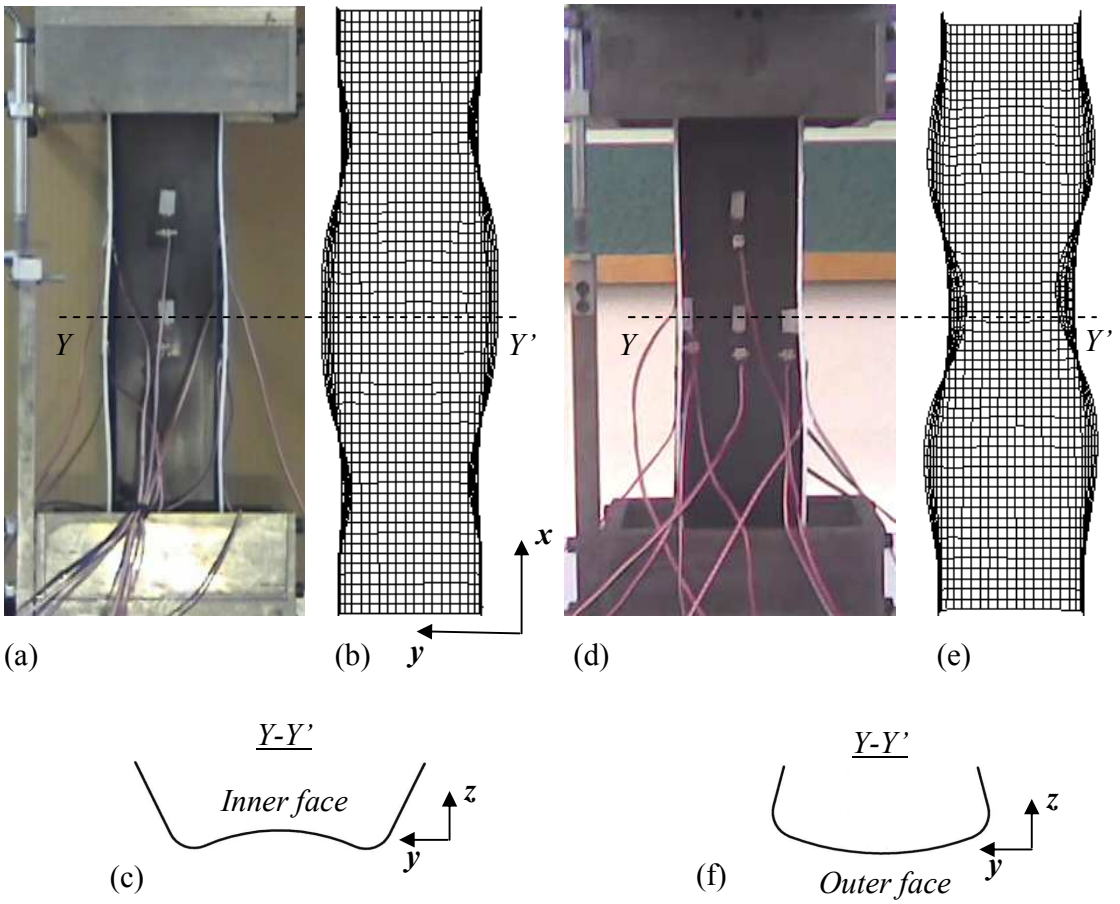

Figure 7.6. (a, b, d, e) Planar and (c, f) cross-sectional view of the (a, b, c) “positive” and (d, e, f) “negative” buckling mode configurations as formed by (a, d) experimental testing and (b, e) finite element analysis.

Preliminary finite element models with built-in positive and negative overall imperfections (in the form of a single half-sine wave along the length of the channel-section strut and within realistic amplitudes) demonstrated that an imperfection of such a type would have no qualitative influence over the evolution of the buckling mode. Thus, regardless of the direction of the overall imperfection a positive mode developed. The

latter finding was in agreement with those of Rothwell (1974) and Kwon and Hancock (1992), who demonstrated that channel-section struts, are rather insensitive to this type of imperfections. Nevertheless, a localized mode may have a profound influence on the evolution of the buckling configuration. Therefore, localized imperfections with positive and negative amplitudes of the first eigenvalue solution were utilized in order to investigate the sensitivity of the structure to geometric imperfections.

The results revealed that the transition point at which the buckling configuration switched from a "positive mode" to a "negative mode" was not at zero amplitude (that is, no imperfection imposed), but between *-0.4%* and *-0.45%* of the thickness of the channel-section strut. Or more simply, for negative amplitudes higher than *–0.4%* the buckling configuration would ultimately evolve to a "positive mode". The latter finding was also verified experimentally and is illustrated with the aid of a detail from the load versus strain plots of the mid-point of the skin in Figures 7.7 (a) and (b). More specifically in the finite element analysis, for an imperfection of *-0.4%* amplitude the inner face of the skin at mid-length constitutes the compressive face of the plate. When critical buckling occurs it switches to a tensile face, Figure 7.7(a). However, for *-0.45%* imperfection amplitude the region under discussion maintains its compressive state, Figure 7.7(b). The likelihood therefore of the development of either mode would be dependent upon the configuration of the initial imperfection.

It is therefore valid to state that in thin-walled open mono-symmetric structures, such as the one under investigation, small imperfection amplitudes may alter the anticipated buckling configuration and behaviour. To a certain extent the latter observation brings forward the issue of the effect of damage induced imperfections on the structural behaviour. Finally, it should be noted that typically an investigation of imperfection sensitivity involves the superposition of various modes of imperfection (eigenvectors). For the structure under investigation the superposition of all the critical modes that were produced by the eigenvalue analysis (up to *4* times the buckling load) did not alter the results.

(a) -*0.4% Imperfection Amplitude*

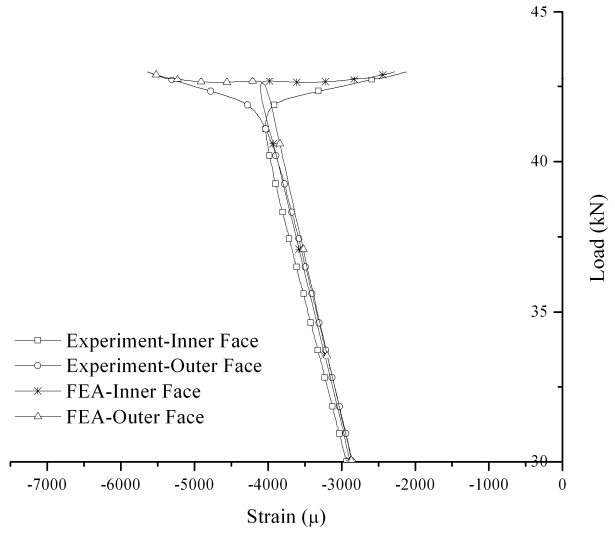

(b) -*0.45% Imperfection Amplitude*

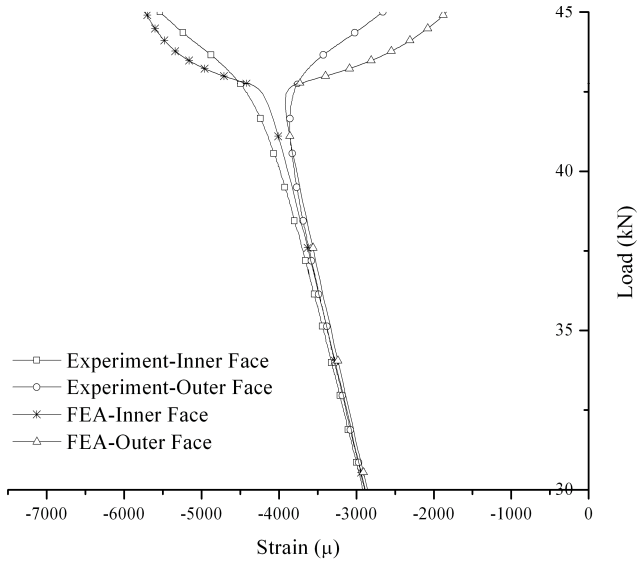

Figure 7.7. Detail of the load versus strain plots of the mid-point of the skin, at which the experimental results have been correlated to ones derived from the finite element models with (a) -0.4% and (b) -0.45% amplitude.

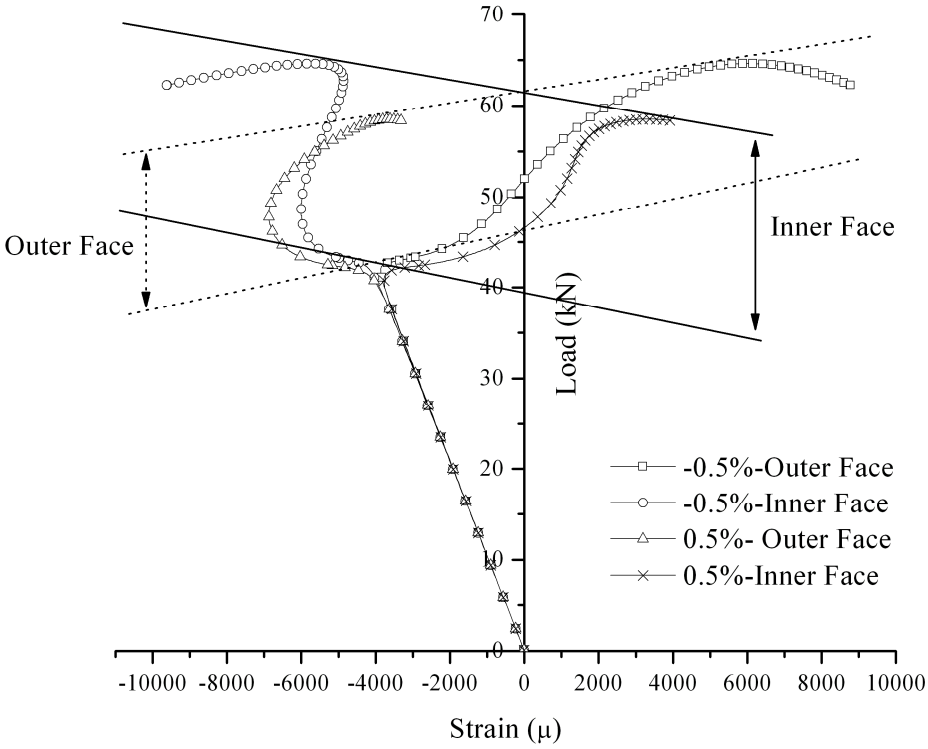

Figure 7.8. Imperfection sensitivity of the channel-section strut and mode variation as illustrated by the FEA at the mid-point of the skin.

7.2.3 Buckling Behaviour of the Channel-Section Strut

According to the previous section, the structure appears to bias towards the "positive mode". This however, implies that the bifurcation point at buckling is not symmetric. This was examined with the aid of the non-linear finite element analysis. The first critical mode was incorporated with both positive and negative imperfection amplitudes of 0.5% of the thickness of the laminate. The predicted back-to-back strain variations with compressive loading at the mid-point of the skin of the two models are plotted in Figure 7.8. Through examination of the predicted longitudinal strain in the inner surface of the skin in two models it is observed that birfucation point is asymmetric and clearly tilted. Moreover, it is of interest to note that the equilibrium paths on the left (negative

mode) and right hand (positive mode) side of the bifurcation represent a path, which lies in the realm of umbilic catastrophes (Thomson and Hunt, 1984). In accordance to Thomson and Hunt (1984), the latter equilibrium path may depict the response of a general stiffened structure, where interactive buckling is observed. This is in line with the findings of Chapter 3, in which it was identified that local instability in the channel-section strut triggers overall deformation (Euler buckling), and consequently, debilitates the ultimate strength.

However, Figure 7.8 shows that the effect of such coupling would be more profound in the case of a positive mode. This may be attributed to the junction areas (that is, the fillet) of the integrally stiffened structure. More specifically, Figures 7.6 (b) and (e) show the buckling configuration of the channel-section strut, in an advanced stage of the post-buckling path, undergoing a positive and negative buckling deformation respectively. From the latter figures it is apparent that when the buckling crests, in which the stiffeners have deflected in the positive direction (that is, towards the outer face of the laminate), are characterized by significantly bigger wavelengths. This suggests a preferred direction of relative distortion between the skin and stiffener plate segments; or otherwise a configuration subject to lower energy in bending.

Therefore, it is believed that the positive mode results in a relief of the stress concentration in the fillet area of the channel-section strut, by effectively reducing the bending curvature. In contrast, the negative mode is subject to increased curvatures in the aforementioned region, and therefore, requires more bending energy. This may also be the reason why the buckling load is higher in the latter and the bifurcation point is tilted. Consequently, larger wavelengths in the positive mode and smaller in the closing mode are generated. In turn, the latter promote higher and lower coupling between the local buckling mode and the global mode. This is also depicted in the overall deformation of the strut, as illustrated in Figure 7.9.

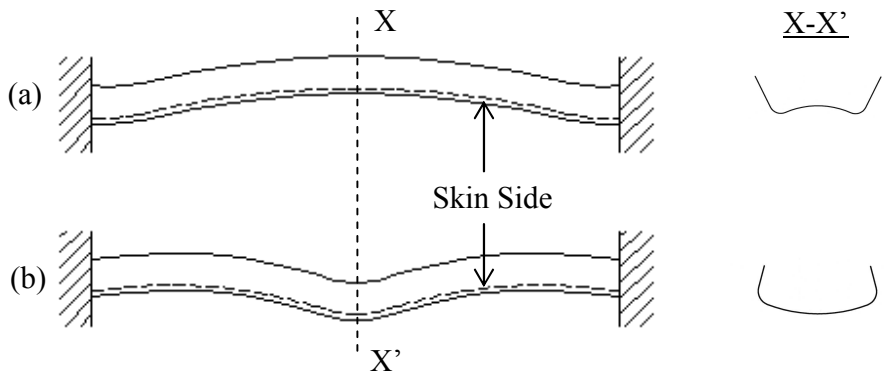

Figure 7.9. Sketches of the side and cross-sectional view of the channel-section strut with global deformation in (a) the positive mode and (b) the negative mode.

7.2.4 Channel-Section Strut with Positive Buckling Mode

Experiment

The pre and post-buckling behaviour of the undamaged channel-section strut is examined in regard to the variations of the longitudinal strains with the applied compressive load that were monitored at selected positions across the mid-length (see Chapter 5). In particular, buckling (P_C) occurred at 42 kN, as evident from the deviation of the back-to-back longitudinal strain measurements in the inner and outer surfaces of the left stiffener (Figure 7.10), skin (Figure 7.11) and right stiffener (Figure 7.12). At that point the inner faces of the stiffeners and skin became compressive and tensile faces respectively; or otherwise the mid-section of the strut deflected in a positive mode. Buckling of the channel-section strut occurred in an asymmetric mode with three half-sine waves along the length of the strut (similar to the one predicted by the linear eigenvalue analysis in Chapter 5). As discussed in that chapter, the asymmetry arises from the bending-twisting coupling effects in the laminate that cause the buckling configuration to skew in a manner such that the buckling crests of the right stiffener precede the ones in the left [looking from the page down in Figure 7.6 (a)].

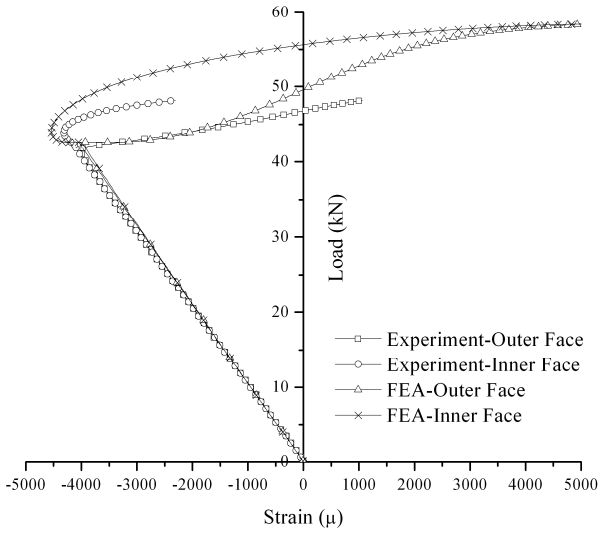

Figure 7.10. Comparison of the experimental and FEA variation of strain at the mid-point of the left stiffener of the channel-section strut undergoing a "positive mode" of buckling.

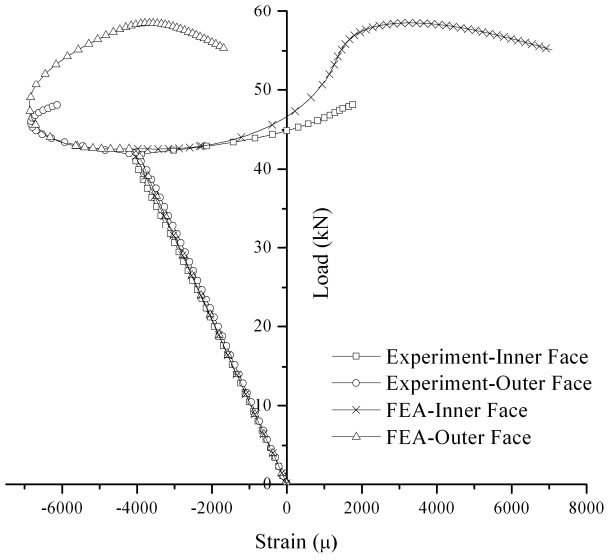

Figure 7.11. Comparison of the experimental and FEA variation of strain at the mid-point of the skin of the channel-section strut undergoing a "positive mode" of buckling.

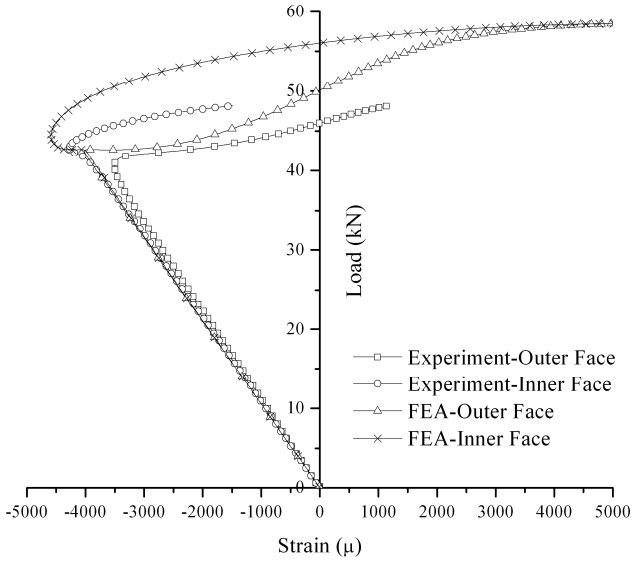

Figure 7.12. Comparison of the experimental and FEA variation of strain at the mid-point of the right stiffener of the channel-section strut undergoing a "positive mode" of buckling.

Moreover, as already mentioned, an initial imperfection was present in the channel-section strut, as evident from the switch of the compression faces to tension, and vice versa, at critical buckling. Such imperfections typically arise following the curing process of composite laminates, but unfortunately the exact shape of the one generated in the structure under investigation has been not been identified.

On the initial post-buckling path the deflection of the asymmetric mode developed in a stable manner. However, at a loading level of 44 kN a change in the stress gradients across the mid-length of the channel-section strut occurred. The change in the stress gradients depicts the evolution of global buckling mode, and in particular, Euler buckling. For example, this is evident in the skin by the transition of the outer face into a more tensile region and the exponential increase in tension in the inner face. The latter indicates the evolution of a longer longitudinal half-sine wave. The global component in the coupled mode evolved rapidly and the structure failed at an ultimate load of 48 kN

with excessive delamination, matrix cracking and fibre fracture at the fixed potting end, as shown in Appendix C.1.

FEA

The pre and post-buckling behaviour of the undamaged channel-section strut that was predicted by the finite element analysis is analysed with the aid of the variations of the longitudinal strains with applied load at the exact experimental positions. The latter are compared to the experimental in Figures 7.10, 7.11 and 7.12 in order to determine the efficiency of the finite element model. More specifically, prior to structural instability the predicted strains are in very good agreement with the experimental. Likewise the predicted buckling load is similar (42.5 kN). Nevertheless, a very satisfactory correlation is also observed along the initial post-buckling path. Some small deviations observed probably arise due to the disparity of the actual imperfection in the specimen and the one incorporated in the finite element model.

However, it can be observed that at 44 kN (that is, the load level at which global buckling deformation becomes more profound) the predicted strains across the mid-length deviate from the experimental. As evident, for example, in Figure 7.11 this is attributed to a more gradual evolution of the global configuration in the analysis in comparison to the experiment. Consequently, this disparity gives rise to higher deviations in the correlated strains with the applied compressive load, but does not affect the similarity of their trends. Similar findings have also been reported by Cerini (2006) on blade-stiffened composite panels that were designed to carry sufficient compressive loading in the post-buckling region. The author suggested that the observed disparity between the experimental and numerical strains was attributed to the mesh density of the finite element model. This was based on the argument that as the curvature of the buckles increased it was described by fewer elements. Therefore, the selected number of elements would have been appropriate for the initial post-buckling phase, but probably too coarse for the advanced post-buckling regime.

The latter argument was not confirmed by the current model, since an increased mesh density (that is, eight times the original one) did not alter the predicted behaviour. Similarly, the accelerated evolution of the global buckling mode was proved to be independent of the rate of strain imposed in the undamaged channel-section strut. This was demonstrated by a dynamic analysis of the problem, where the time over which the total load applied was varied between the real experimental and very short periods.

In the author's opinion, such disparities between the experimental and numerical results arise from the non-linear elastic nature of the material. More specifically, in accordance to Hu et al. (2006) the buckling behaviour of composite laminated skew plates is severely affected by the non-linear nature of the in-plane shear modulus. In a $(45/-45)_{n,S}$ laminate it may account for severe reductions in the buckling load and ultimate strength. The actual effect was dependent on the initial skew angle and the plate aspect ratio (that is, length over width). However, it was also reported that for the $[45/-45/90/0]_S$ laminate the effect of the in-plane shear non-linearity was negligible. This was attributed to the fact that the axial load was mainly carried by the 0^0 layers, with little contribution of the ±45 layers. Therefore, the latter layers are not significant enough to induce non-linearities in the structural behaviour.

The previous paragraph could be related to the experimentally observed behaviour of the undamaged channel-section strut as follows: At structural buckling the plate segments skew as a result of the bending-twisting coupling effects in the laminate. The skew promotes non-linear behaviour of the in-plane shear modulus (Hu et al., 2006). However, in a localized buckling mode (that is, one that evolves under relatively short wavelengths) the load is carried mainly by the 0^0 and 90^0 layers, and therefore, the effect of such non-linearity is negligible. When global buckling initiates, it causes the wavelength of the central buckling crest to grow under higher amplitudes of out-of-plane deflection. This deteriorates the ability of the aforementioned layers to carry the compressive load, and therefore, induces the material non-linearity. Consequently, Euler buckling is accelerated. The exact percentage in the reduction of the ultimate load due to the latter material non-linearity cannot be accurately established. That is, in the

experiment material failure (probably caused by the crippling stresses in the fillets) did not allow the full evolution of the Euler buckling mode. It is worth pointing out that failure occurred near the edges, where higher bending curvatures are observed.

Nevertheless, the observed difference is an imperative design issue which must be investigated further. This issue becomes even more substantial in view of the fact that current weight saving requirements are driving the design ultimate load in the initial post-buckling region, where unanticipated coupling phenomena and global deformations could potentially reduce the anticipated ultimate strength of the structure. Currently, commercial packages, such as ABAQUS, do not provide the ability to include such non-linearities in composites. This could only be achieved by creating sub-routine programs and then connecting them to the software (Hu et al., 2006).

7.2.5 Channel-Section Strut with Negative Buckling Mode

Experiment

In accordance with the previous section the pre and post-buckling behaviour of the second undamaged channel-section strut tested is examined in regards to the strain variations with the applied load that were monitored at similar positions across the mid-length. In particular, buckling (P_C) occurred at 43 kN, as is evident from the deviation of the back-to-back longitudinal strain measurements in the inner and outer surfaces of the left stiffener (Figure 7.13), skin (Figure 7.14) and right stiffener (Figure 7.15). Buckling of the channel-section strut occurred once more in an asymmetric mode with a distinct longitudinal skew and three half-sinwaves. Nevertheless, the skin and stiffeners at the mid-section had deflected towards the negative direction; or otherwise the channel had buckled in the so called “negative mode” configuration, as shown in Figure 7.6(d).

The post-buckling path was mainly characterized by a stable increase in the deflections of the latter mode. However, at a loading level of 49 kN a sudden reversal of the compression and tensile surfaces occurred, as suggested by the abrupt changes in the longitudinal strains in Figures 7.13, 7.14 and 7.15. Immediately after the reversal, Euler

buckling occurred and the channel-section strut failed at approximately 51 kN with matrix and fibre fracture across the mid-length of the strut (Appendix C.1). The latter phenomenon will be examined with the aid of the finite element analysis.

FEA

Once more, prior to structural instability the predicted strains and buckling load (43 kN) are in very good agreement with the experimental. However, significant deviations are observed in the post-buckling region. In particular, in the finite element model at a loading level of approximately 45 kN a change in the stress gradient across the mid-length of the channel-section strut occurs. The change in the stress gradient in the skin suggests that it has shifted in a tensile region, while in the stiffeners to more compressive region. Nevertheless, Euler buckling is not observed at 65 kN, which is the ultimate structural load predicted by ABAQUS. At the ultimate load the mid-section has distorted into a negative mode and deflected towards the outer face of the skin (due to the increased deflections in that mode), but as has been illustrated and discussed in section 7.2.4 this does not result in an overall deformation in the Euler mode.

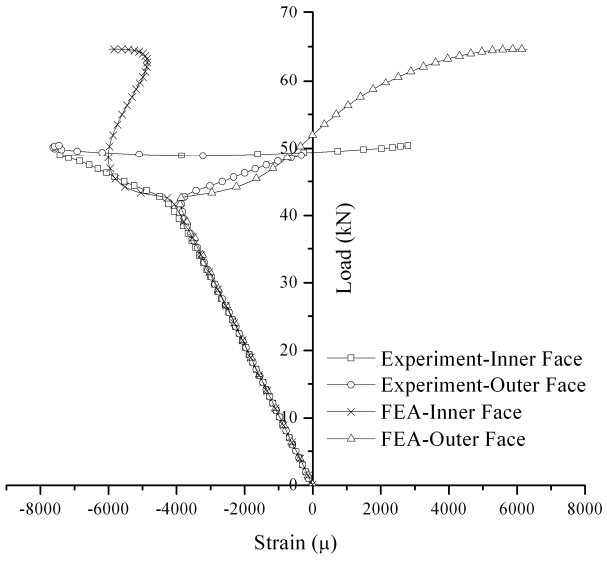

Figure 7.13. Comparison of the experimental and FEA variation of strain at the mid-point of the skin of the channel-section strut undergoing a “negative mode” of buckling.

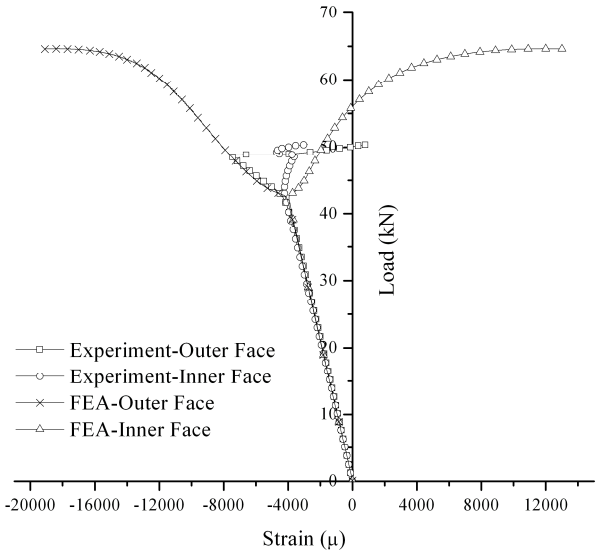

Figure 7.14. Comparison of the experimental and FEA variation of strain at the mid-point of the left stiffener of the channel-section strut undergoing a "negative mode" of buckling.

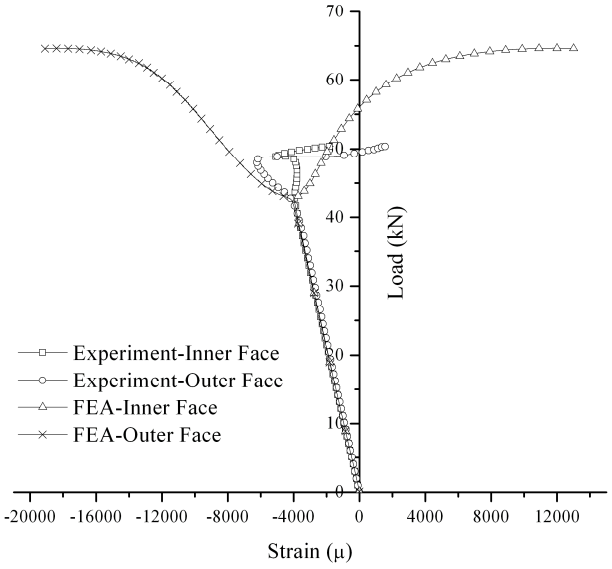

Figure 7.15. Comparison of the experimental and FEA variation of strain at the mid-point of the right stiffener of the channel-section strut undergoing a "negative mode" of buckling.

The disparity between the numerical and experimental strain variations with the applied compressive load may be attributed to the assumed imperfection in the first. Possibly, in the experiment the mid-point of the skewed anti-nodal line of the central buckling crest was not coincident with the mid-length of the strut. This may also be supported by the fact that the stress gradient in the skin is almost linear in the post-buckling region, and therefore, indicate that the mid-point of the strut is closer to the point of contra-flexure of the adjoined buckles, rather than the peak of the negative buckling crest. Consequently, when the negative buckling crest has deflected sufficiently so as to cause the whole cross-section to displace in the negative direction, a mode change occurs. This is suggested by the fact that the latter occurs at the exact load (49 kN) predicted by the FEA for the overall displacement of the cross-section, and may be attributed to the increased wave-length of one of the positive buckles towards the mid-length. It is more likely than not that the oscillating stresses at the mid-length caused delaminations and matrix cracking, and consequently, failure of the structure at that region soon after. The latter phenomenon is in agreement with Falzon and Hitchings (2003) that demonstrated that mode jumping promoted delamination onset and growth in stiffened composite panels.

7.2.6 Discussion on the Undamaged Channel-Section Struts

From a comparison of the results (both numerical and experimental), shown in the load versus end-shortening plot in Figure 7.16, it is evident that the undamaged channel-section strut undergoing a closing mode possesses a higher buckling load and ultimate strength in comparison to the opening mode (theoretically about 3% and 10% respectively). Therefore it logical to say that initial imperfections may actually contribute to the structural integrity of the component. Moreover, it is suggested that composite stiffened structures intended to operate in the post-buckling region would possibly be more tolerant if they were designed to fail under local buckling deformation.

Finally, it should be remembered that the latter test and FEA analyses were conducted for the M21/35%/268/T800S material system. The excellent correlation

though, of the experimental and numerical buckling loads invokes confidence in the utilization of the non-linear analysis results for the M21/35%/268/AS7 material system as benchmarks, with which the experimental structural buckling loads of the damaged channel-section struts will be compared. Due to the similarity of the plots of the two material systems, the ones obtained from the M21/35%/268/AS7 material system have not been provided. Nevertheless, for later comparisons, it should be pointed out that buckling for the latter system is anticipated to occur at 41 kN and 42 kN in the positive and negative mode respectively.

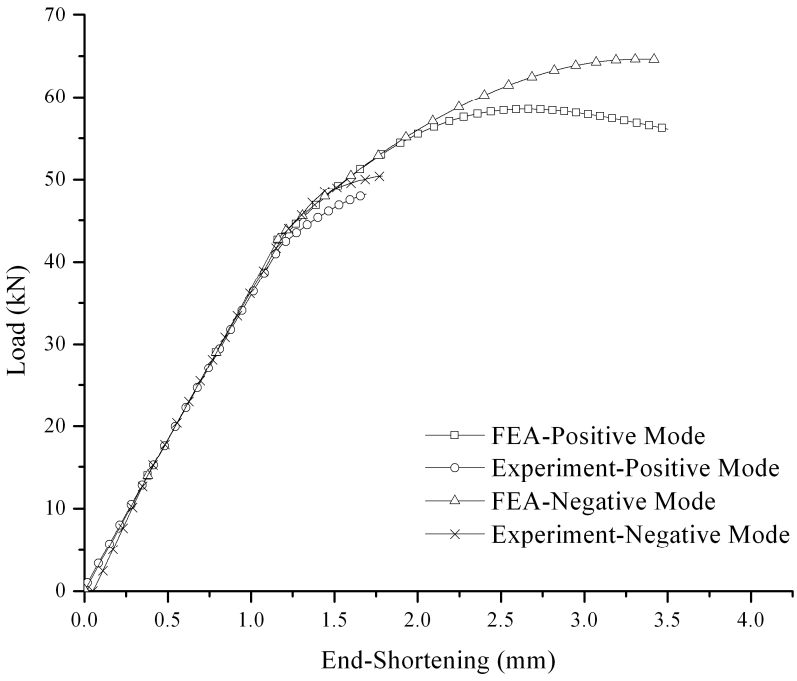

Figure 7.16. Comparison of the experimental and FEA stiffness for the undamaged channel-section struts.

7.3 Damaged Channel-Section Struts Results

The deformation history of the sublaminates is analysed by studying the variation of the out-of-plane deflection at the centre of their free surface with applied load. Snapshots of the buckling configurations of the supporting sublaminate are sketched at critical structural states. The sketches are based on the deformation history, strain measurements and observations during the experiment, but portray primarily the process rather than the exact configurations. In parallel, the pre and post-buckling behaviour of the channel-section strut are examined in regards to the variations of the longitudinal strains positioned across the mid-length (see Chapter 5) with the applied load. At critical states, the latter strains are correlated to the mode shapes. Generally, the numerical results are derived for the exact experimental positions.

It should be noted that during testing of the damaged channel-section strut with *n=2-Skin* delamination the laser distance calibrator was not able to record the deflections of the critical sublaminate. It was later realized that the high emissivity of the laminate body severely affected the ability of the laser beam to deflect back to the receiver. The latter problem was eliminated in the following tests by applying white paint in the region where the laser beam targeted. Likewise, at the time of testing of the damaged channel-section strut with *n=2-Stiffener* delamination the electromagnetic transducer was not available to record the deflections of the critical sublaminate. Therefore, for the latter specimens definite conclusions on the delamition buckling mode, and consequently its evolution, cannot be drawn solely by the deformation history of the supporting sublaminate. However, later comparisons with the finite element analysis elucidate some if not all aspects of delamination buckling.

7.3.1 Damaged Channel-Section Strut with n=2-Skin Delamination

Experiment

The deformation of the supporting sublaminate at the initial loading stage was characterized by small deflections towards the outer face (positive direction), which

were almost linearly related to the applied compressive load, Figure 7.17(a). Similarly, a linear relationship exists between the strain variation near the intersection of the supporting sublaminate and the applied load. However, at 32 kN an abrupt change in the direction of deflection of the thicker sublaminate occurred towards the outer surface (negative normal direction) of the laminate. This is also depicted in the sudden reduction of compressive strain in the outer face of the supporting sublaminate, as shown in Figure C.1 in Appendix C.2. This suggests the advance of bending moments (of opposing directions to its initial displacement) at the perimeter of the delaminated area, and therefore, an offset in the neutral axis of the delaminated plate. In accordance to Chapter 1, such offset typically arises from the increased out-of-plane deflection of the buckling sublaminate and depicts the evolution of an open mode of delamination buckling. It should be noted that the possibility of the abrupt phenomenon being related to delamination growth is eliminated by the unchanged axial stiffness of the structure (Figure C.11 in Appendix C.3). That is, the losses in energy caused by the onset of delamination growth are associated with abrupt changes in axial stiffness.

Even though the critical loading level cannot be defined, nevertheless taking into account the abrupt change in deflection and state of compressive strain of the supporting sublaminate the following possibilities may be considered: (1) Delamination buckling took place prior to 32 kN of compressive loading. At 32 kN the sublaminates buckled in an open mode. (2) Delamination buckling was restrained until 32 kN, Figure 7.17(a). Upon critical instability the sublaminates deflected suddenly towards the preferred positions (that is, in absence of the restraint mechanism), as shown in Figure 7.17(b).

At 42 kN the deflection of supporting sublaminate increased sharply in the positive direction. By examination of the variation of the longitudinal strains across the mid-length of the left stiffener (Figure 7.18), the skin (Figure C.1) and the delaminated right stiffener (Figure 7.19), it is observed that structural buckling (P_C^S) has occurred. This is clearly shown in the latter figures by the deviation of the back-to-back longitudinal strain measurements in the outer and inner surfaces of the laminate from the initial (pre-structural) buckling path.

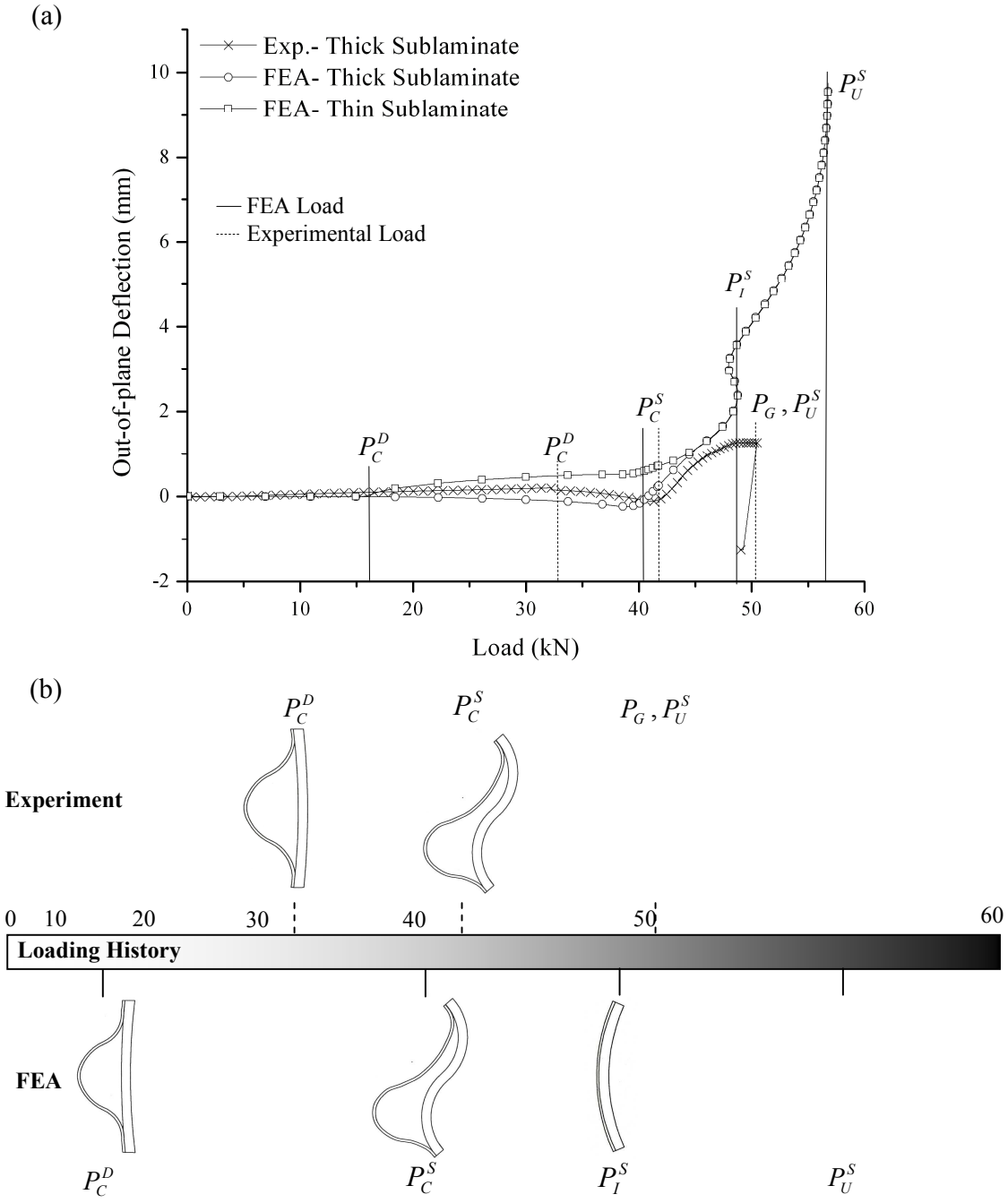

Figure 7.17 Buckling behaviour of the delaminated region of the damaged channel section strut with n=2-Skin delamination, (a) as depicted by the out-of-plane displacement of the centre of the sublaminates vs load plot and (b) sketched at critical values of the loading history.

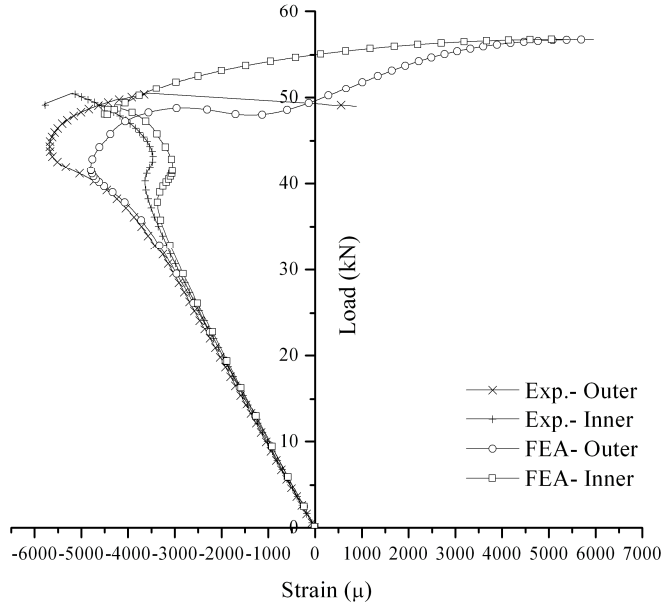

Figure 7.18. Load vs longitudinal strains at the mid-length of the edge of the left stiffener for the n=2-Skin channel-section strut.

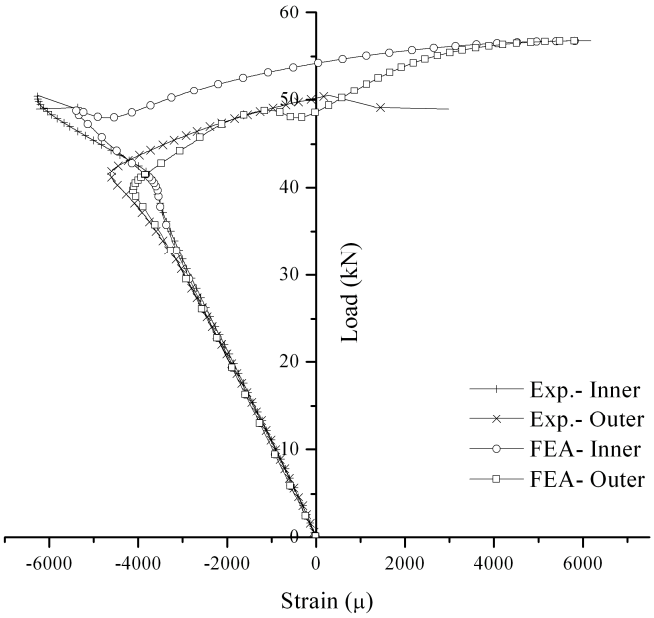

Figure 7.19. Load vs longitudinal strains at the mid-length of the edge of the right stiffener for the n=2-Skin channel-section strut.

For simplicity, the buckling behaviour of the damaged channel-section strut is examined in terms of the distortion of the mid-section. In particular, prior to structural buckling the distortion of the mid-section corresponded to a negative mode (as defined in Chapter 5). This was the direct result of the development of the open mode in the post-critical stage that caused the thicker sublaminate to deflect towards the outer face. As a consequence, deflections towards the inner face of the laminate were instigated in the stiffeners, Figures 7.18 and 7.19. Interestingly enough, the pre-described deformation of the structure (that is, prior to structural buckling) did not evolve into a buckling configuration similar to the undamaged strut with a negative mode of buckling.

By contrast, at structural buckling the closing configuration started to decay. This is both evident in the variation of the back-to-back longitudinal strains in the stiffeners (Figures 7.18 and 7.19) and the reversal in the direction of deflection of the supporting sublaminate. More specifically, at structural instability the damaged channel-section strut buckled in four half-sinewaves (2 longer and 2 shorter), as shown in Figure 7.20(a), in a manner such as the nodal-line between the 2 longer half-sinewaves to develop in the vicinity of the delamination perimeter. As a consequence, the sublaminates deflected in shear, Figure 7.17(b). That is, the reduced shear stiffness of the delaminated region nurtures the development of a nodal-line of the structural buckling mode, and in particular, at locations where the shear stiffness minimum is experienced. For the open delamination buckling mode these are located near the intersection of the sublaminates; a fact also supported by the post-buckling behaviour of the damaged strut that follows.

Hence, in the post-buckling region the stable increase in the amplitudes of the buckling crests was accompanied by a stable shift of the nodal-line between the two longer waves towards the mid-length of the strut. This portrays the transition of the positive longer crest towards the mid-length, and in accordance with Chapter 5, is attributed to the evolution of larger wavelengths in the positive buckling crests of the mode (that is, in comparison to the negative). At 44 kN, the shift of the nodal line, in addition to the skewed modal configuration caused the mid-section to distort in a

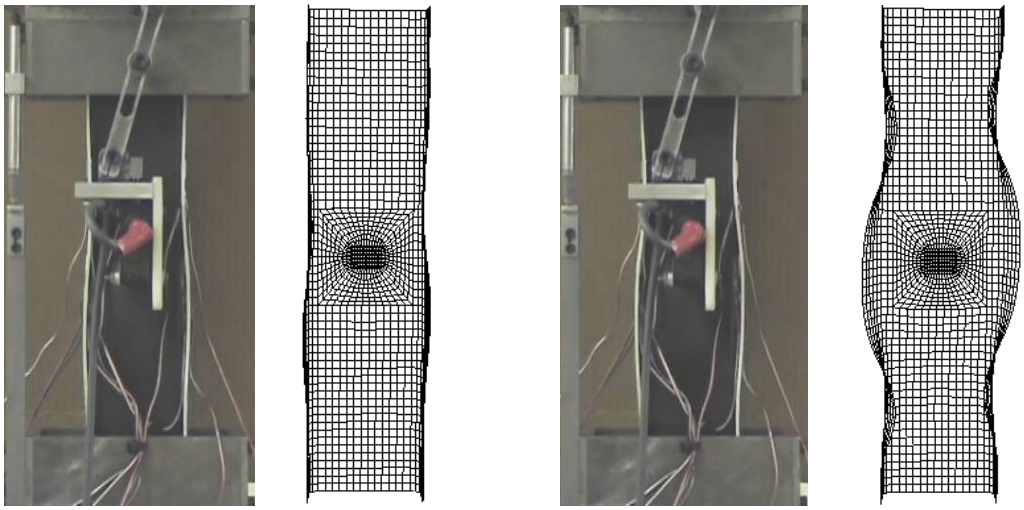

Figure 7.20. Illustration of the experimental and FEA buckling configuration of the n=2-Skin damaged channel-section strut (a), (b) in the initial post-buckling range and (c), (d) near ultimate loading conditions.

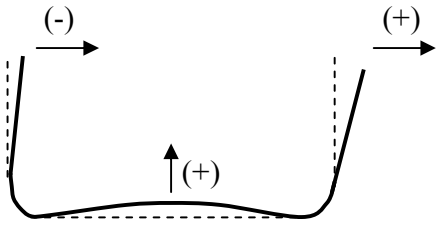

Figure 7.21. Illustration of the twisting mode in the mid-section of the channel-section strut, showing the positive and negative deflections of the plate segments.

manner such that the right and left stiffeners deflect towards the outer face of the second, as shown in Figure 7.21. For convenience reasons, from this point forward, the latter configuration of the section about the mid-length will be referred as the “twisting mode”.

The structural buckling mode continued to develop under this stable process, as is evident from the variation of strain with applied load at the mid-length of the left stiffener, Figure 7.18. At 49 kN, the positive buckling crest had developed enough so as to cause the mid-section to distort in a positive mode, Figures 7.17(a), 7.18 and 7.18. At this loading level, the structural mode is not readily identifiable, but it is believed to be between three and four half-sinewaves. Nevertheless, the stable evolution of the buckling mode was disrupted by a secondary instability at 51 kN. This is clearly seen by the drop in stiffness in the load versus end-shortening plot in Figure C.11 and by the sudden changes of the back-to-back longitudinal strains across or near the mid-length of the strut, Figures 7.18, 7.19 and C.1. The secondary instability manifested a mode jump to a structural configuration equivalent to the one observed in the undamaged channel-section strut undergoing Euler (global) buckling, Figure 7.20(c). At the mode jump, delamination growth occurred that propagated catastrophically and transversely to the applied load and across the stiffeners (Appendix C.1). Whether the mode jump instigated the latter growth, or the opposite phenomenon occurred, cannot be easily determined. Nevertheless, they are both plausible scenarios.

FEA

Hence, at the initial loading stage the FEA analysis predicts a similar experimental deformation to that of the supporting sublaminate, as is evident from their out-of-plane displacements in Figure 7.17(a). Nevertheless, it is apparent that the monitored deflection in the experiment slightly deviates from the predicted one. This is probably attributed to the disparity of the initial imperfection in the specimen and the one assumed in the finite element model. It is noted that in the analysis of all the damaged channel-section struts the first critical structural mode was considered for convergence reasons. Moreover the amplitudes selected, depicted the lowest possible ones in order

for convergence to occur. In general, the latter amplitudes varied between 10^{-3} and 0.2×10^{-4}, and therefore, in the following presentations of the analyses of the remaining damaged channel-section struts the imperfection amplitudes are to be assumed within this range.

It is of worth to note that in the damaged specimen a local imperfection was imposed in the thicker sublaminate, as a result of the lamination process, which would normally be expected to cause deflections of the thicker sublaminate in the opposite direction to the one observed. This may suggest that at least until delamination buckling occurs the dominant imperfection in the specimen is the one that corresponds to the whole structure. However, this may also be dependent on the thickness of the thicker sublaminate and the amplitudes of the interacting imperfections, an issue which will be examined in due course. Despite best efforts to introduce an imperfection which exactly represented the one imposed by the inclusion of the PTFE, it was not possible. This was primarily due to element distortion during the mesh generation, and consequently, convergence difficulties of the solution during the analysis.

Delamination buckling occurs at 16 kN with a smooth separation of the sublaminates. The delamination buckling mode is a typical thin-film configuration, Figure 7.17(b), as is evident from the out-of-plane deflection versus load plot in Figure 7.17(a) and the strain-gauge measurement at the edge of the outer face of the thicker sub-laminate (that is, 10mm from the delamination centre), Figure C.1. In either plot it is observed that in the initial post-critical state the supporting sublaminate is not greatly affected by buckling of the critical sublaminate. Nevertheless, the increasing deflections of the critical sublaminate eventually instigate an open mode, and the supporting sublaminate deflects in the opposite direction, Figure 7.17(a).

This was also observed experimentally, but at much higher loading. Therefore, it is concluded that in the experiment delamination buckling occurred at 32 kN, which corresponds to the second scenario presented in the analysis of the experimental results. It is believed that the latter disparity arises from the initial imperfection of the skin that

imposes bending moments in the sublaminates that counteract the compressive load applied to them, Figure 7.22. To an extent this is in agreement with Thomson and Scott (2000) who suggested that delamination buckling is dependent upon the compliance of the supporting plate.

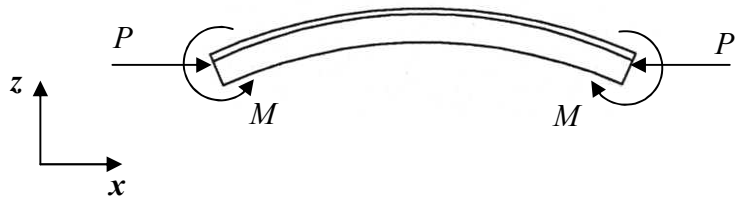

Figure 7.22. Illustration of the forces and moments acting at the delaminated region prior to delamination buckling as a result of the deformation of the surrounding plate.

Similarly to the experiment, the evolution of an open mode of delamination buckling along the post-critical path induced deflections in the damaged structure so as to cause the mid-section to distort in a negative mode until structural instability. The predicted structural buckling load is in good agreement with the experimental (40 kN). The deviation is within 4% and probably arises due to the aforementioned discrepancies in delamination buckling. Likewise, the predicted structural buckling mode, Figure 7.20(b), correlates quite satisfactorily to the experimental and the shear buckling mode of the sublaminates is verified, Figure 7.17(b).

Furthermore, the analysis is able to capture the monitored behaviour of the damaged strut for almost the entire post-buckling path, and therefore, a detailed description of the latter is avoided for reasons of repetition. This is evident in the qualitative similarity of the predicted variations of the longitudinal strains with applied load across (or near) the mid-length to the experimental. Quantitatively, though, some small deviations arise. For example, in Figures 7.18, 7.19 and C.1 the longitudinal strains in the analysis are trailing in comparison to experimental, as a result of structural buckling occurring at slightly

lower levels of loading. The biggest deviation between the monitored and predicted longitudinal strains is observed at 10mm from the centre of the supporting sublaminate (Figure C.1). This is more likely than not also related to the imperfection imposed by the PTFE patch in the thicker sublaminate, an argument further supported by the deviation of the stress gradients prior to structural buckling.

The secondary instability that leads to a mode jump into an Euler (global) configuration, Figure 7.20(d), is calculated at 49 kN. The somewhat reduced level of loading in correlation to the experimental is directly proportional to the one observed between the predicted and monitored structural buckling loads. More importantly, the mode-jump in the analysis implies that the instability in the structure was responsible for the observed delamination growth in the experiment and not vice-versa. Finally, the deviations that arise in the delaminated region after the secondary instability, Figures C.1 and 7.17(a), may be attributed to delamination growth. Contrary to the analysis, where the latter measurements depict a cylindrical deformation of the sublaminates in full contact [Figure 7.17(b)], the ones measured in the experiment suggest an opening mode, and therefore, a Mode I fracture. Nonetheless, in the absence of material failure, material nonlinearity and delamination growth the analysis predicts ultimate levels of loading (P_U^S) at 57 kN.

7.3.2 Damaged Channel-Section Strut with n=3-Skin Delamination

Experiment

Initially the deflections of the sublaminates were small, but gradually increased with loading in an almost linear manner. However, their relative deflection was insignificant, which suggested a uniform deformation of the sublaminates; or otherwise, no separation. The latter scenario was maintained until delamination buckling (P_C^D) occurred at 34 kN. The critical state was marked by a smooth separation of the sublaminates, as shown in Figure 7.23(a), which nevertheless continued to deflect in the same positive direction. As is evident from the strain measurement at its free-surface in Figure C.2 and the

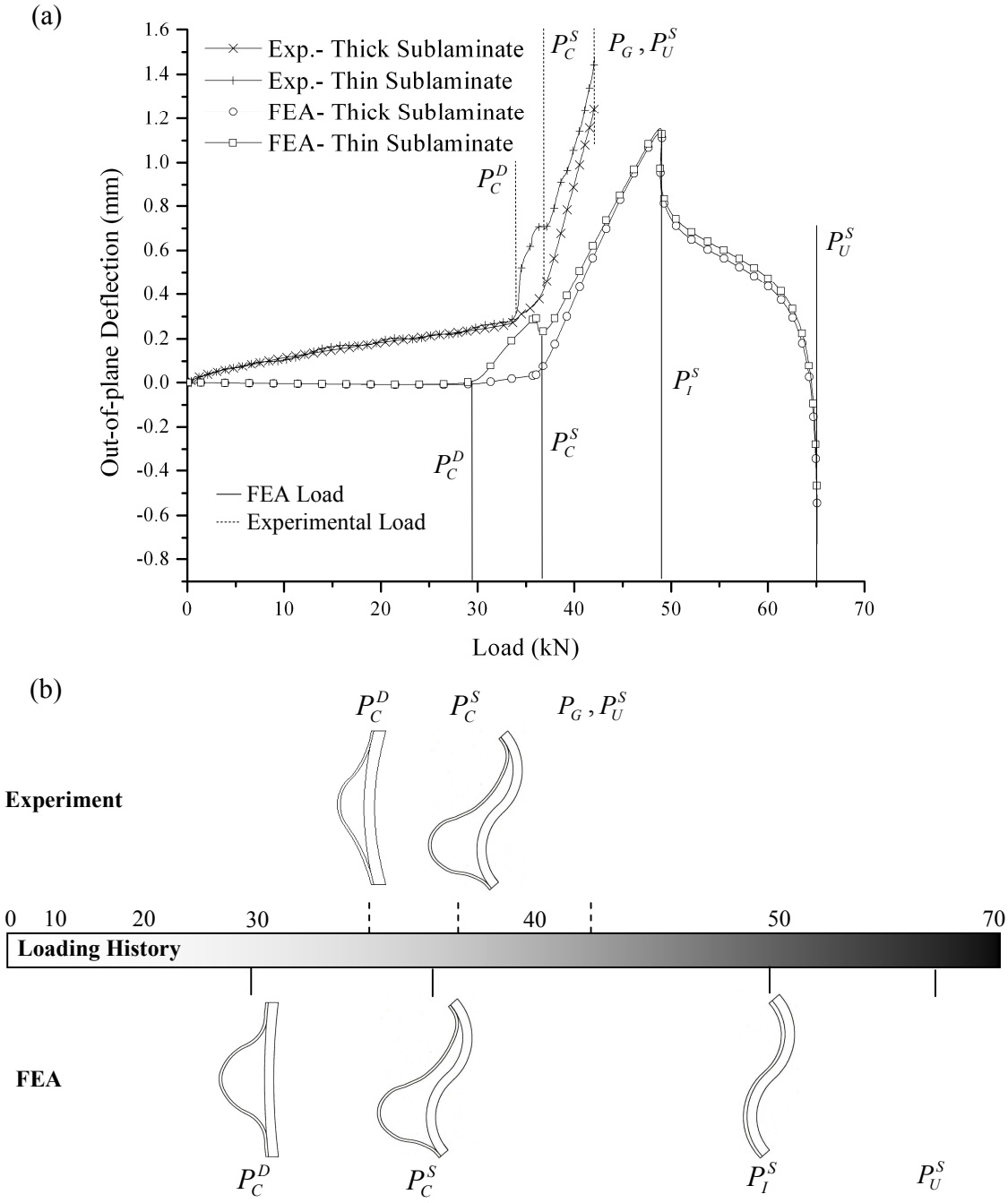

Figure 7.23. Buckling behaviour of the delaminated region of the damaged channel section strut with n=3-Skin delamination, (a) as depicted by the out-of-plane displacement at the centre of the sublaminates vs load plot and (b) sketched at critical values of the loading history.

deformation history [Figure 7.23(a)], buckling of the critical sublaminate affected the deformation of the supporting sublaminate. The initial post-critical state was characterized by sharp and rather moderate deflections of the critical and supporting sublaminate respectively that corresponded to the development of a closed buckling configuration. The latter configuration was maintained until structural instability.

Structural buckling (P_C^S) occurred at 36 kN. This was manifested in the sharp increase in the deflections of the sublaminates [Figure 7.23(a)], but more importantly, in the deviation of the back-to-back longitudinal strains across the mid-length of the left stiffener (Figure 7.24), the delaminated skin (Figure C.2) and right stiffener (Figure 7.25). Structural buckling occurred in a skewed asymmetric mode composed by two long half-sinewaves, as shown in Figure 7.26(a). According to Figures 7.23, 7.24 and 7.25, the aforementioned waves evolved across the length of the channel-section strut in such a manner so as to cause the mid-section to deform in the so called “twisting mode”. The proximity of the nodal-line to the delamination perimeter suggests that the sublaminates deflected in shear, Figure 7.23(b). As stated in the previous section, this is promoted by the reduced shear stiffness of the delaminated region, which in conjunction with the skewness of the structural buckling mode produces the aforementioned distortion in the mid-section.

The post-buckling path was mainly characterized by a stable development of the evolved structural buckling mode. The strain variations with applied load across the mid-length of the strut, and in particular, the exponential strains at the mid-length of the left stiffener imply that the tendency of the positive buckling crest to occupy the mid-section of the strut. However, at 40 kN the process was reversed and the distortion of the mid-section in the “torsional mode” was enhanced; as is more evident from the sudden changes of the back-to-back stress longitudinal strains at the mid-length of the left stiffener, Figure 7.24. Soon after (42 kN) failure occurred under excessive delamination growth that propagated transversely to the applied load and across the stiffeners (Appendix C.1).

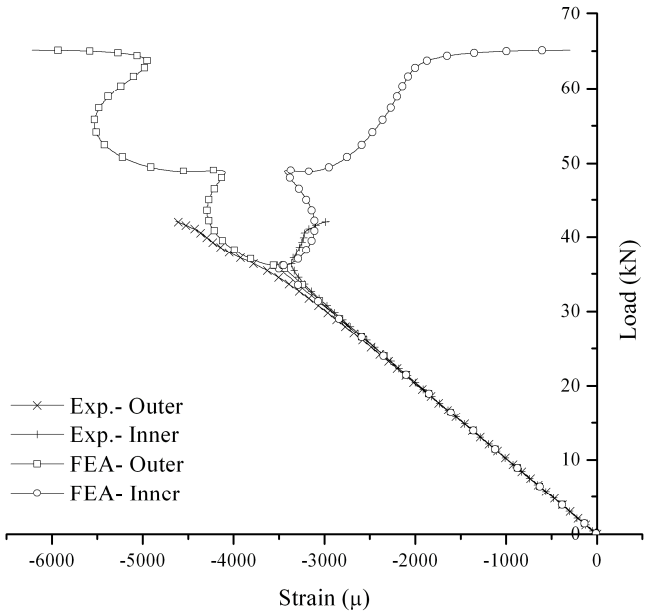

Figure 7.24. Load vs longitudinal strains at the mid-length of the edge of the left stiffener for the n=3-Skin channel-section strut.

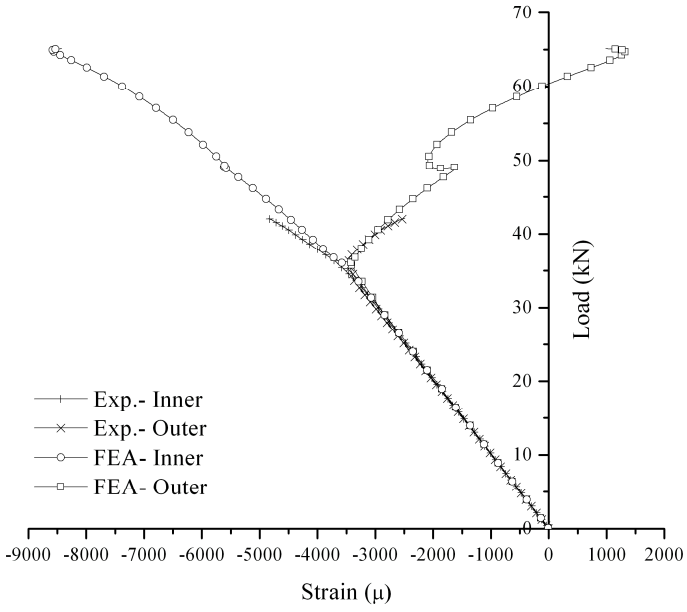

Figure 7.25. Load vs longitudinal strains at the mid-length of the edge of the right stiffener for the n=3-Skin channel-section strut.

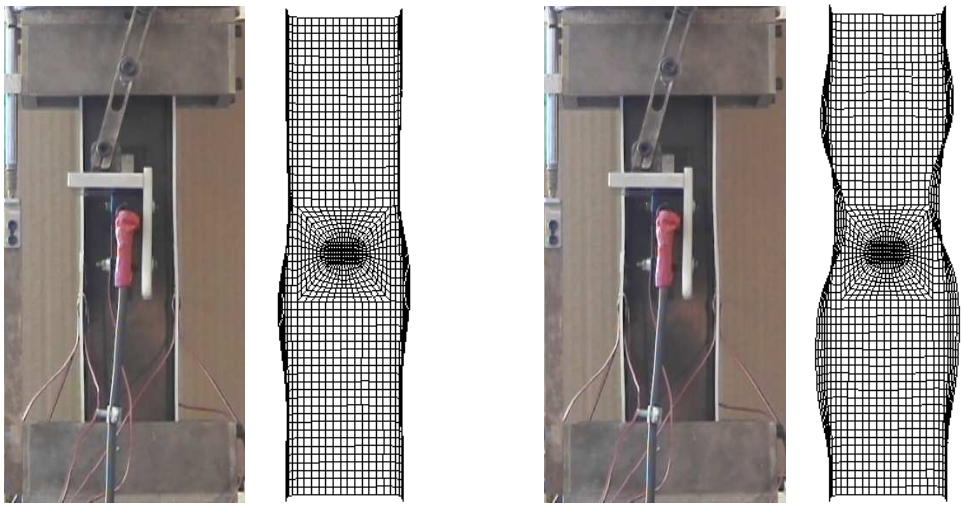

(a) (b) (c) (d)

Figure 7.26. Illustration of the experimental and FEA buckling configuration of the n=3-Skin damaged channel-section strut (a), (b) in the initial post-buckling range and (c), (d) near ultimate loading conditions.

FEA

Delamination buckling (P_C^D) occurs around 30 kN with a smooth separation of the sublaminates, as shown in Figure 7.23(a). The buckling mode approximates the thin-film configuration, Figure 7.23(b), as is evident in the deformation history of the sublaminates [Figure 7.23(a)] and the predicted strain with applied load plot for the supporting sublaminate (Figure C.2). In the post-critical path the sublaminates deflect in a closed mode. However, the predicted buckling behaviour of the sublaminates does not fully represent the condition monitored in the experiment. This is also expressed in terms of the critical load (P_C^D), which is estimated to be 11% lower than the experimental.

The reasoning for the latter discrepancies is attributed to the imperfection amplitude and configuration incorporated in the finite element model. More specifically, in Figure 7.23(a) it is evident that the monitored deflections of the sublaminates reflected an overall deformation of the delaminated plate, which was induced from zero loading

conditions by the presence of an overall imperfection in the strut. In contrast, the imperfection assumed in the analysis does not produce notable pre-critical deformation in the delaminated plate. The sublaminates sustain a field of plane strain with almost no out-of-plane deformation prior to delamination buckling.

In accordance with the previous section, though, the pre-critical deformation reduces the compliance of the structure to delamination buckling. Therefore, in comparison with the finite element analysis, in the experiment the latter mechanism is restrained until higher loading levels are attained. As a consequence, at critical instability the sublaminates buckled directly in the post-critical configuration (closed mode) that would have evolved theoretically at the particular loading level in the absence of the overall imperfection. The quantitative differences observed between the monitored and predicted post-critical configurations are also related to the pre-critical deformation of the delaminated plate in the first.

The transition of the buckling configuration of the sublaminates from a closed mode to a shearing mode, Figure 7.23(b), is marked by a sharp change in the deflection of the critical sublaminate just before structural buckling, a phenomenon which was also observed experimentally. The predicted structural buckling load (P_C^S) is in excellent agreement with the experimental at 36 kN. Likewise, a satisfactory correlation is observed in terms of the structural buckling mode, Figure 7.26(b). The structure buckles in two long half-sinewaves in a manner that causes the mid-section to distort in the so called “twisting mode”.

Generally, in the post-buckling region small deviations are observed between the monitored and predicted strains across (or near) the mid-section of the strut in Figures 7.24, 7.25 and C.2. These are more likely than not related to a small departure of the calculated position of the nodal-line in respect to the one evolved experimentally. By comparison of the experimental and numerical stress gradients across the mid-length of the strut it is suggested that in the experiment the nodal line is generated slightly closer to the mid-length. Nonetheless, the finite element analysis offers the opportunity to

investigate aspects of the post-buckling behaviour of the damaged structure that were not particularly distinct in the experiment due to the early failure.

In particular, from the strain variations with applied load at the mid-section of the strut it is shown that similar to the experiment the structural buckling mode has the tendency to precipitate in a way such that the mid-section undergoes a positive mode of distortion; or otherwise the positive buckling crest occupies the mid-section. At 49 kN the process is interrupted by a secondary instability. The structure releases energy (Figure C.12) by jumping to a mode composed by three half-sinewaves, Figure 7.26(d). The waves evolve along the length of the strut in a manner such that distortion of the mid-section in a torsional mode is enhanced, whilst the sublaminates deflect uniformly in shear [Figure 7.23(b)]. Such an abrupt enhancement of the torsional mode in the mid-section was also observed experimentally, but at much lower level of loading. This may have been induced by some sort of damage in the structure.

More importantly, taking into account that Euler buckling in the *n=2-Skin* damaged strut was instigated at about the same level of loading by a secondary instability in the structure, it is concluded that the sublaminates fashioned by the particular level of delamination cannot escape the shear configuration, and therefore, the structure jumps to a global mode of deformation in which the shear buckling configuration is preserved. At 55 kN it becomes evident that the latter mode has similar attributes to the one described in the undamaged channel-section with negative mode of buckling, Figure 7.9. By contrast to the latter case, the mid-section distorts in torsion, and therefore, from this point forward the latter mode of global deformation will be referred as “flexural-torsional”. At 65 kN ultimate loading is attained.

7.3.3 Damaged Channel-Section Strut with n=5-Skin Delamination

Experiment

At the initial loading stage the sublaminates deflected uniformly towards the inner face of the laminate and are almost linearly related to the applied load. At 18 kN the critical sublaminate separated smoothly from the initial path of deflection, Figure 7.27(a). However, the latter process does not necessarily imply delamination buckling. It is believed that P_C^D occurred at 31 kN, when a sudden enlargement in the deflections of the sublaminates increased their relative distance. The latter phenomenon is attributed to the sudden shift of the neutral axis towards the buckling sublaminate, which effectively enhanced the bending moments formulated at the supporting sublaminate during its pre-critical deformation. Thus, at critical instability the sublaminates buckled in an open mode. This mode was amplified in the post-critical region.

Structural buckling (P_C^S) occurred at 37 kN, as is evident from the deviation of the back-to-back longitudinal strains measured across or near the mid-length of the damaged strut, Figures 7.28, 7.29 and C.3. In the deformation history this is depicted by the sharp change in the direction of deflection of the critical sublaminate. Structural buckling occurred in a skewed asymmetric mode that was composed of two long half-sinewaves, as shown in Figure 7.30(a). The proximity of the nodal-line to the delamination perimeter instigated distortion of the mid-section in a "twisting mode", Figures 7.27(a), 7.28 and 7.30, and deformation of the sublaminates in a shearing mode, Figure 7.27(b).

Initially, the post-buckling behaviour of the damaged structure was characterized by the stable evolution of the aforementioned mode. The amplitudes of the buckling crests increased as the nodal-line shifted in a manner such that the positive buckling crest occupied the mid-length of the strut. As for the previous damaged strut, this is implied by the strain variations with applied load at the mid-section of strut, and more evidently, by the back-to-back strain-gauges on the left stiffener (Figure 7.28). In particular, the

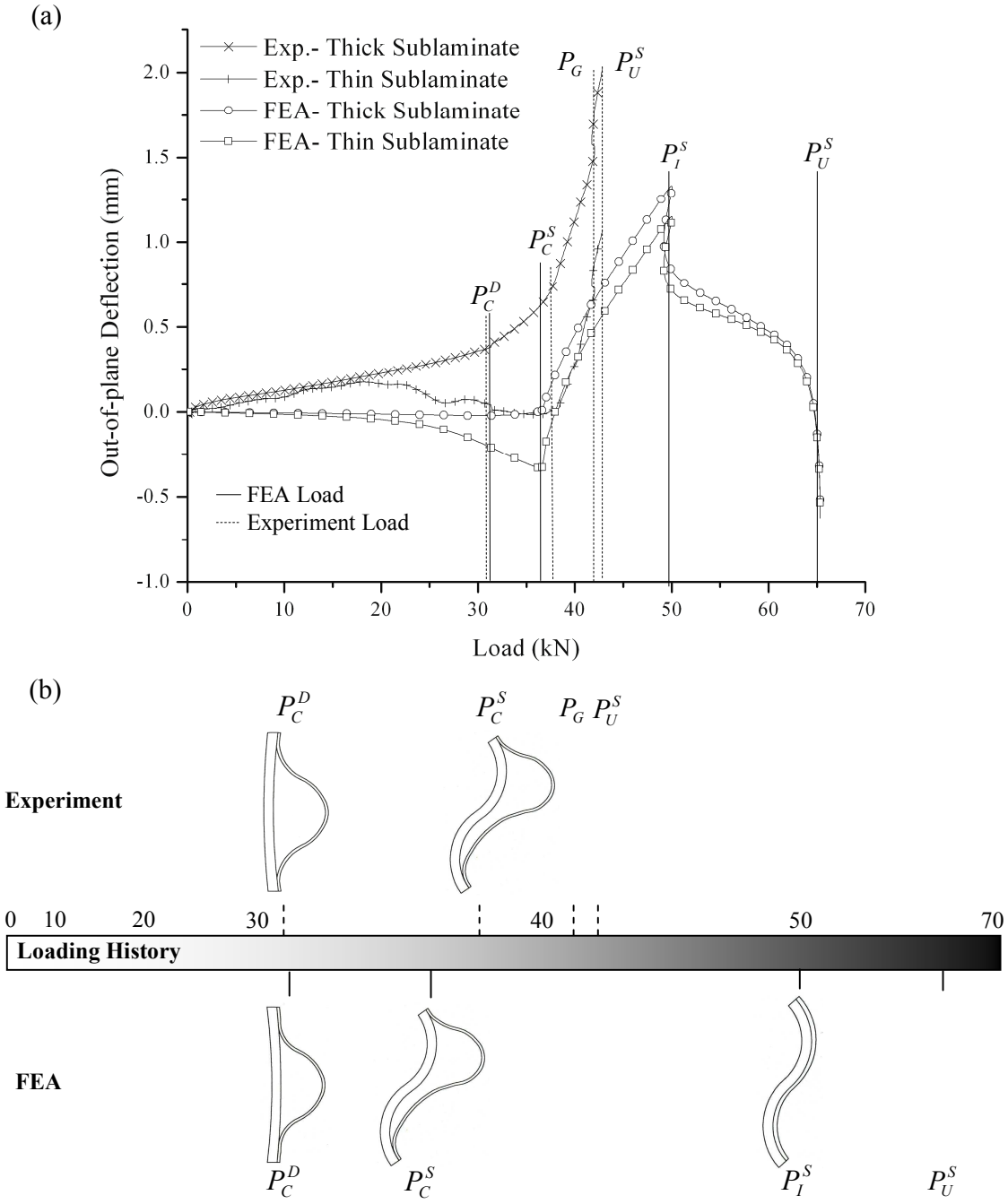

Figure 7.27. Buckling behaviour of the delaminated region of the damaged channel-section strut with n=5-Skin delamination, (a) as depicted by the out-of-plane displacement at the centre of the sublaminates vs load plot and (b) sketched at critical values of the loading history.

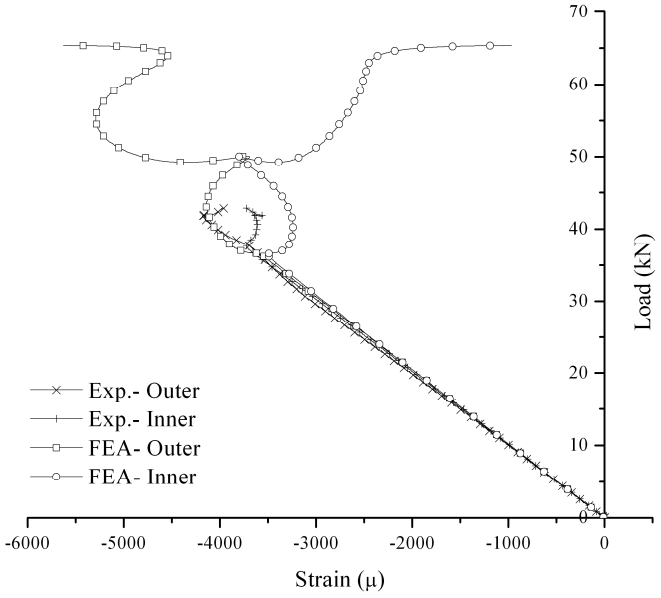

Figure 7.28. Load vs longitudinal strains at the mid-length of the edge of the left stiffener for the n=5-Skin channel-section strut.

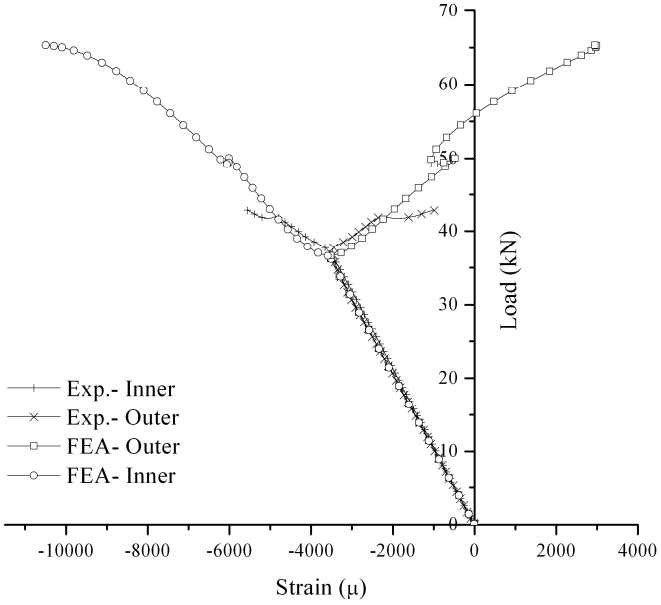

Figure 7.29. Load vs longitudinal strains at the mid-length of the edge of the right stiffener for the n=5-Skin channel-section strut.

reversal of the back-to-back stress gradients in the left stiffener at 40 kN undeniably portray the distortion of the mid-section in a positive mode. Nevertheless, the mode transition of the mid-section (that is, from the twisting to the positive mode) was soon interrupted by a secondary instability at 41 kN. Whether the secondary instability arises from structural instability or delamination growth is an issue which will be examined with the aid of the finite element analysis. Nonetheless, with reference to Figures 7.28, 7.29 and C.3 it appears that the buckling mode jumped to a more advanced state. Finally, failure occurred at 42 kN under excessive delamination growth that propagated catastrophically and transversely to the applied load and across the stiffeners (Appendix C.1).

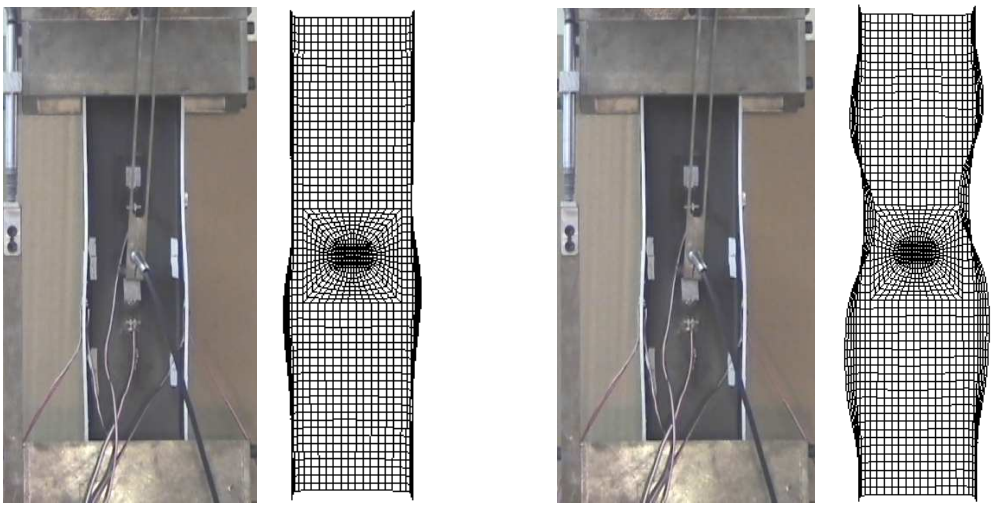

(a) (b) (c) (d)

Figure 7.30. Illustration of the experimental and FEA buckling configuration of the n=5-Skin damaged channel-section strut (a), (b) in the initial post-buckling range and (c), (d) near ultimate loading conditions.

FEA

In the initial loading stage the analysis predicts almost a zero out-of-plane deformation of the sublaminates. As the applied load increases very small deflections in the critical sublaminate arise towards the outer face of the laminate. Nevertheless, the

onset of sublaminate separation is considered to be the loading point of 19 kN, where the critical sublaminate starts to deflect exponentially to the applied load Figure 7.27(a). This approximates well the experimental point of separation of 18 kN. In either case the gradual separation of the sublaminates is attributed to the local imperfection present in the critical layer. It is noted that in the analysis the first eigenmode was utilized in order to represent the imperfection imposed by the PTFE patch.

Contrary to the experiment though, characteristics of delamination buckling cannot be traced either in the deformation history or the predicted strain with applied load plot for the supporting sublaminate in Figure C.3. However, from observation of the deformed shapes plotted in ABAQUS over the loading history of the damaged structure it is suggested that delamination buckling, P_C^D, occurs at 31 kN approximately. Even though this is in good agreement with the experimental load, nevertheless it is provided with caution due to the method of derivation.

At critical instability the sublaminates buckle essentially in a thin-film configuration [Figure 7.27(b)]. As evident in the deformation history in Figure 7.23(a), the deflection of the supporting sublaminate remains in a plateau of almost zero displacement until structural buckling. Furthermore, the stress gradient of the outer face of the supporting sublaminate does not appear to deviate from the linearized pre-critical path (Figure C.3). However, a closer inspection of the deformation history reveals very small deflections of the supporting sublaminate towards and away from the critical one, before and after critical instability respectively. This implies sublaminates have a tendency to deform into an open mode at critical instability. More importantly, it is in line with the experimental buckling behaviour, in which the presence of the overall imperfection enhanced the predisposition of the sublaminates to deflect into an open mode.

Structural buckling, P_C^S, occurs at 36 kN, which is 3% lower than the experiment. The small deviation may be related to the aforementioned differences in delamination buckling. In similarity with the experiment, the structure buckles in a skewed asymmetric mode composed of two long half-sinewaves, Figure 7.30(b). The mode

evolves in a manner that causes the mid-section to distort in the “twisting mode” and the sublaminates to deflect in shear [Figure 7.23(b)]. The post-buckling path is qualitatively similar to the one observed in the experiment, as is evident from the similar trends in the post-buckling variation of strain with apllied load across or near the mid-section of the strut, Figures 7.24, 7.25 and C.2. The mode progresses as the nodal-line shifts in a direction that enhances the distortion of the mid-section in a positive mode. Quantitative differences are primarily attributed to a small mismatch between the monitored and predicted position of the nodal-line and structural buckling load.

The analysis predicts a similar post-buckling behaviour to the *n=3-Skin* damaged strut, and therefore, a detailed description is avoided for reasons of repetition. Briefly, a secondary instability occurs at 50 kN and in a mode of three half-sinewaves, Figure 7.30(d). This induces global deformation in the strut in the flexure-torsional mode and ultimate loading is attained at 65 kN. Thus, it is concluded that in the experiment the secondary instability was initiated by delamination growth. This is supported not only by the experimental and numerical disparities in the loading levels, upon which the secondary instabilities occurred, but also by the subsequent modes of buckling. Contrary to the analysis, the secondary instability did not affect the order of the buckling mode, but perhaps accelerated the evolution of it.

7.3.4 Damaged Channel-Section Strut with n=6-Skin Delamination

Experiment

At the initial loading stage the sublaminates deflected uniformly towards the inner face of the strut and were almost linearly related to the applied compressive load, Figure 7.31(a). At 27 kN delamination buckling (P_C^D) occurred with a rather smooth separation of the critical sublaminate from the initial deflection path. In accordance with the deformation history [Figure 7.31(a)] and the strain variation with applied load at the free face of the supporting sublaminate (Figure C.4), the sublaminates buckled in a thin-film buckling mode [Figure 7.31(b)]. In the post-critical path the latter transformed to an open mode of delamination buckling.

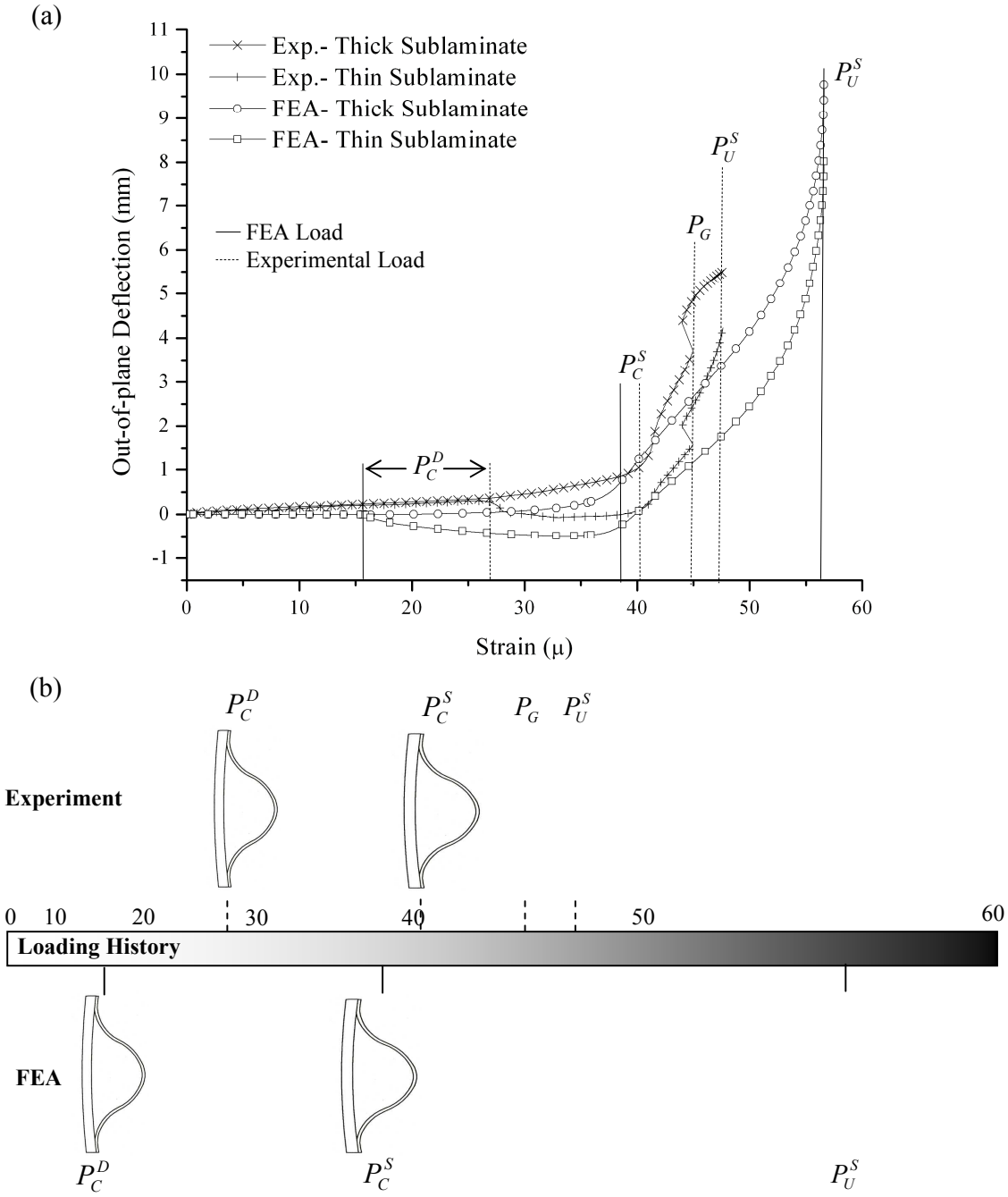

Figure 7.31. Buckling behaviour of the delaminated region of the damaged channel-section strut with n=6-Skin delamination, (a) as depicted by the out-of-plane displacement at the centre of the sublaminates vs load plot and (b) sketched at critical values of the loading history.

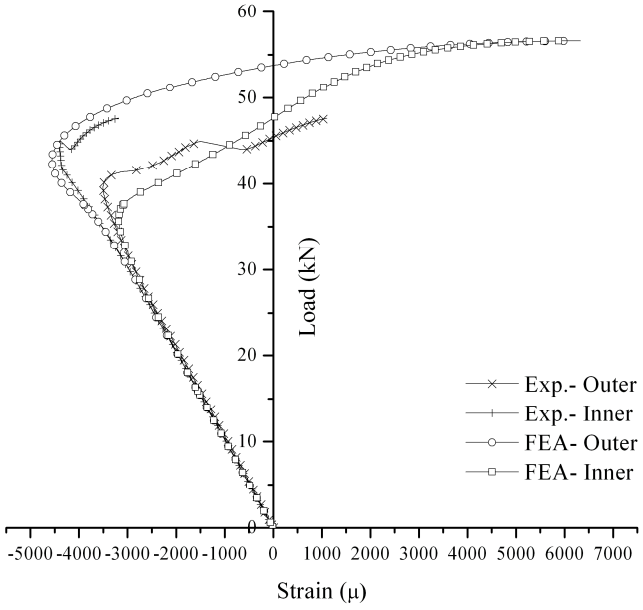

Figure 7.32. Load vs longitudinal strains at the mid-length of the edge of the left stiffener for the n=6-Skin channel-section strut.

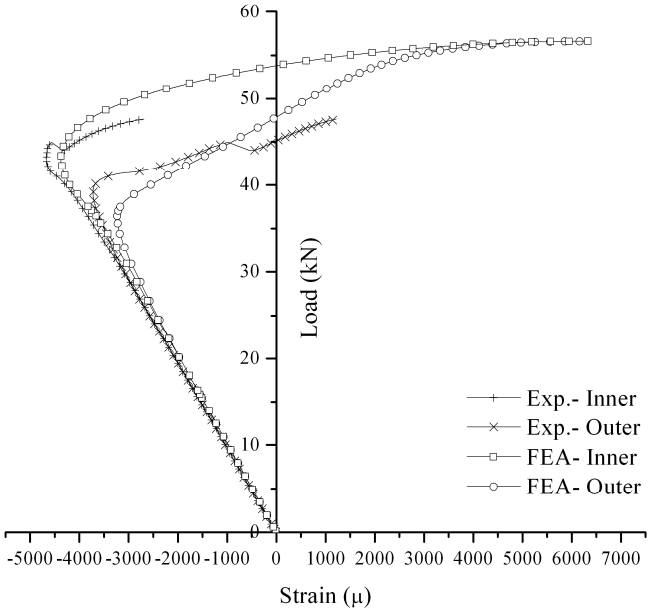

Figure 7.33. Load vs longitudinal strains at the mid-length of the edge of the right stiffener for the n=6-Skin channel-section strut.

At 40 kN structural buckling (P_C^S) occurred, as is evident from the deviations of the back-to-back strains across or near the mid-section, shown in Figures 7.32, 7.33 and C.4. The damaged structure buckled in three half-sinewaves and similarily to the undamaged channel-section strut with positive mode of buckling [Figure 7.34(a)]. This resulted in the amplification of the open mode of the sublaminates that was suspended just before structural instability, by the uniform deflection of the sublaminates in the positive direction, Figure 7.31(a). The initial post-buckling path was characterized by a stable development of the structural buckling mode.

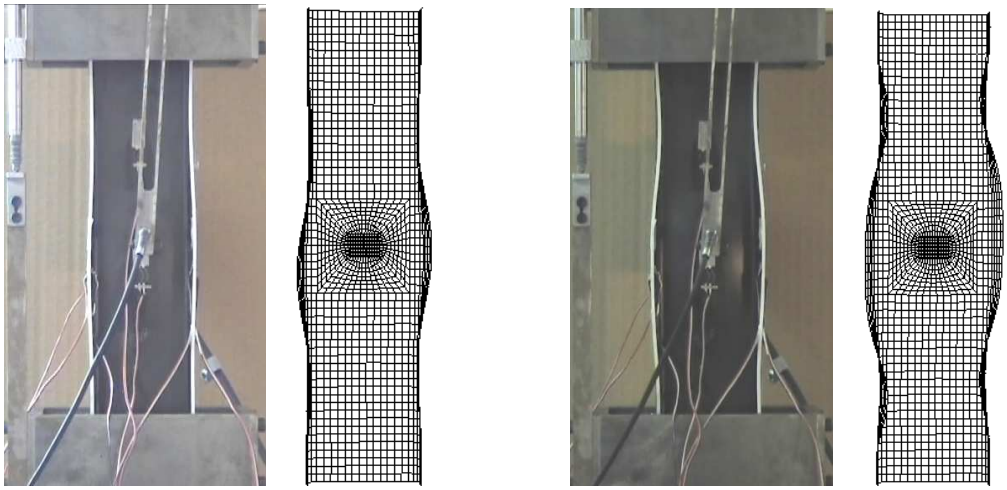

(a) (b) (c) (d)

Figure 7.34. Illustration of the experimental and FEA buckling configuration of the n=6-Skin damaged channel-section strut (a), (b) in the initial post-buckling range and (c), (d) near ultimate loading conditions.

In accordance with the undamaged strut, the structural buckling mode developed in a stable manner, which instigated a global mode of deformation (i.e Euler) at 43 kN. This is evident from the transition of the back-to-back strains in the skin and stiffeners into a more tensile region. However, the process was interrupted at 45 kN by a secondary instability in the structure. Nevertheless, the latter did not affect qualitatively the structural buckling mode, as is evident in Figures 7.32, 7.33 and C.4, which continued to develop rapidly in an Euler configuration, Figure 7.34(c). Therefore, it is concluded that

the energy released (Figure C.14) was the result of delamination growth, which was soon arrested by the stabilizing presence of the stiffeners (discussed in more detail in Chapter 1). Due to the opening mode of the sublaminates in the post-buckling path it is logical to say that the strain energy release at the crack tip was primarily expended in fracture in Mode I. The validity of the argument raised will be examined with the aid of finite element analysis. Finally, structural failure occurred at 48 kN with excessive delamination growth that propagated catastrophically and transversely to the applied load and across the stiffeners (Appendix C.1).

FEA

In the finite element analysis delamination buckling (P_C^D) occurs at 16 kN, which is significantly lower than the experimental critical load. In accordance with the previous sections the latter disparity is related to the standard deviation (observed for all the channel-section struts with skin delamination) between the monitored and predicted deformation of the delaminated plate prior to critical instability. In turn, this originates from the assumed overall imperfection in the analysis, which contrary to the experiment does not induce notable deformation in the delaminated plate. The sublaminates sustain plane strain conditions until critical instability occurs, Figure 7.31(a).

Nonetheless, the numerical analysis captures the thin-film buckling configuration, Figure 7.31(b), and its subsequent transition to an open mode. Structural buckling, P_C^S, takes place at 38 kN, which is approximately 5% lower than the experimental value. As stated in the previous section, such small deviations could be related to the disparities that arise in delamination buckling, and subsequently, to the sources that exhibit a prominent influence on the latter (i.e. imperfections). This is an issue which will be investigated in the next section by reexamination of the current damaged strut, but with a more profound local imperfection in the delaminated region.

Similar to the experiment, and the undamaged channel-section strut with positive buckling mode, the structure buckles in a skewed asymmetric mode composed of three half-sinewaves, Figure 7.34(b). Furthermore, the initial post-buckling path correlates

quite agreeably with the one monitored in the experiment. The small deviations observed in the longitudinal strains across the mid-section of the strut, Figures 7.32, 7.33 and C.4, are mainly attributed to the underestimation of the structural buckling load at the analysis. However, no secondary instability occurs in the analysis in any stage of the post-buckling process. The mode evolves in an Euler buckling configuration, Figure 7.34(d), and ultimate loading conditions are reached at 57 kN. This supports the argument raised in the presentation of the experimental results that secondary instability was instigated by delamination growth. Finally, it should be noted that the slightly accelerated evolution of Euler buckling in the experiment (that is, in comparison to the FEA) probably resides in material non-linearity.

.

7.3.5 Damaged Channel-Section Strut with n=6-Skin Delamination and 0.25mm PTFE Patch

Testing of *n=6-Skin* damaged channel-section strut was repeated in order to study the influence of the overall imperfection in delamination buckling, and subsequently, in structural buckling. This was achieved by embedding a thicker PTFE patch (0.25mm) in the structure in order to generate increased amplitude of local imperfection in the critical sublaminate. Thus, as shown in Figure 7.35(a), the incorporation of a thicker PTFE patch in the delaminated region induced separation of the sublaminates almost immediately after the compressive load was applied (approximately at 5kN). The critical sublaminate separated smoothly from the supporting sublaminate, while the latter continued to deflect almost linearly related to the applied load towards the inner face of the laminate. Delamination buckling is believed to have occurred at 15 kN, where a small, but quite rapid, increase in the deflection slope of the critical slope is observed. In correlation to the damaged counterpart examined earlier, the critical load is significantly reduced and approximates the theoretical one. This suggests that the amplified amplitude of the local imperfection effectively alleviates the influence of the overall imperfection in the structure.

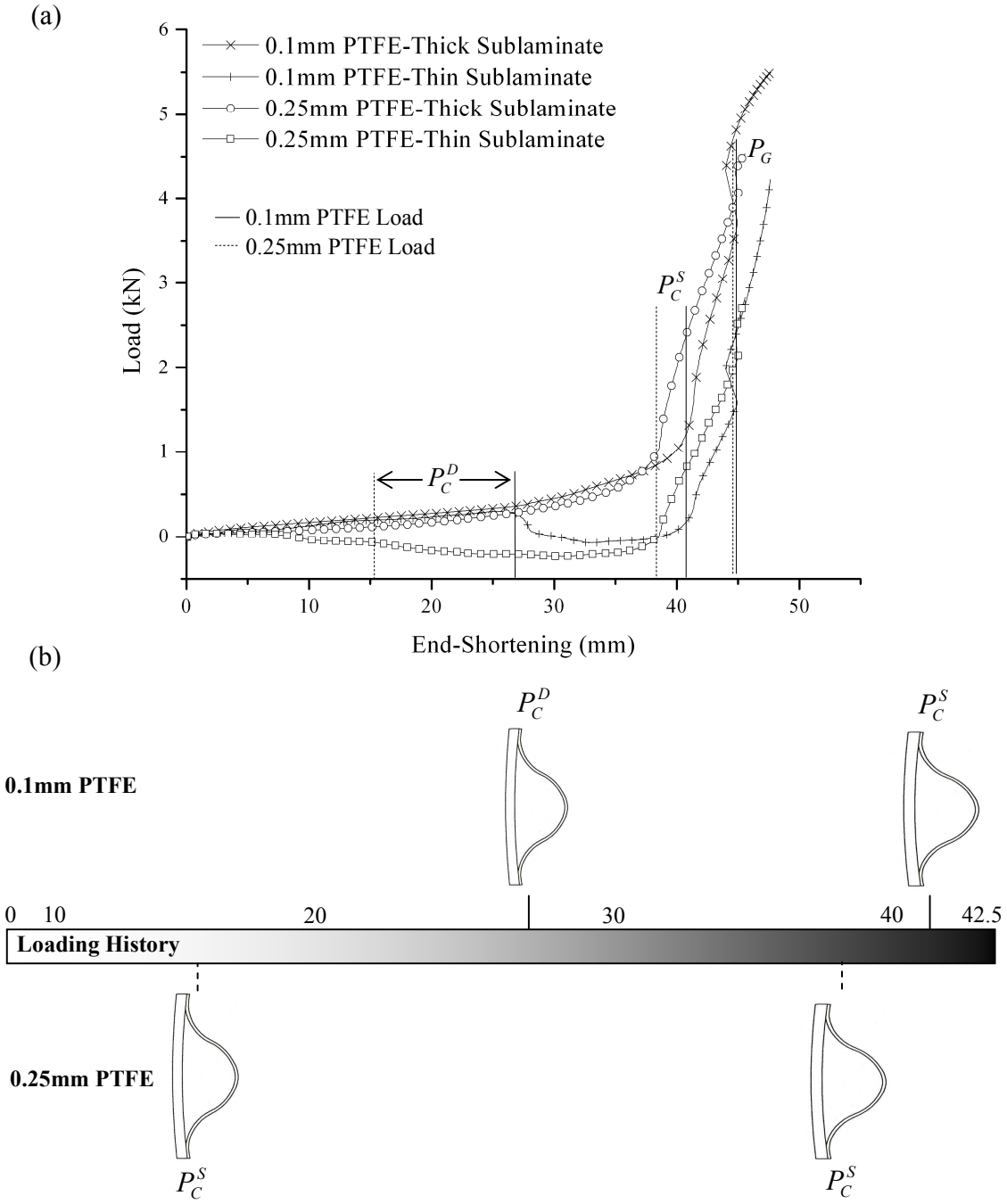

Figure 7.35. Experimental buckling behaviour of the delaminated region of the n=6-Skin damaged channel-section struts with 0.1 and 0.25mm PTFE patches, (a) as depicted by the out-of plane displacements at the centre of the sublaminates vs load plot and (b) sketched at critical values of the loading history.

Delamination buckling occurred in a thin-film configuration, Figure 7.35(b), which transformed into an open mode in the post-critical path. Even though, this is in agreement with the behaviour of the damaged counterpart examined earlier, nevertheless the structural buckling load is somewhat lower (38 kN). On the contrary, it is coincident to the loading level predicted by the finite element analysis. That is, both in the experiment and analysis the supporting sublaminates deflect under similar bending curvatures, as is evident in Figure 7.36. This suggests similar post-critical stiffness of the supporting sublaminates, and subsequently, similar stresses in the delaminated plates. Thus, the critical loads are identical. More importantly, the higher amplitude of deflection of the delaminated plate in the experiment (Figure 7.37) suggests that the relative deformation of the sublaminates affects most the structural buckling load.

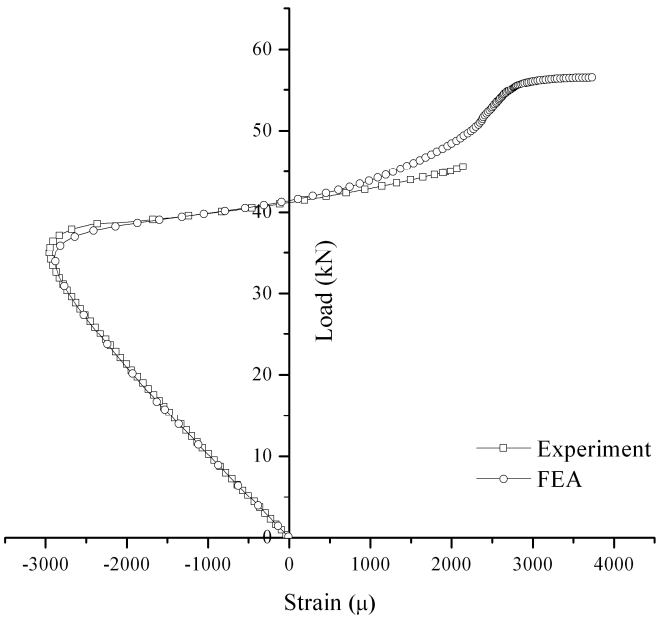

Figure 7.36. Comparison of the experimental longitudinal strain variation near the centre of the inner skin for the n=6-Skin channel-section with 0.25 mm PTFE insert to the one predicted by the FEA.

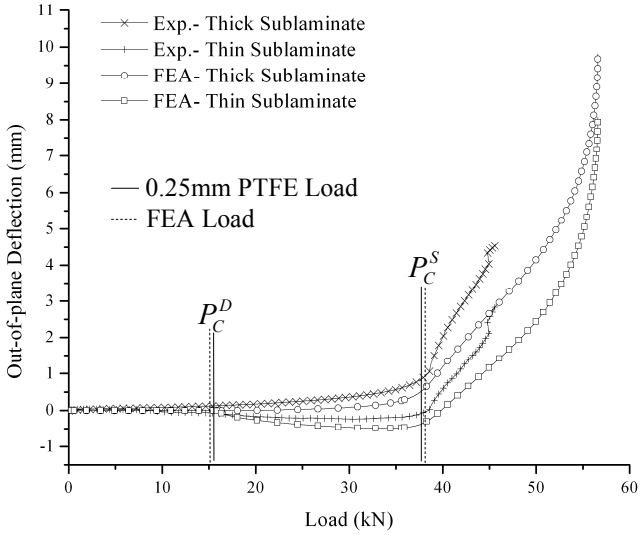

Figure 7.37. Comparison of the experimental deformation history of the delaminated channel-section strut with n=6-Skin delamination and 0.25mm PTFE insert to the one predicted by the FEA.

This is also supported by the the higher bending curvature of the supporting sublaminate in the current specimen, in correlation to the damaged counterpart with sufficiently high critical load (Figure C.5). Despite similar amplitudes of deflection of the delaminated plate [Figure 7.35 (a)], the higher bending curvature induced higher stresses in the delaminated plate, and consequently, accelerated structural instability. This implies that the pre-critical deformation of the delaminated plate induces milder deformations in the structure, which moderate the ones imposed by delamination buckling at higher loading levels.

The structural buckling mode [Figure 7.38(b)] and post-buckling behaviour was qualitatively similar to the one that evolved in the damaged channel-section strut with 0.1mm PTFE patch. Initially, the structure buckled in the same way as the undamaged strut with positive mode of buckling, and ultimately, in an Euler configuration. It should be noted, though, the earlier occurrence of structural instability (that is, in relation to the

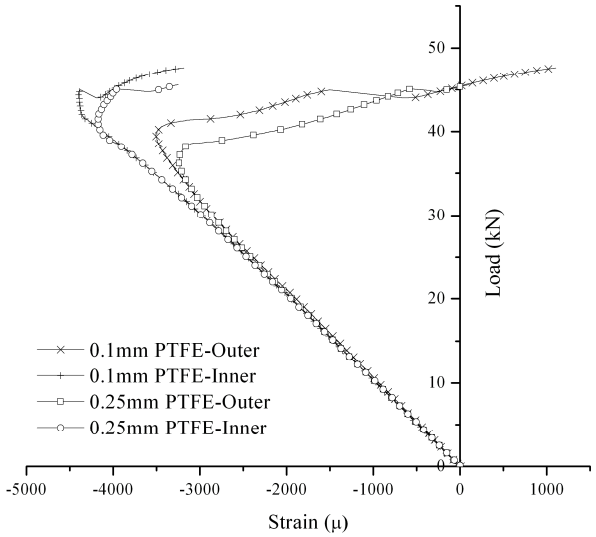

Figure 7.38. Load vs longitudinal strains at the mid-length of the edge of the left stiffener for the n=6-Skin damaged channel-section struts with 0.1 and 0.25 mm PTFE patches.

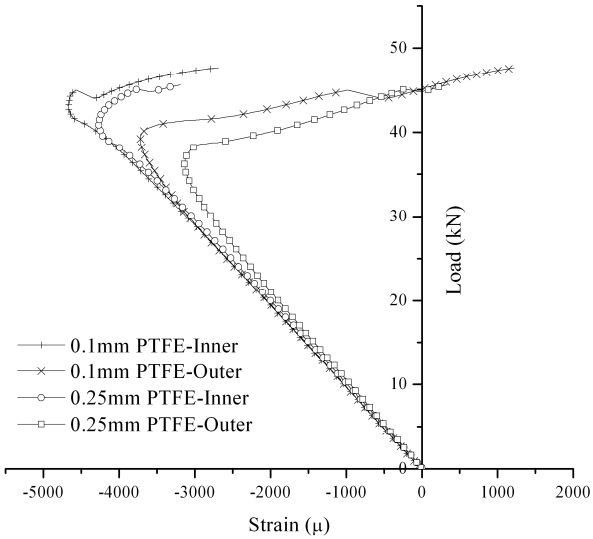

Figure 7.39. Load vs longitudinal strains at the mid-length of the edge of the right stiffener for the n=6-Skin channel-section struts with 0.1 and 0.25 mm PTFE patches.

one observed in the previous specimen) instigated the global deformation component of the buckling mode at slightly reduced level of loading. Nevertheless, this did not affect the onset of delamination growth, which occurred at the exact level of compressive loading (45 kN, see Figure C.15). Delamination growth was immediately arrested, for the reasons presented in the previous section, but failure occurred soon after (45 kN, see Figure C.15). The ultimate load level is somewhat reduced in relation to the one monitored in the damaged counterpart with the thinner PTFE insert, and is attributed to the aforementioned earlier evolution of global deformation, and consequently, material non-linearity.

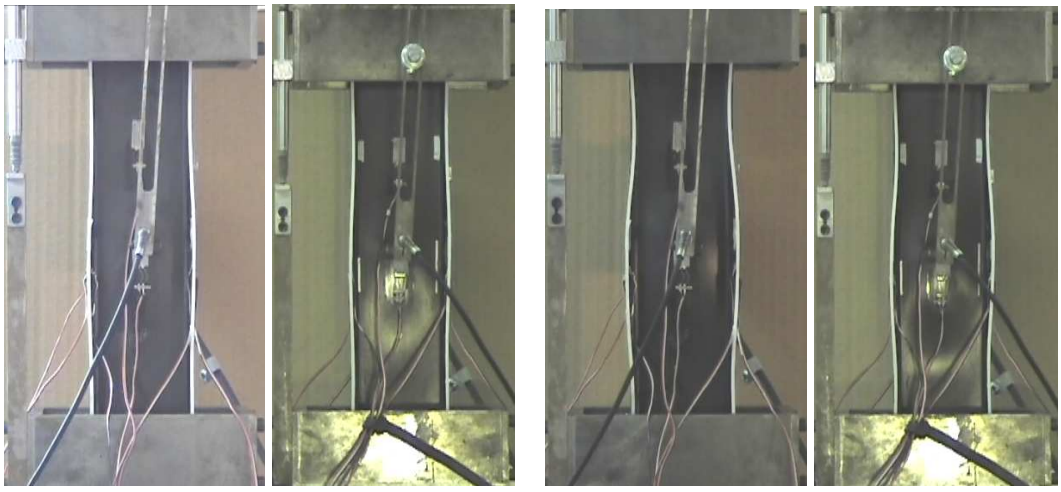

(a) (b) (c) (d)

Figure 7.40. Illustration of the buckling configurations of the n=6-Skin damaged channel-section struts with 0.1 and 0.25mm PTFE patches (a), (b) in the initial post-buckling range and (c), (d) near ultimate loading conditions respectively.

7.3.6 Damaged Channel-Section Strut with n=2-Stiffener Delamination

Experiment

The deformation of the supporting sublaminate prior to structural instability was characterized by negligible deflections towards the outer face (positive direction), which was linearly related to the applied compressive load, Figure 7.41(a). Similarly, a linear relationship exists between the strain variation near the intersection of the supporting sublaminate and the applied load. It is therefore logical to say that either the sublaminates buckled in a thin-film configuration or delamination buckling did not occur at all. Observation during the experiment supports the latter. However, the experience gained throughout this experimental program suggests that delamination buckling may involve rather small deflections, and therefore, the experimental observations cannot be considered as conclusive evidence.

At 40 kN structural buckling (P_C^s) occurred. This was marked by a sharp increase in the deflection of the supporting sublaminate in the positive direction [Figure 7.41(a)] and the deviation of the back-to-back strains in the mid-length of the left stiffener (Figure 7.42), the skin (Figure 7.43) and the delaminated right stiffener (Figure C.6). Buckling of the damaged channel-section strut occurred in a skewed asymmetric mode. The number of the half-sinewaves of the latter mode is not readily defined. In accordance with Figure 7.44(a), though, it is believed to be of the order of two or three half-sinewaves. A nodal-line was generated within the delaminated area, which caused the sublaminates to deflect in shear [Figure 7.41(b)], and subsequently, the mid-section to distort in a twisting mode, Figures 7.42, 7.43 and 7.41(a). It should be noted that the latter differs from the one drawn in Figure 7.21 in terms of the direction of deflection of the skin. As evident in Figure 7.43, the skin deflected in the negative direction.

In the intial post-buckling region the mode evolved in a stable manner, as suggested by the increasing distortion of the mid-section in the twisting mode. However, shortly after structural instability, the mode progressed to a torsional-flexural configuration.

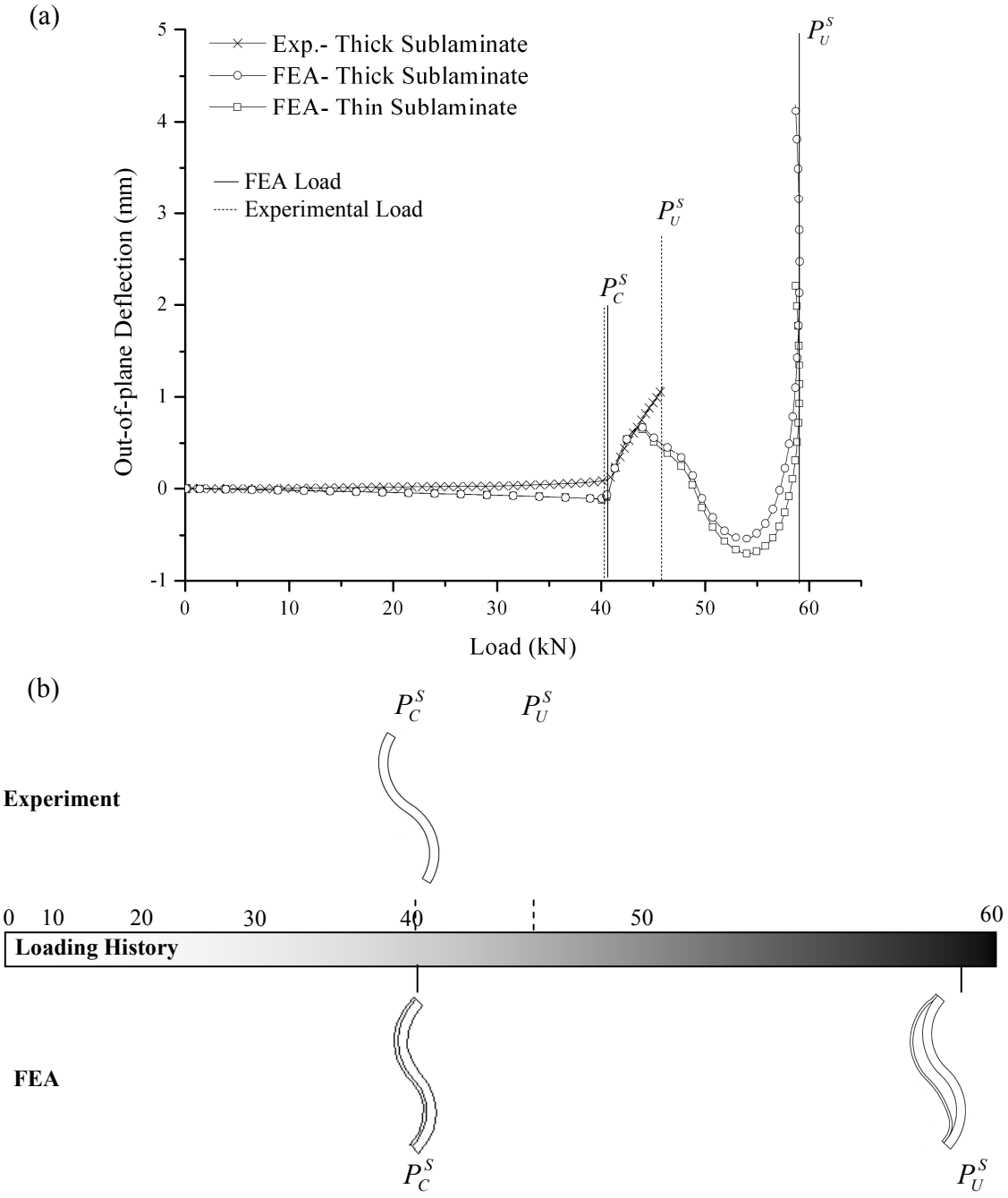

Figure 7.41. Buckling behaviour of the delaminated region of the damaged channel-section strut with n=2-Stiffener delamination, (a) as depicted by the out-of-plane displacement of the mid-point of the edge of the delamination vs load plot and (b) sketched at critical values of the loading history.

Note: The FEA plot shows the deflection of a point at 5.2mm below the delamination center

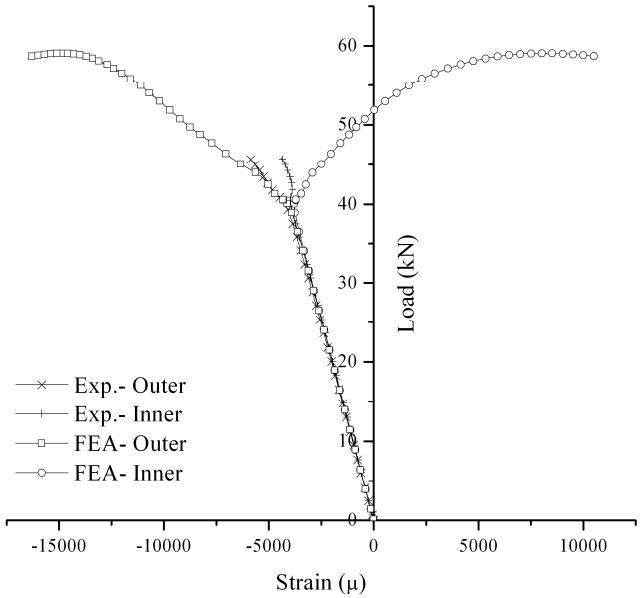

Figure 7.42. Load vs longitudinal strains at the mid-length of the edge of the left stiffener for the n=2-Stiffener channel-section strut.

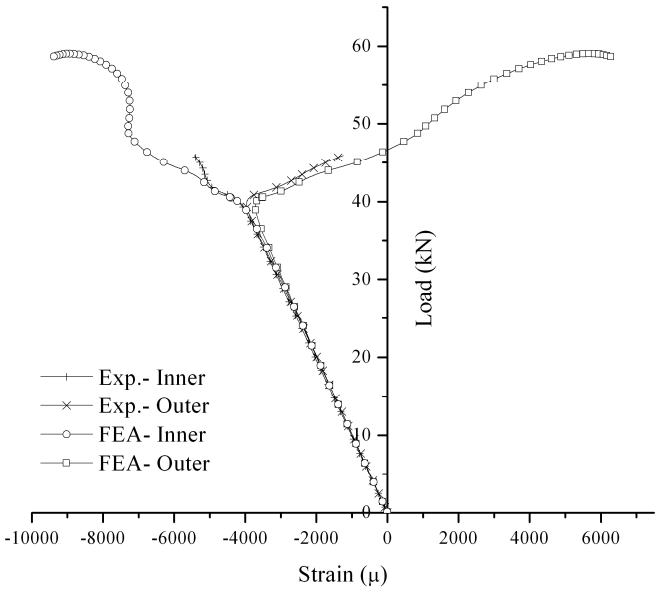

Figure 7.43. Load vs longitudinal strains at the centre of the skin for the n=2-Stiffener channel-section strut.

This is evident from the changes of the stress gradients monitored at 42 kN. In particular, at the mid-section, the skin and left stiffener shifted to tensile and compressive structural regions respectively; whereas, the delaminated stiffener continued to deflect towards the outer face. Failure took place at 46 kN with intralaminar fracture and delamination growth in the delaminated stiffener and across the mid-length of the skin and stiffeners, Appendix C.1.

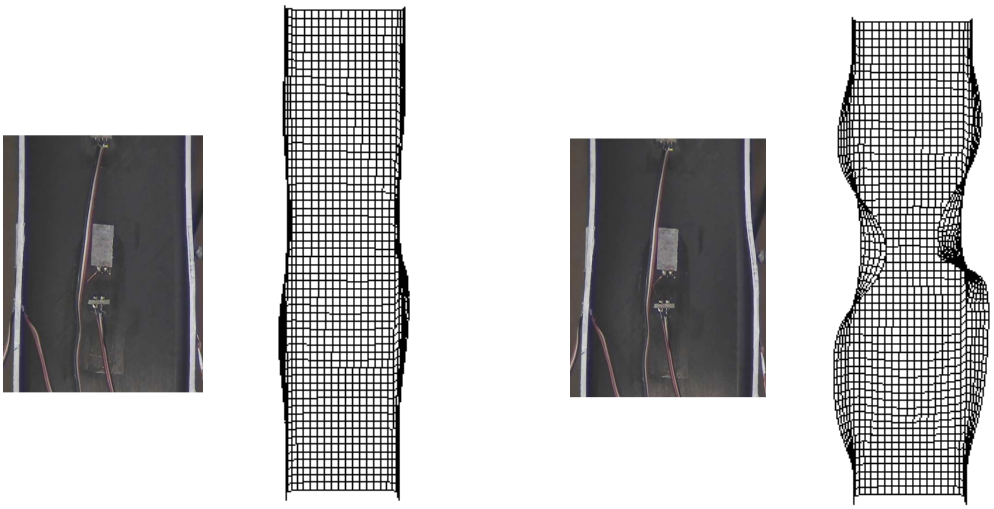

(a) (b) (c) (d)

Figure 7.44. Illustration of the experimental and FEA buckling configuration of the n=2-Stiffener damaged channel-section strut (a), (b) in the initial post-buckling range and (c), (d) near ultimate loading conditions.

FEA

In the finite element analysis the deformation history is analysed by monitoring the variation of the out-of-plane deflection of the sublaminates with applied load, Figure 7.41(a), at 5.2mm lower than the delamination centre. The particular point was chosen in view of the fact that the predicted deflections correlated better with the experimental results and were qualitatively similar to the ones in the delamination center. The reason for the latter observation probably resides in the local imperfection that was imposed on

the supporting sublaminate as a result of the manufacturing process, and could influence the shear configuration of the sublaminates.

Hence, prior to critical instability the analysis predicts that the sublaminates deflect uniformly and almost linearly related to the applied compressive load. Therefore, taking into account the arguments raised in the presentation of the experimental results and the linearity of the pre-buckling deformation of the supporting sublaminate, observed both experimentally and analytically, it is concluded that more likely than not delamination buckling did not take place in the experiment. It is worth noting that the small deviations observed between the predicted and monitored deflections of the supporting sublaminate are attributed to the lack of local imperfection in the finite element analysis similar to the one imposed by the PTFE patch in the thicker sublaminate of the damaged specimen.

The predicted structural buckling load is in excellent agreement with the experimental (just above 40 kN). Structural buckling occurs in a skewed asymmetric mode composed of three half-sinewaves; 2 longer and a shorter (as shown in Figure 7.44(b) and sketched in Figure 5.9). Similar to the experiment, a nodal-line develops within the delaminated region causing the sublaminates to deflect uniformly in shear, Figure 7.41(b), and the mid-section to distort in the shearing mode. Thus, it is suspected that an analogous mode developed in the experiment. This is also supported by the positive correlation of the predicted and monitored longitudinal strains in the initial post-buckling region, shown in Figures 7.42, 7.43 and C.6. However at 42 kN, the experimental and the numerical post-buckling paths diverge. In contrast to the first, the numerical method predicts that the buckling mode precipitates in a stable manner until 48 kN. As the amplitudes of the evolved buckling crests increase, the nodal-line shifts in a direction that enhances the distortion of the mid-section in a negative mode. The latter mechanism portrays the tendency of the negative buckling crest to occupy the mid-section and is attributed to the wavelength augmentation of the minor positive buckling crest. This is evident in the reversal in the direction of deflection of the mid-points of the sublaminates in Figure 7.41(a).

Consequently, at 48 kN, an overall deformation component is introduced to the damaged strut, similar to the one observed in the undamaged channel-section strut with negative buckling mode. This is exemplified by the shift of the skin at the mid-section of the strut (Figures 7.43) into a tensile region of the latter. However, as discussed in section 7.2.3, the evolution of the latter mode promotes the amplification of the wavelengths of the positive buckling crests. Nevertheless, in the damaged strut this is not symmetric in the two stiffeners due to the reduced stiffness of the delaminated region. As a result, the positive buckling crest of the delaminated stiffener occupies the mid-section and induces a twisting mode, Figures 7.41(a), 7.42 and 7.43. Thus, the global mode of deformation transforms to the so called "torsional-flexure" mode, Figure 7.44(d), and ultimate loading conditions are attained soon after (59 kN). Finally, it should noted that the development of the local-torsional mode in the experiment at an earlier loading stage than the one predicted in the analysis may be related to material non-linearity. Moreover, the transition of the back-to-back longitudinal strains monitored at the mid-length of the left stiffener in a compressive region of the strut, suggests a more profound torsional component of global deformation than observed in the analysis. It is suspected that the latter phenomenon is related to the local imperfection (PTFE patch) of the supporting sublaminate in the specimen and is an issue which is investigated further in the following section.

7.3.7 Damaged Channel-Section Strut with n=2-Stiffener Delamination and 0.25mm PTFE Patch

Testing of *n=2-Stiffener* damaged channel-section strut was repeated in order to investigate the effect of the local imperfection introduced in the supporting sublaminate of the free-edge delamination. As for the *n=6-Skin* delaminated strut, a thicker PTFE patch of 0.25mm was incorporated in the specimen. The deformation history [Figure 7.45(a)] and the recorded variations of strain across the mid-section (Figures 7.46, 7.47 and C.7) are compared to these of the delaminated counterpart examined in the previous section. Sketches of the delaminated region and structural mode shapes are presented in Figures 7.45(b) and 7.48 respectively.

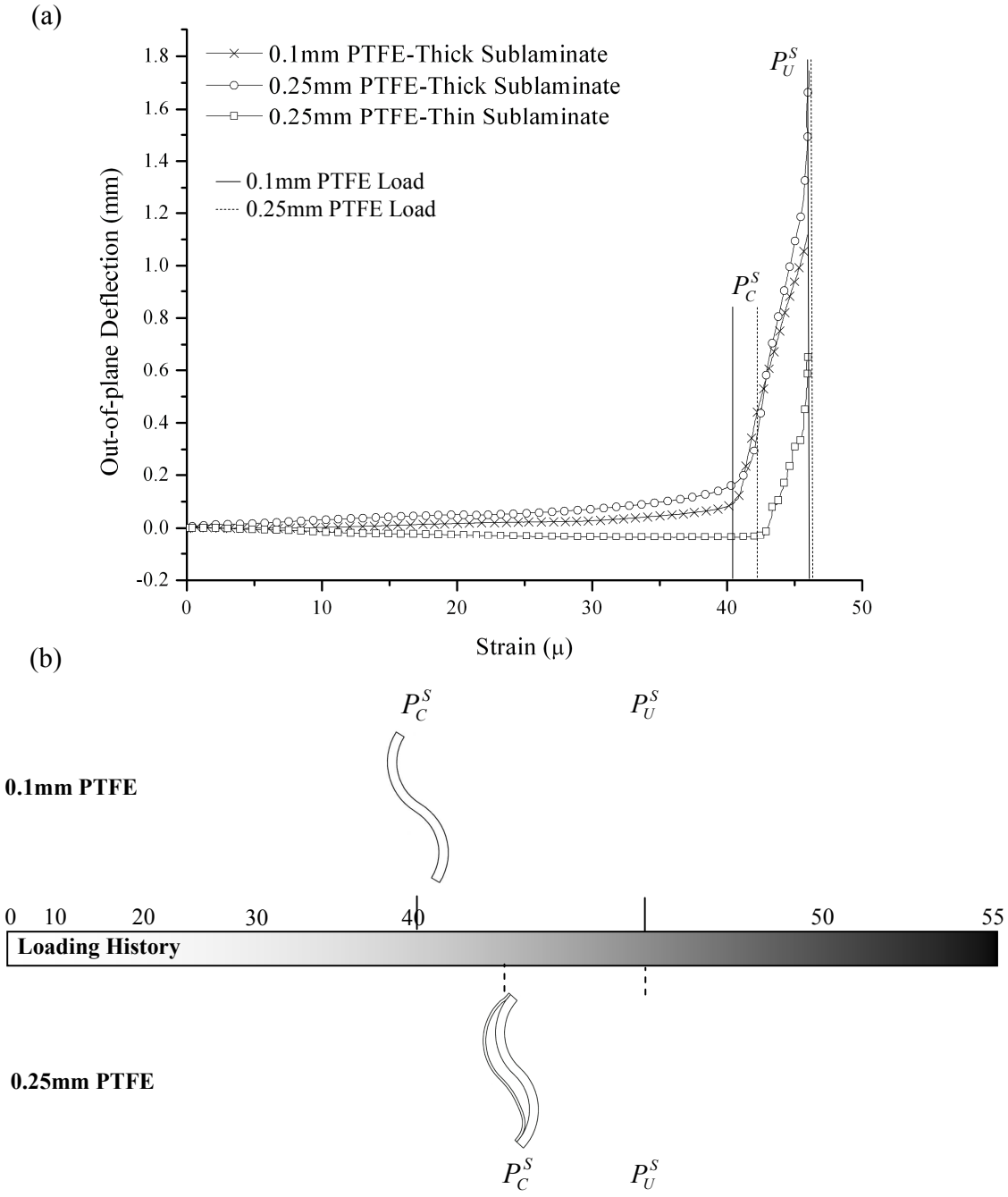

Figure 7.45. Experimental buckling behaviour of the delaminated region of the n=2-Stiffener damaged channel-section struts with 0.1 and 0.25 PTFE patches, (a) as depicted by the out-of plane displacement of the mid-point of the edge of the delamination vs load plot and (b) sketched at critical values of the loading history.

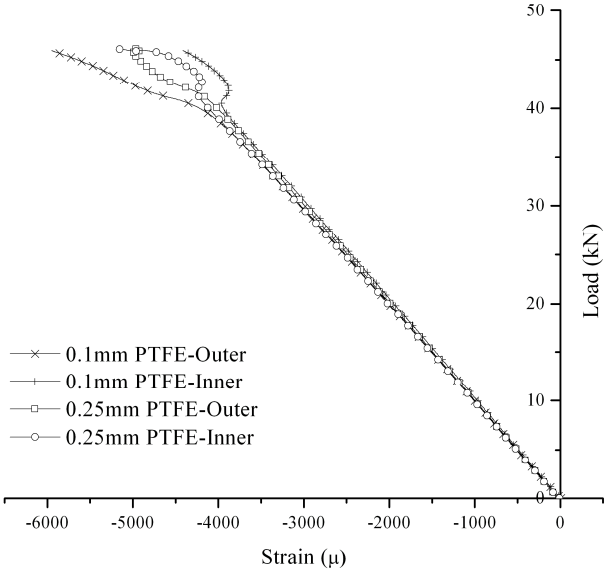

Figure 7.46. Load vs longitudinal strains at the mid-length of the edge of the left stiffener for the n=2-Stiffener damaged channel-section struts with 0.1 and 0.25 mm PTFE patches.

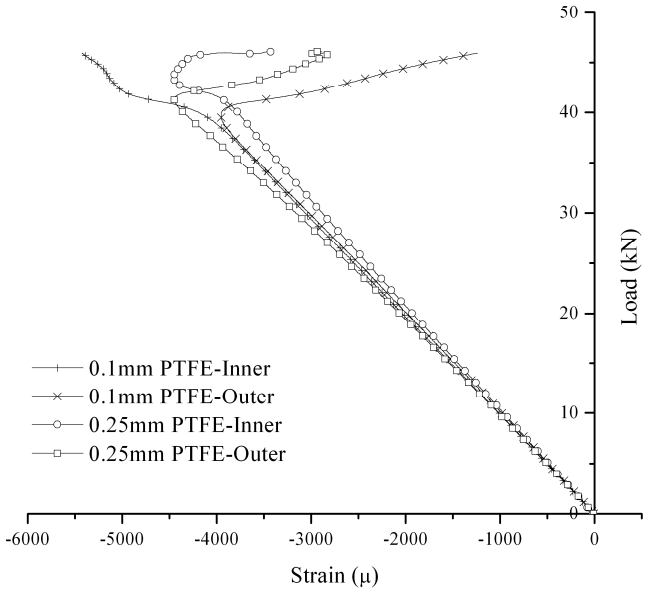

Figure 7.47. Load vs longitudinal strains at the centre of the skin for the n=2-Stiffener channel-section struts with 0.1 and 0.25 mm PTFE patches.

Thus, as shown in Figure 7.45(a), the incorporation of a thicker PTFE patch in the delaminated region induced separation of the sublaminates from initial loading conditions. The sublamintes deflected in opposing directions and were almost linearly related to the applied compressive load. This is attributed to the initial deformation of the supporting sublaminate that induces an effective shift in the neutral axis of the delaminated region and instigates opposing rotations in the critical sublaminate. It is suspected that a similar behaviour occurred in the *n=2-Stiffener* damaged strut with 0.1mm PTFE patch due to the similarity of the monitored deflection paths of the supporting sublaminates. Nonetheless, the introduction of a thicker insert induced slightly higher deflections in the supporting sublaminate of the specimen under investigation, Figure 7.45(a), and probably in the critical sublaminate also. However, as for the damaged strut examined earlier, delamination buckling did not come into being. Thus, it is concluded that the arrest of delamination buckling more than likely originates from geometric non-linearity of the structure, rather than the imperfections that arise during the manufacturing process.

The inclusion of the thicker insert (or otherwise a local imperfection with bigger amplitude) acted beneficialy in terms of structural stability. Structural buckling occurred at 42 kN, as is evident from the variations of the back-to-back strain gauges in Figures 7.46, 4.47 and C.7 and the sudden change in the direction of deflection of the critical sublaminate in Figure 7.45(a). The 5% increase in the structural buckling load, in relation to the damaged counterpart examined earlier, is attributed to the pre-buckling deformation of the damaged strut. Contrary to the latter, the considerable deflection of the supporting sublaminate in the positive direction promoted a positive mode of distortion in the mid-section, and therefore, an equilibrium path with a higher bifurcation point.

This did not significantly influence the structural buckling mode, since the reduced shear stiffness of the delaminated region attracted once again a nodal-line of the buckling mode. In similarity to the damaged strut with the thinner PTFE insert, buckling occurred in three half-sinewaves along the length strut [Figure 7.48(b)], causing the mid-

section to deform in the twisting mode, while the sublaminates deflected in shear, Figure 7.45(b). Shortly after structural instability, and about the same level of loading monitored in the previous experiment, a global deformation component was introduced in the buckling mode. By examination of the strain variations with applied load across the mid-length, Figures 7.45(a), 7.46 and 7.47, it is observed that the mid-section deformed in a pure torsional mode.

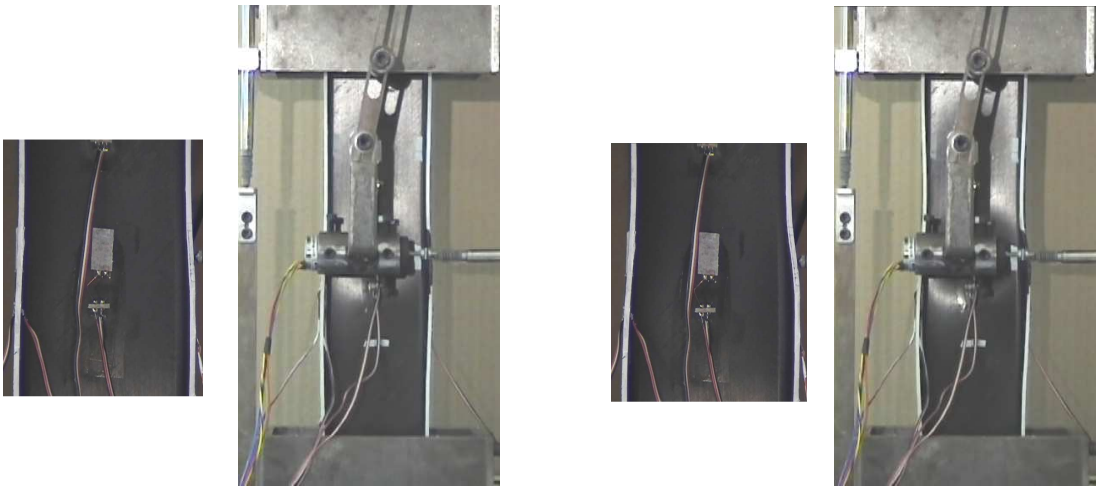

(a) (b) (c) (d)

Figure 7.48. Illustration of the buckling configuration of the n=2-Stiffener damaged channel-section struts with 0.1mm and 0.25 PTFE patches (a), (b) in the initial post-buckling range and (c), (d) near ultimate loading conditions respectively.

This suggests that the rise in amplitude of the local imperfection of the supporting sublaminate promoted global deformation in the damaged strut under a twisting mode. Due to the comparable deflection amplitudes [Figure 7.45(a)] and bending curvatures (Figure C.7) of the supporting sublaminates in the post-buckling region, it is suspected that the enhancement of the torsional mode is related to the increased separation of the sublaminates. Therefore, it is logical to say that the degradation of the torsional rigidity of the delaminated stiffener is analogous to the relative displacement of the sublaminates. To an extent this is supported by the correlation of the previous

experiment with the finite analysis, where a more profound torsional component of global deformation was observed in the first. Finally, failure occurred about the same level of loading (46 kN) and in an equivalent fashion (Appendix C.1).

7.3.8 Damaged Channel-Section Strut with n=3-Stiffener Delamination

Experiment

The pre-critical path was characterized by particularly small deflections of the sublaminates that approximately outlined a plateau of zero displacement in the deformation history. At 37 kN delamination buckling (P_C^D) occurred with a sudden increase in the deflections of the sublaminates towards the inner face of the strut, Figure 7.49(a). In contrast to the supporting sublaminate, the abrupt increase in deflection of the critical sublaminate was quite substantial. In the post-critical state the supporting and critical sublaminate deflected non-linearly with the applied load with rather small and moderate deflections respectively. Evidently, the delamination buckling mode at critical instability does not lie within the thin-film assumption, Figure 7.49(a). Conversely, the strain variation with applied load monitored at the free-surface of the laminate does not comply with the closed configuration. That is, after the sudden increase in the longitudinal strain, the latter varies in a manner that denotes the evolution of a tensile face. This is an issue which will be examined further with the aid of the finite element analysis.

At 39 kN structural buckling (P_C^S) occurred, as is evident from the deviation of the back-to-back strains in the mid-length of the left stiffener (Figure 7.50), the skin (Figure 7.51) and the delaminated right stiffener (Figure C.8). Buckling of the damaged channel-section strut occurred in a skewed asymmetric mode that was composed of three half-sinewaves along its length, Figure 7.52(a). A nodal-line was generated within the delaminated area, causing the mid-section to distort in the negative mode (Figures 7.50, 7.51 and C.8) and the sublaminates to deflect in shear. This is clearly visible in Figures 7.52(a) and (c). However, the post-buckling path is relatively short, and therefore,

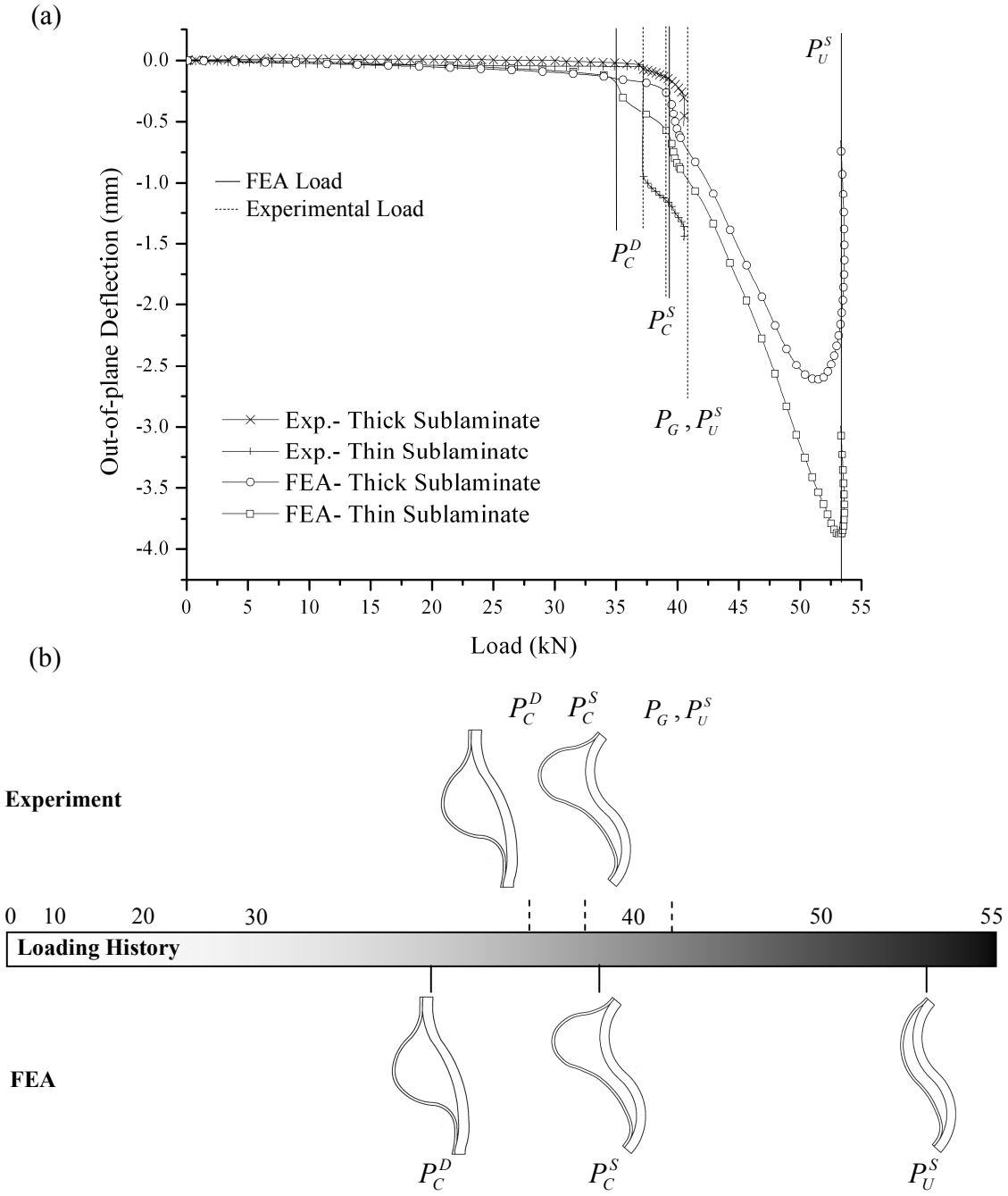

Figure 7.49. Buckling behaviour of the delaminated region of the damaged channel-section strut with n=3-Stiffener delamination, (a) as depicted by the out-of-plane displacement of the mid-point of the edge of the delamination vs load plot and (b) sketched at critical values of the loading history.

Note: The FEA plot shows the deflection of a point at 5.2mm below the delamination centre

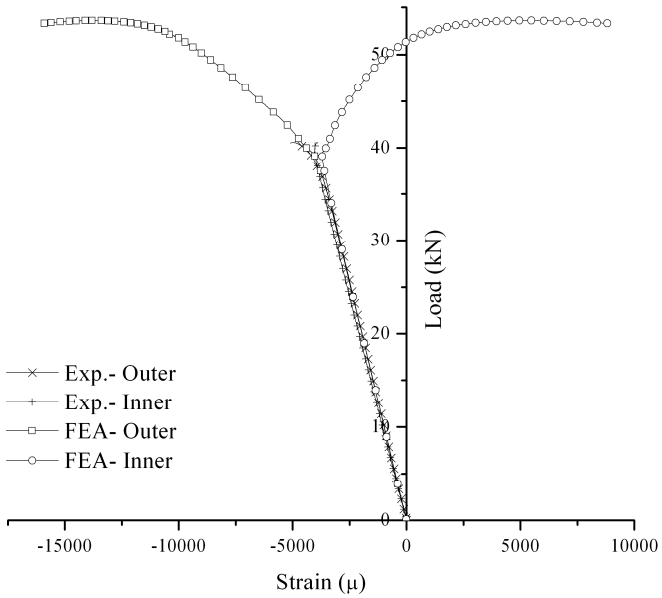

Figure 7.50. Load vs longitudinal strains at the mid-length of the edge of the left stiffener for the n=3-Stiffener channel-section strut.

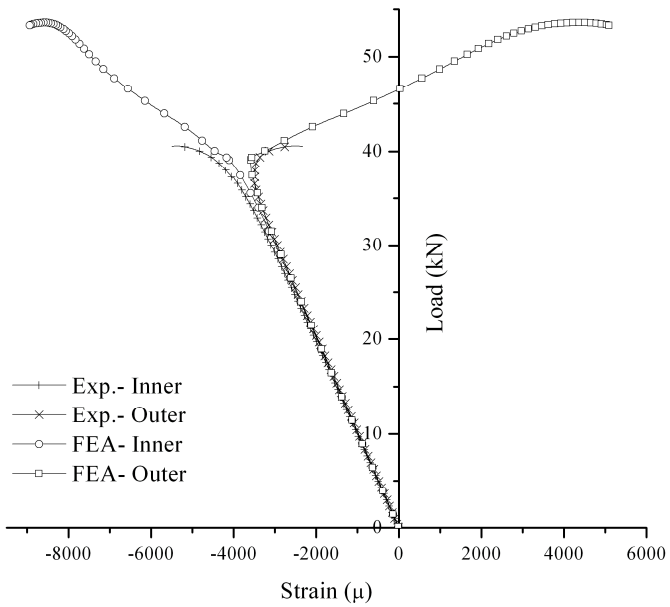

Figure 7.51. Load vs longitudinal strains at the centre of the skin for the n=3-Stiffener channel-section strut.

judgments on the behaviour of the damaged strut within this region cannot be drawn. Failure occurs at 41 kN with excessive delamination growth in the right stiffener and intralaminar fracture across the mid-section, Appendix C.1

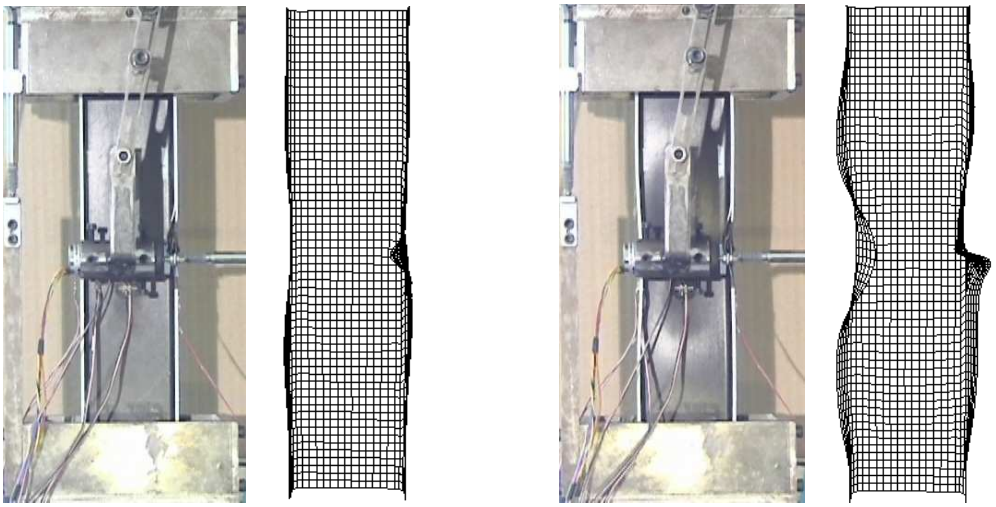

(a) (b) (c) (d)

Figure 7.52. Illustration of the experimental and FEA buckling configuration of the n=3-Stiffener damaged channel-section strut (a), (b) in the initial post-buckling range and (c), (d) near ultimate loading conditions.

FEA

In the finite element analysis the deformation history is analysed by monitoring the variation of the out-of-plane deflection of the sublaminates with applied load, Figure 7.49(a), at 5.2mm lower than the delamination centre. The particular point was chosen for the same reasons presented in the finite element analysis of the *n=2-Stiffener* channel-section strut. Hence, prior to critical instability the analysis predicts that the sublaminates deflect uniformly towards the inner face and were almost linearly related to the applied compressive load. At 35 kN delamination buckling (P_C^D) takes place with a smooth separation of the sublaminates, as shown in Figure 7.49(a). As illustrated in the latter figure, the sublaminates buckle in a thin-film configuration. However, a closer inspection of the deformation plot of the damaged structure at critical instability reveals

a thin-film with in-plane distortion buckling configuration, Figure 7.49(b). By comparison of the predicted and monitored strain variations with applied load plots for the supporting sublaminate in Figure C.8, it is observed that the latter are qualitatively similar, and therefore, it is concluded that an analogous delamination buckling mode developed in the experiment, but at a more advanced state of evolution.

This is primarily attributed to the occurrence of delamination buckling at a later stage of the loading process in the experiment. That is, the finite element analysis predicts critical instability at 35 kN; or otherwise, 7% lower than the experiment. In turn, the latter disparity originates in the local imperfection placed in the supporting sublaminate of the damaged specimen, which instigated very small, but opposing, deflections to the ones predicted by the analysis. Nonetheless, the predicted structural buckling load (P_C^S) is in very good agreement with the experimental (39 kN). Likewise, the structural buckling mode develops in three half-sinewaves that produce a negative mode of distortion in the mid-section and a shear mode in the delaminated region, Figure 7.52(b).

Comparisons with respect to the post-buckling path of the damaged structure would be of no consequence since failure occurred in the experiment at an early stage. However, in the absence of delamination growth and material non-linearity the analysis offers the opportunity to investigate the post-buckling behaviour of the strut. Thus, from the strain variations with applied load across the mid-section of the strut, Figures 7.50, 7.51 and C.8, it is observed that essentially the aforementioned buckling mode develops in a stable manner in the post-buckling region. The increasing deflections of the negative buckling crest that occupies the mid-section induce an overall deformation component similar to the undamaged strut with negative buckling mode. As already mentioned, the latter enhances the wavelengths of the positive buckling crests. In addition to the reduced stiffness of the delaminated region, this causes the asymmetric development of the positive buckling crest [Figure 7.52(d)], and consequently, induces a twisting mode in the mid-section [Figures 7.49(a), 7.50 and 7.51]. In the region of 53 kN ultimate loading conditions are attained.

7.3.9 Damaged Channel-Section Strut with n=5-Stiffener Delamination

Experiment

Initially the out-of-plane deflections of the sublaminates were small, but finite, and almost linearly related to the applied load. Their relative deflection was insignificant, which suggested little or no separation at all of the sublaminates. However, at an applied load of 19 kN a small separation of the sublaminates occurred, where the critical sublaminate deviated from the linear deflection path. Nonetheless, the small non-linear deflections of the critical sublaminate with applied load do not suggest buckling. This is attributed to the imperfection imposed in the specimen by the PTFE patch.

Delamination buckling (P_C^D) occurred in the region of 31 kN. This was marked by a very sharp increase in the deflections of the critical sublaminate in the initial post-critical state, Figure 7.53(a). In contrast, the deflection of the supporting sublaminate did not deviate significantly from the pre-critical deformation path. Thus, the buckling behaviour lies within the thin-film assumption. Evidently though, upon buckling a small change occurred in the stress gradient of the free face of the supporting sublaminate, Figure C.9. A closer examination reveals a sudden increase in compressive strain. This is in line with the development of thin-film buckling with in-plane distortion that was observed in the previous experiment, but once again the lack of more conclusive evidence requires the aid of the finite element analysis.

In the post-critical range a buckling mode developed with higher deflections of the sublaminates towards the outer surface. However, at 37 kN there was a small, but sudden, decrease in the out-of-plane deflection of the supporting sublaminate. Such phenomenon could be correlated with the onset of delamination growth or with the initiation of an opening delamination buckling mode. Nevertheless, losses in energy are associated with sudden abrupt changes in stiffness. This is not observed in Figure C.19, and thus, eliminates the possibility of delamination growth. Likewise, an opening buckling mode would be contradictory, since immediately after the aforementioned drop

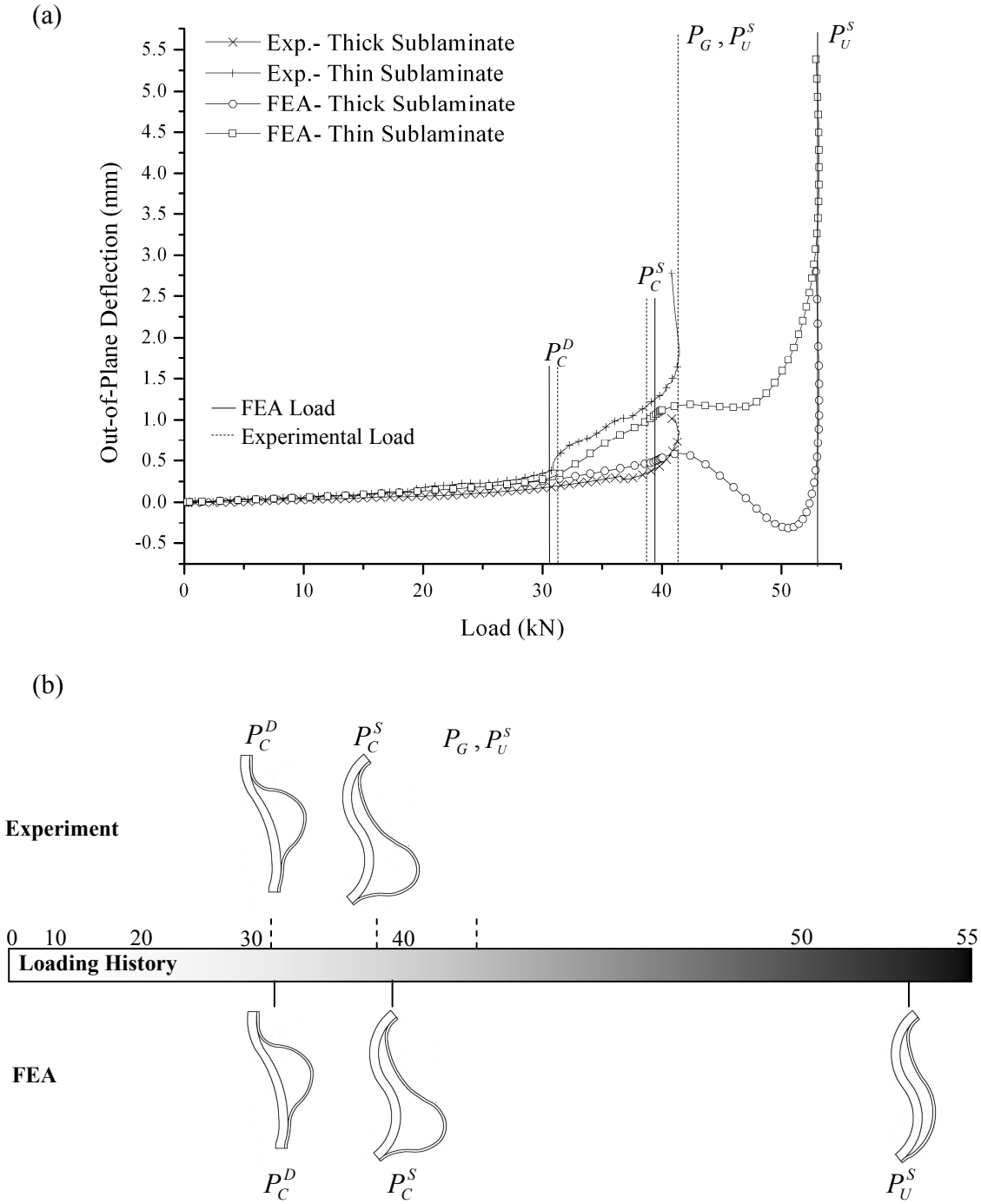

Figure 7.53. Buckling behaviour of the delaminated region of the damaged channel-section strut with n=5-Stiffener delamination, (a) as depicted by the out-of-plane displacement of the mid-point of the edge of the delamination vs load plot and (b) sketched at critical values of the loading history.

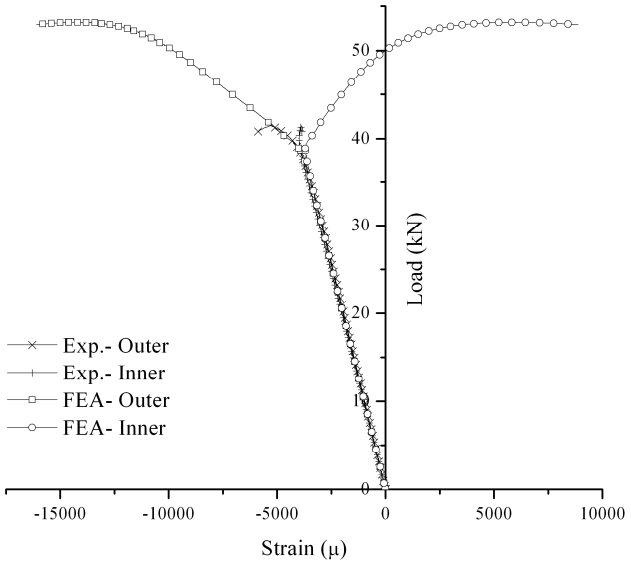

Figure 7.54. Load vs longitudinal strains at the mid-length of the edge of the left stiffener for the n=5-Stiffener channel-section strut.

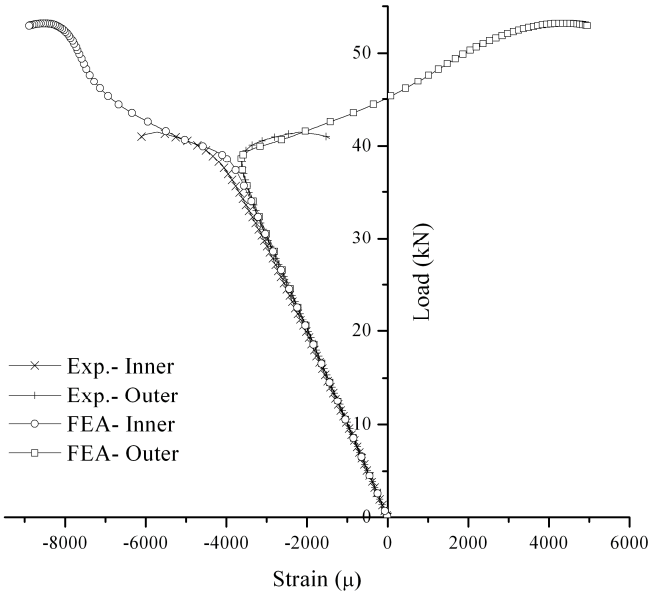

Figure 7.55. Load vs longitudinal strains at the centre of the skin for the n=5-Stiffener channel-section strut.

the sublaminates continued to deflect in the same direction. Thus, it is concluded that at the given loading the shearing mode initiates, and the drop in deflection depicts the transition to a shearing buckling mode.

The latter argument is also supported by the fact that soon after (39kN) structural buckling (P_C^S) occurred with no qualitative influence on the deflection of the sublaminates. This suggests a smooth transition of delamination buckling mode from the structural pre-buckled state to the postbuckled. The structural buckling load was identified by examination of the variation of the longitudinal strains across the mid-length of the left stiffener (Figure 7.54), the skin (Figure 7.55) and the delaminated right stiffener (Figure C.9). This is clearly shown in the latter figures by the deviation of the back-to-back longitudinal strain measurements in the outer and inner surfaces of the laminate from the initial (pre-structural) buckling path.

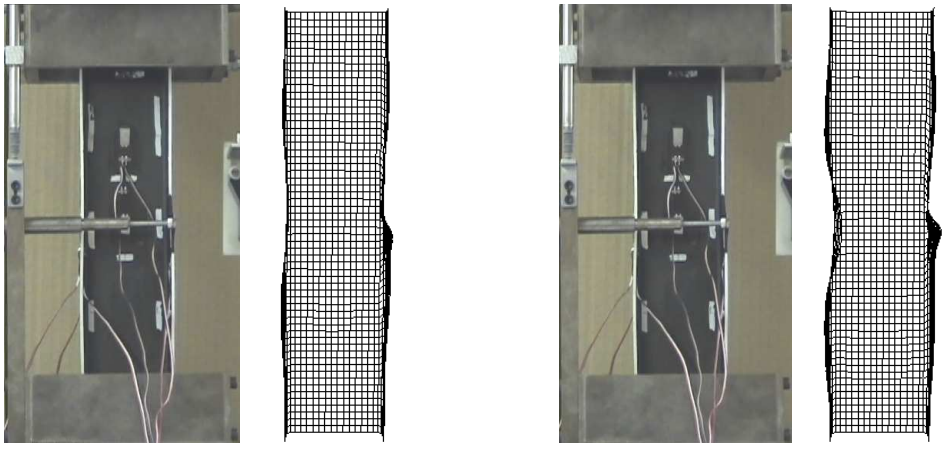

Figure 7.56. Illustration of the experimental and FEA buckling configuration of the n=5-Stiffener damaged channel-section strut (a), (b) in the initial post-buckling range and (c), (d) near ultimate loading conditions.

In particular, buckling of the damaged channel-section strut occurred in an asymmetric mode with three half-sinewaves, as shown in Figure 7.56(a). The mode evolved in a manner such that the mid-section to distort in the twisting mode, while the sublaminates deflected in shear [Figure 7.53(b)]. However, as for the *n=3-Stiffener* strut, the post-buckling path was relatively short. At 41 kN an ultimate limit point was attained where delamination growth occurred. The structure unloaded under a twisting mode of the cross-section, as evident from Figures 7.53(a), 7.55 and 7.56, and failed immediately after (almost at 40 kN) with delamination growth at the right stiffener and intralaminar fracture that propagated transversely to the applied load and across the mid-length of the skin and stiffeners, Appendix C.1.

FEA

The FEA predicts a similar deformation of the sublaminates to the experimental, as is evident from their out-of-plane displacements in Figure 7.53(a). The small deviation observed after 20 kN is more likely than not related to the geometrical disparity of the actual imperfection imposed by the PTFE patch and the one incorporated in the finite element analysis. Nonetheless, the predicted delamination buckling load is in excellent agreement with the experimental (31 kN). More importantly, a closer inspection of the deformation plot of the damaged structure at critical instability reveals a thin-film with in-plane distortion buckling configuration, Figure 7.53(b). The similarities observed in the FEA and experiment in terms of the post-critical strain variations near the intersection and deflections of the sublaminates [Figures 7.53(a) and C.9], in addition to the excellent agreement in the delamination buckling load, suggests that a similar delamination buckling mode occurred in the experiment.

Structural buckling occurs at 40 kN approximately, which is in very good agreement with the experiment (i.e less than 2% deviation). Likewise, at structural instability the damaged structure and sublaminates respectively deform in the asymmetric [Figure 7.56(b)] and shearing mode [Figure 7.53(b)] observed experimentally. In particular, the structure buckles in three half-sinewaves in a manner such that the mid-section deforms in the twisting mode and the sublaminates deflect in shear. For the relative short post-

buckling region that evolved in the experiment until the onset of delamination growth, the analysis predicts similar trends in respect to the variations of strain at the mid-section. The small differences observed in Figures 7.54, 7.55 and C.9 may be attributed to a small mismatch in the positions of the predicted and monitored nodal-lines.

Like to the *n=3-Stiffener* damaged strut, the analysis offers the opportunity to investigate the post-buckling behaviour of the strut in the absence of delamination growth and material limitations. Thus, from the strain variations with applied load across the mid-section of the strut, Figures 7.53(a), 7.54 and 7.55, it is observed that essentially the damaged structure exhibits an analogous behaviour to the one described in the numerical analysis of the *n=3-Stiffener* damaged strut. Thus, ultimate loading conditions are attained at 53 kN under a flexural-torsional mode of global instability, Figure 7.56(d). Finally, it is of interest to note that the delamination growth induced failure in the strut in the aforementioned mode, as evident primarily in Figure C.9, and is primarily attributed to the accelerated degradation of the stiffness of the delaminated stiffener.

7.3.10 Damaged Channel-Section Strut with n=6-Stiffener Delamination

Experiment

At first the deflections of the sublaminates were small, but gradually increased with loading in an almost linear manner. However, their relative deflection was insignificant, which suggested little if no separation at all of the sublaminates. This scenario was maintained until delamination buckling (P_C^D) occurred at 34 kN. The critical state was characterized by a smooth separation of the sublaminates, which nevertheless continued to deflect in the positive direction in the initial post-buckling state. The buckling behaviour was a typical thin-film buckling, Figure 7.57(b). This is both evident from the out-of-plane deflection versus load plot in Figure 7.57(a) and the strain-gauge measurement at the edge of the outer face of the thicker sub-laminate (that is, 10mm from the delamination centre), Figure C.10. At the post-critical path the sublaminates deflected in a closed mode.

(a)

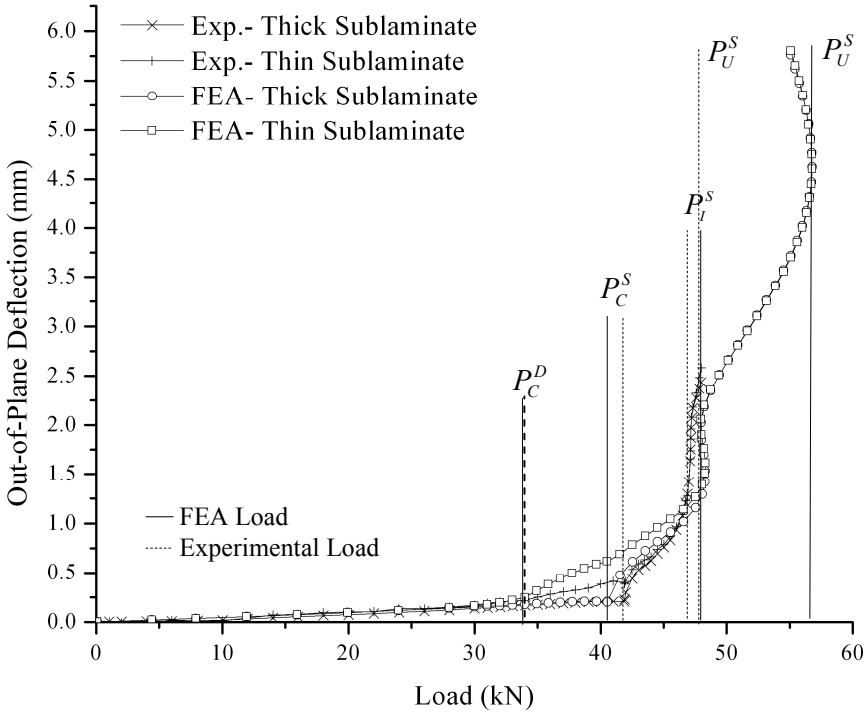

(b)

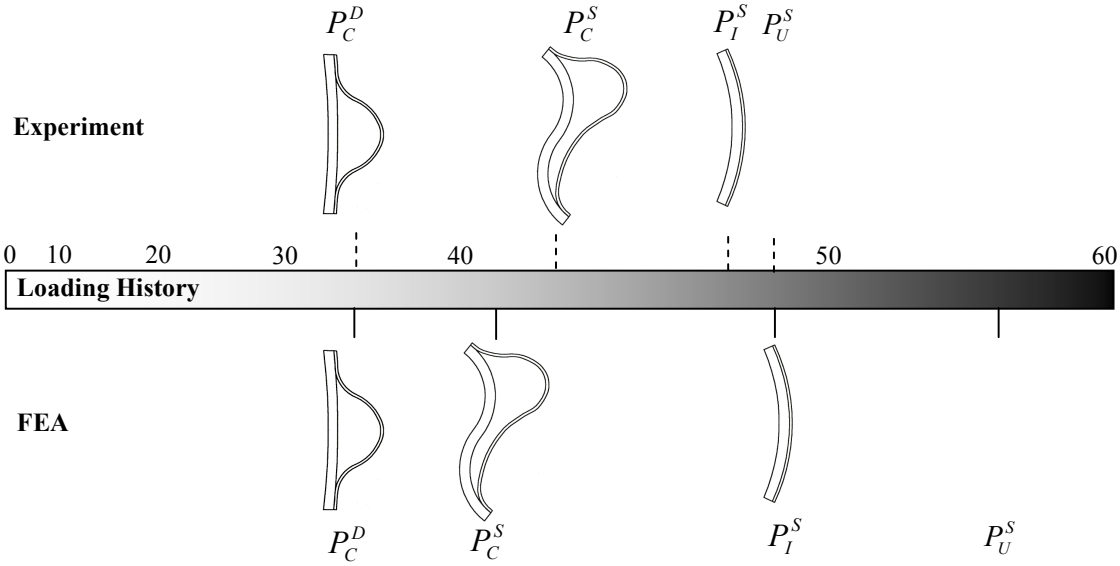

Figure 7.57. Buckling behaviour of the delaminated region of the damaged channel-section strut with n=6-Stiffener delamination, (a) as depicted by the out-of-plane displacement of the mid-point of the edge of the delamination vs load plot and (b) sketched at critical values of the loading history.

At 42 kN a sharp increase in the deflections of both sublaminates took place. By examination of the variation of the longitudinal strains across the mid-length of the left stiffener (Figure 7.58), the skin (Figure 7.59) and the delaminated right stiffener (Figure C.10), it is observed that structural buckling (P_C^S) has occurred. Structural buckling occurred in a skewed asymmetric mode that was composed of three half-sinewaves, as shown in Figure 7.60(a). A nodal line was formed in the vicinity of the delaminated region, which caused the mid-section to deform in the positive mode and the sublaminates to deflect in shear, Figure 7.57(b).

At the initial post-buckling path the deflections of the asymmetric mode developed in a stable manner that was mainly characterized by the amplification of the buckling crests, and consequently, the significant distortion of the mid-section in a positive mode. However, at 47 kN a secondary instability (P_I^S) occurred at 47 kN that instigated a dynamic mode jump to a global buckling configuration similar to the undamaged channel-section strut with positive mode of buckling (that is, Euler buckling), Figure 7.60(c). At the new equilibrium state the sublaminates were in full contact and had deformed cylindrically (global delamination buckling), Figure 7.57(b). The secondary instability in the structure is primarily portrayed by the reversal in strains of the compressed faces (that is, prior to the secondary instability) in the left stiffener and skin, Figures 7.58 and 7.59. However, the phenomenon in the delaminated region is highlighted by the consecutive reversals in strain at the inner face of the right stiffener, Figure C.10. In particular, the first reversal observed in the latter figure represents the transition of the shearing buckling mode to a global one and the second one the overall Euler buckling deformation in the channel-section strut.

Finally, failure occurred at 48 kN with excessive delamination, matrix cracking and fibre fracture at the fixed potting end, as shown in Appendix C.1. The failure mechanism was similar to the undamaged channel-section strut with a positive buckling mode. In the absence of optical or acoustic evidence of delamination growth at failure it is concluded that propagation of the delamination did not transpire.

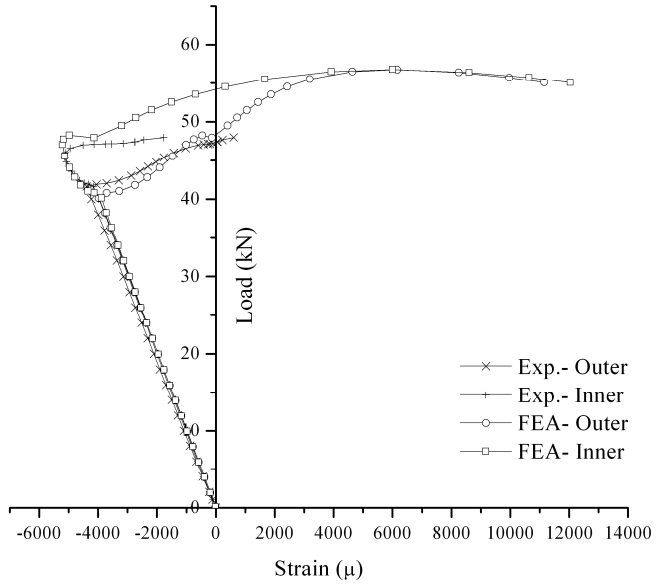

Figure 7.58. Load vs longitudinal strains at the mid-length of the edge of the left stiffener for the n=6-Stiffener channel-section strut.

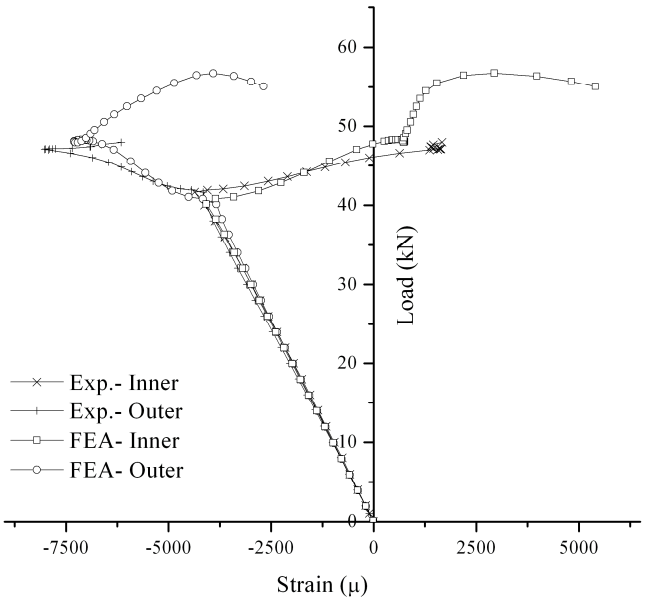

Figure 7.59. Load vs longitudinal strains at the centre of the skin for the n=6-Stiffener channel-section strut.

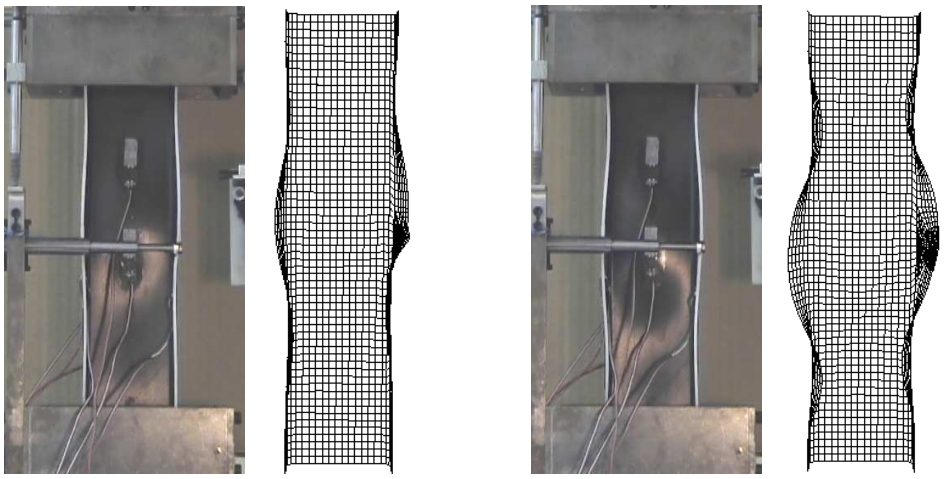

(a) (b) (c) (d)

Figure 7.60. Illustration of the experimental and FEA buckling configuration of the n=6-Stiffener damaged channel-section strut (a), (b) in the initial post-buckling range and (c), (d) after the mode jump.

FEA

The FEA analysis predicts a similar to the experimental pre-buckling deformation of the sublaminates, as is evident from their out-of-plane displacements drawn in Figure 7.57(a). Moreover, the predicted delamination buckling load is in excellent agreement with the experimental (34 kN). The thin-film buckling configuration, Figure 7.57(b), is confirmed not only by the examination of the appropriate deflections and strains, but also by investigation of the deformed shape at the critical state. Likewise, the sublaminates buckle in a closed mode. However, in correlation with the experiment the critical sublaminate experiences higher out-of-plane deflections.

This resulted in a small deviation between the monitored and predicted structural buckling load (2.5%), for the reasons stated in the previous sections. In particular, structural buckling occurs at 41 kN. The structure and sublaminates buckle in an asymmetric and shearing mode, respectively shown in Figures 7.57(b) and 7.60(b). A comparison of the above with the experimental deformed configuration of the damaged

channel-section at the initial post-buckling path shows a very good correlation. The behaviour of the damaged structure in the post-buckling region is analogous to the one observed in the experiment, and therefore, a detailed description of it would be unnecessary.

Generally, the predicted strains were found to be in good agreement with the experimental results, especially along the pre- and the majority of the post-critical path of structural buckling mode. The deviations observed in Figures 7.58, 7.59 and C.10 more likely than not reside in a small mismatch of the formulated nodal-lines in the experiment and the analysis. The secondary instability takes place at 49 kN, which is within 2% of the experiment. The small disparity probably relates to the one observed between the experimental and predicted structural buckling loads. Nonetheless, the local delamination and structural modes transcended to the global configurations identified in the experiment and shown in Figures 7.57(b) and 7.60(d) respectively.

However, the mode jump to a global buckling configuration severely affects the correlation of strains. Contrary to the experiment the finite element analysis predicts a more gradual overall buckling deformation. This observation supports once more the argument of the effect of the material nonlinearity, which becomes profound once higher deflections in the structure occur. Disregarding the material effect and taking into account the very good correlation of critical loads and strain trends across the mid-length, it could be said that the FEA results were found to be in very good agreement with the experimental data. Finally, the analysis predicts ultimate levels of loading at 57 kN.

7.3.11 General Discussion and Comparisons of the Damaged Channel-Section Struts

Delamination Buckling

It is well acknowledged that in slender structures the imperfections induced during the manufacturing process are amplified, and consequently, the pre-critical deformations

become more profound. This is particularly true for the plate segments, such as the skin of the channel-section strut, in which the imperfection amplitude coincides with the lateral displacement of the structural segment. However, the deformation of a delaminated plate prior to critical instability can significantly delay and affect delamination buckling. This was evident in the correlations drawn between the experiments and the finite element analyses of the damaged channel-section struts with skin delamination. Furthermore, it was exemplified experimentally by the repetition of the test of the *n=6-Skin* damaged, in which the incorporation of a thicker PTFE insert (0.25mm) eliminated the effect of the overall imperfection and reduced the critical load to the theoretical loading levels (Table 7.2). It should be noted that these levels for the damaged struts with skin delamination are almost identical, regardless of the method of investigation (i.e. linear and non-linear). That is, in the non-linear analyses of the damaged struts the selected overall imperfection amplitudes and modes served primarily as a convergence parameter with no significant influence on structural deformation.

As is evident from the comparison of the experimental results to the FEA in Table 7.2, the delaminations positioned near the surface of the skin (*n=2*and *n=6*) are affected most by the pre-critical deformation of the delaminated plate. In contrast, small or no increases are observed in the delamination buckling loads of the deeper-sited delaminations (*n=3* and *n=5*). This may be attributed to the rise of the bending moments acting at the critical sublaminate, as the delamination level increases and the neutral axis shifts away from the mid-surface of the surrounding laminate. Nonetheless, in Table 7.2 it is also apparent that the critical loads of symmetrically positioned delaminations - in respect to the mid-surface of the laminate - are notably different. In particular, the delaminations positioned closer to the inner face of the laminate have critical loads that are somewhat higher than the ones closer to the outer face of the laminate.

The cause of the latter discrepancy is probably a result of the local imperfections of the critical sublaminates closer to the outer of the laminate, but is also suspected that it could be related to the pre-critical deformation of the delaminated plate. That is, the pre-critical deformation of the delaminated plate effectively generates compressive and

tensile regions. Consequently, the critical sublaminates formulated by symmetric delaminations would be in a state of compression or tension depending on the relative position of the delamination (that is, in respect to the mid-surface of the laminate). Clearly, less energy would be required in order to instigate instability in the critical sublaminate from a compressive state in comparison to the one in tension. In either case, symmetry in the critical load of symmetrically positioned delaminations is broken. Nevertheless, this does not amend the variation of the delamination buckling load with the delamination level. As manifested in Table 7.2, regardless of the method of investigation, the delamination buckling load increases as the delamination level shifts towards the mid-surface of the laminate.

Channel	*ABAQUS*		*Experiment*
	Linear (kN)	*NonLinear (kN)*	*(kN)*
Damaged-Skin-2nd Level	16	16	32
Damaged-Skin-3rd Level	30	30	34
Damaged-Skin-5th Level	30	31	31
Damaged-Skin-6th Level	16	16	27
Damaged-Skin-6th Level (0.25)	(16)	(16)	15
Damaged-Stiffener-2nd Level	33	-	-
Damaged-Stiffener-2nd Level (0.25)	(33)	(-)	-
Damaged-Stiffener-3rd Level	31	35	37
Damaged-Stiffener-5th Level	31	31	31
Damaged-Stiffener-6th Level	34	34	34

Table 7.2. Comparison of the linear, non-linear and experimental delamination buckling loads for the damaged channel-section struts.

The pre-critical deformations of the delaminated plates, though, suggest that delamination buckling in a thin-film configuration, where the supporting sublaminate sustains a field of plane strain with no out-of-plane deformation prior to delamination buckling, is not a realistic scenario. However, even under the supposition of thin-film

being the configuration upon which buckling of the critical sublaminate does not result in significant deviations between the pre-critical and initial post-critical deformation path of the supporting sublaminate, this was hardly the case monitored in the experiments. At critical instability the majority of the delaminated regions buckled directly into a post-critical configuration (i.e. open or closed mode). As evident in Table 7.3, this is not in line with the thin-film predictions of the finite element analyses. Therefore, it is concluded that the delamination buckling mode is significantly affected by the compliance of the delaminated plate; a finding which was also reported by Thomson and Scott (2000).

However, the exception of the *n=6-Skin* damaged strut (in which the sublaminates buckled in a thin-film configuration) suggests that a special condition may arise upon which the compliance of the delaminated plate would not influence the delamination buckling mode. That is, the restraint imposed in delamination buckling by the pre-critical deformation of the delaminated plate is not sufficient to attain the previous deflection amplitudes that would lead to a mode change. This is more likely to occur for delaminations positioned near the surface of the laminate that despite the fact that they experience the highest restraint, their critical load is the lowest. Furthermore, comparisons of the delamination buckling configurations monitored in the experiments and predicted by the analyses (Table 7.3) reveal that the post-critical configurations that evolved in the first at critical instability are similar to those that eventually occurred in the post-critical regions of the latter. This suggests that the compliance of the surrounding plate does not possess any qualitative influence on the post-critical configuration of the sublaminates.

Thus, a critical delamination depth, where the post-critical configuration of the sublaminates switched from an open to a closed mode (or vice versa), does not exist either in theory or in practice (Table 7.3). Contrary to the delaminations positioned near the surface of the laminate, the deeper-sited delaminations deflected in different configurations. This may be related to the preferred stability (deflection) path that the structure follows upon critical instability. That is, in comparison to near-surface

delaminations in the skin, deeper-sited induce higher reductions in the stiffness of the structure, and subsequently, higher deformation of the damaged strut. In turn, this drives the deflection of the supporting sublaminates on to particular deformation path. Thus, the post-critical configurations anticipated in respect to a critical depth that was identified by coupon testing may be amended by the structural configuration.

Channel	*Critical Mode*		*Post-Critical Mode*		*At Structural Buckling*	
	ABAQUS	*Experiment*	*ABAQUS*	*Experiment*	*ABAQUS*	*Experiment*
Skin-2nd Level						
Skin-3rd Level						
Skin-5th Level						
Skin-6th Level						
Skin-6th Level (0.25)						
Stiffener-2nd Level	-	-	-	-		
Stiffener-2nd Level (0.25)	-	-	-	-		
Stiffener-3rd Level			-	-		
Stiffener-5th Level			-	-		
Stiffener-6th Level						

 :Thin-film  :Thin-film with in-plane distortion  : Opening mode

 :Closing Mode  :Shearing Mode

Table 7.3. Comparison of the buckling configurations of the sublaminates, as monitored in the experiments and predicted by the analyses.

Similar findings can be observed for the damaged channel-section struts with stiffener delamination. In particular, the free-edge delaminations positioned close to the inner face of the laminate are restrained considerably from buckling. This is evident in the deviation of the critical loads predicted by the non-linear and linear finite element analysis (Table 7.2). In contrast, very agreeable predictions are recorded for the delaminations located closer to the outer face (Table 7.2). Thus, the symmetrically

positioned free-edge delaminations do not exhibit symmetry in terms of the critical loads.

The reason for the above differences between delaminations positioned close to the inner surface and those close to the outer surface is not fully understood. However, since both the FEA and the experiments give the same results it is thought not to be related to local or overall imperfections in the experiments or numerical model set-ups. This is supported by the repetition of the test of the *n=2-Stiffener* damaged strut with a thicker PTFE insert (0.25mm). The higher amplitude local imperfection imposed in the supporting sublaminate did not result in delamination buckling, despite the significant separation of the sublaminates from initial loading conditions. Similarly to damaged channel-section struts with skin delamination, though, the variation of the critical load with delamination depth is not compromised by the aforementioned asymmetry. As is manifested in Table 7.2, regardless of the method of investigation the delamination buckling load decreases as the delamination level shifts towards the mid-surface of the laminate.

In accordance with the eigenvalue analyses, the deeper-sited delaminations in the stiffener buckled in the thin-film with in-plane distortion mode (Table 7.3). That was despite the effective restraint imposed on the free-edge delamination located closer to the inner face of the laminate. Nevertheless, the correlations drawn between the finite element analysis and experimental results of the *n=3-Stiffener* damaged strut demonstrated that the presence of a restraining mechanism (such as the local imperfection) may inflict higher in-plane distortion at critical instability. Analogous distortions, though, arise as the mode develops in the post-critical region. Therefore, it was concluded that more likely than not in the experiment buckling occurred at an early post-critical stage of the mode. This behaviour is in line with the one observed in the experiments of the damaged channel-section struts with skin delamination, in which the pre-critical deformation of the delaminated plate acted as the restraining mechanism. Likewise, a critical delamination depth is not readily defined due to the absence of

delamination buckling in the free-edge delamination located close to the inner face of the laminate.

Structural Buckling and Strength

Generally, the most critical structural position for delamination damage is the skin of the channel-section strut, where the highest reductions in the structural buckling load are observed. In particular, the deeper-sited delaminations in the skin are potentially the most dangerous for structural stability (Table 7.4). Taking into account the lowest critical load derived by the non-linear analyses of the undamaged strut composed of the M21/AS7 material system as the benchmark value, they induce reductions in the structural buckling load up to 12%. In contrast, the deeper-sited delaminations in the stiffener lead to a reduction of less than 5%. Approximately similar or lower reductions were produced by near-surface delaminations located either in the skin or the stiffener. Thus the non-linear finite element analyses, and more importantly, the tests conducted on the damaged channel-sections validate the preliminary conclusions drawn in Chapter 5, where the manner in which the delamination level and position affects structural stability has been thoroughly discussed.

However, the reduced compliance of the structure to delamination buckling may slightly reduce the degradation of structural stability. This is evident in the damaged channel-section struts with skin delaminations positioned near the surface of the laminate (i.e *n=2* and *n=6*). In relation to the non-linear finite element analyses, structural buckling in the experiments occurred at somewhat higher loading levels (5%). This reasoning was exemplified experimentally by the repetition of the test of the *n=6-Skin* damaged strut, but with a thicker PTFE insert (0.25mm). Briefly, it was concluded that the pre-critical deflections of the delaminated plate moderate the deformation of the sublaminates, and subsequently, induce milder distortions in the critical plate. Thus, a smaller reduction in the structural buckling load is observed.

.

Channel	*ABAQUS*		*Experiment*
	Linear (kN)	*NonLinear (kN)*	*(kN)*
Undamaged Channel (M21/AS7) *Positive buckling mode*	41	41*	-
Undamaged Channel (M21/AS7) *Negative buckling mode*	42	42	-
Undamaged Channel (M21/T800) *Positive buckling mode*	42	42	42
Undamaged Channel (M21/T800) *Negative buckling mode*	-	43	43
Damaged-Skin-2nd Level	40	40	42
Damaged-Skin-3rd Level	35	36	36
Damaged-Skin-5th Level	35	36	37
Damaged-Skin-6th Level	40	38	40
Damaged-Skin-6th Level (0.25mm)	(40)	(38)	38
Damaged-Stiffener-2nd Level	40	40	40
Damaged-Stiffener-2nd Level (0.25mm)	(40)	(40)	42
Damaged-Stiffener-3rd Level	39	39	39
Damaged-Stiffener-5th Level	39	40	39
Damaged-Stiffener-6th Level	41	41	42

*Benchmark value for structural buckling

Table 7.4. Comparison of the linear, non-linear and experimental structural buckling loads for the damaged and undamaged channel-section struts.

In contrast for the *n=2-Skin* damaged strut the structural buckling load monitored in the experiment is slightly higher than the benchmark value. This is in line with the findings of Falzon (2001) who observed higher critical loads in stiffened panels with circular cut-outs in comparison to the undamaged ones. This was attributed to the load path being redirected into the stiffer region of the structure. However, it was also observed that the buckling mode of the structure was significantly influenced by the presence of the damage. Thus, the structural buckling configuration of the damaged

structure corresponded to an equilibrium path with a higher bifurcation point. As discussed in the section of the undamaged channel-section struts, imperfections can induce deformations prior to structural buckling that lead to equilibrium paths with higher bifurcation points than the perfect structure. Therefore, a situation may arise upon which small reductions in the stiffness of the structure may be over-compensated by its pre-critical deformation.

The effect of the pre-critical deformation is illustrated in the non-linear finite element analyses of the symmetric delaminations located near the surface of the skin (*n=2* and *n=6*). The development of the open delamination mode for the *n=6* and *n=2* delaminations induced pre-buckling deformations in the structures such that their mid-sections to distort in the positive and negative mode respectively. This resulted in distinct equilibrium paths, and subsequently, structural buckling loads (Table 7.4). The latter phenomenon has also been observed experimentally in the repetition of the test of damaged strut with *n=2-Stiffener* delamination. The incorporation of a thicker PTFE insert instigated higher deflections in the supporting sublaminate, which in turn affected the pre-buckling deformation of the structure. Thus, the delaminated region could potentially act as an imperfection, and therefore, drive the structure to a particular equilibrium path. However, as explained earlier, this would be dependent on the relative through-thickness position of the delamination, and to an extent, the compliance of the structure to delamination buckling. Nevertheless, it appears that near-surface delaminations would be more likely to act as a driving mechanism.

Generally, though, the pre-buckling deformation of the damaged channel-section struts was not depicted in the structural buckling configurations that were generated. That is, the reduced shear stiffness of the delaminated region attracted nodal-lines of the buckling mode, which induced significant changes not only in respect to their pre-buckling deformation, but also in correlation to the structural buckling modes of the undamaged struts. Thus, it is logical to say that the presence of the delamination in the structure can have a profound effect on the structural buckling mode.

In particular, for the damaged struts with skin delamination it was observed that the shape of the buckling mode would be dependent on the delamination depth. In contrast to delaminations located near the faces of the laminate, deeper-sited delaminations induced longer half-sinewaves with milder distortions. As more thoroughly discussed in Chapter 5, this is attributed to the smaller degradation of the shear rigidity of the delaminated region, as the delamination depth shifts towards the mid-surface of the laminate. Similar disparities in the order of the buckling mode were not observed for the damaged struts with stiffener delamination, regardless the level of delamination. As argued in the eigenvalue analyses of the damaged struts, this may be attributed to the position of the delamination in a non-critical plate of the structure with no significance in reagard to the shear stiffness of the critical plate. In any case, the development of a nodal-line in the delaminated region caused the sublaminates to deflect in shear (i.e shearing mode). As is evident in Table 7.4, the ability of the critical sublaminate to penetrate the supporting one in the shearing configurations predicted in the eigenvalue analyses, essentially does not affect the structural buckling load.

The post-buckling behaviour of the damaged channel-section struts under the evolved localized buckling modes was essentially governed by the tendencies of the structure. For the channel-section strut under investigation this was portrayed by the disproportional amplification of the positive wavelengths (that is, in comparison to the negative) in a stable manner. In theory, the localized modes that evolved in the damaged struts with skin delamination under a shearing mode of the delaminated region effectively uncoupled the local-overall deformation that was observed in the undamaged channel-sections struts. Nonetheless, the subsequent degradation of stiffness of the buckled structures eventually instigated secondary instabilities, in which the localized modes jumped to global modes of deformation. More specifically, the *n=2-Skin* strut jumped to an Euler configuration similar to the *n=6-Skin* and the undamaged strut with a positive mode of buckling. In contrast, a torsional-flexural mode evolved in the deeper-sited delaminations, and was attributed to the inability of the sublaminates to escape the shearing configuration. As is evident in Figure 7.61(a), the latter mode induced a stiffer post-buckling path in the structure, and consequently, a higher ultimate load.

Realistically, the occurrence of such an event is not a plausible scenario due to the material limitations. In accordance to Gu and Chattopadhyay (1999) the post-buckling strength of a delaminated plate would be dependent on the load-carrying capability of the supporting sublaminate. Therefore, in comparison to near-surface delaminations, the reduced bending stiffness of the supporting sublaminate in deeper-sited (delaminations) implies higher bending stresses at comparable levels of loading, and consequently, earlier material failure. Moreover, delamination growth can significantly impair the post-buckling capacity of laminated plates/structures by inducing failure at sufficiently lower levels of loading than the post-buckling strength of the sublaminates. In the experiments the channel-section struts with deeper-sited delaminations in the skin failed at significantly lower levels of loading in comparison to the near-surface ones, Figure 7.61(b).

However, in accordance with knowledge gained by tests conducted at the coupon level this would appear to be a paradox. That is, the critical depth for delamination growth has been identified at 10-20% of the laminate thickness (Butler et al., 2007), in which the sublaminate configuration is the open mode. As a consequence, the delamination propagates under the lowest fracture energy mode (i.e. Mode I) and results in failure at sufficiently lower levels than deeper-sited delaminations, which propagate in Mode II due to the closed mode of the sublaminates (Chai and Babcock, 1985).

The reason for this lies in the structural configuration. In particular, even for sufficiently high structural buckling loads/strains, for which the channel-section struts were designed, delamination growth did not take place prior to structural instability. That is, the stress redistribution within the structure prevented large deformations in the sublaminates. Consequently, the sublaminates did not attain the required energy to initiate fracture. At structural instability the deeper-sited delaminations buckled in the shearing mode, which induced high transverse shear stresses at the delamination front. However, the increased depth of the delamination amplified the latter stresses, and

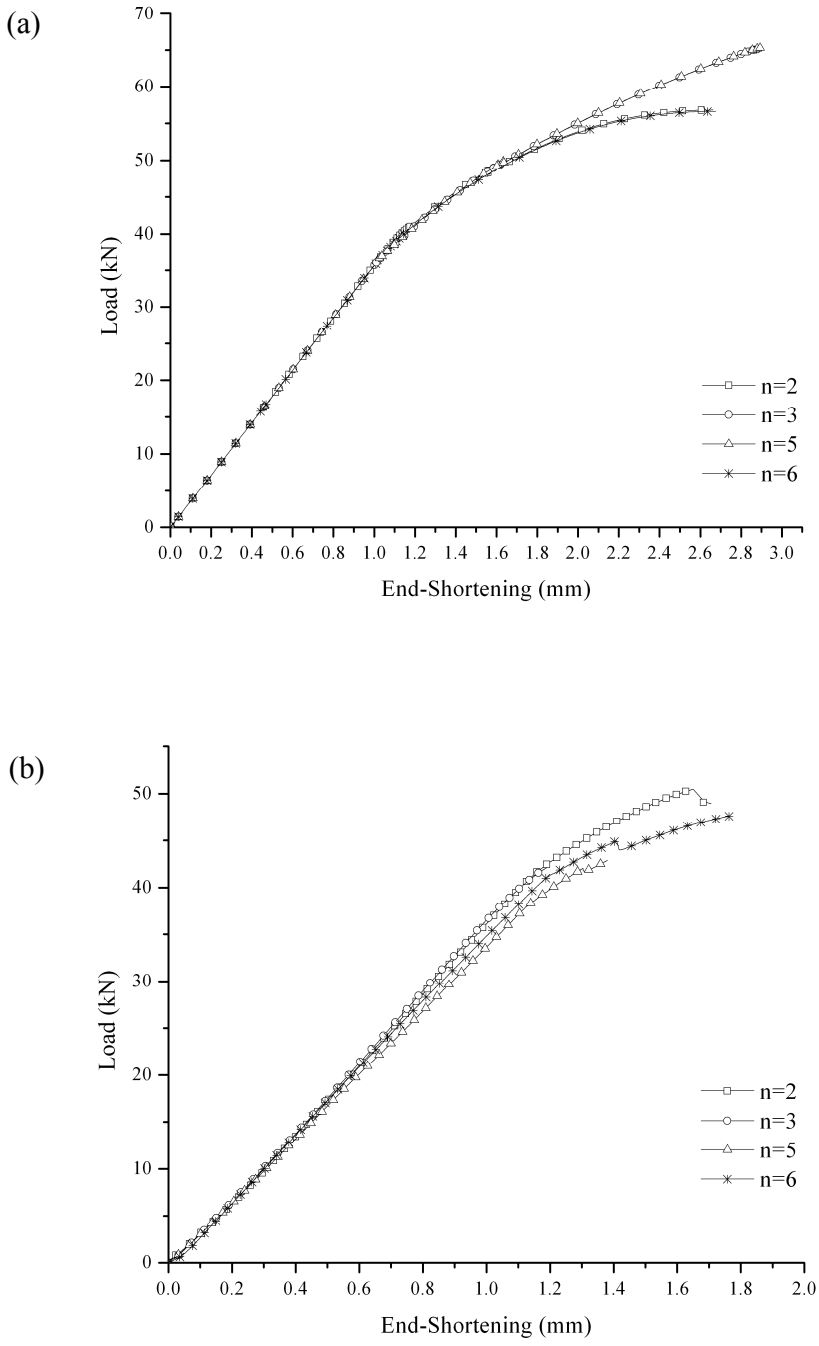

Figure 7.61. Comparison of the (a) FEA and (b) experimental end-shortening versus the applied compressive load plots for the damaged channel-section struts with skin delamination.

subsequently, instigated the shear mode (i.e. Mode II) fracture process at particularly low levels of loading. This is evident in view of the fact that the shearing mode in the *n=2-Skin* damaged strut (near-surface delamination) did not initiate delamination growth. In contrast, the open mode of delamination that was developed in the *n=6-Skin* damaged strut caused delamination growth, but at sufficiently higher loading levels than the shearing mode of the deeper-sited delaminations. Thus, at the structural level deeper-sited delaminations are established to be the most dangerous scenario for the structural strength.

This is also in agreement with the channel-section struts with stiffener delamination, Figure 7.62(a). Delamination growth was instigated at deeper-sited delaminations in the stiffener, and consequently, the highest reductions in the structural strength were monitored. However, the finite non-linear analyses demonstrated that deeper-sited delaminations in the stiffener possessed a more debilitating effect on the structural strength even in the absence of the material limitations, Figure 7.62(b). That is, the stiffeners' performance is directly related to the load-carrying capability of the structure. The higher reductions induced by deeper-sited delaminations in the bending stiffness of the stiffeners effectively weakened their performance.

The majority of the delaminations located in the stiffener did not induce secondary instabilities. The reasoning probably lies in the reduced torsional rigidity of the delaminated region, which allows the asymmetric evolution of the positive half-sinewaves towards the latter [for example see Figure 7.52(d)]. Thus, the localized buckling modes progressed in a stable manner into a torsional-flexure mode of global deformation. Nonetheless, the mode-jump predicted and observed in the *n=6-Stiffener* strut in an Euler configuration suggests that this would be dependent on the initial structural buckling mode.

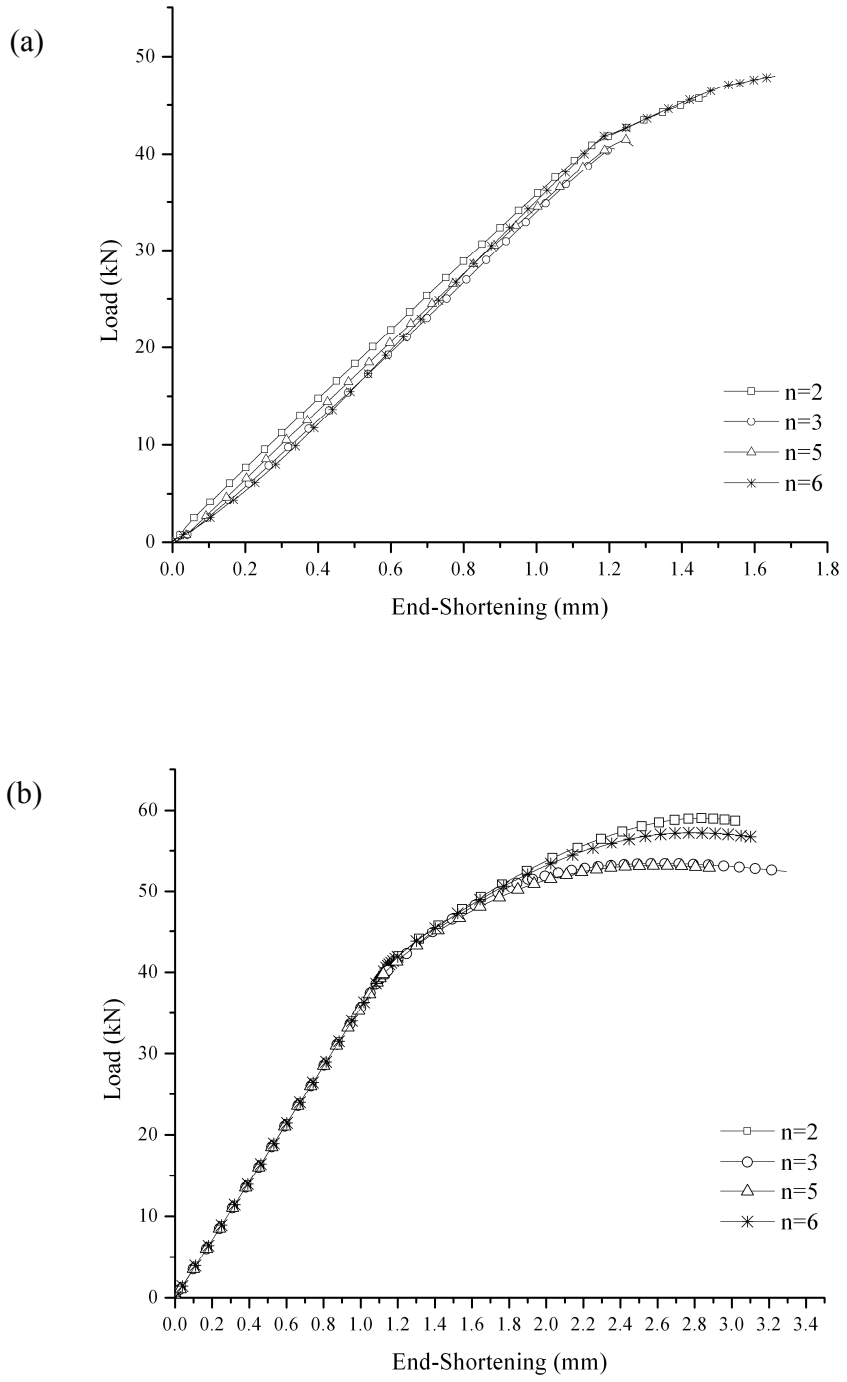

Figure 7.62. Comparison of the (a) experimental and (b) FEA end-shortening versus the applied compressive load for the damaged channel-section struts with stiffener delamination.

Generally, it could be argued that the de-coupling of the local-overall deformation that was induced by the presence of the delamination acted beneficialy in terms of the structural strength. Theoretically, only deeper-sited delaminations in the stiffener would result in a reduction in the structural strength. In relation to the undamaged channel-section strut with positive mode of buckling, for which the lowest ultimate load was observed, a 7% decrease was predicted. Experimentally, the latter percentage was about 15 % due to the aforementioned material limitations (i.e. strength and non-linearity) and delamination growth. The latter, also induced a significant reduction in the structural strength of the damaged struts with deeper-sited delaminations in the skin (13%). However, taking into account both the experimental and numerical results it is evident that the most dangerous delamination position for the structure is in the stiffener. Near-surface delaminations either in the skin or stiffener had small or no effect on the structural strength. More importantly, though, for any location or level of the delamination the structural strength did not fall below the design limit load. The ultimate loading levels predicted by the non-linear analyses and monitored in the experiments have been summarized in Table 7.5.

Finally, it is worth noting that in accordance with Falzon and Hitchings (2003) mode jumping could severely affect the structural integrity of the component. That is, the oscilating stresses generated during this process promote the onset of delamination growth. This is suspected to be the case for the *n=2-Skin* damaged strut, in which the mode jump to a global mode of deformation probably instigated delamination growth in Mode I. However, from the test conducted on the remaining channel-sections struts with skin delamination, this appears to be a reciprocal phenomenon. That is, delamination growth in the latter tests preceded structural instability. Even though, this did not induce a mode change in the structure, nevertheless it accelerated somewhat the evolution of the buckling mode. It could be said that this is a qualitative difference between the secondary instabilities that arise in the delaminated structure, as a result of structural instability (i.e mode-jumping) and delamination growth.

Channel	*ABAQUS (kN)*	*Experiment (kN)*
Undamaged Channel (M21/AS7) Positive buckling mode	57*	-
Undamaged Channel (M21/AS7) Negative buckling mode	63	-
Undamaged Channel (M21/T800) Positive buckling mode	59	48*
Undamaged Channel (M21/T800) Negative buckling mode	65	51
n=2-Skin	57	51
n=3-Skin	65	42
n=5-Skin	65	42
n=6-Skin	57	48
n=6-Skin (0.25mm)	(57)	45
n=2-Stiffener	59	46
n=2-Stiffener (0.25mm)	(59)	46
n=3-Stiffener	53	41
n=5-Stiffener	53	41
n=6-Stiffener	57	48

*Benchmark value for structural strength

Table 7.5. Comparison of the non-linear analyses and experimental ultimate loading levels for the damaged and undamaged channel-section struts

7.4 Concluding Remarks

This Chapter covers the main bulk of work and findings of this thesis. To avoid repetition an overall summary is presented in Chapter 8.

Chapter 8

Conclusions and Future Work

8.1 Concluding Remarks

In the current work, the tolerance and structural behaviour of an integrally composite stiffened structure with artificial delaminations located in a variety of through-thickness positions in the skin and stiffener plate segments was investigated both theoretically and experimentally. The selected geometry was a channel-section strut, in view of the fact that such geometry bares comparisons with stiffened panels. The channel-section was designed to buckle (DUL) at somewhat higher levels of strain than the current industrial specifications and allowed for sufficient post-buckling strength.

The work conducted provides a significant contribution in the understanding of the effect of delamination damage in the structural level and explores the limitations of weight reductions in composite stiffened structures. Generally, deeper-sited delaminations in the skin are potentially the most dangerous scenario for structural stability, while deeper-sited delaminations in the stiffener are the most hazardous for the load-carrying capacity of the structure. For well designed composite structures in the sense that sufficient post-buckling strength allowables are provided, the design ultimate loading conditions (DUL) will not be compromised even in the presence of significant delaminations, regardless their location within the structure and depth. Thus, reductions in weight of composite stiffened structures may be achieved by designing for higher buckling strain allowables without comprising safety requirements.

8.2 Achievements and Findings

The design of the channel-section strut was based on the simplified Shanley model. The methodology developed was found to be in good agreement with the FEA for an infinite length strut and particularly successful in reducing the parametric investigation of the geometry of a finite length composite strut to the absolute minimum (i.e. length of the strut). Similarly, the design of the delaminated structures was based on a semi-analytical and semi-numerical approach that allowed the estimation of the critical load. Correlations with experimental results on delaminated coupons, found in literature, and the eigenvalue analyses of the damaged struts validated to a satisfying extent the efficiency of the method developed. Both the aforementioned methodologies developed offered significantly less computational and labour cost in comparison to the more complex finite element designs.

A number of material-test coupons, undamaged and damaged channel-sections were manufactured and tested. Significant experience and knowledge was gained in the manufacturing processes involved in composite structures. A single-tool lay-up method was developed as an alternative to the two-part manufacturing process of channel-section struts currently utilized that requires more labour and could potentially introduce damage during the transfer of the laminate from the lamination to the curing tool. Furthermore, an efficient and accurate trimming system was produced for composite structures in order to ensure the loading edges were flat and parallel. This is a significant issue for the thinner walled structures, where the deviations from the latter conditions are considerable.

More importantly, it was demonstrated that scaling down the thickness of the laminate may give rise to notable bending-coupling twisting effects (in the laminate). At global instability, the latter coupling promoted material non-linearity and reduced the ultimate loading capacity of the structure. Therefore, it is concluded that composite stiffened structures intended to operate in the post-buckling region would be more efficient if they were designed to fail under local buckling deformation. The exact

percentage in the reduction of the ultimate load due to material non-linearity could not be accurately established, but in accordance with the material tests conducted a reduction of 9% and 18% was recorded for the axial compressive and shear modulous respectively. Thus, the non-linear elastic nature of CFRP is a significant design issue, which contrary to current practice must be taken into account for highly strained post-buckling laminates.

The rather conservative material values utilized in the industry, known as the B-basis, may somewhat moderate the disparity of the predicted and actual ultimate loading capacity of a composite, but could also lead to underestimation of the critical loading levels. Furthermore, design approximations that were found to be standard practice in the literature could result to unrealistic overall stiffness estimations. In particular, the exclusion of the structural parts potted in the resin blocks produced a 16% increase in the pre-buckling stiffness in relation to the experimental. Thus, the boundary conditions severely affect the stiffness distribution in the structure by the formation of areas of localized stiffness, which even in the pre-buckling state (uniform strain) may vary significantly in relation to the overall stiffness of the structure.

In accordance with the literature the channel-section strut was rather insensitive to overall imperfections, but significantly influenced by local ones. Both amplitude and configuration were found to be significant factors. Furthermore, it was demonstrated that the bifurcation point of channel-section geometry was asymmetric and tilted. In accordance to the structural buckling mode, increased and reduced couplings with the global mode of deformation were generated and leading respectively to higher and lower ultimate loading levels. Therefore, it is suggested that particular imperfection configurations and amplitudes could act beneficially in terms of the structural integrity of the channel-section strut.

The structural configuration exhibits a significant effect on the delamination buckling mode due to the ability to redistribute the stress within the adjoining plate segments, and therefore, prevent large deformations at the delaminated region. Thus,

contrary to the general perception established by coupon testing, in the finite element analyses of the damaged struts the deeper-sited delaminations buckled in a thin-film configuration. For the deeper-sited delaminations in the stiffener a particular case of thin-film buckling with in-plane distortion was discovered. This depicted the lowest energy mode in the delaminated stiffener. The variation of critical strain varies in accordance to the delamination depth and the structural location. For the damaged channels with skin delamination the critical load increased with depth. By contrast, for the ones with stiffener delamination it decreased.

Pre-critical deformations induced by imperfections in the damaged structure and non-linear geometric effects can reduce the compliance of the structure to delamination buckling. This may affect the delamination buckling load, the delamination buckling mode and/or the post-critical configuration. The manner upon which the latter parameters are affected is dependent on the position of the delamination within the structure, the delamination level and the relative position of the delamination in respect to the mid-surface of the laminate. The reduced compliance of the structure to delamination buckling affects the most the delamination buckling loads of the near-surface delaminations and in particular the ones positioned towards the inner face of the structure. Furthermore, restraining mechanisms in delamination criticality trigger a post-critical delamination mode of deformation. Generally, delamination buckling at the structural level is not a symmetric phenomenon, as observed in delaminated coupons.

Thus a critical depth, where the post-critical configuration of the sublaminates switches from an open to a closed mode (or vice versa) does not exist in any structural position. By contrast, a critical depth that separates competing mechanisms of pre-buckling deformation was identified for the damaged channel-section struts with skin delamination. The delamination buckling modes of near-surface delaminations are more likely to drive the damaged structure to particular equilibrium paths. By contrast, the buckling modes of deeper-sited delaminations are more likely to be influenced by the preferred stability (deflection) path of the structure.

The depth and structural location of the delamination exhibits a significant effect upon the structural buckling load. Delaminations positioned in the critical plate segment (i.e. skin) are the most dangerous for structural stability, while the deeper-sited delaminations induce the highest degradation of the structural buckling load. In relation to the undamaged channel-section strut, the deeper-sited delaminations in the skin caused a reduction of 12%. By contrast, the deeper-sited delaminations in the stiffener led to a reduction of less than 5%. Similar, lower or no reductions were produced by near-surface delaminations located either in the skin or the stiffener. The occurrence of the latter event is dependent on the pre-buckling equilibrium path of the structure and the pre-critical deformation of the delaminated plate.

The presence of the delamination in the structure has a profound effect in the structural buckling mode. At structural instability the reduced shear stiffness of the delaminated region attracted nodal-lines of the buckling mode, and therefore, induced significant changes in correlation to the structural buckling modes of the undamaged struts and their pre-buckling deformation. For the damaged struts with skin delamination the configuration of the buckling mode is dependent on the delamination depth. By contrast, the configuration of the buckling mode of the damaged struts with stiffener delamination does not alternate in respect to the level of delamination. The development of a nodal-line in the delaminated region causes the sublaminates to deflect in a shearing mode of deformation.

In the absence of material limitations and delamination growth, the actual effect of the delamination in the post-buckling response of the strut is primarily dependent on the structural position of the delamination and to a smaller extent on the delamination depth. The presence of the delamination in the majority of damaged struts with skin delamination effectively uncoupled the local-overall deformation, but induced mode-jumping to the global modes of deformation. The latter modes are dependent on the delamination depth. By contrast, the post-buckling path of the majority of the damaged struts with stiffener delamination developed in a stable manner. The global mode of deformation was significantly affected by the local degradation of stiffness in the

delaminated region. In the finite element analyses only deeper-sited delaminations in the stiffener possessed a debilitating influence in the structural strength.

Contrary to delaminated coupons, at the structural level deeper-sited delamination are established to be the most dangerous scenario for the structural strength. The shearing configuration in conjuction with the high transverse shear stresses that arise at the front of deeper-sited delaminations instigate the shear mode (i.e. Mode II) fracture process at particularly low levels of loading. The highest reductions in the structural strength were monitored in the damaged struts with stiffener delamination that accounted for a 15 % cutback in relation to the undamaged strut. Significant reductions in the structural strength of the damaged struts with deeper-sited delaminations in the skin (13%) were also observed. By contrast near-surface delaminations either in the skin or stiffener had a small or no effect in the structural strength. Finally, delamination growth may accelerate the evolution of the structural buckling mode, but mode jumping may instigate delamination growth.

8.3 Future Work

The methodology developed in Chapter 4 for modeling the delamination buckling load has already been incorporated in the investigation of the compressive strength of delaminated plates with enclosed delaminations (Butler et al, 2007) and with particular success. Modeling the buckling load and threshold load for delamination gowth of the particular thin-film configuration with in-plane distortion that was discovered in this work is an area of great interest, which is currently being investigated by these authors.

The inclusion of structural interactions in the design methodology developed for the undamaged channel-section strut could prove to be a very efficient tool in the design of composite stiffened structures. Ultimately the model is intended to incorporate damage considerations, which currently suffer from lack of analytical solutions and extremely complicated numerical models.

Furthermore, it would be of great interest for design purposes to investigate the influence of the laminate architecture of stiffened structures on material non-linearity and compare experimental results with those obtained by commercial FEA packages, such as ABAQUS.

Finally, the restraint imposed by the channel-section strut in the delaminations positioned towards the inner face of the stiffener is an issue which ought to be investigated further.

Appendices

Appendix A

A.1 Correlation of the Critical Delamination Load to Axial Strain

In accordance to the Classical Lamination Theory the in-plane strain field acting on the laminate, is correlated to the in-plane forces as follows;

$$\begin{aligned} N_x &= A_{11}\varepsilon_X + A_{12}\varepsilon_y + A_{16}\gamma_{xy} + B_{11}\kappa_x + B_{12}\kappa_y + B_{16}\kappa_{xy} \\ N_y &= A_{12}\varepsilon_X + A_{22}\varepsilon_y + A_{26}\gamma_{xy} + B_{12}\kappa_x + B_{22}\kappa_y + B_{26}\kappa_{xy} \\ N_{xy} &= A_{16}\varepsilon_X + A_{26}\varepsilon_y + A_{66}\gamma_{xy} + B_{16}\kappa_x + B_{26}\kappa_y + B_{66}\kappa_{xy} \end{aligned} \tag{A.1}$$

For a balanced-symmetric laminate the *B*-matrix and the extensional coupling terms are zero. Thus, for the laminate under discussion, subject solely to axial loading, the above equation reduces to,

$$\begin{aligned} N_x &= A_{11}\varepsilon_X + A_{12}\varepsilon_y \\ 0 &= A_{12}\varepsilon_X + A_{22}\varepsilon_y \\ 0 &= A_{66}\gamma_{xy} \end{aligned} \tag{A.2}$$

which yields the strain ratio,

$$\varepsilon_y = -\frac{A_{12}}{A_{22}}\varepsilon_x \tag{A.3}$$

Substituting the latter strain ratio in the axial load equation we have

$$N_x = \left(A_{11} - \frac{{A_{12}}^2}{{A_{22}}^2} \right)\varepsilon_x \tag{A.4}$$

And multiplying the load with the width of the laminate in order to convert the load per unit width to load, we have:

$$P = b_y \left(A_{11} - \frac{{A_{12}}^2}{{A_{22}}^2} \right) \varepsilon_x \qquad \text{(A.5)}$$

Appendix B

B.1 Manufacturing Process for the Material-Test Coupons

Lay-up Process

Both in-plane shear and compression material testing were to be conducted according to the international standards procedures detailed in *EN ISO 14129:1998* and *EN ISO 14126:1999* respectively. According to the latter, the *Type A* specimens were preferred for the determination of the material properties under discussion. *Type A* specimen is a fixed thickness end-tabbed, and non-tapered, laminated coupon composed by unidirectional fibre reinforced laminas with specified orientations, Figure B.1. In particular, for the axial and transverse compression material tests their lay-ups are constructed solely by 0^0 and 90^0 respectively, while for the in-plane shear material test a balanced symmetric lay-up of $\pm 45^0$ is required. Since the cured thickness t_{ply} of the M21/35%/268/AS7 prepreg was *0.25 mm*, the resulting lay-ups, which would satisfy the proposed thicknesses for the *Type A* specimens, were $[0^0]_8$ and $[90^0]_8$ for the axial and transverse compression test-coupons respectively, Figure B.1(a) and $[45^0/-45^0/45^0/-45^0/45^0/-45^0/45^0/-45^0]_s$ for the in-plane shear test-coupons, Figure B.1(b).

The *5* test-coupons required for each test were produced from a single laminated plate that was constructed for each specimen, by cutting laminas in the appropriate orientations and dimensions, which were obtained as follows,

$$\textit{Lamina length} = 5 \times (\textit{Required specimen length}) + 4 \times (\textit{Edge trimming length})$$

and

$$\textit{Lamina width} = 5 \times (\textit{Required specimen width}) + 4 \times (\textit{Edge trimming length})$$

Where, the required dimensions of the in-plane compression and shear coupons have been summarized in Table B.1. It should be noted that the selected factor of *4* selected for the trimming length arises from the fact that the operation under discussion would occur twice for each edge of the laminate (before and after tabbing, as it will be discussed further in due course).

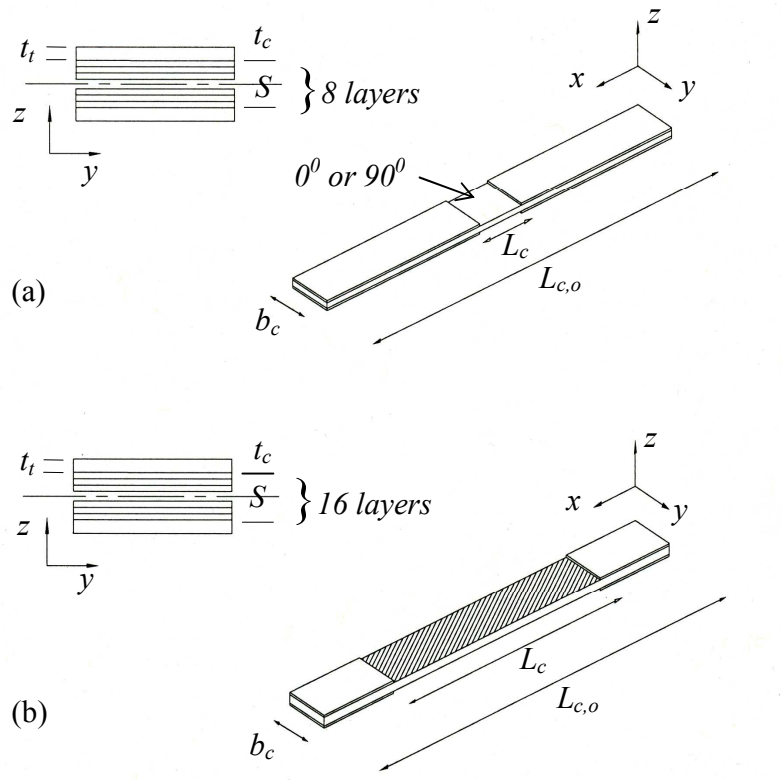

Figure B.1. Illustration of (a) the axial and transverse and (b) in-plane shear material-test coupons Type A.

	t_c	t_t	b_c	L_c	$L_{c,o}$
Compression Coupons	2	1	10	10	110
Shear Coupons	4	1	25	150	250

Table B.1. Dimensions (all in *mm*) of the axial and transverse compression and in-plane shear material-test coupons.

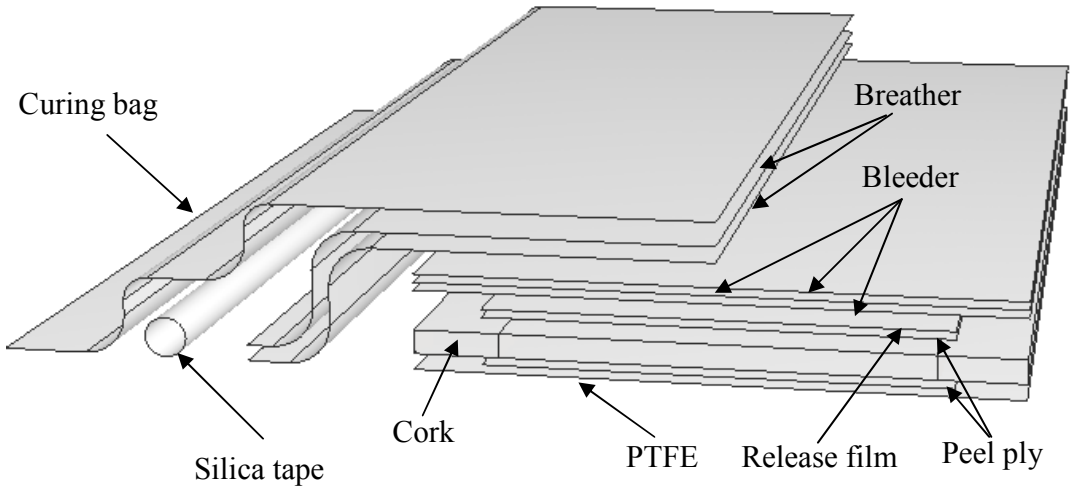

Figure B.2. Bagging systems for for the material-test coupons.

The material test coupons were laminated on a PTFE sheet that was adhered on a steel table, which had been thoroughly cleaned from grease and foreign particles. The PTFE is incorporated in order to allow separation of the laminate from the laying-up surface after curing of the specimen. In addition, during the adhering process care was taken to alleviate any trapped air that could potentially comprise the quality of the laminate (i.e. scratches in the surface by wrinkles in the PTFE film or out-flatness of the laminate by the trapped air underneath). Prior to the lamination of the first layer the local area was heated in order to soften the layer and increase its adhesive qualities, or otherwise, assist in preserving the laminate in position. The uncured layers were laminated face-to-face with the aid of a square steel block that certified alignment of the fiber orientation in the required angles to the principal axis of the laminate. Finally debulking and bagging of the coupons was conducted on the same principles presented in Chapter 6. An illustration of the bagging system is shown in Figure B.2.

Tabbing of the Material-Test Coupons

Following the curing cycle of the M21 epoxy resin, presented in Chapter 6, the edges of the material-test plates were trimmed (*5 mm*). However, prior to cutting the material-test plates into strips/coupons, bonding of tabs was required. Since the tabs were responsible for the transmission of load to the specimen, the quality of the bond was essential. Therefore, the surfaces of the coupon were filed with fine wet abrasive paper (400-grit) in order to remove any surface imperfection that may existed, but more importantly to improve their susceptibility to bonding. The surfaces were immediately cleaned with acetone. The fiberglass tabs and the high shear-strength epoxy adhesive layer (Redux 322) were cut into shape and size and positioned accurately on the surfaces of the laminates. Steel sheets of similar thickness to tabs, which were covered with the aforementioned release agent, were fitted at the unsupported faces of the plates. That is, during curing cycle the laminates, and in particular the unidirectional (which display lower flexural stiffness), would have distorted due the absence of a flat surface. All the laminates were bagged, Figure B.3, and cured for 1 hour at 175^0 C (heat up rate of 3^0 C/min) and under a 73.5 psi pressure. Finally, all the material-test coupons produced were found to be within the tolerance margins specified by ISO.

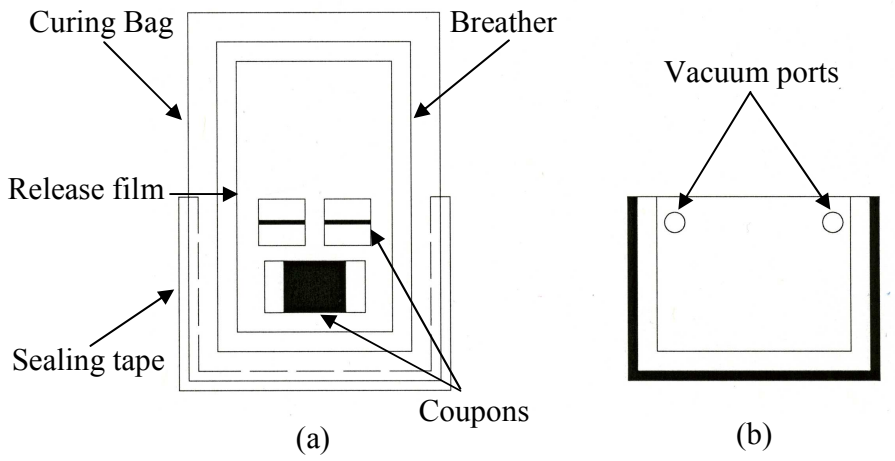

Figure B.3. (a) Open and (b) closed envelope type bagging system for curing of the adhesive bonding layer between the material-test laminates and the tabs.

B.2 Experimental Set-up and Testing of the Material-Test Coupons

The compressibility and shear deformation of the material-test coupons were monitored with the aid of strain-gauges. In particular, 2 and 4 strain-gauges were attached in the compression-test and the in-plane shear-test coupons respectively, as shown in Figure B.4. All the strain-gauges were positioned to measure the strain in the axial direction, except in the case of the in-plane shear-test coupons where readings both in the axial and transverse direction were required, Figure B.4(b).

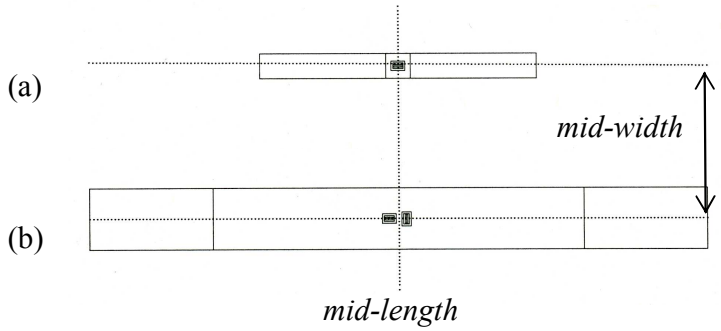

Figure B.4. Plan view of the back-to-back strain gauges positioned in (a) the compression-test coupons and (b) the in-plane shear-test coupons.

Testing of the Compression-Test Coupons

In accordance with EN ISO 14126:1999 the Celanese Fixture, Figure B.5, was employed to test the Type A axial and transverse compression coupons. The specified fixture restricted the out-of-plane displacements of the coupons, while allowing a uniform strain of the material. Two loading plates (the faces of which were machined to the highest possible accuracy) were attached to the tension/compression "Instron 1332" testing machine. The Celanese fixture was positioned within the testing machine, taking care that its center was aligned with that of the loading head of the machine. The back-to back strain gauges were connected to the Spider-8 600Hz data acquisition system and the output was fed into the computer database that also monitored the load and displacement of the loading head. The specimens were loaded in compression until failure under a controlled end-shortening speed of 1 mm/min.

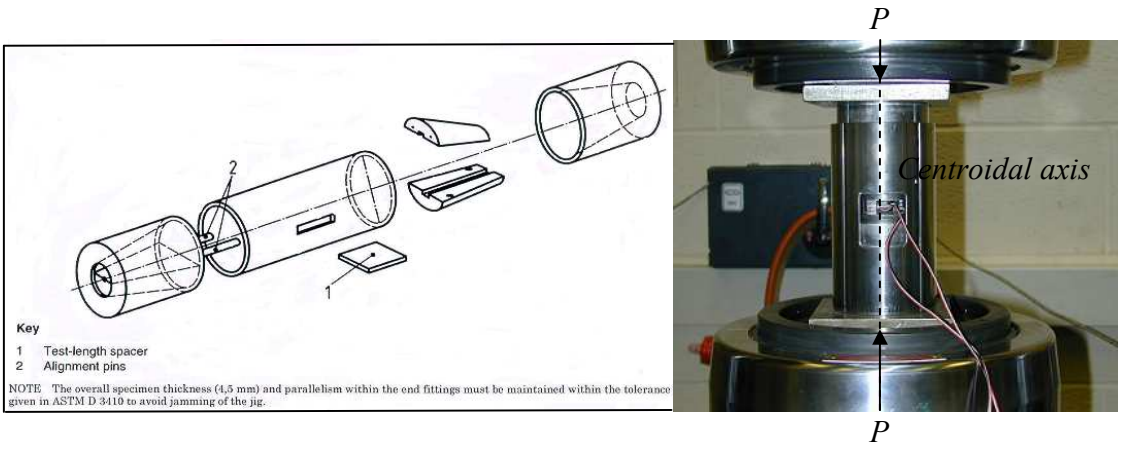

Figure B.5. Illustration of the components of the Celanese Fixture (taken from EN ISO 14126:1999) and loading action in the tension/compression testing machine.

Figure B.6. Illustration of the tensile experimental set-up for the determination of the in-plane shear properties.

Testing of the In-Plane Shear-Test Coupons

In accordance to *EN ISO 14129:1998* the tensile method was utilized in order to determine the in-plane shear properties of the material. In particular, the specimen was placed between the jaws of the tension/compression "Instron 1332" testing machine, ensuring once more alignment of the longitudinal axis of the testing machine to the specimens, Figure B.6. The pairs of back-to back strain gauges were connected to the Spider-8 600Hz data acquisition system and the output was fed into the computer database that also monitored the load and displacement of the loading head. Finally, the specimens were loaded in tension with a controlled end-shortening absolute speed of 2 mm/min until failure. It should be noted that failure did not necessarily imply material failure but strains in excess of 5%, where the tests where terminated.

B.3 Axial and Transverse Compression Modulus

In accordance with EN ISO 14126:1999 the axial and compressive modulous would be calculated within the region of 500-2500 micro-strain (approximately) according to the following formula:

$$E_c = \frac{\sigma_c^{''} - \sigma_c^{'}}{\varepsilon_c^{''} - \varepsilon_c^{'}} \tag{B.1}$$

Where $\sigma_c^{''}, \sigma_c^{'}$ are the compressive stresses at 500 and 2500 μ-strain respectively, and $\varepsilon_c^{''}$, $\varepsilon_c^{'}$ are the shear strains at 500 and 2500 μ-strain respectively. The compressive stresses are given by,

$$\sigma_c = \frac{F}{b_c t_c} \tag{B.2}$$

Where F is the compressive load, b_c is the specimen width and t_c the thickness. The measured geometry of each coupon has been summarized in Table B.2 and Table B.3.

	Dimensions				
	Overall length (mm)* *ISO:* $L_{c,0}$*=110±1*	*Width (mm)* *ISO:*b_c*=10±0.5*	*Thickness at the gauge (mm)* *ISO:* t_c*=2±0.2*	*Thickness at the tabs (mm)* *ISO:* t_c+2t_t*=4±0.2*	
C01	110.87	10.49	2.01	4.32	4.43
C02	110.73	10.39	2.02	4.43	4.48
C03	110.51	10.42	2.04	4.54	4.61
C04	111.32	10.46	2.03	4.49	4.45
C05	110.29	10.47	1.99	4.65	4.56

*All the specimen had longitudinal edges parallel within the 0.2 mm margin specified by ISO.

Table B.2. Geometry of the axial compression test-coupons

	Dimensions				
	Overall length (mm)* *ISO:* $L_{c,0}$*=110±1*	*Width (mm)* *ISO:*b_c*=10±0.5*	*Thickness at the gauge (mm)* *ISO:* t_c*=2±0.2*	*Thickness at the tabs (mm)* *ISO:* t_c+2t_t*=4±0.2*	
C901	111.60	10.49	2.09	4.48	4.49
C902	110.92	10.42	2.03	4.54	4.58
C903	110.19	10.44	2.02	4.55	4.68
C904	109.55	10.43	2.02	4.66	4.64
C905	110.51	10.49	2.03	4.52	4.48

*All the specimen had longitudinal edges parallel within the 0.2 mm margin specified by ISO.

Table B.3. Geometry of the transverse compression test-coupons

The specified stresses are obtained by the individual stress-strain relationships, illustrated in Figures B.7 and B.8 and summarized in Tables B.4 and B.5. It should be noted that the modulous prediction of each specimen is considered to be the mean value of the measurements taken from Side A and Side B, while the compression modulous would be the mean value of all five specimens in each case. Furthermore, the ultimate stresses illustrated in the graphs do not necessarily correspond to failure stresses, but to the selected maximum measuring range of the strain-gauge data acquisition system.

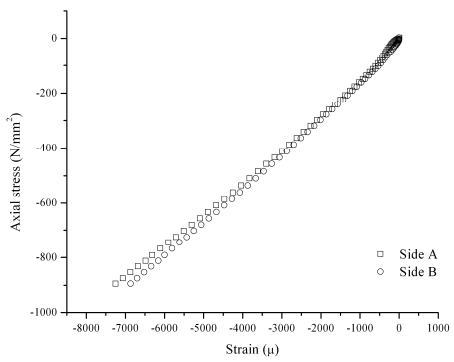

C01

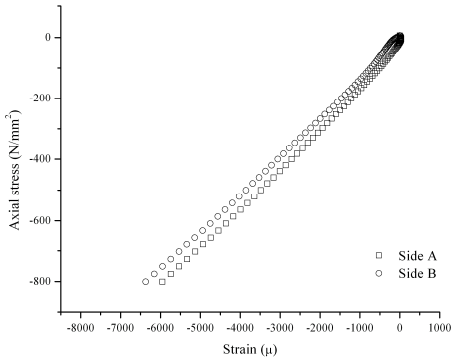

C02

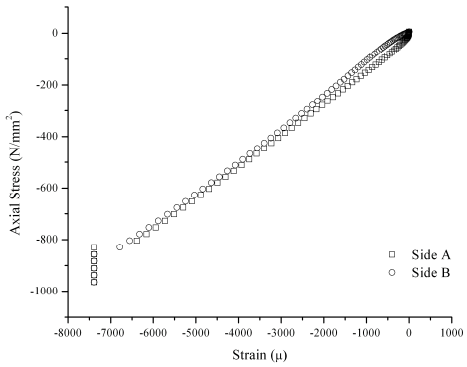

C03

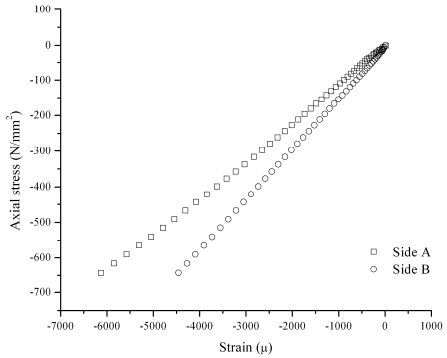

C04

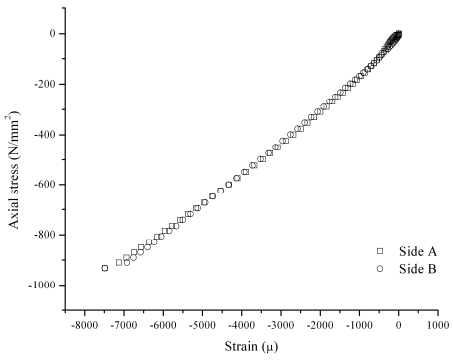

C05

Figure B.7. Stress-strain relationships of the axial compression test-coupons.

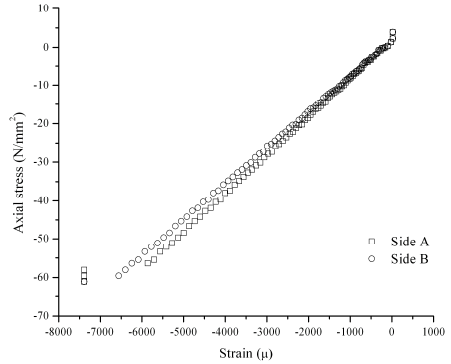

C901

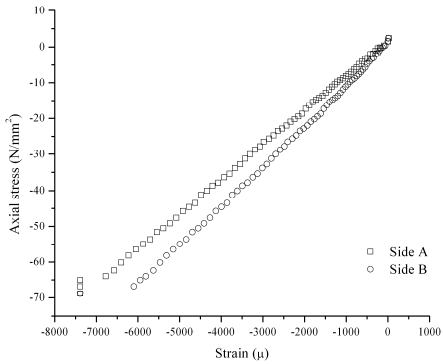

C902

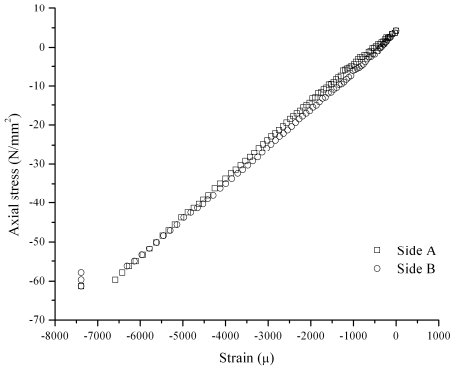

C903

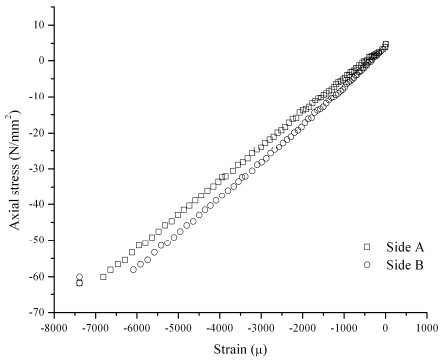

C904

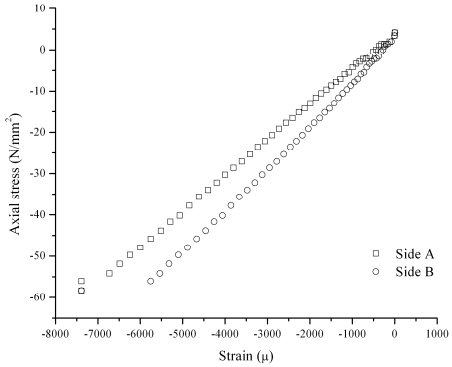

C905

Figure B.8. Stress-strain relationships of the transverse compression test-coupons.

		$\sigma_C^{''}$ (N/mm^2)	$\sigma_C^{'}$ (N/mm^2)	$\varepsilon_C^{''}$ (μ-strain)	$\varepsilon_C^{'}$ (μ-strain)	$E_{11,s}$ (kN/mm^2)	$E_{11,c}$ (kN/mm^2)
C01	*A*	-348.409	-84.282	-2497.14	-505.143	132.388	131.21
	B	-363.054	-98.186	-2514.29	-508.343	130.040	
C02	*A*	-369.902	-101.30	-2485.26	-494.629	134.933	134.90
	B	-329.519	-62.399	-2492.80	-512.457	134.885	
C03	*A*	-336.002	-84.377	-2503.89	-494.423	125.219	129.69
	B	-311.916	-41.796	-2520.79	-507.493	134.167	
C04	*A*	-336.002	-84.377	-2503.89	-494.423	125.219	127.31
	B	-311.916	-41.796	-2520.79	-507.493	134.167	
C05	*A*	-383.000	-99.350	-2560.00	-512.743	138.600	136.51
	B	-368.400	-95.700	-2514.29	-486.400	134.460	

Table B.4. Tabulated results obtained by the stress-strain relationships of the axial compression test coupons along with the calculated axial compressive modulus.

		$\sigma_C^{''}$ (N/mm^2)	$\sigma_C^{'}$ (N/mm^2)	$\varepsilon_C^{''}$ (μ-strain)	$\varepsilon_C^{'}$ (μ-strain)	$E_{11,s}$ (kN/mm^2)	$E_{11,c}$ (kN/mm^2)
C901	*A*	-23.540	-3.384	-2533.63	-500.732	9.914	9.63
	B	-21.135	-2.574	-2466.03	-483.380	9.361	
C902	*A*	-22.836	-3.078	-2537.01	-486.761	9.636	10.60
	B	-27.790	-4.756	-2484.06	-494.873	11.579	
C903	*A*	-18.490	-0.896	-2486.09	-596.732	9.312	9.38
	B	-21.268	-1.952	-2544.00	-499.831	9.448	
C904	*A*	-19.248	-0.596	-2511.78	-555.268	9.533	10.02
	B	-22.662	-2.052	-2472.11	-510.648	10.507	
C905	*A*	-17.702	-0.480	-2563.61	-508.394	8.379	9.55
	B	-23.504	-2.282	-2461.97	-483.831	10.728	

Table B.5. Tabulated results obtained by the stress-strain relationships of the transverse compression test coupons along with the calculated transverse compressive modulus.

In accordance to ISO standards, upon which the tests were conducted, validity of the compression modulus calculated for the individual compression-test specimens are subject to two criteria; the bending criterion and the failure criterion. In particular, the bending criterion specifies that bending in the specimens would be allowable, or otherwise, the compression-tests would be valid when,

$$\left|\frac{\varepsilon_A - \varepsilon_B}{\varepsilon_A + \varepsilon_B}\right| \leq 0.1 \tag{B.3}$$

Where ε_A and ε_B are the axial strains on the surfaces of the specimen. The compliance of the axial and transverse compression-test coupons to the bending criterion have been illustrated in Figures B.9 and B.10 respectively.

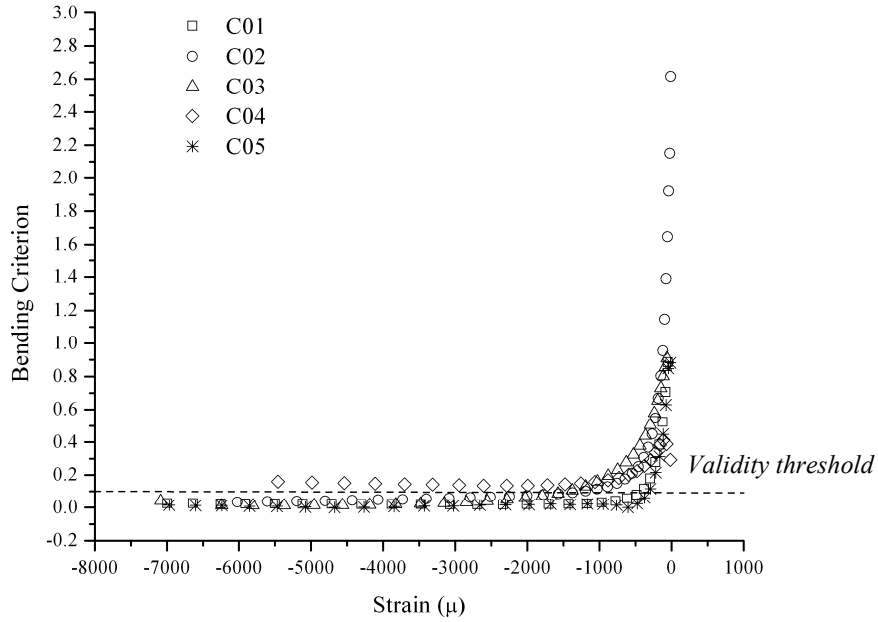

Figure B.9. Illustration of the validity of the axial compression-test specimens in accordance with the Bending Criterion.

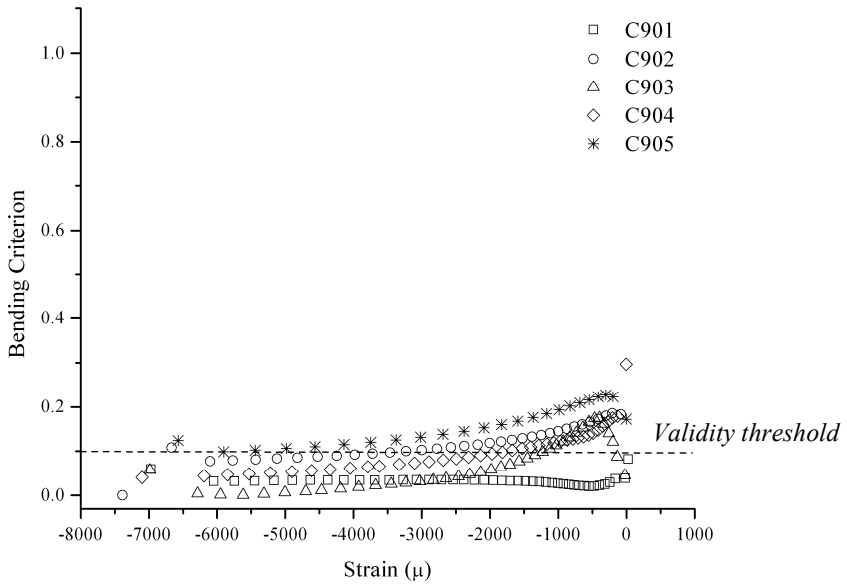

Figure B.10. Illustration of the validity of the axial compression-test specimens in accordance with the Bending Criterion.

From Figures B.9 and B.10 it was apparent that the compression test specimens were well above the validity threshold of the bending criterion for the region of 0%- 0.05% strain. However, as the compressive strain/load increased most of the specimens satisfied the Bending Criterion. The latter observation, suggested that the initial bending monitored was more probable to be the result of self-alignment of the specimen within the Celanese Fixture, rather to an initial flexural configuration of the specimens. That is, care was taken during the manufacturing process to eliminate the possibility of an influential out-of-flatness of the specimen (see Chapter 6) and inspection of the latter suggested the process was successful. More importantly, the fixture suggested by ISO and utilized in the current work operates on the principle of increasing pressure at the tabs of the specimens with increasing compressive loading conditions, where the load is transferred to the material through shear. Even though, the fixture was manufactured to the highest possible accuracy, possible imperfections, small deviations in the thicknesses of the specimen and the initial set-up of the specimen in the fixture induced initial

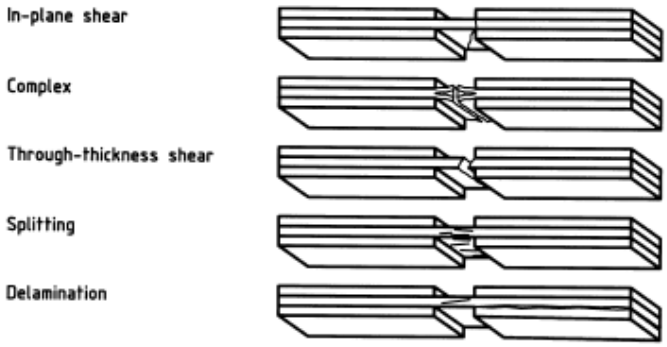

(a)

(b) (c)

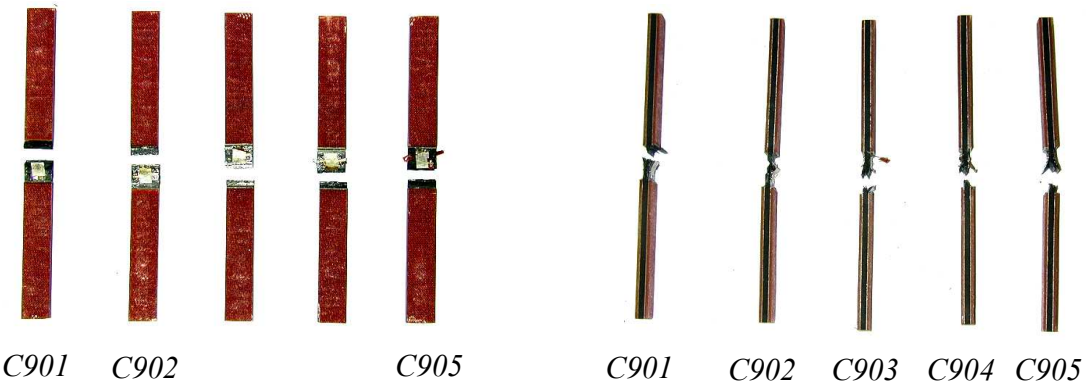

(d) (e)

Figure B.11. Illustration of (a) the acceptable modes of failure in accordance to the Failure Criterion specified (taken from EN IS0 14126:1999), (b) planar and (c) side view of the failed axial compression-test specimen and (d) planar and (e) side view of the failed transverse compression-test specimen.

bending in the specimens. Nevertheless, in rather low levels of loading the clamping jaws were rigidly fixed in the conical supporting mediums and uniform compression was achieved. The experienced gained through-out the duration of testing suggested that such initial effects could not be completely eliminated in the specific testing configuration, and therefore, it is the author's opinion that such initial effects should be anticipated and disregarded.

Even though in specimen *C04* and *C905* bending/twisting was not reduced below the required validity threshold (but still reduced), nevertheless they were still included in the determination of the axial and transverse compression modulus due to their proximity. That is, the deviations observed in modulus from the mean value of the remaining specimens were 4.3% and 3.6% for the *C04* and *C905* specimens respectively. The more pronounced bending/twisting effects in the latter specimen may be attributed to the inability of proper alignment of the clamps throughout the duration of the test, or more likely, to an induced flexural configuration that was inherited by the initial misalignment. Finally, all the specimens were found to be within the Failure Criterion, Figure B.11, which requires failure to occur within or at the end of the specimen gauge length at specified modes of failure, Figure B.11(a).

B.4 In-Plane Shear Modulus

In accordance with EN ISO 14129:1998 the in-plane shear modulus would be calculated within the region of 1000-5000 micro-strains (approximately) according to the following formula:

$$G_{12} = \frac{\tau_{12}^{''} - \tau_{12}^{'}}{\gamma_{12}^{''} - \gamma_{12}^{'}} \tag{B.4}$$

Where $\tau_{12}^{''}$, $\tau_{12}^{'}$ are the compressive stresses at 1000 and 5000 μ-strain respectively, and $\gamma_{12}^{''}$, $\gamma_{12}^{'}$ are the shear strains at 1000 and 5000 μ-strain respectively. The shear stresses are given by,

$$\tau_{12} = \frac{F}{2b_C t_c} \tag{B.5}$$

And the shear strains are given by,

$$\gamma_{12} = \varepsilon_x - \varepsilon_y \tag{B.6}$$

Where F is the tensile load, b_c is the specimen width, t_c the thickness, ε_x the axial and ε_y the transverse strains. The measured geometry of each coupon has been summarized in Table B.6.

	Dimensions				
	Overall length (mm)* *ISO:* $L_{c,0}$*=250*	*Width (mm)* *ISO:*b_c*=25±0.5*	*Thickness at the gauge (mm)* *ISO:* t_c*=4±0.2*	*Thickness at the tabs (mm)* *ISO:* t_c+2t_t*=N/S*	
S01	250.20	25.42	4.17	6.61	6.53
S02	250.20	25.40	4.15	6.61	6.67
S03	250.24	25.50	4.20	6.65	6.64
S04	250.30	25.67	4.18	6.63	6.58
S05	250.31	25.63	4.19	6.68	6.66

*All the specimen had longitudinal edges parallel within the 0.2 mm margin specified by ISO.

Table B.6. Geometry of the in-plane shear test-coupons.

The specified shear stresses are obtained by the individual shear stress-strain relationships, illustrated in Figure B.12 and summarized in Table B.7. It should be noted that the modulus prediction of each specimen is considered to be the mean value of the measurements taken from Side A and Side B, while the compression modulus would be the mean value of all five specimens. Furthermore, the tensile strain ε_x is positive, and thus, the transverse strain ε_y negative.

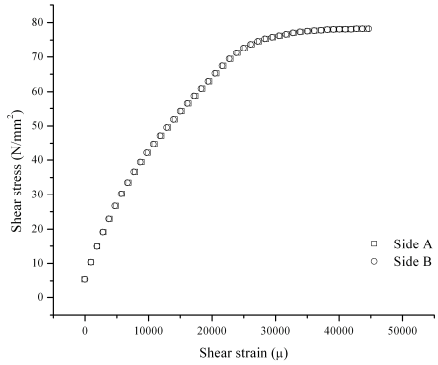

S01

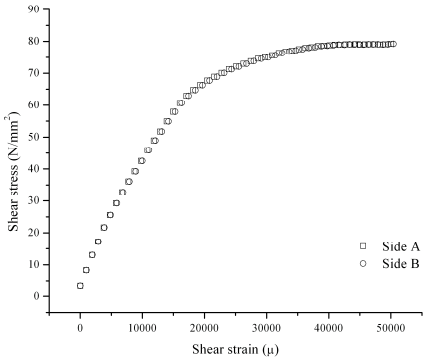

S02

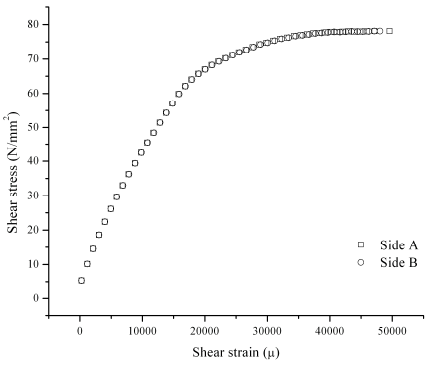

S03

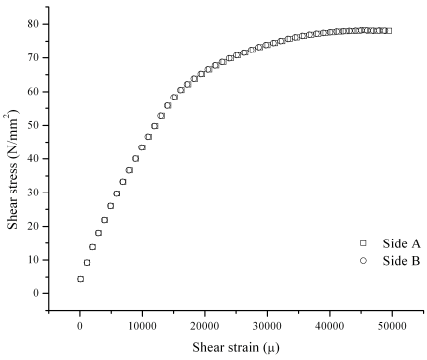

S04

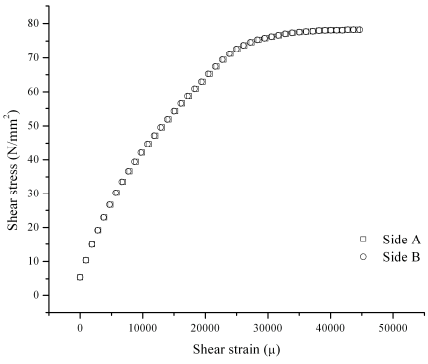

S05

Figure B.12. Shear stress-strain relationships of the in-plane shear test-coupons.

		$\tau_{12}^{''}$ (N/mm^2)	$\tau_{12}^{'}$ (N/mm^2)	$\gamma_{12}^{''}$ (μ-strain)	$\gamma_{12}^{'}$ (μ-strain)	$G_{12,s}$ (kN/mm^2)	$G_{12,c}$ (kN/mm^2)
C901	*A*	26.666	8.161	5054.376	964.800	4525.010	4.58
	B	26.666	8.161	4889.114	907.658	4647.890	
C902	*A*	27.278	9.052	4953.829	998.857	4608.394	4.64
	B	27.278	9.052	4841.029	941.943	4674.447	
C903	*A*	27.367	9.404	5005.943	1070.171	4572.185	4.62
	B	27.367	9.404	4839.315	996.114	4672.947	
C904	*A*	27.149	9.578	4885.029	1034.514	4563.276	4.59
	B	27.149	9.578	4809.372	1010.057	4624.772	
C905	*A*	27.517	9.566	5066.972	1136.914	4570.177	4.61
	B	27.517	9.566	4973.714	1098.057	4655.951	

Table B.7. Tabulated results obtained by the shear stress-strain relationships of the in-plane shear-test coupons along with the calculated in-plane shear modulous.

In contrast to the strain measurement range of the compression-test specimen, the one selected for the in-plane shear-test specimen allowed the full range of the axial and transverse strains to be monitored. However, all the tests were terminated at 50000 micro-strains since where beyond that value the ISO standards assume that failure has occurred. Or in other terms, the fibres have distorted sufficiently so as not to support higher loading levels. The latter, is evident in the shear stress-strain relationships, Figure B.12, where within the region of 40000-50000 micro-strains the load level remains almost constant. Additionally, at the conclusion of the tests fibre splitting at the edges of the coupons was observed, which suggested that the orientation of the fibres have distorted significantly. In accordance to Figure B.12 such distortions become more prominent and influential within the region of 5000-10000 micro-strains, where the response of the stress-strain relationship becomes clearly non-linear.

Finally, almost identical straining of the opposing surfaces was observed for all the specimens were observed. More importantly an excellent agreement was obtained in terms of the in-plane shear modulus, where deviations from the mean value were found to be below 1.5%.

B.5 Concluding Remarks

The axial and transverse compression modulus and the in-plane shear modulus were determined following the guidelines provided by ISO. Generally, relatively good agreement was observed in the predicted modulous values in each set of testing. Upon validation of the compression-test results it was observed that for the fixture employed an initial loading period must be allowed until alignment of the coupon within the fixture, and hence, the applied load is achieved. Therefore, the loading region under discussion does not necessarily invalidate the results. Furthermore, the proximity of the specimens (one in each set of compression-testing) that to an extent displayed bending/twisting, to the validity threshold of the bending criterion and the small deviations of modulus from the mean value of the remaining specimens allowed their incorporation in the determination of the axial and transverse compression modulus. The predicted values have been summarized in Table 7.1 along with the shear modulus in Chapter 7, where the nature and behaviour of carbon-fibre reinforced plastics (CFRP) is discussed in more detail. All the material properties established were found to be well within the expected range by the manufacturer (Hexcel Composites Ltd.).

Finally, it is worth mentioning that the cumbersome process of establishing the compressive properties of CFRP with the employment of the Celanese Fixture can be simplified. That is, by the design of coupons, whose geometry would restrict buckling to occur prior to ultimate failure, so as to allow the specimens to be directly positioned in the clamps of the compression testing machine. Such coupons were designed and tested in the University of Bath and predicted properties correlated reasonably well to the ones established under the ISO specifications.

Appendix C

C.1 Failure Modes of the Undamaged and Damaged Stuts

⇨ Fibre fracture
➡ Intralaminar fracture

A: Inner face
B: Outer face

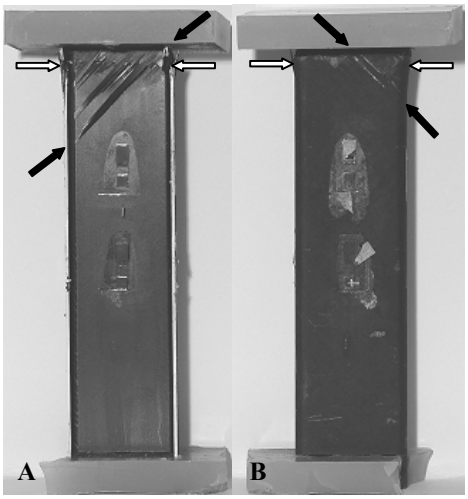

Undamaged-Positive buckling mode

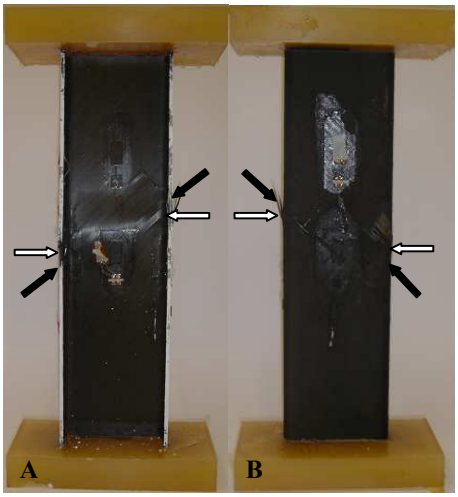

Undamaged-Negative buckling mode

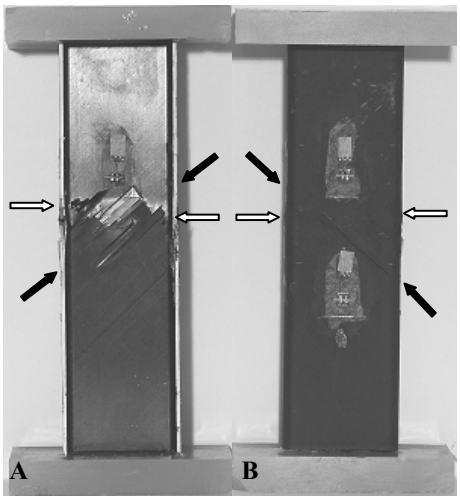

n=2-Skin

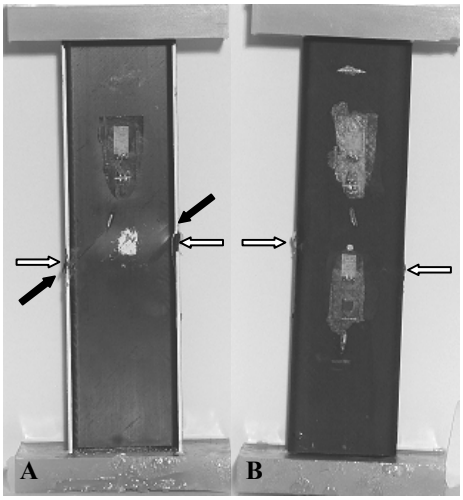

n=3-Skin

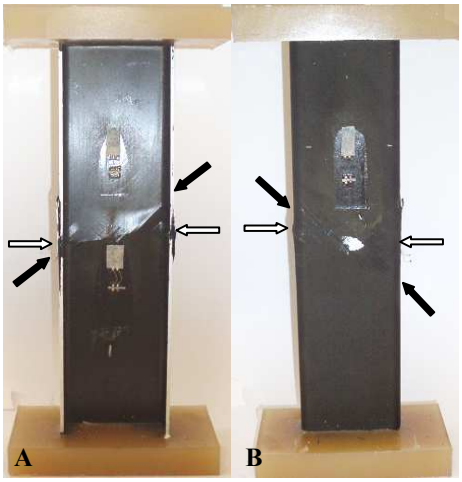

n=5-Skin

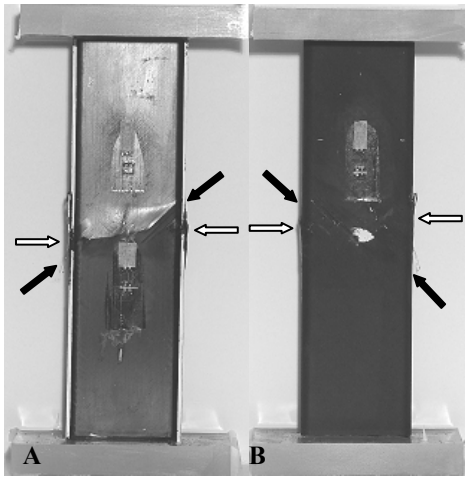

n=6-Skin

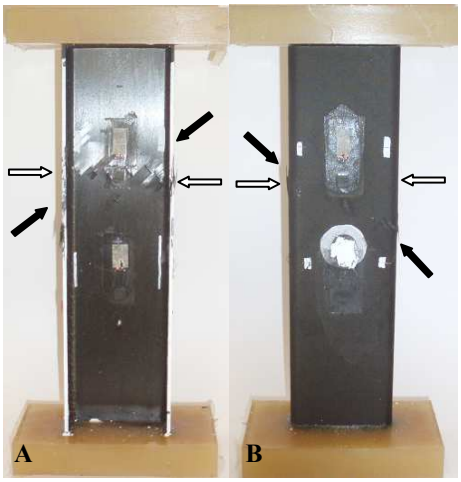

n=6-Skin: 0.25mm PTFE

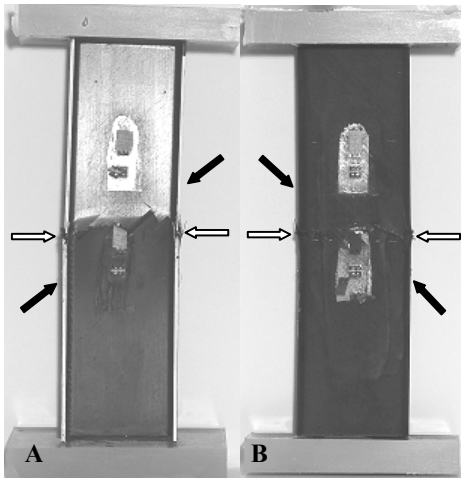

n=2-Stiffener

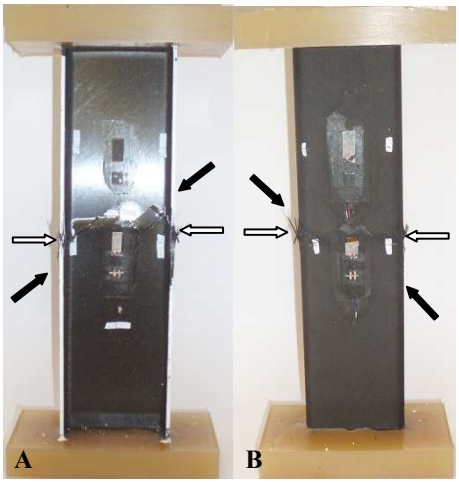

n=2-Stiffener: 0.25mm PTFE

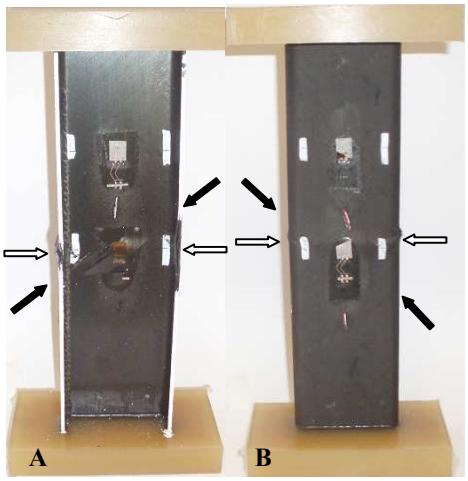

n=3-Stiffener

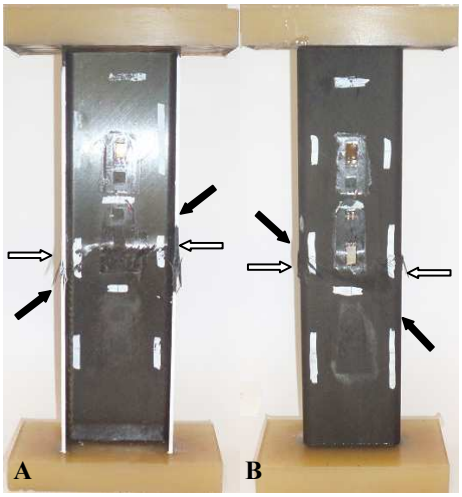

n=5-Stiffener

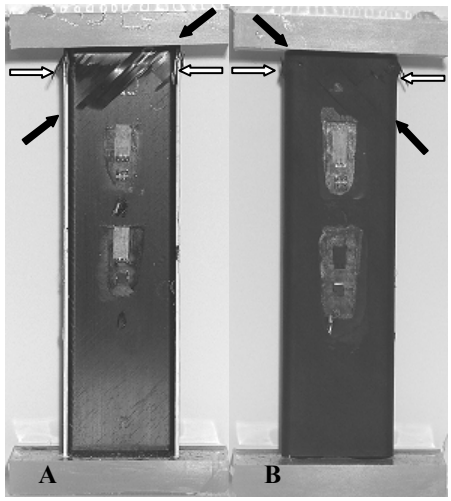

n=6-Stiffener

C.2 Longitudinal Strains at the Thicker Sublaminate of the Damaged Stuts

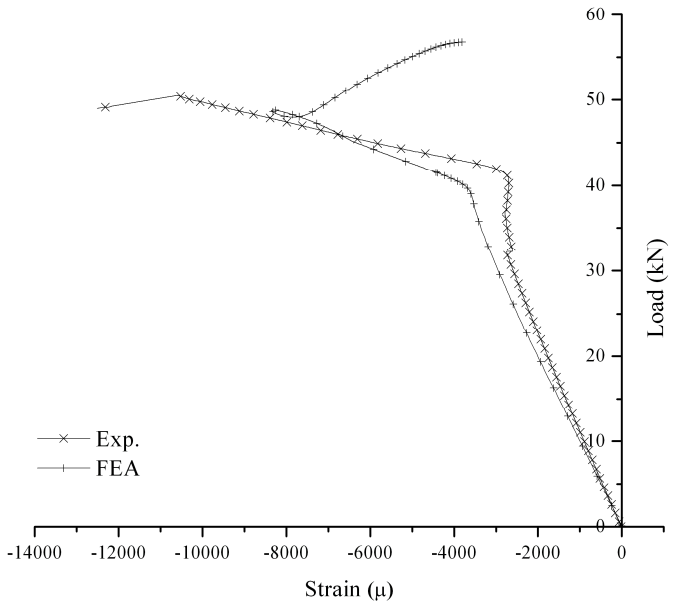

Figure C.1. Load vs longitudinal strains at 10mm from the centre of the outer skin for the n=2-Skin channel-section strut.

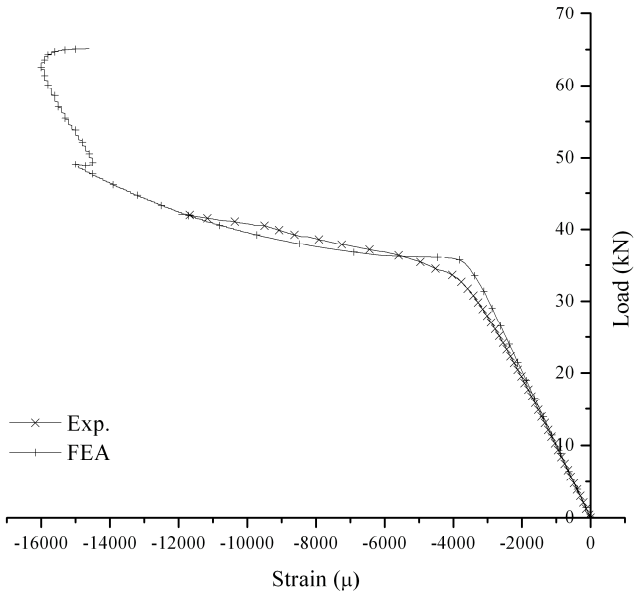

Figure C.2. Load vs longitudinal strains at 10mm from the centre of the outer skin for the n=3-Skin channel-section strut.

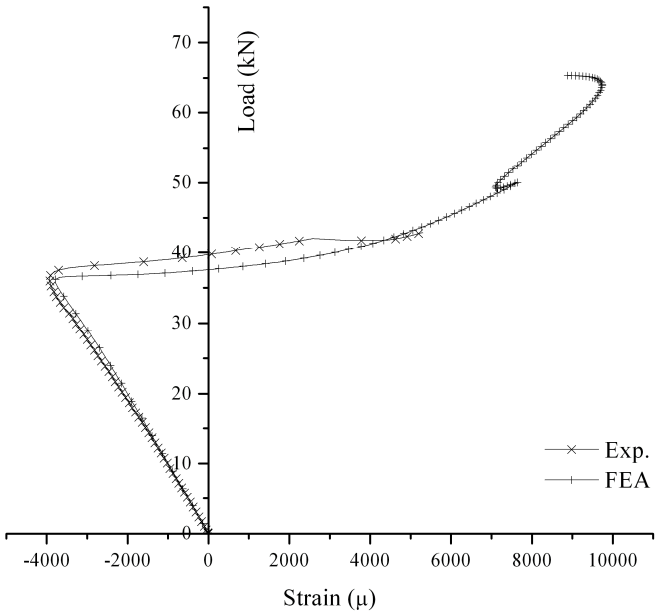

Figure C.3. Load vs longitudinal strains at 10mm from the centre of the outer skin for the n=5-Skin channel-section strut.

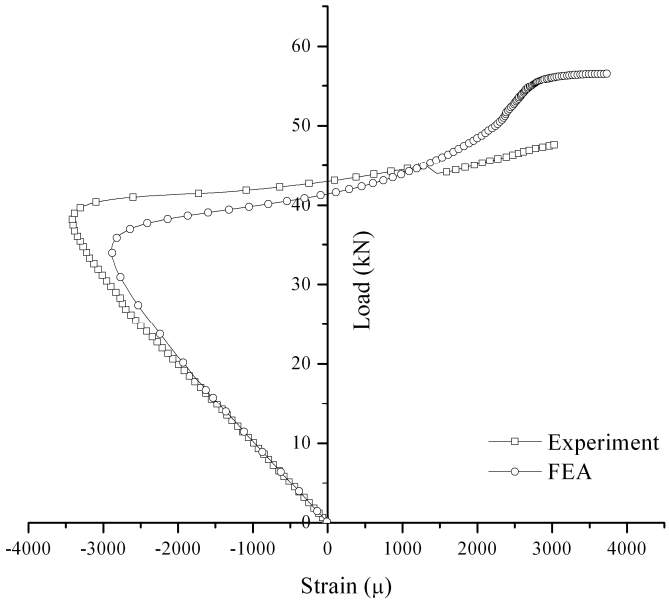

Figure C.4. Load vs longitudinal strains at 10mm from the centre of the outer skin for the n=6-Skin channel-section strut.

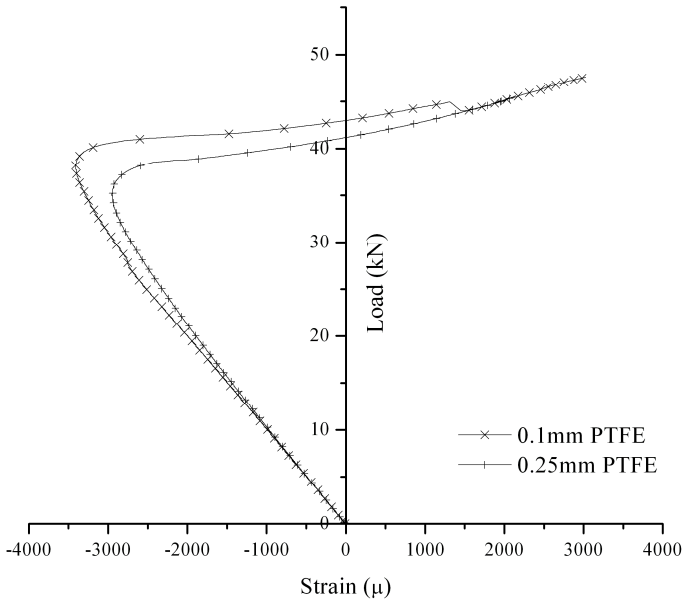

Figure C.5. Load vs longitudinal strains at 10mm from the centre of the inner skin for the n=6-Skin channel-section struts with 0.1 and 0.25 mm PTFE patches.

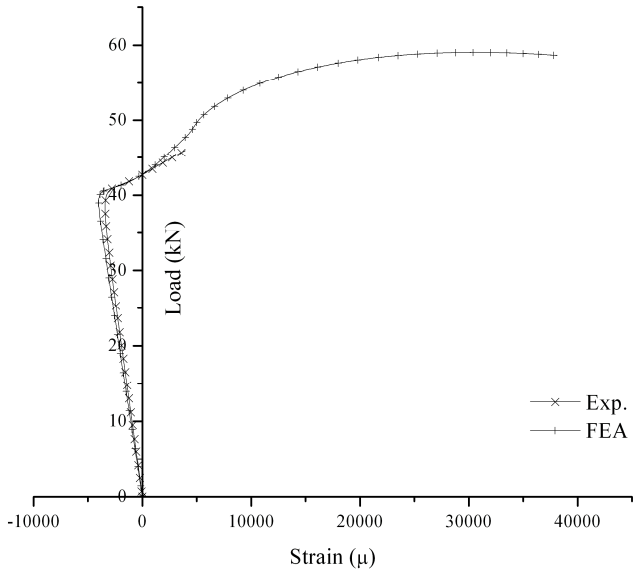

Figure C.6. Load vs longitudinal strains at 10 mm from the mid-length of the outer edge of the right stiffener for the n=2-Stiffener channel-section strut.

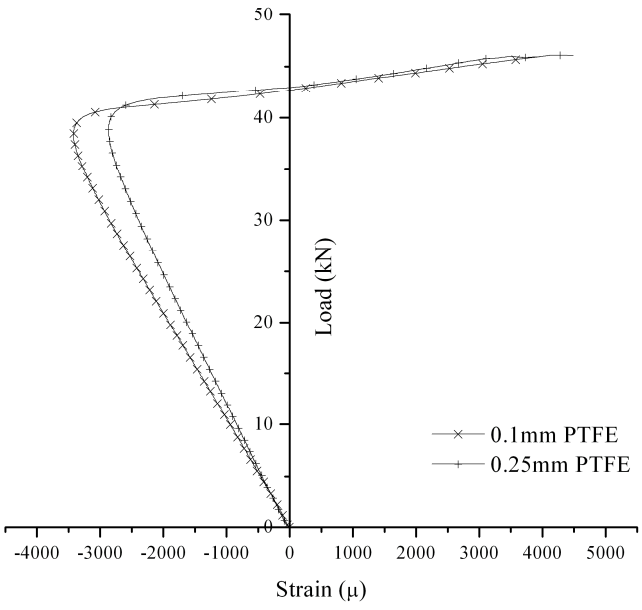

Figure C.7. Load vs longitudinal strains at 10 mm from the mid-length of the outer edge of the right stiffener for the n=2-Stiffener channel-section struts with 0.1 and 0.25 mm PTFE patches.

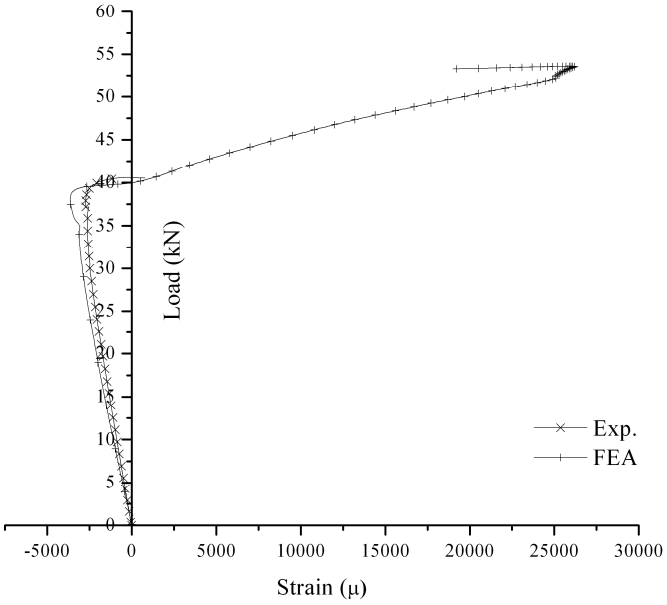

Figure C.8. Load vs longitudinal strains at 10 mm from the mid-length of the outer edge of the right stiffener for the n=3-Stiffener channel-section strut.

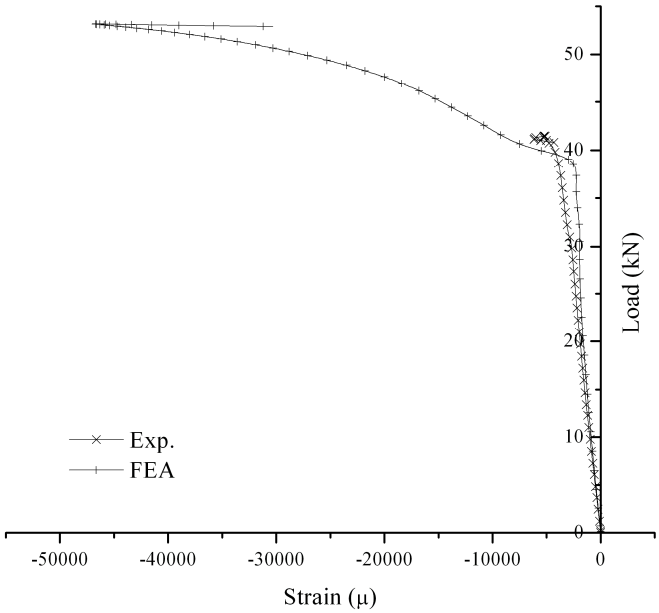

Figure C.9. Load vs longitudinal strains at 10mm from the mid-length of the inner edge of the right stiffener for the n=5-Stiffener channel-section strut.

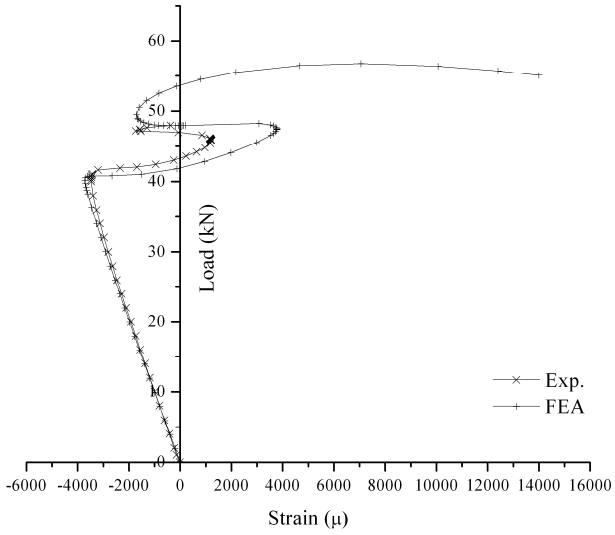

Figure C.10. Load vs longitudinal strains at 10mm from the mid-length of the inner edge of the right stiffener for the n=6-Stiffener channel-section strut.

C.3 Experimental and FEA Stiffness Plots of the Damaged Stuts

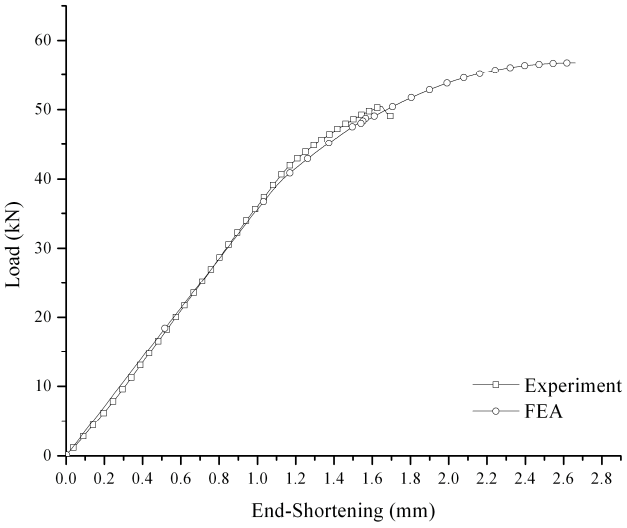

Figure C.11. Load vs end-shortening curve of the n=2-Skin channel-section strut.

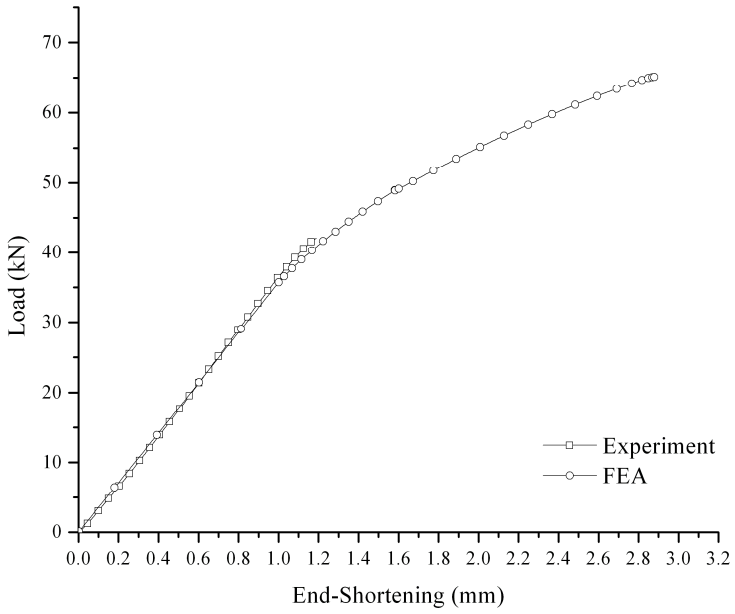

Figure C.12. Load vs end-shortening curve of the n=3-Skin channel-section strut.

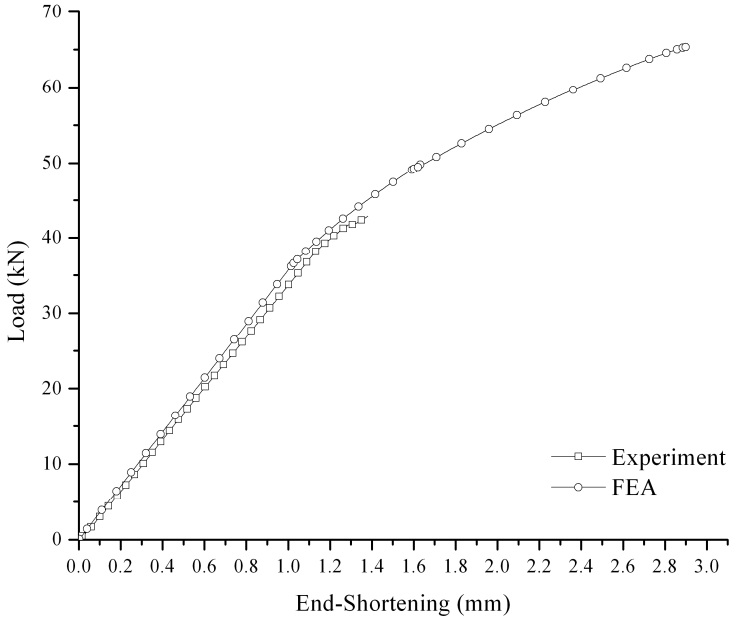

Figure C.13. Load vs end-shortening curve of the n=5-Skin channel-section strut.

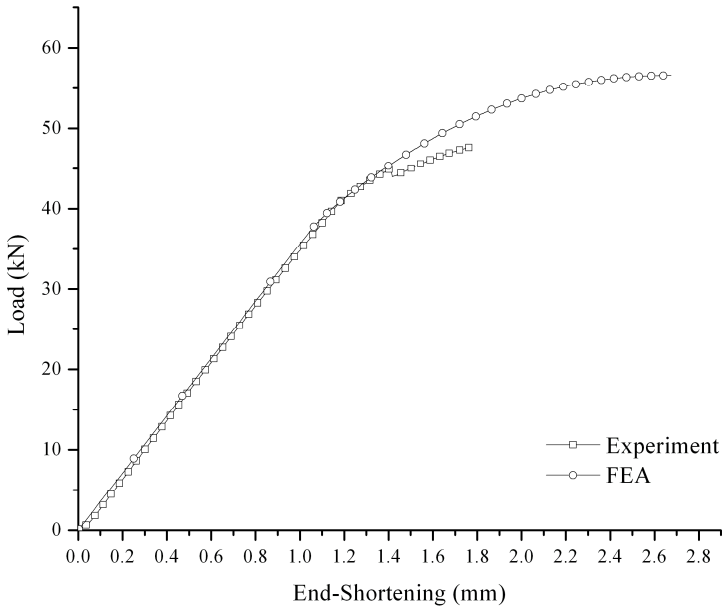

Figure C.14. Load vs end-shortening curve of the n=6-Skin channel-section strut.

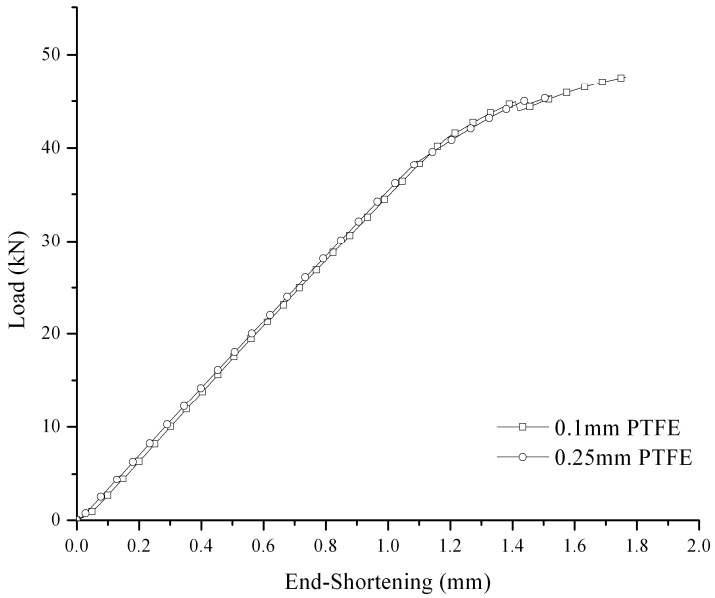

Figure C.15. Load vs end-shortening curves of the n=6-Skin channel-section struts with 0.1 and 0.25mm PTFE patches.

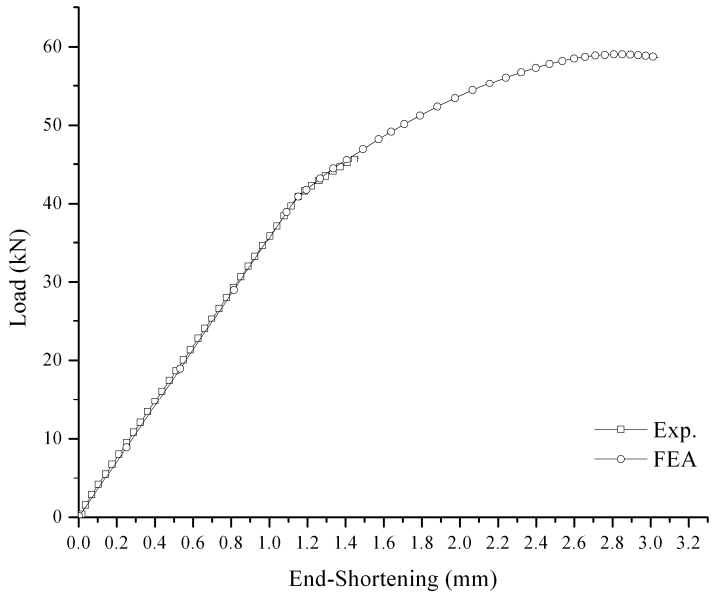

Figure C.16. Load vs end-shortening curve of the n=2-Stiffener channel-section strut.

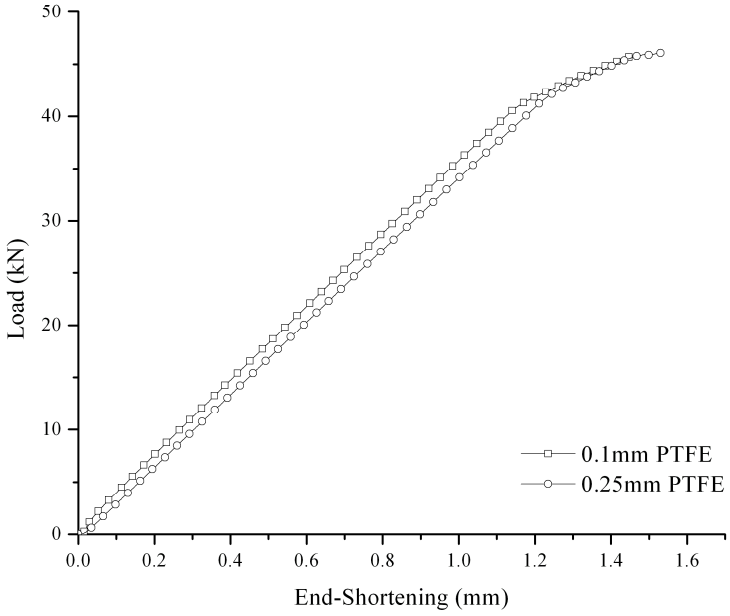

Figure C.17. Load vs end-shortening curves of the n=2-Stiffener channel-section struts with 0.1 and 0.25mm PTFE patches.

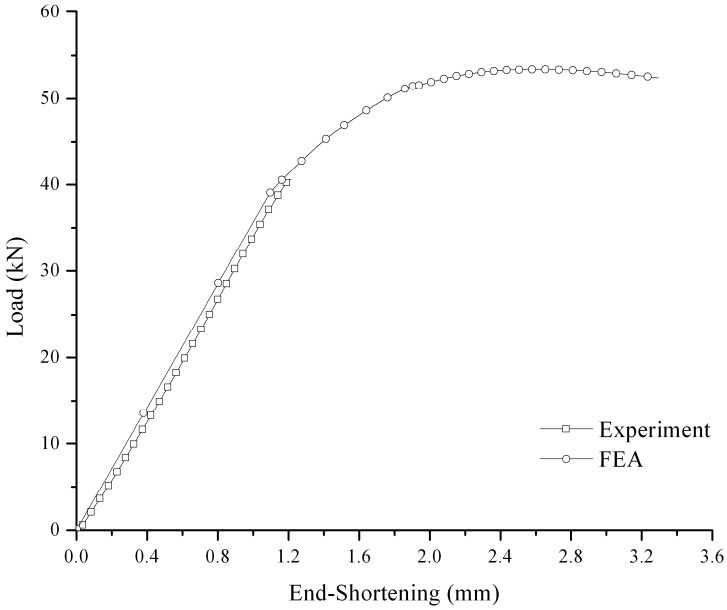

Figure C.18. Load vs end-shortening curve of the n=3-Stiffener channel-section strut.

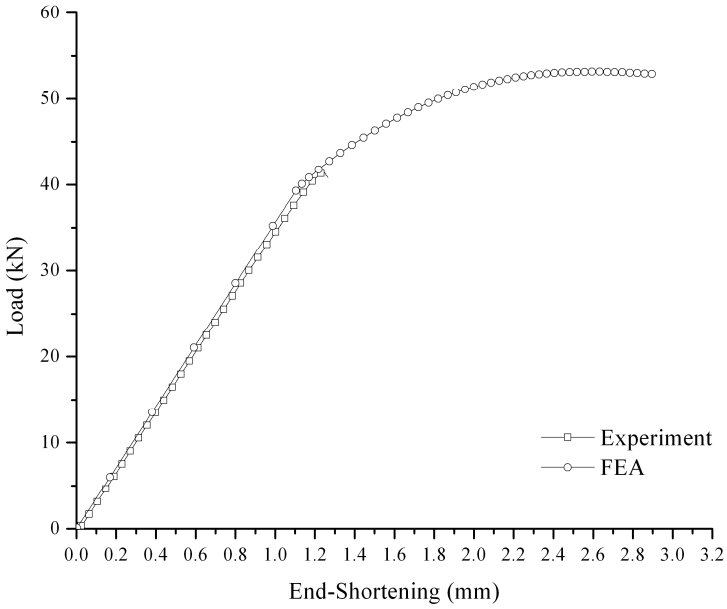

Figure C.19. Load vs end-shortening curve of the n=5-Stiffener channel-section strut.

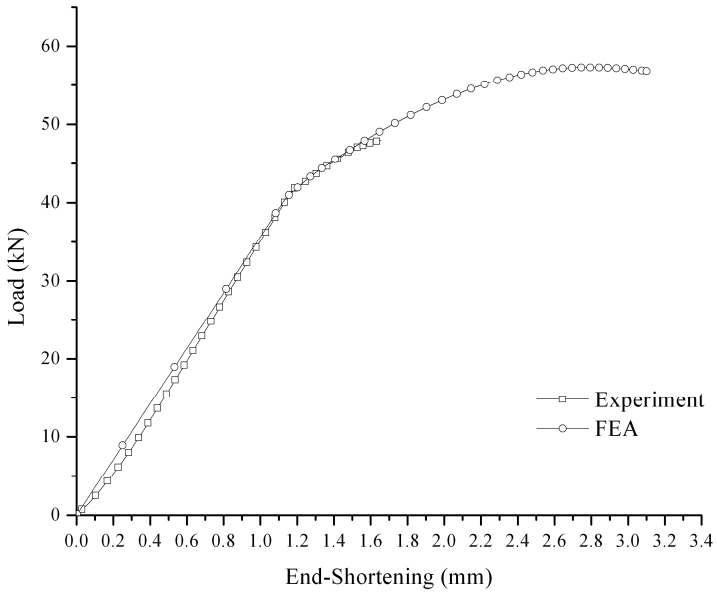

Figure C.20. Load vs end-shortening curve of the n=6-Stiffener channel-section strut.

References

ABAQUS, 2001a. *ABAQUS/Standard User's Manual Vol. 2*, Version 6.2. Hibbitt, Karlsson and Sorensen Ltd., U.K.

ABAQUS, 2001b. *Standard User's Manual Vol. 3*, Version 6.2. Hibbitt, Karlsson and Sorensen Ltd., U.K.

ABAQUS, 2001b. *Standard User's Manual Vol. 1*, Version 6.2. Hibbitt, Karlsson and Sorensen Ltd., U.K.

Allegri, G. and Zhang, X., 2007. On the delamination and debond suppression in structural joints by Z-fibre pinning, *Composites: Part A*, Vol. 38, pp. 1107-1115.

Anderson, Jr., J. D., 1999. *Aircraft performance and design*, WCB/McGraw-Hill, International editions.

Arnold, R., R. and Mayers, J., 1984. Buckling, postbuckling, and crippling of materially nonlinear laminated composite plate, *International Journal of Solids and Structures*, Vol. 20, No. 9/10, pp. 863-880.

Asp, L. E., Nilsson, S. and Singh, S., 2001. An experimental investigation of the influence of the delamination growth on the residual strength of impacted laminates. *Composites:Part A*, Vol. 32, pp. 1229-1235.

Bader, M., G., 1996. Materials selections, preliminary design and sizing for composites laminates, *Composites: Part A*, Vol. 27A, pp. 65-70

Bai, R.-X. and Chen, H.-R., April 2004. Numerical analysis of delamination growth for stiffened composite laminated plates, *Applied Mathematics and Mechanics*, English Edition, Vol. 25, No. 4, pp. 405-417.

Baker, A. A., Jones, R. and Callinan, R. J., 1985. Damage tolerance of graphite/epoxy composites, *Composite Structures*, Vol. 4, pp. 15-44.

Banks, W., M. and Rhodes, J., 1981. The post-buckling behaviour of composite box sections, *First International Conference on Composite Structures, Paisley College of Technology, Paisley, Scotland, in Composite Structures, Marshall, I., H., editor*, Applied Science Publishers, London, 1981, pp. 402-414.

Bazant, Z., P. and Cedolin, L., 1991. *Stability of Structures: Elastic, Inelastic, Fracture, and Damage Theories*, Oxford University Press, Oxford.

Bibo, G. A. and Hogg, P. J., 1996. The role of reinforcement architecture on impact damage mechanisms and post-impact compression behaviour, *Journal of Materials Science*, Vol. 31, pp. 1115-1137.

Bibo, G. A. and Hogg, P. J., 1998. Influence of reinforcement architecture on damage mechanisms and residual strength of glass-fibre/epoxy composite systems, *Composites Science and Technology*, Vol 58, pp. 803-813.

Bibo, G. A., Leicy, D., Hogg, P. J. and Kemp, M., 1994. High-temperature damage tolerance of carbon fibre-reinforced plastics part1: impact characteristics, *Composites*, Vol. 25, pp 114-424.

Bonora, N., La Barbera, A. and Marchetti, M., 1993. Experimental verification and theoretical simulation of fracture behaviours of composite materials, *Composite Structures*, Vol. 23, pp. 87-97.

Bottega, W. J. and Maewai, A., March 1983. Delamination buckling and growth in laminates, *Journal of Applied Mechanics*, Vol.50, pp. 184-189.

Butler, R., 1990. *Exact buckling design for advanced aerospace structures.* Thesis (PhD). University of Wales College, Cardiff.

Butler, R., Rhead, A. and Hunt, G. W., 2007. Enhanced compressive fatigue (strength) model for impact damaged laminates. *16TH International Conference on Composite Materials*, July 8-13, 2007 Kyoto International Conference Center, Kyoto, Japan.

Butler, R., and Liu, W. "*Optimisation of stiffened panels using finite strip models", in "Buckling and Postbuckling Structures*", *Computational and Experimantal methods in structures, Buckling and Post-buckling* Strucures, *Vol. 1* edited by Falzon B.G., and Aliabadi, M.H., Imperial College Press, London UK (Schedualed Spring, 2008 press).

Cantwell, W. J. and Morton, J., 1989 Geometrical Effects in the low velocity impact response of CFRP, *Composite Structures*, Vol. 12, pp. 39-59.

Cantwell, W. J. and Morton, J., 1991. The impact resistance of composite materials – a review, *Composites*, Vol. 22, No. 5, pp. 347-362.

Cantwell, W. J., Curtis, P. T. and Morton, J., 1986. An assessment of the impact performance of CFRP reinforced with high-strain carbon fibres, *Composites Science and Technology*, Vol. 25, pp. 133-148.

Cerini, M., 2006. *Investigation of secondary instabilities in postbuckling stiffened composite structures.* Thesis (PhD). Imperial College, London.

Chai, H. and Babcock, C. D., January 1985. Two-dimensional modeling of compressive failure in delaminated laminates, *Journal of Composite Materials*, Vol. 19, pp. 67-97.

Chai, H., Babcock, C. D. and Knauss, W. G., 1981. One-dimensional modeling of failure in laminated plates by delamination buckling, *Int. Journal of Solids and Structures*, Vol. 17, No. 11, pp. 1069-1083.

Chen, H.- P., January 1993. Transverse shear effects on buckling and postbuckling of laminated and delaminated plates, *Journal of American Institute of Aeronautics and Astronautics*, Vol. 31, No. 1, pp. 163-169.

Chen, P., Shen, Z. and Wang, J., 2001. Damage tolerance analysis of stiffened composite panels, *Journal of Composite Materials*, Vol. 35, No. 20, pp. 1844-1867.

Cheung, Y. K., 1976. *Finite strip method in structural analysis*. Pergamon Press Ltd., Oxford, U.K.

Curtis, P. T., Gates, J. and Molyneux, G. G., 1993. Impact damage growth in carbon fibre composites. Defence Research Agency, Farnborough, Hampshire, Technical Report 93009.

Cutler, J., 1999 *Understanding aircraft structures*. Blackwell Science, New York, London, 3rd edition.

Daniel, M. I., January 1980. Behavior of graphite/epoxy plates with holes under biaxial loading, *Experimantal Mechanics*, Vol. 20, pp. 1-8.

Davies, G. A. O. and Zhang., X., 1995. Impact damage prediction in carbon composite structures, *International Journal of Impact Engineering*, Vol. 16, No. 1, pp 149-170.

Davies, G. A. O. and Zhang., X., Frebruary 2000. Predicting impact damage in carbon composite structures, *Aeronautical Journal*, Vol. 1004, No. 1032, pp. 97-103.

Davies, G. A. O., Zhang, X., Zhou, G. and Watson, S., 1994. Numerical modeling of impact damage, *Composites*, Vol. 25, No. 5, pp. 342-350.

De Florio, F., 2006. *Airworthiness: An introduction to aircraft certification. A guide to understanding JAA, EASE, FAA standards*, Elsevier, Ltd.

Desmond, T., P., Pekoz, T. and Winter, G., 1981. Intermediate stiffeners for thin-walled members, *ASCE J. Struct. Div.*, Vol. 107, No. 4, pp. 627-648.

Diaconu, C., G. and Weaver, P., M.., 2004. Approximate solution and optimum design for postbuckling of infinite laminated composite plates subjected to compression loading, *45th AIAA/ASME/ASCE/AHS/ASC Structures, Structural Dynamics and Material Confereence, 19-22 April 2004, Palm Springs, California*.

Edwards, K. I., 1998. An overview of the technology of fibre-reinforced plastics for design purposes. *Materials and Design*, Vol. 19, pp. 1-10.

Elder, D. J., Thompson, R. S., Nguyen, M. Q. and Scott, M. L., 2004. Review of delamination predictive methods for low speed impact of composite laminates. *Composite Structures*, Vol. 66, pp. 677-683.

EN ISO 14126:1999. Fibre-*reinforced plastics composites - Determination of compressive properties in the in-plane direction*.

EN ISO 14129:1998. *Fibre-reinforced plastics - Determination of the in-plane shear stress/shear strain response, including the in-plane shear modulus and strength by the* $\pm 45^0$ *tension test method.*

ESDU 76023, *Buckling of struts. Lipped and unlipped channel section*, November 1976.

ESDU 78020, *Local buckling and crippling of I-, Z- and channel section struts*, July 1978.

ESDU 78021, *Guide to items on the strength and stability of struts*, October 1978.

European Commission, January, 2001. European Aeronautics: A vision for 2020. Retrieved September 18, 2006, from European Commission, The Strategic Research Agenda. Website: http://ec.europa.eu/research/aeronautics/policy/agenda_en.html.

Falzon, B. G., 2001. The behaviour of damage tolerant hat-stiffened composite panels loaded in uniaxial compression, *Composites: Part A*, Vol. 32, pp. 1255-1262.

Falzon, B. G. and Hitchings, D., 2003. Capturing mode-switching in postbuckling composite panels using a modified explicit procedure, *Composite Structures*, Vol. 60, pp. 447-453.

Falzon, B. G., Stevens, K. A. and Davies, G.O., 2000. Postbuckling behaviour of a blade-stiffened composite panel loaded in uniaxial compression, *Composites: Part A*, Vol. 31, pp. 459-468.

Flesher, N. D. and Herakovich, C. T., 2006. Predicting delamination in composite structures, *Composites Science and Technology*, Vol. 66, pp. 745-754.

Gadke, M., Geier, B., Goetting, H.-Chr., Klein, H., Rohwer, K. and Zimmermann, R., 1996. Damage influence on the buckling load of CFRP stringer-stiffened panels, *Composite Structures*, Vol. 36, pp. 249-275.

Gibson, R. F., 1994. *Principles of composite material mechanics*. McGraw-Hill, Inc., London.

Gill, R. M., 1972. *Carbon fibres in composite materials*. The Butterworth Group, London.

Graesser, D. L. and Tuttle, M. E., 1996. Damage tolerance predictions for stiffened composite panels – Part II: Application of a failure criteria, *Journal of Composites Technology and Research*, Vol. 18, pp. 102-108.

Greenhalgh, E., Singh, S., Hughes, D. and Roberts, D., 1999. Impact damage resistance and tolerance of stringer stiffened composite structures, *Plastics Rubber and Composites*, Vol. 28, No. 5, pp. 228-251.

Griffith, A. A., 1920. The phenomena of rupture and flow in solids, *Philosophical Transactions of the Royal Society*, 221A, pp. 163-198.

Gu, H. and Chattopadhyay, A., 1999. Experimental investigation of delamination buckling and postbuckling of composite laminates, *Composites Science and Technology*, Vol. 59, pp. 903-910.

Hady, F., A. and Vautrin, A., 1987. Characterization of the time-dependent shear response of unidirectional carbon/epoxy laminate in torsion, *Composites Evaluation, Proceedings of the second international conference on Testing, Evaluation and Quality Control of Composites- TEQC-87, University of Surrey, Guildford , U.K. 22-24 September 1987,* Herriot, J., editor, pp. 194-200.

Hancock, G. J., Kwon, Y. B. and Bernard, E., S., 1994. Strength design curves for thin-walled structures undergoing distortional buckling, *Journal of Construction and Steel Research*, Vol. 31, pp. 169-186.

Harik, V. M., October 2003. Control of damage in composite laminates by ply-stacking designs: Characteristic failure signatures and safety criteria, *Journal of Engineering Materials and Technology*, Vol. 125, pp 385-393.

Harper, J. F. and Heumann, T. O., 1987. The strain dependence of elastic modulous in unidirectional composites, *Composites Evaluation, Proceedings of the second international conference on Testing, Evaluation and Quality Control of Composites-TEQC-87, University of Surrey, Guildford , U.K. 22-24 September 1987,* Herriot, J., editor, pp. 189-193.

Harris, B., editor, 2003. *Fatigue in composites.* CRC Press, Woodhead Publishing Ltd., Cambridge, England.

Harris, C. E., Starnes, Jr., J. H. and Shuart M. J., July-August 2002. Design and manufacturing of aerospace composite structures, state-of-the-art assesement. *Journal of Aircraft*, Vol. 39, No. 4, pp. 545-560.

Harris, G., Z., 1975. The buckling and post-buckling behaviour of composite plates under axial loading, *International Journal of Mechanical Science*, Vol. 17, pp. 187-202.

Harisson C. and Butler, R., 2001. Locating delaminations in composite beams using gradient techniques and a genetic algorithm. *Journal of American Institute of Aeronautics and Astronautics*, Vol. 39, No. 7, pp. 1383-1389.

Herszberg, I. and Weller, T., 2006. Impact damage resistance of buckled carbon/epoxy panels, *Composite Structures*, Vol. 73, pp. 130-137.

Hong, S. and Liu, D., 1989. On the relationship between impact energy and delamination area*, Experimantal Mechanics*, Vol. 29, No. 2, pp. 115-120, 1989.

Horne, D. F., 1986. *Aircraft production technology*. Cambridge University Press, Cambridge.

Hoskin B. C. and Baker A. A., editors, 1986. *Composite materials for aircraft structures*. American Institute of Aeronautics and Astronautics, Inc., Washington, DC.

Hughes, J. D. H., 1991. The carbon fibre/epoxy interface-A review. *Composites Science and Technology*, Vol.41, pp. 13-45.

Hu, B., Butler, R., Almond, D. P. and Hunt, G. W., 2004. Post-buckling and fatigue limit of artificially delaminated composites, *Collection of Technical Papers - AIAA/ASME/ASCE/AHS/ASC Structures, Structural Dynamics and Materials Conference*, v 1, *Collect. of Tech. Pap. - 45th AIAA/ASME/ASCE/AHS/ASC Struct., Struct. Dyn. and Mater. Conf.; 12th AIAA/ASME/AHS Adapt. Struct. Conf.; 6th AIAA Non-Deterministic Approaches Forum; 5th AIAA Gossamer Sp*, 2004, p 646-658.

Hu, H-T, Yang, C-H and Lin F.M, 2006. Buckling analyses of composite laminate skew plates with material nonlinearity. *Composites: Part B*, Vol. 37, pp. 26-36.

Hu, N., Fukunaga, H., Sekine, H. and Ali, K. M., 1999. Compressive buckling of laminates with an embedded delamination, *Composite Science and Technology*, Vol. 59, pp. 1247-1260.

Hull, D. and Shi, Y. B., 1993. Damage mechanism characterization in composite damage tolerance investigations, *Composite Structures*, Vol. 23, pp. 99-120.

Hunt, G. W. and Burgan, B. A., 1985. Hidden asymmetries in the Shanley model, *Journal of Mechanics, Physics and Solids*, Vol. 33, No. 1, pp. 83-94.

Hunt, G. W., Hu, B., Butler, R., Almond, D. P. and Wright, J. E., November 2004. Nonlinear modeling of delaminated struts, *Journal of American Institute of Aeronautics and Astronautics*, Vol. 42, No. 11, pp. 2364-2372.

Hutchinson, J. W. and Suo, Z., 1992. Mixed mode cracking in layered materials, *Advances in Applied Mechanics*, Vol. 29, Academic Press, pp. 63-191.

Jegley, D. C, November 1992. Study of compression-loaded and impact damaged structurally efficient graphite-thermoplastic trapezoidal-corrugation sandwich and semisandwich panel, Technical report, NASA TP-17129, NASA Langley Research Center, Hampton, VA 23681-0001.

Jen, M.-H. R., Kau, Y. S. and Hsu, J. M., 1993. Initiation and propagation of delamination in a centrally notched composite laminate, *Journal of Composite Materials*, Vol. 27, No. 3, pp. 272-302.

Joint Airworthiness Requirements (JAR), ACJ 25.603, 1994.

Jones, R., Paul, J., Tay, T. E. and Williams, J. F., 1988. Assessment of the effect of impact damage in composites: Some problems and answers, *Composite Structures*, Vol. 10, No. 1, pp. 51-73.

Ishikawa, T., Matsushima, M., Hayashi, Y. and Noguchi, T., 1991. *Proceedings of the 8th International Conference on Fibrous composites in structural design, 1989*, Department of Defense-National Aeronautics and Space Administration-Federal Aviation Authority, Part 2, pp. 101-129.

Kachanov, L. M., 1988. *Delamination buckling of composite materials*, Kluwer Academic Publishers Group, The Netherlands.

Kalfon, E., Harel, H., Marom, G., Drukker, E., Green, A. K. And Kressel, I., 2005. Delamination of laminated composites under the combined effect of nonuniform heating and absorbed moisture, *Polymer Composites*, Vol. 26, pp. 770-777.

Kardomateas, G. A. and Schmueser, D. W., March 1988. Buckling and postbuckling of delaminated composites under compressive loads including transverse shear effects, *Journal of American Institute of Aeronautics and Astronautics*, Vol. 26, No. 3, pp. 337-343.

Kim, H.- J., 1997. Postbuckling analysis of composite laminates with a delamination, *Computers and Structures*, Vol. 62, No. 6, pp. 975-983.

Kolakowski, Z. and Kubiack, T., 2005. Load-carrying capacity of thin-walled composite structures, *Composite Structures*, Vol. 67, pp. 417-426.

Koiter, W., T. and Pignataro, M., 1976. *A general theory for the interaction between local and overall buckling of stiffened panels*, Delft University Report, WTHD-83.

Kollar, P., L. and Springer, G., S., 2003. *Mechanics of Composite Structures*, Cambridge University Press, The Edinburgh Building, Cambridge.

Kortschot, M. T. And Zhang, C. J., 1995. Characterization of composite mesostructures and damage by de-ply radiography, *Composite Science and Technology*, Vol. 53, pp. 175-181.

Kwon, Y. B. and Hancock, G., J., 1992. Tests of cold-formed channels with local and distortional buckling, *ASCE Journal of Structural Engineering*, Vol. 117, pp. 1786-1803.

Lanzi, L. and Giavotto, V., 2006. Post-buckling optimization of composite stiffened panels: Computations and experiments, *Composite Structures*, Vol. 73, pp. 208-220.

Lammerant, L. and Verpoest, I., 1994. The interaction between matrix cracks and delaminations during quasi-static impact of composites, *Composites Science and Technology*, Vol. 51, pp. 505-516.

Lillico, M., Butler, R., Hunt, G., W., Watson, A. and Kenneddy, D, 2003. Postbuckling of stiffened panels using strut, strip, and finite element methods, *American Institute of Aeronautics and Astronautics*, Vol. 41, No. 6, pp.1173-1179.

Liu W., 2005. *Analysis and testing of composite stiffened compression panels for integrated design and manufacture*. Thesis (PhD). University of Bath, Bath.

Lorriot, Th., Marion, G., Harry, R. and Wargnier, H., 2003. Onset of free-edge delamination in composite laminates under tensile loading, *Composites: Part B*, Vol. 34, pp. 459-471.

Mazumdar, S. K., 2002. *Composites Manufacturing. Materials, Product, and Process Engineering*, CRC Press, London.

Megson, T. H., 1999. *Aircraft structures for engineering students*. Elsevier Butterworth-Heinemann, London, 3rd edition.

Murray, N., W., 1984. *Introduction to the theory of thin-walled structures*, Oxford: Clarendon.

Moaveni, S., 1999. *Finite element analysis: Theory and application with ANSYS*. Prentice-Hall International Ltd., London, U.K.

Naik, N. K. and Ramasimha, R., 2001. Estimation of compressive strength of delaminated composites, *Composite Structures*, Vol. 52, pp. 199-204.

Nemeth, M., P., 1986. Importance of anisotropy on buckling of compression-loaded symmetric composites. *AIAA Journal*, Vol. 24, No. 11, pp. 1831-1835.

van der Neut, A., 1969. The interaction of local buckling and column failure of thin-walled compression members, *Proceedings 12th IUTAM Congress in Stanford, California, 1968, Hetenyi, M. and Vincenti, W. G. editors,* Springer-Verlag, Berlin, pp. 389-399.

Nilsson, K. –F., Asp, L. E., Alpman, J. E. and Nystedt, L., 2001a. Delamination buckling and growth for delaminations at different depths in a slender composite panel, *International Journal of Solids and Structures*, Vol. 38, pp. 3039-3071.

Nilsson, K. –F., Asp, L. E. and Sjogren, 2001b. On the transition of delamination growth behaviour for compression loaded composite panels, *International Journal of Solids and Structures*, Vol. 38, pp. 8407-8440.

Niu, M., C., Y., 1992. *Composite Airframe Structures: Practical Design Information and Data*, Conmilit Press Ltd, Hong Kong.

Noor, A. K., 1999. *Structures Technology: Historical perspective and evolution*. American Institute of Aeronautics and Astronautics, Inc., Reston, Virginia.

Novozhilov, V., V., 1959. *The theory of thin shells*, P. Noordhoff Ltd., Groningen, The Netherlands.

O'Brien, T. K., 1982. Characterization of delamination onset and growth in a composite laminate, *Damage in Composite Materials*, ASTM STP 775, Reifsnider, K. L., editor, American Society for Testing and Materials, pp. 140-167.

Peters, S. T., editor, 1998. *Handbook of composites*, Chapman & Hall, second edition.

Powell, S., M., Williams, F., W., Askar, A.,-S. and Kennedy, D., 1998. Local postbuckling analysis for perfect and imperfect longitudinally compressed plates and panels, *AIAA/ASME/ASCE/AHS/ASC Structures, Structural Dynamics, and Materials Conference and Exhibit, 39th, and AIAA/ASME/AHS Adaptive Structures Forum, Long Beach, CA, Apr. 20-23, 1998, Collection of Technical Papers. Pt. 1 (A98-25001 06-39).*

Prevorsek, D. C., Chin, H. B. and Bhatnagar, A., 1993. Damage tolerance: design for structural integrity and penetration, *Composite Structures*, Vol. 23, pp. 137-148.

Rajbhandari, S. P., Scott, M. L., Thomson, R. S. and Hachenberg, D., 2002. An approach to modeling and predicting impact damage in composite structures, *Proceedings-ICAS 2002 23rd International Congress of Aeronautical Sciences*, Grant, I., editor, Optimage Ltd., Edinburgh, U.K.

Reid S. R. and Zhou G., editors, 2000. *Impact behaviour of fibre-reinforced composite material and structures*. Woodhead Publishing, Ltd., Cambridge, England.

Reissner, E. and Stavsky, Y., 1961. Bending and stretching of certain types of heterogeneous aeolotropic elastic plates, *Journal of Applied Mechanics*, Vol. 28, pp. 402-408.

Riccio, A., Scaramuzzino, F. and Perugini, P., 2001. Embedded delamination growth in composite panels under compressive load, *Composites: Part B*, Vol. 32, pp. 209-218.

Rothwell, A., September 1974. An experimental investigation of the efficiency of a range of channel section struts, *Aeronautical Journal*, pp. 426-430.

Shanley, F. R., 1947. Inelastic column theory, *Journal of Aeronautical Science*, Vol. 14, No. 5, pp. 261-268.

Sheinman, I., Kardomateas, G. A. and Pelegri, A. A., 1998. Delamination growth during pre- and post-buckling phases of delaminated composite laminates, *International Journal of Solids and Structures*, No. 1-2, pp. 19-31.

Sheinman, I., and Soffer, M., 1991. Post-buckling analysis of composite delaminated beams, *International Journal of Solids and Structures*, No. 5, pp. 639-646.

Short, G. J., Guild, F. J. and Pavier, M., J., 2001. The effect of delamination geometry on the compressive failure of composite laminates. *Composite Science and Technology*, Vol. 61, pp. 2075-2086.

Sierakowski, R. L. and Newaz, G. M., 1995. *Damage tolerance in advanced composites*, Lancaster, PA, Technomics Publication.

Silberschmidt, V. V., 2006. Effect of micro-randomness on macroscopic properties and fracture of laminates, *Journal of Material Science*, Vol. 41, pp. 6768-6776.

Simitses, G. J., Sallam, S. and Yin, W. L., September 1985. Effect of delamination of axially loaded homogeneous laminated plates, *Journal of American Institute of Aeronautics and Astronautics*, Vol. 23, No. 9, pp. 1437-1444.

Singer, J., Arbocz, J. and Weller, T., 1998. *Buckling Experiments: Experimental Methods in Buckling of Thin-Walled Structures, Basic Concepts, Columns, Beams and Plates-Volume 1*, John Wiley and Sons, Inc., New York.

Singer, J., Arbocz, J. and Weller, T., 2002. *Buckling Experiments: Experimental Methods in Buckling of Thin-Walled Structures, Shells, Built-up Structures, Composites and Additional Topics- Volume 2*, John Wiley and Sons, Inc., New York.

Soutis, C., 2005. Fibre reinforced composites in aircraft construction. *Progress in Aerospace Sciences*, Vol. 41, pp. 143-151.

Sridharan, S., 1982. A semi-analytical method for the post-local-torsional buckling analysis of prismatic plate structures, *International Journal of Numerical Methods for Engineering*, Vol. 18, pp. 1685-1697.

Stavsky, Y., 1964. On the general theory of heterogeneous aeolotropic plates, *Aeronautical Quarterly*, Vol. 15, pp. 29-38.

Stein, M., 1983. Postbuckling of orthotropic composite plates loaded in compression, *Journal of American Institute of Aeronautics and Astronautics*, Vol. 21, No. 12, pp. 1729- 1735.

Thompson, J., M., T. and Hunt, G. W., 1984. *Elastic instability phenomena*, John Wiley and Sons Ltd., Chichester.

Thompson, J., M., T., Tulk, J., D. and Walker, A. C., 1976. An experimental study of imperfection-sensitivity in the interactive buckling of stiffened plates, *Buckling of Structures*, edited by Budiansky, B., Springer-Verlag, Berlin, Germany, pp. 149-159.

Thomson, R. S. and Scott, M. L., 2000. Modelling delaminations in postbuckling stiffened composite shear panels, *Computational Mechanics*, Vol. 26, pp. 75-89.

Vu-Khanh, T., December, 1987. Survey of current status and future trends in reinforced plastics composites, *Polymer Composites*, Vol. 8, No. 6, pp. 363-370.

Wadsworth, J. and Lesuer, D. R., 2000. Ancient and modern laminated composites-from Great Pyramid of Gizeh to Y2K, *Materials Characterization*, Vol45, pp. 289-313.

Wang, S. S., Zahlan, N. M. and Suemasu, H., July 1985. Compressive stability of delaminated random short-fiber composites, Part II – Experimental and analytical results, *Journal of Composite Materials*, Vol. 19, pp. 297-315.

Weaver, P. M., 2002. Designing composite structures: lay-up selection, *Proc Institution of Mechanical Engineers*, Vol. 216, Part G: J Aerospace Engineering, pp 105-116.

Weaver, P. M., 2006. Physical insight into the buckling phenomena of composite structures, *47th AIAA/ASME/ASCE/AHS/ASC Structures, Structural Dynamics, and Materials Conference*, Newport, Rhode Island, AIAA 2006-2031, 1-4 May.

Wiggenraad, J. F. M., Aoki, R., Gadke, M., Greenhalgh, E., Hachenberg, D., Wolf, K. and Bubl, R., 1996. Damage propagation in composite structural elements - analysis and experiments on structures, *Composite Structures*, Vol. 36, pp. 173-186.

Wilkins, D. J., Eisenmann, J. R., R. Camin, A., Margolis, W. S. and Benson, R. A., 1982. Characterizing Delamination Growth in Graphite-Epoxy, *Damage in Composite Materials*, ASTM STP 775, K. L. Reifsnider, Ed., American Society for Testing and Materials, pp. 168-183.

Williams, F. W., Kennedy, D., Anderson, M. S. and Edwards, D. A, 1996. *User manual for VICONOPT. An exact analysis and optimum design program covering the buckling and vibration of prismatic assemblies of flat and curved in-plane loaded, anisotropic*

plates, with approximations for tapered plates, discrete supports and connections, transverse stiffeners and attachments to three-dimensional supporting frames. Release 1.3, Cardiff School of Engineering, University of Wales, Cardiff.

Wright, J. E., 2006. *Compound bifurcations in delamination buckling*. Thesis (PhD). University of Bath, Bath.

Yap, J. W. H., Thomson, R. S., Scott, M. L. and Hachenberg, D., 2004. Influence of post-buckling behaviour of composite stiffened panels on the damage criticality, *Composite Structures*, Vol. 66, pp. 197-206.

Yin, W.-L., June 1988. The effects of laminated structure on delamination buckling and growth. *Journal of Composite Materials*. Vol. 22, pp. 502-517.

Yin, W.-L., Sallam, S. N. and Simitses, G. J., January 1986. Ultimate axial loading capacity of a delaminated beam-plate, *Journal of American Institute of Aeronautics and Astronautics*, Vol. 24, No. 1, pp. 123-128.

Zhang, X., Hounslow, L. and Grassi, M., 2006. Improvement of low-velocity impact and compression-after-impact performance by z-fibre pinning, *Composites Science and Technology,* Vol. 66, pp. 2785-2794.

Results of this thesis were partially presented in the following publication:

Kontis, N., Butler, R., and Hunt, G. W., 2006. Post-buckling of stiffened composite structures with delaminations. *AIAA/ASME/ASCE/AHS/ASC 47th Structures, Structural Dynamics & Materials (SDM) Conference,* Newport, Rhode Island, May 2006.